# Strain-driven tuning of properties in magnetic thin films: Towards Flexible Spintronics

*By*

**Esita Pandey**

**Enrolment No. PHYS11201704013**

**National Institute of Science Education and Research, Bhubaneswar**

*A thesis submitted to the*

*Board of Studies in Physical Sciences*

*In partial fulfillment of requirements*

*for the Degree of*

**DOCTOR OF PHILOSOPHY**

*of*

**HOMI BHABHA NATIONAL INSTITUTE**



**April 2024**

# Homi Bhabha National Institute[1]

## Recommendations of the Viva Voce Committee

As members of the Viva Voce Committee, we certify that we have read the dissertation prepared by **Esita Pandey** entitled **"Strain-driven tuning of properties in magnetic thin films: Towards Flexible Spintronics"** and recommend that it may be accepted as fulfilling the thesis requirement for the awardof Degree of Doctor of Philosophy.

Chairman – Prof. Sanjay Kumar Swain _____ 19/04/2024
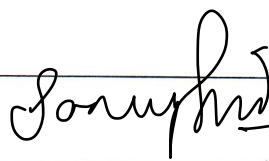
Guide / Convener - Prof. Subhankar Bedanta _____ 19/04/2024.
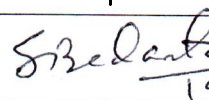
Co-guide - Name & Signature with date (if any) _____

Examiner – Prof. Pranaba Kishor Muduli _____ 19-A-24
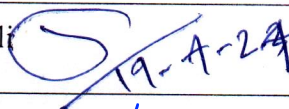
Member 1- Dr. Anamitra Mukherjee _____

Member 2- Dr. Pratap Kumar Sahoo _____ 19/04/2024

Member 3- Dr. Satyaprakash Sahoo _____ 19/04/2024
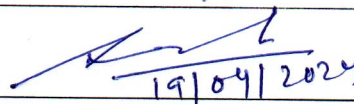
Final approval and acceptance of this thesis is contingent upon the candidate's submission of the final copies of the thesis to HBNI.

I/We hereby certify that I/we have read this thesis prepared under my/our direction and recommend that it may be accepted as fulfilling the thesis requirement.

Date: 19/04/2024.

Place: Jatni

Signature
Co-guide (if any)

Signature
Guide

---

[1] This page is to be included only for final submission after successful completion of viva voce.

# STATEMENT BY AUTHOR

This dissertation has been submitted in partial fulfillment of requirements for an advanced degree at Homi Bhabha National Institute (HBNI) and is deposited in the library to be made available to borrowers under rules of the HBNI.

Brief quotations from this dissertation are allowable without special permission, provided that accurate acknowledgement of source is made. Requests for permission for extended quotation from or reproduction of this manuscript in whole or in part may be granted by the Competent Authority of HBNI when in his or her judgment the proposed use of the material is in the interests of scholarship. In all other instances, however, permission must be obtained from the author.

*Esita Pandey*

Esita Pandey

# DECLARATION

I, hereby declare that the investigation presented in the thesis has been carried out by me. The work is original and has not been submitted earlier as a whole or in part for a degree / diploma at this or any other Institution / University.

*Esita Pandey*

Esita Pandey

# CERTIFICATION ON ACADEMIC INTEGRITY

**Undertaking by the Student:**

1. I, **Esita Pandey**, HBNI Enrolment No. **PHYS11201704013** hereby undertake that the Thesis, titled "**Strain-driven tuning of properties in magnetic thin films: Towards Flexible Spintronics**" is prepared by me and is the original work undertaken by me.

2. I also hereby undertake that this document has been duly checked through a plagiarism detection tool and the document is found to be plagiarism free as per the guidelines of the Institute/UGC.

3. I am aware and undertake that if plagiarism is detected in my thesis at any stage in the future, suitable penalty will be imposed as applicable as per the guidelines of the Institute/UGC.

*Esita Pandey*
25·04·2024
Signature of the Student with date

**Endorsed by the Thesis Supervisor:**

I certify that the thesis written by the Researcher is plagiarism free as mentioned above by the student.

*SBedanta*
25/04/2024.

Signature of the Thesis Supervisor with date

Name: Prof. Subhankar Bedanta

Designation: Professor

Department/Centre: School of Physical Sciences

Name of the CI/ OCC: National Institute of Science Education and Research, Bhubaneswar

# List of Publications arising from the thesis

## Journal

**1.** #Strain-engineered domain structure and their relaxation in perpendicularly magnetized Co/Pt deposited on flexible polyimide, **E. Pandey**, B. B. Singh, P. Sharangi, and S. Bedanta, Nano Ex. 01, 010037 **(2020)**

**2.** #Emergence of sizeable interfacial Dzyaloshinskii-Moriya interaction at cobalt/fullerene interface, **E. Pandey**, B. Ojha, and S. Bedanta, Phys. Rev. Appl. 19, 044013 **(2023)**

**3.** #A perspective on multifunctional ferromagnet/organic molecule spinterface, **E. Pandey**, P. Sharangi, A. Sahoo, S. P. Mahanta, S. Mallik, and S. Bedanta, Appl. Phys. Lett. 123, 040501 **(2023)**

## Communicated

**1.** #Structural deformation and irreversible magnetic properties in Co/Pt and Co/Pd thin films prepared upon Kapton, **E. Pandey** and S. Bedanta *et al.*

## Manuscript in preparation

**1.** #Strain-driven domain wall dynamics and spin-reorientation transition in perpendicularly magnetized Co/Pd film for flexible spintronics, **E. Pandey** and S. Bedanta *et al.*

**2.** #Tuning PMA and iDMI strength via strain in flexible $[Co/Pd]_N$ multilayer stack, **E. Pandey** and S. Bedanta *et al.*

**3.** #Strain modulated magnetic properties of flexible Pd/Co/$C_{60}$ thin film, **E. Pandey** and S. Bedanta *et al.*

#Publications related to the thesis

## Others

**1.** Spinterface-induced modification in magnetic properties in $Co_{40}Fe_{40}B_{20}$/fullerene bilayers, P. Sharangi, **E. Pandey**, S. Mohanty, S. Nayak and S. Bedanta, The Journal of Physical Chemistry C 125 (45), 25350 **(2021)**

**2.** Magnetization reversal and domain structures in perpendicular synthetic antiferromagnets prepared on rigid and flexible substrates, S. Mohanty, M. Sharma, A. K. Moharana, B. Ojha, **E. Pandey**, B. B. Singh and S. Bedanta, JOM 74, 2319 **(2022)**.

 **3.** Effect of fullerene on the anisotropy, domain size and relaxation of a perpendicularly magnetized Pt/Co/$C_{60}$/Pt system, P. Sharangi, A. Mukhopadhyaya, S. Mallik, **E. Pandey**, B. Ojha, Md. E. Ali and S. Bedanta, J. Mater. Chem. C 10, 17236 **(2022)**

*Esita Pandey*

Esita Pandey

*Dedicated to my parents*

# ACKNOWLEDGEMENTS

me with different experiments, simulations and analysis whenever needed. I also thank all my lab mates Dr. Palash Kumar Manna, Dr. Minaxi Sharma, Dr. Anupama Swain, Dr. Bibhuti Bhushan Jena, Dr. Antarjami Sahoo, Dr. Koustuv Roy for many fruitful discussions on different topics. I also thank all my juniors Mr. Kshitij Singh Rathore, Ms. Swayang Priya Mahanta, and Ms. Rupalipriyadarsini Chhatoi for their help in many academic and non-academic work.

It is needless to mention that the thesis work would not have been completed without the assistance and support of my friend, lab mate, and husband Mr. Brindaban Ojha. I consider myself really fortunate to have someone as kind as him during my PhD adventure. In every up and down, he always stood by me. Over this whole process, we worked together and had several discussions about problems pertaining to research. His presence, belief, and support helped me to overcome the difficult times and continue producing good work.

Last but not least, I extend my special thanks to my parents Mr. Gopal Chandra Pandey and Mrs. Joli Pandey for their unconditional love, care, and support throughout this long journey. I also thank my brothers (Debjit, and Subhojit), and my sister (Ispita) for being there all the time and pampering my all-mood swings. I extend my heartfelt thanks to my in-laws for being very supportive during this journey. A special thanks also to my best friends Lovely and Swati for being available whenever I needed them in different phases of my PhD journey. You all are the backbone of my life and I thank you for being there in every situation.

# CONTENTS

# Summary

Today's electronic devices are rapidly achieving flexibility, giving rise to a new field of study known as "flexible electronics". A few remarkable inventions in this field are flexible solar cells, flexible displays, flexible sensors, and electronic skin. Apart from flexibility, they are also light in weight, lower in cost, easily portable, and provide comfort for healthcare applications in comparison to their rigid counterparts. As spintronic devices are an integral part of future electronics, today's spintronic devices must become flexible to bridge the gap between these two fields. In this context, as perpendicular magnetic anisotropic (PMA) thin films are prime components for spintronic devices, a lot of research work is going on fabricating flexible counterparts of them. This will have enormous applications starting from data storage technology, and sensors to healthcare applications. Integration of a flexible magnetic film into a curvilinear surface generates strain on the film. Depending upon the magnetostriction coefficient ($\lambda$) of a ferromagnet, it may or may not modify the magnetic properties of the film under strain. If $\lambda \approx 0$, the magnetic properties will remain constant under varied strain conditions. However, if $\lambda \neq 0$, then a significant strain tuning of magnetic property become possible. In this thesis work, Co ($\lambda \neq 0$) based standard PMA systems are considered (i.e., Co/Pt and Co/Pd), and the impact of strain application on both the structural and magnetic properties of the samples are studied. The samples are prepared upon both rigid Si and flexible polyimide (PI) substrates. To generate strain, the flexible samples are mounted upon both convex and concave-shaped molds (of different radii) which generate tensile and compressive strain (in the sample plane), respectively.

First, we studied the structural and magnetic properties of a flexible Pt/Co/Pt film at both unstrained (i.e., flat) and strained (i.e., bent) states of the sample. It is important to note that no structural deformation (e.g., cracking, buckling) is observed within the elastic limit of applied strain. However, the impact of tensile and compressive strain was found to be opposite on modulating magnetic properties (e.g., magnetization reversal, magnetic relaxation, domain wall dynamics, etc.), owing to the induction of magnetoelastic anisotropy in the system. As the thickness of the sample was far from the spin-reorientation transition (SRT) region of Co/Pt, the impact of compressive strain was lower than the tensile strain. In this context, we further prepared Pd/Co/Pd films by varying Co thickness and found

that the flexible samples close to the SRT of Co/Pd show high strain sensitivity (within the elastic limit). Application of tensile strain increases the coercivity, whereas compressive strain decreases it, due to an opposite modulation of PMA under strain. Further, the domain wall (DW) velocity increases (~3 times) under compressive strain in comparison to the unstrained state of the sample. Within the elastic limit of strain, all the changes are reversible in nature. We also investigated the impact of a high-strain application (beyond the elastic limit) on both the Co/Pt and Co/Pd samples which inevitably introduced significant structural damage (e.g., cracking, buckling) to the film. In addition, magnetic properties alter significantly and become irreversible, indicating the impact of a plastic strain. As asymmetric and/or symmetric superlattice PMA structures show high interfacial Dzyaloshinskii-Moriya interaction (iDMI), they are a potential candidate for chiral DW-based device applications. In this context, we prepared a series of asymmetric $Pd/Co/C_{60}$ samples and found a non-zero iDMI (~ $0.11 \text{mJ/m}^2$) originating from the $Co/C_{60}$ interface. Here, the spinterface formed at the $Co/C_{60}$ interface helps to tune both the DW velocity and relaxation mechanism of the samples. The impact of strain application on the magnetic properties (e.g., magnetization reversal phenomena, DW dynamics, etc.) of the $Pd/Co/C_{60}/Pd$ samples is also investigated. In order to understand the impact of elastic strain application on the iDMI strength, we further prepared multilayered $[Co/Pd]_N$ samples, where, N = 1, 2, 3, 5, 10. Micromagnetic simulations are performed to mimic the experimentally obtained hysteresis loops and extract the iDMI strength qualitatively. It revealed that the strength of both the magnetic anisotropy and iDMI can be tailored significantly via elastic strain. Thus, the tuning of magnetic anisotropy, DW velocity, and iDMI strength via strain is extremely promising for fabricating high-performance flexible spintronic devices.

# List of Figures

orientation of the analyzer and polarizer are shown w.r.t the normally reflected amplitude ($N$) and Kerr amplitude ($K$). The image is taken from ref. [123].

**2.10:** Three different kinds of MOKE geometries, (a) L-MOKE, (b) T-MOKE, and (c) P-MOKE depending upon the magnetization orientation of the sample and the plane of incidence of the polarized light.

**2.11:** (a) Schematic illustration of the domain image formation process using MOKE-based microscopy setup, (b) MOKE microscopy facility available in our laboratory (LNMM) at NISER. The concept of the schematic is taken from ref. [129].

**2.12:** (a) Side and (b) top view of the sample and coil mounting geometry for pulsed magnetic field-induced DW velocity measurement using a MOKE microscope.

**2.13:** Schematic illustration of the DW velocity measurement protocol. The nucleated, propagated, and subtracted domain images are shown in the right-side column. The area of each domain image is 415 μm × 375 μm. The concept of the image is taken from ref. [134].

**2.14:** (a) The tilted $x$-$y$ plane of the electromagnet originates a tilted IP magnetic field ($\pm H_x$) which in turn gives rise to an OP magnetic field, and (b) Tilt corrected properly aligned electromagnet where the IP applied field does not have any component along OP direction. The concept of the image is taken from ref. [81].

**2.15:** Schematic diagram of asymmetric domain propagation in the presence of both OP pulsed field and (a) positive IP bias field, (b) negative IP bias field. R and L represent the right, and left sides of the DW respectively. Here, $\pm S_x$ and $S_y$ represent the DW displacement along $\pm x$ and $y$ directions, respectively. (c) A schematic of the DW velocity ($v_{DW}$) vs. IP field ($\pm H_x$) plot (at a constant $H_z$), in the presence and absence of DMI. The minima in the velocity curve give a measurement of the DMI field ($H_{DMI}$) present in the sample. The concept of the image is taken from ref. [140].

**2.16:** (a) A schematic of the detection coil geometry and voltage vs. sample position plot while centering a sample in the SQUID magnetometer. (b) The MPMS3 SQUID magnetometer facility is available in our laboratory (LNMM, NISER).

**2.17:** Schematic representation of (a) two-step model describing XMCD technique, (b) XAS and XMCD spectra obtained for right and left circularly polarized X-rays. The image is taken from ref. [146].

**2.18:** (a) A general layout of the BACH beamline is presented and the image is taken from ref. [153], (b) XAS and XMCD measurements performed at the end station of BACH beamline, Elettra synchrotron facility, in Italy.

**2.19:** Schematic of four-probe measurement geometry, the image is taken from ref. [155], (b) a home-made four-point-probe set-up used for measuring the sheet resistance of thin films.

**3.1:** Experimental strain generation method using (a) convex and (b) concave molds. The sample is fixed on the mold using Kapton tapes. (c-d) Schematic of the tensile and compressive strain generation in the sample at convex and concave geometries, respectively.

# List of Tables

# List of Abbreviations

| | |
|---|---|
| BSE | Back-scattered electron |
| CVD | Chemical vapor deposition |
| CCD | Charge-coupled device |
| DOS | Density of states |
| DW | Domain wall |
| DMI | Dzyaloshinskii-Moriya interaction |
| EA | Easy axis |
| FM | Ferromagnet |
| FESEM | Field emission scanning electron microscope |
| HA | Hard axis |
| HDD | Hard disk drive |
| HM | Heavy metal |
| IP | In-plane |
| IMA | In-plane magnetic anisotropy |
| iDMI | Interfacial Dzyaloshinskii-Moriya interaction |
| LL | Landau – Lifshitz |
| LLG | Landau-Lifshitz-Gilbert |
| LCP | Left circularly polarized |
| LINAC | Linear accelerator |
| MA | Magnetic anisotropy |
| MEA | Magnetoelastic anisotropy |
| MCA | Magnetocrystalline anisotropy |
| MOKE | Magneto-optic Kerr effect |
| MRAM | Magnetic random-access memory |
| 1D | One-dimensional |
| OM | Organic molecule |
| OP | Out-of-plane |
| PMA | Perpendicular magnetic anisotropy |
| PVD | Physical vapor deposition |
| PSM | Plane strain modulus |

| | |
|---|---|
| PI | Polyimide |
| QCM | Quartz crystal microbalance |
| RCP | Right circularly polarized |
| RT | Room temperature |
| RPM | Rotations per minute |
| RKKY | Ruderman, Kittel, Kasuya, and Yosida |
| SEM | Scanning electron microscope |
| SE | Secondary electron |
| SOC | Spin-orbit coupling |
| SOT | Spin-orbit torque |
| STT | Spin-transfer-torque |
| SRT | Spin-reorientation transition |
| SQUID | Superconducting quantum interference device |
| 2D | Two-dimensional |
| UHV | Ultra-high vacuum |
| XAS | X-ray absorption spectra |
| XRD | X-ray diffractometer |
| XMCD | X-ray magnetic circular dichroism |
| XRR | X-ray reflectivity |

**Chapter 1: Introduction and Fundamentals**

**1.1 Introduction:**

The theoretical proposal of flexible electronics was introduced nearly a few decades ago. However, the first experimental achievement was gained in 1960, during the space race of fabricating lighter solar cells for satellites [1,2]. In this context, Si wafers successfully thinned down to ~100 μm and were used in satellites to increase the power-to-weight ratio with added flexibility. In successive years, a large step toward flexibility and processability was made with the development of conductive polymers, organic semiconductors, and amorphous silicon which served as the foundation for flexible electronic device applications [3–5]. The rapid expansion in the field of "flexible electronics" brought a remarkable evolution in the notion of traditional rigid electronic devices. These smart electronics are light-weight, less costly, suitable for large-scale fabrication, and provide superior comfort in healthcare applications than their rigid counterparts [6]. Flexible solar cells, flexible displays, flexible sensors, and electronic skins are only a few examples of numerous important advancements [2]. The successful commercialization of flexible electronics urgently requires flexible counterparts of all rigid spintronic devices. As magnetic thin films are an essential component of spintronic devices, considerable effort has been given to fabricate flexible counterparts of them. Flexible magnetic films can be prepared via two methods, namely (i) transfer and bonding, and (ii) direct fabrication on a flexible substrate [7]. In the transfer and bonding approach, high-quality flexible film can be prepared, however, it does not support large-area production and requires high cost. The direct fabrication technique can overcome the above issues, however, requires finding a suitable flexible substrate that survives the film deposition techniques. In this context, several substrates starting from thin metal foils, to flexible glass to organic polymers are explored [6]. Among them, organic polymers are found to be most suitable due to their high mechanical flexibility, good thermal stability, low elastic modulus, and safe bending radii down
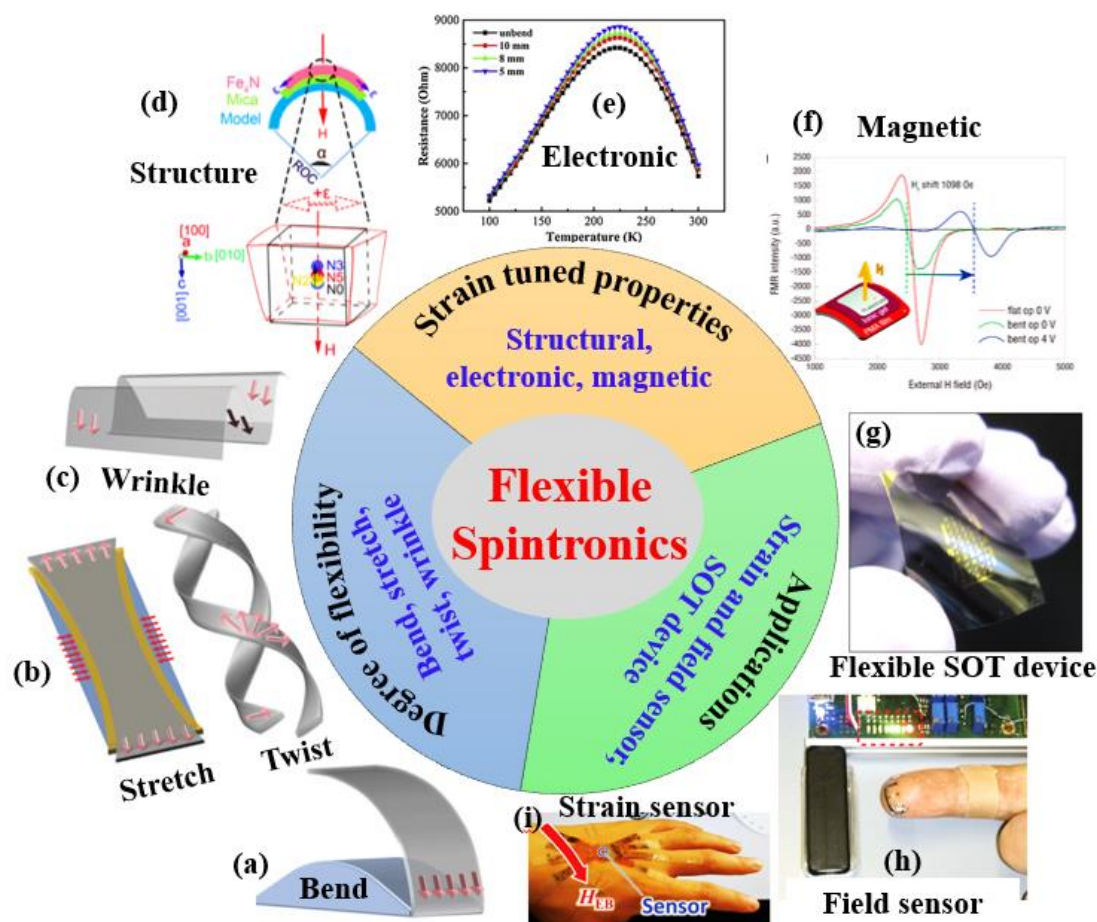
Figure 1.1 Overview of the field of flexible spintronics. Different degrees of flexibility proposed in the field are (a) bend, (b) stretch, twist, and (c) wrinkle [7]. The impact of bending-induced strain on the (d) on the structural property of $Fe_4N$/mica [8], (e) electronic property of LSMO [9], and (f) magnetic property of Co/Pt [10] films. A few important inventions are (g) flexible spin-orbit torque (SOT) devices [11], (h) flexible field, and (i) strain sensors [12,13] for flexible spintronics and healthcare monitoring applications. The figures are taken from the references that are cited along with each caption.

to 5 mm (for 100 μm thick film). A few common polymers used in flexible film preparation are polyethylene terephthalate (PET), polyethylene naphthalate (PEN), polyimide (PI), polydimethylsiloxane (PDMS), polycarbonate (PC), polythersulfone (PES), and polyetheretherketone (PEEK). In comparison to the single crystal rigid substrates, these

polymers have a high surface roughness which requires a spin-coating or thick buffer layer deposition before the thin film preparation. Thus, recently a few layered materials (e.g., mica, graphene, etc.) are also considered as potential flexible substrates to grow epitaxial films [7]. It is worth mentioning that the use of flexible substrates also allows to study the impact of systematic mechanical strain on the magnetic film, which overcomes the scarcity of epitaxial strain and helps in understanding the physics of flexible spintronics. Different degrees of flexibility proposed in the field are, bending, stretching, twisting, wrinkling, etc. Bending and stretching modes generate uniaxial stress ($\sigma$) whereas twisting and wrinkling modes generate multidimensional stress. The response of a magnetic film to such applied strain depends on the magnetostrictive co-efficient ($\lambda$) of the material [14]. The mechanical strain may affect the crystal structure, band structure, and electronic structure of a magnetic thin film. In addition, the modulation in magnetic properties observed under strain is known as the inverse magnetostrictive effect or the Villari effect [14]. The applied strain induces a magnetoelastic anisotropy (MEA), which in turn affects the global anisotropy of a magnetic system and changes the magnetic properties. Thus, for flexible magnetic thin films, three conceivable outcomes are possible in the strained environment, (i) positive response ($\lambda \neq 0$), (ii) negative response ($\lambda \neq 0$), and (iii) resilience ($\lambda = 0$). The durability or resilience of flexible magnetic films is essential in the realm of wearable spintronic applications, whereas the system with positive and negative responses has significant potential for sensor and healthcare applications. An overview of the field of flexible spintronics is shown schematically in Fig. 1.1. The different modes of flexibility, e.g. bend, stretch, twist, and wrinkle are shown schematically in Fig. 1.1 (a-c). The impacts of bending-induced strain on the structural property of $Fe_4N$/mica (Fig. 1.1 (d)), electronic property of LSMO (Fig. 1.1 (e)), and magnetic properties of Co/Pt (Fig. 1.1 (f)) are shown briefly. In addition, a few important inventions e.g., flexible SOT devices, field sensors, strain sensors, etc. are also depicted pictorially in Fig. 1.1 (g-i).

Magnetic anisotropy has always been at the center of research in the magnetism community as it not only decides the direction of magnetization but also controls the efficiency and power consumption of spintronic devices. The broad family of magnetic thin films can have mainly two types of magnetic anisotropy (MA), (i) in-plane magnetic anisotropy (IMA) and (ii) perpendicular magnetic anisotropy (PMA). However, tilted magnetic anisotropy is also reported in a few special cases [15]. In this context, flexible in-plane (IP) magnetic anisotropic films are fabricated and the impact of external strain on their electronic and magnetic properties is studied quite well [16,17]. However, the research on flexible PMA thin films is still in its early stages. PMA thin films are essential in the field of magnetic data storage technology, such as hard disk drives (HDDs) and magnetic random-access memory (MRAM) [18,19]. Their high PMA enables improved areal density while reducing crosstalk between adjacent bits. This provides a better signal-to-noise ratio leading to more consistent data reading and writing processes. In addition, the high PMA provides better thermal stability compared to the IMA thin films. This feature is essential for data retention and durability in high-temperature conditions, which make them suitable for industrial and automotive applications. Furthermore, the PMA thin films are used in various sensor applications, e.g., magnetoresistive sensors, magnetic field sensors, biosensors, etc. [20,21]. Notably, PMA thin films comprised of heavy metal (HM)/ferromagnet (FM) systems have the potential to originate chiral domain wall (DW) and skyrmions, due to the presence of significant Dzyaloshinskii-Moriya interaction (DMI) at the HM/FM interface. A symmetric magnetic stack (say, HM1/FM/HM1) do not originate a significant effective DMI, owing to the cancellation of DMI from the top and bottom HM/FM interfaces. In contrast to this, asymmetric structures (say, HM1/FM/HM2, HM1/FM/Oxide) were found to generate a strong DMI, making them a promising candidate in the field of spintronics and spinorbitronics [22–25]. As a HM layer enhances the damping of a system, the search for alternative DMI host material composed of light atoms has also drawn enough

research attention. A few recent studies revealed that the light atom carbon (C) based graphene can originate a significant Rashba-DMI from the graphene/Co interface [26,27]. Thus, to find alternative DMI host candidates, it is important to explore different FM/C-based interfaces. In this context, fullerene ($C_{60}$), carbon nanotubes (CNTs) could be promising due to their expected high spin-orbit coupling (SOC) strength originating from the curved structure [28,29]. Thus, both the symmetric and asymmetric HM/FM-based stacks are very promising for future spintronic device applications. However, only little is known about the impact of strain application on the magnetic properties of flexible PMA thin films. A few reports show the possibility of modifying the strength of PMA via strain in flexible Co/Pt thin film [30,31]. Further, magnetization switching in a flexible Co/Pt thin film is also accomplished by passing a modest voltage through an ionic gel [10]. Recently, the strength of DMI in the Co/Pt system was shown to be regulated by strain, paving the door for strain-based stabilization of chiral structures and skyrmions [32]. A few recent investigations have also reported on the fabrication of flexible spin valves employing perpendicular anisotropic Co/Pd structures [33,34]. Apart from this, significant attention is still required in fabricating symmetric and asymmetric flexible PMA films and studying their magnetic characteristics at various strained conditions. In this context, this thesis focuses on fabricating both symmetric and asymmetric flexible PMA films and studying their structural and magnetic properties systematically under bending-induced strain. Flexible symmetric (Pt/Co/Pt, Pd/Co/Pd) and asymmetric (Pd/Co/fullerene) thin films are deposited upon both rigid Si and flexible polyimide substrates and their basic magnetic properties (e.g., magnetization reversal, magnetic anisotropy, DW dynamics, DMI, etc.) are studied. Further, the impact of bending-induced strain (tensile/compressive) on the structural and magnetic properties of the flexible films is investigated in detail.

The first chapter of this thesis is devoted to the introduction and basic ideas required to comprehend the thesis work. The second chapter discusses all the experimental techniques

employed throughout the thesis work. The third chapter studies the impact of applying elastic strains on both the structural and magnetic properties (e.g., magnetization reversal, relaxation dynamics, and magnetic anisotropy) of symmetric Pt/Co/Pt flexible film. A reversible and opposite modulation of magnetic properties is observed under bending-induced tensile and compressive strain. Chapter 4 discusses the remarkable modulation in DW dynamics, SOC, and magnetization reversal phenomena via strain in a symmetric Pd/Co/Pd flexible film, owing to the high $\lambda$ of the Pd/Co system. Notably, a switching of magnetic anisotropy from out-of-plane (OP) to IP direction is also achieved by applying a minimal strain. The fifth chapter shows the impact of applying a large peeling strain (beyond the elastic limit) on the structural and magnetic properties of both flexible Pt/Co and Pd/Co films deposited on Kapton. Structural deformation, e.g., cracking, buckling, and blister formation is observed under such high strain. Further, the damage to the film introduced irreversible changes in the magnetic properties of the film. In Chapter 6 of the thesis, asymmetric Pd/Co/$C_{60}$/Pd samples are prepared and a non-zero interfacial DMI is reported for the first time from a Co/$C_{60}$ interface. The impact of interfacial hybridization (present at the Co/$C_{60}$ interface) on the magnetic properties is also studied in detail. Further, the effect of applying bending-induced strain on the magnetic properties of the samples is also explored. In Chapter 7, we discussed the magnetic properties of [Co/Pd]$_N$ multilayer structure. With increasing N, a systematic change in coercivity, loop shape, and domain structure is observed. Micromagnetic simulations revealed that a systematic modification in the magnetic anisotropy, demagnetizing energy, and DM interactions are the key factors behind the observed changes. It also indicates that the strength of the magnetic anisotropy and the interfacial DMI (iDMI) possibly could be tailored via external strain. As a result, while adding to the field of flexible spintronics, this thesis work also demonstrates that strain engineering could be a promising technique to meet the quest of designing smaller, faster, and more energy-efficient future spintronic devices.

## 1.2 Magnetic anisotropy:

Magnetic anisotropy is defined as the directional dependence of magnetic properties (e.g., spontaneous magnetization, coercivity, magnetization reversal, etc.) in any material. The shape of a hysteresis loop (*M-H* or *B-H* curve) is strongly affected by the magnetic anisotropy of a material. As magnetic anisotropy holds significant importance in deciding the performance of a spintronic device, a thorough understanding of the subject is very crucial. Depending on the origin, there could be several types of magnetic anisotropy as mentioned in the following [35,36], (a) magnetocrystalline anisotropy (origin is spin-orbit coupling), (b) shape anisotropy (origin is dipolar interaction), (c) stress anisotropy (origin is magnetostriction and SOC), (d) surface/interface anisotropy (origin is interfacial in nature).

**1.2.1 Magnetocrystalline anisotropy:** Magnetocrystalline anisotropy (MCA) arises mainly due to the spin-orbit coupling (SOC) of a material. In a lattice composed of atoms, the atomic orbitals having nearly quenched orbital momentum are coupled strongly with the lattice. This orbit-lattice coupling is considered strong compared to the spin-orbit coupling because unlike spins the external magnetic field cannot rotate the orbital magnetic moments. Thus, the spin is coupled to the orbit, and the orbit is coupled to the lattice. Therefore, when a magnetic field is applied to rotate the spin of an electron, it gets affected by the SOC. Here, the energy required to align the spins is mainly the energy needed to overcome the SOC [36]. This energy is well known as the magnetic anisotropy energy. Along the easy axis (EA) the energy required to align the spins will be minimal, whereas along the hard axis (HA) the energy will be maximum. In a crystalline material, the spontaneous magnetization aligns along a certain crystal axis direction, known as the EA. Here, as the nature of anisotropy is related to the crystallinity of the material, it is well-known as magnetocrystalline anisotropy or MCA. The MCA energy ($E_{crys}$) can be represented as a series expansion of the direction cosines ($\beta$) of saturation magnetization ($M_s$) w.r.t the crystal axes, as written below [35,36],

$$E_{crys} = E_0 + \sum_{ij} a_{ij}\beta_i\beta_j + \sum_{ijkl} a_{ijkl}\beta_i\beta_j\beta_k\beta_l \qquad (1.1)$$

where, *a* is the anisotropy energy coefficient. Depending upon the crystallinity (e.g., uniaxial, cubic, or hexagonal) there can be one or several EA and HA in a crystalline material. For uniaxial anisotropy, only one EA exists in between 180° intervals. However, for cubic anisotropy two EAs are located mutually perpendicular to each other within a 180° interval.

**1.2.2 Shape anisotropy:** In the case of a polycrystalline material the random orientation of its grains does not contribute to MCA. Instead, here shape anisotropy comes into play due to the dipolar interaction. In the case of finite size of samples free poles appear at their surfaces. Depending on the shape it may or may not create a preferential orientation for the magnetization. In the case of a spherical shape, no preferential orientation of magnetization is found as it has the same diameter in all directions. However, if we consider a rectangular shape then the number of free poles along the short axis will be higher than that of the long axis. These free poles will generate a stray field outside the object which in turn will generate a strong demagnetizing field inside the object. Thus, the total field acting inside the material will be reduced. To reduce such stray fields the magnetization of the object tries to align along the long axis. Thus, the shape of a material also creates a preferential orientation for its magnetization, known as shape anisotropy. In general, the stray field energy density for a magnetic sample is given by [35,36],

$$E_{stray} = -\frac{1}{2}\int \mu_0 \boldsymbol{M}.\boldsymbol{H_{demag}}\, dV \qquad (1.2)$$

where, $H_{demag}$ is the demagnetizing field present inside a sample. For a homogeneously magnetized specimen, $H_{demag} = -N.M$, which depends on both the magnetization and the shape of a specimen. For an infinitely long and extremely thin plate, the stray field energy can be written as [35,36],

$$E_{stray} = \frac{1}{2}\mu_0 M^2 cos^2\theta \tag{1.3}$$

where, $\theta$ is the angle between the magnetization ($M$) and the normal of the sample plane (i.e., $z$-axis). For $\theta = 90°$, the stray field energy becomes minimum, which indicates that the stray field energy favours the magnetization to be oriented in the sample plane. Thus, it induces an IP magnetic anisotropy in the magnetic thin films and multilayers. To reduce the stray field further, a specimen is usually divided into domains having different spontaneous magnetization.

**1.2.3 Stress anisotropy:** Stress anisotropy arises due to the presence of stress/strain in a magnetic material. In other words, applying mechanical pressures or stresses to a material can change the alignment of its magnetic domains or spins. Magnetostriction plays a crucial role in this context. Thus, to understand the origin of such stress anisotropy we will first discuss about the direct and inverse magnetostrictive effects.

**Direct and inverse magnetostrictive effects:** Magnetostriction is the phenomenon where the application of a magnetic field changes the dimension of a material [14,37,38]. In the year 1842 Joule found that the length of a Fe rod changes when magnetized by applying a field along its length. This effect is known as the Joule effect [39]. The origin of magnetostriction lies in the SOC of a material. Due to the SOC, the electron's spin is coupled to the orbit, and the orbit is coupled to the lattice as explained earlier. The relation between SOC and magnetostriction can be explained in a crude way as shown in Fig. 1.2. Above Curie temperature ($T_C$), all the spins of a FM are randomly oriented, whereas, below $T_C$ they achieve a spontaneous magnetized state due to the exchange interaction. Such alignment of spins causes a slight alignment of the electron orbits as they are coupled via SOC and induce spontaneous magnetostriction in the material, as shown in Fig. 1.2. When a magnetic field is applied along a non-easy direction the rotation of the spin moments further introduces field-induced magnetostriction in the material.

However, the rotation of the electron orbit as shown in Fig. 1.2 is only for illustration purposes and is far from reality. In reality, only a small orientation of the electronic orbit takes place and hence, the magnitude of magnetostrictive strain becomes very small. The magnetostrictive strain is denoted by $\lambda$ $(= \frac{change\ in\ length}{original\ length} = \frac{\Delta l}{l})$, to distinguish it from the strain $\varepsilon$ that occurs due to an applied stress $\sigma$. Depending upon the material, $\lambda$ can be either positive (tensile strain), negative (compressive strain), or even zero [40,41]. However, the magnitude of $\lambda$ is usually very small ($\sim 10^{-5}$) even for highly magnetic materials owing to their quenched orbital angular momentum. Generally, a strain gauge is used to measure the magnetostrictive strain, where the change in length is measured in terms of resistance. Due to the smallness of magnetostriction, the impact of the direct magnetostrictive effect is usually neglected for real-life applications. However, an inverse effect also exists where the application of stress changes the magnetic properties of a sample, known as the inverse magnetostrictive effect or the Villari effect [14].
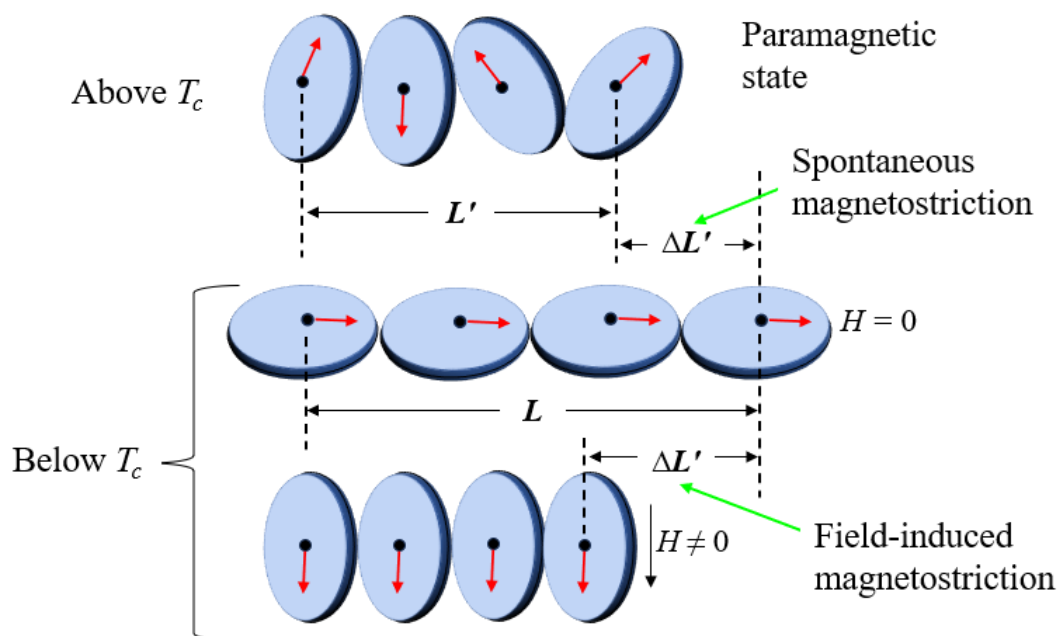


Figure 1.2. Schematic representation of the mechanism of magnetostriction. The concept of the image is taken from ref. [37].

The anisotropy associated with this effect is known as stress-induced anisotropy or magneto-elastic anisotropy (MEA). However, under large applied stresses, permanent deformation occurs which leads to strong irreversible changes in structural and magnetic properties. If a material has isotropic magnetostriction ($\lambda_i$) then the magnetoelastic energy per unit volume can be written as [14],

$$E_{MEA} = \frac{3}{2}\lambda_i\sigma sin^2\theta \tag{1.4}$$

where, $\sigma$ is the applied stress and $\theta$ is the angle between the saturation magnetization ($M_S$) and the applied stress axis. Stress anisotropy is also uniaxial in nature, where the anisotropy constant can be written as, $K_{MEA} = \frac{3}{2}\lambda_i\sigma$. The strength of $E_{MEA}$ depends on the sign of the product of $\lambda_i\sigma$. If $\lambda_i\sigma = (+)$ve, $E_{MEA}$ will be minimum at $\theta = 0°$, indicating that the EA will be oriented along the stress axis. Figure 1.3 represents a simple example of this effect considering a specimen with positive magnetostriction ($\lambda_i > 0$). Initially, the specimen is in a demagnetized flux closure state, as depicted by four domains of different colours. Upon application of tensile stress ($\sigma > 0$), the product of $\lambda_i\sigma$ becomes positive which prefers the growth of domains parallel to the stress axis. Whereas the perpendicular domains contract as they possess high $E_{MEA}$. With further increasing stress, two 90° domains disappear giving rise to a two-domain state which are parallel to the stress axis. Thus, the stress axis becomes EA when $\lambda_i\sigma > 0$. In the other case, if $\lambda_i\sigma = (-)$ve, then the stress anisotropy will act along a direction i.e., perpendicular to the stress axis. Thus, applied stress alone can induce an EA of magnetization, in the absence of other anisotropies. However, in the presence of other anisotropies (e.g., crystal or interface anisotropy) the EA is decided by the stronger one. The strain generated via different methods e.g., lattice-mismatch, temperature annealing, and mechanical deformation can originate a MEA in the magnetic thin films and multilayers.
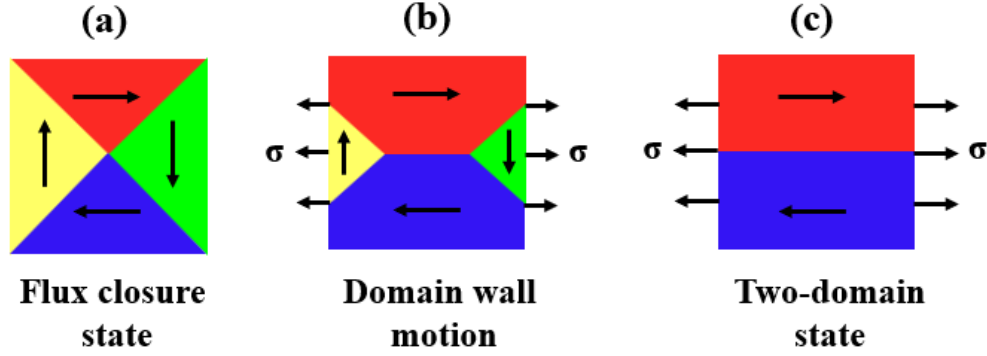
Figure 1.3. Schematic of the magnetization orientation in a specimen having positive magnetostriction ($\lambda_i > 0$) under the application of tensile stress ($\sigma > 0$). (a) The initial demagnetized state of the specimen, (b) the application of tensile stress helps to grow the domains parallel to the stress axis, and (c) the final two-domain state in the presence of high stress [14,42]. The concept of the image is taken from ref. [36].

**1.2.4 Surface and interface anisotropy:** All the above-mentioned anisotropies originate from the volume of the system and hence give rise to mainly a volume anisotropy ($K_V$), which prefers to lie in the plane of the sample. However, in the case of reduced dimensionality, e.g., for ultrathin magnetic films, the surface/interface plays a crucial role due to the broken inversion symmetry there. Thus, a surface/interface anisotropy ($K_S$) comes into play which may dominate the volume anisotropy. Hence, the effective anisotropy ($K_{eff}$) of a magnetic system can be divided phenomenologically into two parts as written below [35,43,44],

$$K_{eff} = K_V + \frac{2K_S}{t} \tag{1.5}$$

where, $t$ is the thickness of the ferromagnetic film. Factor 2 in the second term of the right-hand side is due to the two surfaces or interfaces of a magnetic film where the inversion symmetry is found to be broken. Depending upon the thickness ($t$) of the magnetic film a sample may have an IP or an OP magnetic anisotropy, as shown in Fig. 1.4. If we plot $K_{eff}.t$

vs. $t$, then for $t > t_C$, the sample will have an IP anisotropy due to the dominant volume contribution. Whereas, for $t < t_C$, the sample will have an OP anisotropy due to the dominance of surface contribution. Thus, above a critical thickness ($t_C$) the spin-reorientation transition (SRT) takes place which changes the anisotropy from the OP to the IP direction. At $t_C$, as the effective anisotropy goes to zero, it can be deduced as, $t_C = -\frac{2K_S}{K_V}$. The slope of the $K_{eff}.t$ vs. $t$ curve helps to determine $K_V$, whereas the intercept helps to determine the surface anisotropy ($K_S$), as indicated in Fig. 1.4 [35,43]. As the shape anisotropy has a dominant volume contribution ($K_V$), the IP magnetic anisotropy is usually negative, whereas the OP anisotropy is positive. Apart from the above-discussed anisotropies, the magnetization of a magnetic material also can be influenced by several external stimuli such as magnetic annealing, stress annealing, plastic deformations, temperature changes, and magnetic irradiation. These processes also may induce an anisotropy to magnetic materials known as induced magnetic anisotropy [45].
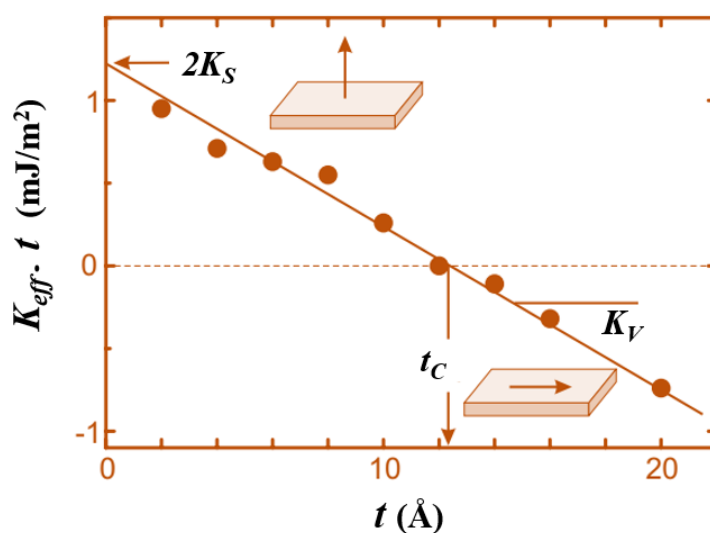


Figure 1.4. SRT is observed in a Co/Pd multilayer by varying the thickness ($t$) of the Co layer. Here the slope of the graph represents volume anisotropy ($K_V$) whereas the intercept represents surface anisotropy ($K_S$) [35,43]. The image is taken from ref. 35.

**1.3 Magnetic Interactions:** The behaviour of a magnetic material is controlled by different kinds of magnetic interactions that act between the magnetic moments (such as atomic or molecular spins). These interactions are essential in determining the overall magnetic characteristics of a substance. Several kinds of magnetic interactions that can exist in a magnetic material are as follows, exchange interaction (direct and indirect), magnetostatic or dipolar interaction, anisotropic interaction, and Zeeman interaction [35,46].

**1.3.1 Exchange interaction:** The exchange interaction acts between the spins of two neighbouring atoms. It is short-range and strongest interaction between two adjacent magnetic spins which decides the magnetic order in a material. Considering all the nearest neighbour atomic spins the exchange energy for a magnetic system can be written as [35,46],

$$E_{exchange} = -\sum_{ij} J_{ij} \boldsymbol{S_i} \cdot \boldsymbol{S_j} \qquad (1.6)$$

where, $S_i$ and $S_j$ are the two neighbouring spins and $J_{ij}$ is the exchange coupling constant between these two spins. If $J_{ij} > 0$, the neighbouring spins are coupled parallel to each other leading to a ferromagnetic order. However, if $J_{ij} < 0$, the adjacent spins are aligned antiparallel giving rise to an anti-ferromagnetic order. When the two adjacent spins directly interact with each other, it is called a direct exchange interaction. However, it cannot explain magnetic ordering in all materials due to inadequate direct overlap between the nearest atomic orbitals. Hence, several indirect exchange interactions also have been explored as discussed below [46].

**RKKY interaction:** This indirect exchange interaction acts between two metallic magnetic ions mediated by a conduction electron [47]. Here, the magnetic moment of a metallic ion induces spin-polarization to the conduction electrons which then couples the adjacent magnetic ion at a distance *r* apart. It is named as RKKY interaction, by taking the initial letters of the last name of its discoverers i.e., Ruderman, Kittel, Kasuya, and Yosida. It is a long-range oscillatory interaction that depends on the distance *r* between the magnetic ions as written below [46],

$$J_{RKKY}(r) \, \alpha \, \frac{\cos(2k_F r)}{r^3} \qquad (1.7)$$

where, $k_F$ is the radius of a spherical Fermi surface.

**Anisotropic exchange interaction:** It is an anti-symmetric exchange interaction where the excited state of one magnetic ion (produced by the SOC of that ion) couples with the ground state of another magnetic ion. It falls under the category of indirect exchange interaction since it is mediated through the spin-orbit interaction, and is well known as Dzyaloshinskii-Moriya interaction (DMI) [48–50]. The Hamiltonian for the DMI interaction can be written as [46],

$$H_{DMI} = -\sum_{ij} \boldsymbol{D}_{ij} \cdot (\boldsymbol{S}_i \times \boldsymbol{S}_j) \qquad (1.8)$$

where, $\boldsymbol{D}_{ij} = D(\hat{\boldsymbol{u}}_{ij} \times \hat{\boldsymbol{z}})$ is the DMI constant. Here, $\hat{\boldsymbol{u}}_{ij}$ is the unit vector along the line joining the two spins $\boldsymbol{S}_i$ and $\boldsymbol{S}_j$ and $\hat{\boldsymbol{z}}$ is the unit vector along the surface's normal direction. The strength of $\boldsymbol{D}_{ij}$ depends on several factors, e.g., the crystal structure, the SOC strength, etc. Minimization of DMI energy favours the two adjacent spins $\boldsymbol{S}_i$ and $\boldsymbol{S}_j$ to be aligned perpendicular to each other.

**Superexchange interaction:** This indirect interaction takes place between two magnetic ions separated by a non-magnetic ion. As the interaction couples two non-neighbouring magnetic ions via an intermediate non-magnetic ion, this does not fall into the category of short-range exchange interaction. Hence, it is also called as superexchange interaction [35,46]. This kind of interaction mainly occurs in ionic oxides or fluorides e.g., MnO, where two $Mn^{2+}$ ions interact via an $O^{2-}$ ion [51].

**1.3.2 Magnetostatic interaction:** This interaction takes place between two magnetic dipoles, whose strength depends upon the relative alignment and distance between the two dipoles. It is a long-range interaction and does not affect the local magnetic ordering. The energy

associated with this interaction is known as magnetostatic stray field energy or demagnetizing energy and can be expressed as equations 1.2 and 1.3, as discussed earlier.

**1.3.3 Zeeman interaction:** The splitting of atomic energy levels under the application of a magnetic field is well known as the Zeeman effect. In the case of a magnetic material, it describes an interaction between the magnetic moment of an atom and the applied magnetic field. The energy associated with this interaction is called the Zeeman energy and is expressed as [35],

$$E_{Zeeman} = -\boldsymbol{m}.\boldsymbol{B} \tag{1.9}$$

where, $\boldsymbol{m}$ is the magnetic moment and $\boldsymbol{B}$ is the applied field. To minimize Zeeman energy, the magnetic moment tends to align along the applied field direction.

An interplay between the above-mentioned energy terms leads to the observed magnetic phenomena in a material, including the shape of the hysteresis curve, domain structure, and magnetization dynamics.

**1.4 Magnetic domain and domain wall:**

**1.4.1 Formation of domain and domain wall:** A domain is a region in magnetic material where all the magnetic moments align parallel to each other, as introduced by Pierre Weiss in 1907 [52]. In an ideal case, a magnetic material with a finite exchange and anisotropy energy should exist in a single domain state, where all the spins will be aligned in a particular direction. However, in such cases, stray field energy increases abruptly. To reduce such energy a single domain state gets divided into multiple domains, where the spontaneous magnetization of each domain can be randomly oriented [53]. Two domains having different magnetization orientations are separated by a wall of finite width, known as a domain wall (DW) [54]. Within the DW, magnetic moments rotate continuously to change their orientation from one easy direction to the other [52,53]. As exchange energy favours the parallel orientation of spins, the

antiparallel magnetization of two adjacent domains gives rise to a large exchange energy. In order to minimize the exchange energy, it tries to form a wide DW where the adjacent spin moments rotate at a very small angle. However, the presence of crystalline anisotropy does not prefer such a small rotation due to the alignment of a large number of spins along non-easy directions. Thus, anisotropy energy tries to make the width of the wall very thin. A balance of these two energies finally gives rise to a finite width of the DW. As the spin moments in the wall are neither parallel to each other nor aligned along the EA, it acquires some finite energy, known as DW formation energy ($\sigma_{DW}$). The width and energy of the wall can be calculated using a continuum model. As the magnetization rotates continuously inside the DW, one can write, $\varphi = f(x)$. Thus the exchange energy with a continuum model can be expressed as [53],

$$E_{ex} = -2A \cos\left(\frac{d\varphi}{dx}\right)$$

where, $A \left(= \frac{nJS^2}{a}\right)$ is the exchange stiffness expressed in terms of $n$ (no. of atoms per unit cell) and $a$ (lattice parameter). Here, $\frac{d\varphi}{dx}$ represents the rate of change in local magnetization direction with the position inside the DW. Using the series expansion of $\cos\left(\frac{d\varphi}{dx}\right)$ and neglecting the higher order terms due to the smallness of $\varphi$, the above equation can be rewritten as [53],

$$E_{ex} = -2A + A\left(\frac{d\varphi}{dx}\right)^2 \tag{1.10}$$

where, the first term is a constant and the second one represents the exchange energy associated with the wall. Further, the anisotropy energy in general can be written as,

$$E_K = g(\varphi) \tag{1.11}$$

where, $\varphi$ is the angle between the magnetization (**M**) and the easy axis. In the case of a finite wall width, the torque resulting from the exchange and anisotropy energy should balance each other, giving rise to zero net torque. The torque due to exchange energy is [53],

$$L_{ex} = \frac{\partial E_{ex}}{\partial \varphi} = A \frac{\partial \left(\frac{\partial \varphi}{\partial x}\right)^2}{\partial \varphi} = 2A \frac{\partial \varphi}{\partial x} \frac{\partial^2 \varphi}{\partial x^2} \frac{\partial x}{\partial \varphi} = 2A \frac{d^2 \varphi}{dx^2}$$

Similarly, the torque due to the anisotropy energy is [53],

$$L_K = \frac{\partial E_K}{\partial \varphi} = \frac{\partial g(\varphi)}{\partial \varphi}$$

At the equilibrium position, the resultant torque should be zero. Thus,

$$2A \frac{\partial^2 \varphi}{\partial x^2} + \frac{\partial g(\varphi)}{\partial \varphi} = 0 \tag{1.12}$$

at each point of the wall [53]. Therefore, multiplying equation 1.12 by $\left(\frac{\partial \varphi}{\partial x}\right)$ and integrating

over $x$, the first term of equation 1.12 becomes $A \left(\frac{d\varphi}{dx}\right)^2$, whereas the second term becomes

$g(\varphi)$. This indicates that the balance of torque requires [53],

$$A \left(\frac{d\varphi}{dx}\right)^2 = g(\varphi) \tag{1.13}$$

Therefore, the DW formation energy can be written as,

$$\sigma_{DW} = \sigma_{ex} + \sigma_K = \int_{-\infty}^{+\infty} \left[ A \left(\frac{d\varphi}{dx}\right)^2 + g(\varphi) \right] dx.$$

Using equation 1.13, $\sigma_{wall}$ can be rewritten as [53],

$$\sigma_{DW} = \int_{-\infty}^{+\infty} 2g(\varphi) \, dx$$

For uniaxial anisotropy, $g(\varphi) = K_U \sin^2\varphi$, the DW energy for a 180º wall will take the

form [53],

$$\sigma_{wall} = 2\sqrt{AK_U} \int_0^\pi \sin\varphi \, d\varphi = 4\sqrt{AK_U} \tag{1.14}$$

Now the DW thickness can be considered as the value of $\frac{d\varphi}{dx}$ obtained at the center of the wall. In the case of uniaxial anisotropy, $\frac{d\varphi}{dx}$ obtains a value $\sqrt{\frac{A}{K_U}}$ at the center of the wall, and hence, the effective wall thickness can be written as [53],

$$\delta_{DW} = \pi \sqrt{\frac{A}{K_U}} \qquad (1.15)$$

Notably, the formation of a multi-domain ground state entirely depends upon the balance between the stray field energy and the DW formation energy. The stray field energy can be reduced to zero by the formation of flux closure-type domain states proposed by Landau and Lifshitz, as shown in Fig. 1.5 [55].
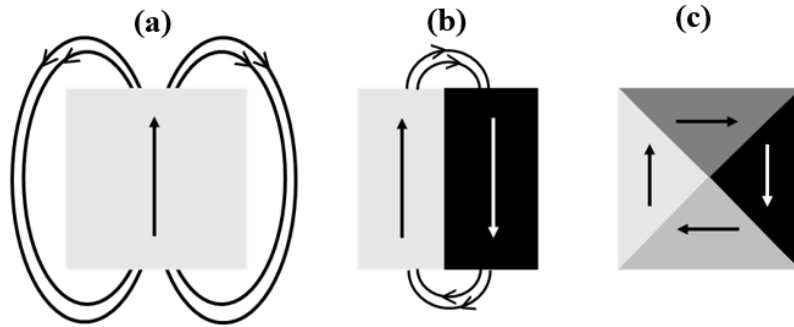


Figure 1.5. Flux closure-type domain formation to reduce the stray field energy, (a) single domain state (with high stray field energy), (b) two-domain state (with reduced stray field energy), and (c) flux-closure domain state (with zero stray field energy).

**1.4.2 Different types of DWs:** Depending upon the magnetization orientation of two neighbouring domains the DW can be classified into several types as described below [35,53].

(a) 180° DW: Here the DW separates two domains having opposite orientations of spontaneous magnetization. This type of DW occurs mainly in uniaxial FMs, e.g., Co.

(b) 90º DW: Here the DW lies between two domains having magnetization perpendicular to each other. In the case of triaxial FMs, e.g., bcc-Fe, such 90° DWs are observed.

Apart from the above, a material with four axes e.g., fcc-Ni (with EA along (111) direction) may show 180º, 109º, and 71º DWs [35,42,53].

**Bloch wall and Néel wall:** 180º DWs can be divided into two types, Bloch wall [54] and Néel wall [56], depending upon the rotation of spins in the wall. In the case of a Néel wall, the spins rotate perpendicular to the plane of the DW as shown in Fig.1.6 (a). Whereas for a Bloch wall, the spins rotate parallel to the plane of the DW, as shown in Fig. 1.6 (b). In the case of magnetic thin films with a thickness comparable to the thickness of the DW, the formation of Bloch wall creates free poles near the surface of the thin film. To reduce the stray field from these poles, thin film usually consists of Néel wall where the poles are created at the surface of DW. In contrast to this, for perpendicular magnetic anisotropic thin film, the formation of Bloch wall sometimes found to be preferable over Néel wall, to reduce the stray field energy of the system. However, in presence of sufficient DMI, Néel wall also can be formed in PMA samples. Irrespective of the kind of DW, the DW width ($\delta_{DW}$) is always proportional to $\sqrt{\frac{A}{K_u}}$, whereas, the DW energy ($\sigma_{DW}$) is proportional to $\sqrt{AK_u}$, where, $A$ and $K_u$ are the exchange and uniaxial anisotropy constants, respectively [35,53,57]. For magnetic thin films and multilayers, the DW width can be a few hundred of angstroms.
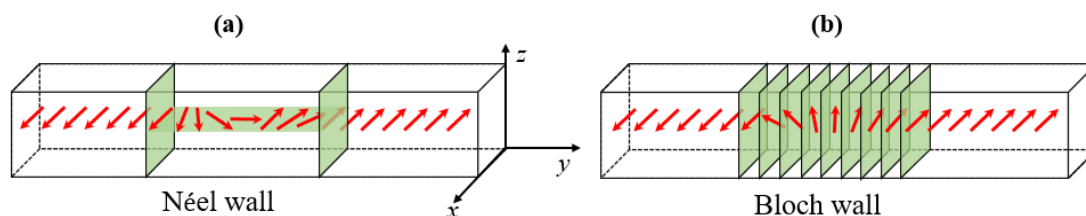


Figure 1.6. Magnetization rotation in the case of (a) Néel wall and (b) Bloch wall.

**1.4.3 Magnetization reversal:** Magnetization reversal is a process where the magnetization orientation in a FM reverse from its initial saturation state to the other opposite state via different external stimuli e.g., magnetic field, temperature, stress, spin-transfer-torque, SOT, etc. The study of magnetization reversal holds significant importance starting from fundamental understanding to spintronic device applications. When a magnetic field is applied to a ferromagnetic sample, it exerts a torque ($\boldsymbol{\tau} = \boldsymbol{M} \times \boldsymbol{H}$) on the magnetic moments and tries to align them along the applied field direction to minimize the energy. However, due to the internal domain structure in a FM film, rotation of the spin moment does not happen linearly with the applied field. Instead, the magnetization always lags the field. Due to this, the magnetic field ($\boldsymbol{H}$) versus magnetization ($\boldsymbol{M}$) graph takes the shape of a loop, known as a hysteresis loop, as shown in Fig. 1.7. The magnetization reversal phenomena occurs mainly via two dominant mechanisms, DW motion and coherent rotation of spins [58,59]. If a ferromagnetic sample initially exists in a demagnetized state, the application of a magnetic field grows the domains that are aligned parallel to the field direction at the expense of the other unfavourable domains. As the sample acquires a small magnetization, the initial portion OA of the hysteresis loop is quite reversible in nature, as shown in Fig. 1.7. Further with increasing field a considerable increase in magnetization achieved by irreversible DW displacement, indicated by the portion AB of the loop. At the saturation field ($H_S$), all domains rotate to align along the field direction and attain the magnetic saturation ($M_S$) as indicated by point C in Fig. 1.7. The ferromagnetic sample acquires a finite magnetization even upon removal of the field, known as remanent magnetization or remanence ($M_r$). The magnetization eventually goes to zero at a finite negative applied field, known as magnetic coercivity ($H_C$). The ratio of $\frac{M_r}{M_S}$ is known as the squareness ($S$) of a loop. In the case of a highly anisotropic magnetic sample, $S$ attains a value 1 along EA, and 0 along HA. The two main mechanism that governs a magnetization reversal phenomenon is discussed in the following.
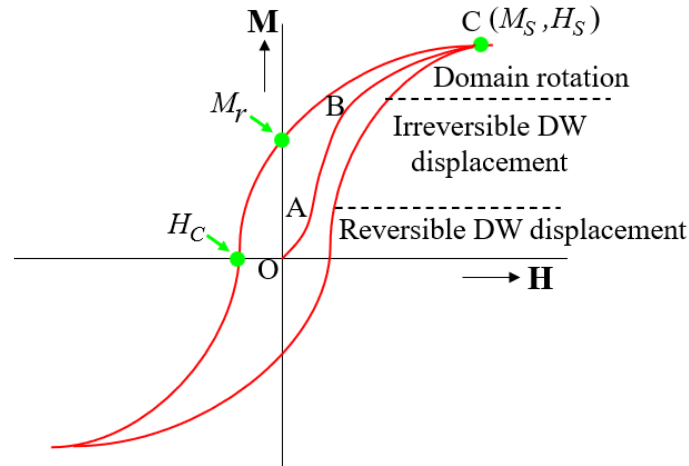
Figure 1.7. A hysteresis loop showing the variation of magnetization (*M*) with applied magnetic field (*H*).

**1.4.3.1 Domain wall motion:** In the case of a thin film, a DW can be considered as a one-dimensional (1D) elastic interface moving through a two-dimensional (2D) disordered media. Along EA, a hysteresis loop usually resembles a square shape with a value of $\frac{M_r}{M_S}$ nearly equal to 1, as shown in Fig.1.8 (a). Here at the positive saturation, the sample exhibits a single-domain state. By reversing the field direction domain nucleation event occurs from the impurities or low anisotropic regions of the sample. The blue line represents the DW between two adjacent domains with opposite magnetization orientations. A sample may have more than one nucleation site depending on the quality of the film. With increasing the applied field DW moves and more spins switch to increase the area of the nucleated domains. At coercivity, a sample should have an equal amount of oppositely magnetized domains, leading to zero net magnetization. Finally, the sample achieves the opposite saturation by converting again to a single domain state, as shown schematically in Fig. 1.8 (a). Along EA, the magnetization switches from one saturation state to the other only above a particular field value. However, along HA a gradual rotation of spins is observed with increasing the field values.
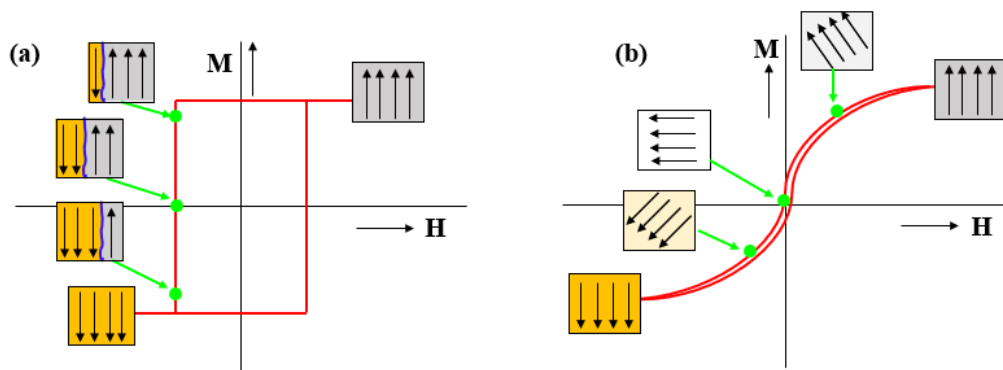
Figure 1.8. Schematic representation of the magnetization reversal phenomena via two dominant mechanisms, (a) DW motion and (b) coherent rotation.

**1.4.3.2 Coherent rotation:** Coherent rotation usually describes the magnetization reversal of single-domain nanoparticles. However, in the case of an anisotropic magnetic thin film such rotation is also observed along the HA of the system, as shown in Fig. 1.8 (b). Along HA the hysteresis loop takes *S* shape. Here, all the spins rotate coherently from a single domain state without forming any domain. Coherent rotation is an easier process than DW motion, as for the latter case, a complex interaction between the 1D wall with the structural inhomogeneity takes place. So, it can be concluded that the DW motion and coherent rotation are the two dominant mechanisms via which magnetization reversal takes place. Apart from these, magnetization reversal may also occur via both partial rotation of spins and DW motion, depending upon the pinning energy barrier in the sample. Understanding these processes is important for the development of magnetic memory, storage devices, and sensor applications [57].

**1.5 Magnetization dynamics:** In the case of a magnetic material, the evolution of magnetization with time is known as the magnetization dynamics. The Landau-Lifshitz-Gilbert (LLG) equation describes the change in magnetization vector with time in the presence of a magnetic field and damping. This is mainly a torque equation, developed first by Landau and Lifshitz [60], where the damping term was introduced later by Gilbert [61]. The magnetic

moment associated with an electron motion in a circular loop of radius $r$ can be written as, $\boldsymbol{\mu} = i\boldsymbol{A}$, where $A = \pi r^2$, is the area of the loop. The angular momentum $(\boldsymbol{L})$ for electrons circular motion can be written as, $\boldsymbol{L} = \boldsymbol{r} \times \boldsymbol{p} = \boldsymbol{r} \times m_e \boldsymbol{v}$, where $\boldsymbol{m_e}$ is the mass of an electron. Then the magnetic moment can be expressed in terms of angular momentum as,

$$\boldsymbol{\mu} = i\boldsymbol{A} = -\frac{ev}{2\pi r} \times \pi r^2 = -\frac{e}{2m_e}\boldsymbol{L} = -\gamma\boldsymbol{L} \tag{1.16}$$

where, $\gamma = \frac{e}{2m_e}$ is the gyromagnetic ratio. The time variation of magnetic moment can be written as,

$$-\frac{1}{\gamma}\frac{d\boldsymbol{\mu}}{dt} = \frac{d\boldsymbol{L}}{dt} = \boldsymbol{\tau} \tag{1.17}$$

where, $\boldsymbol{\tau}$ is the torque applied to the magnetic moments. In the presence of a magnetic field, the torque can be written as, $\boldsymbol{\tau} = \boldsymbol{M} \times \boldsymbol{H}_{eff}$, where $\boldsymbol{M} = N\boldsymbol{\mu}$, is the total magnetic moment of the material considering $N$ number of atomics spins. $\boldsymbol{H}_{eff}$ is the effective magnetic field which can be written as, $\boldsymbol{H}_{eff} = \boldsymbol{H}_{external} + \boldsymbol{H}_{exchange} + \boldsymbol{H}_{anisotropy} + \boldsymbol{H}_{demag}$. Hence, equation 1.17 can be re-written as,

$$\frac{d\boldsymbol{M}}{dt} = -\gamma(\boldsymbol{M} \times \boldsymbol{H}_{eff}) \tag{1.18}$$

The R.H.S. of the above equation represents a precessional motion of the magnetization around the effective magnetic field. However, in the case of a real system, the precession does not continue for an infinite time. Instead, it gets slowly damped out and aligns along the field direction. Thus, Landau – Lifshitz (LL) introduced a damping term in equation 1.18 and the modified equation can be written as,

$$\frac{d\boldsymbol{M}}{dt} = -\gamma(\boldsymbol{M} \times \boldsymbol{H}_{eff}) - \frac{\lambda}{M_s^2}[\boldsymbol{M} \times (\boldsymbol{M} \times \boldsymbol{H}_{eff})] \tag{1.19}$$

where, $\lambda$ is a phenomenological LL damping term and $M_S$ is the saturation magnetization. Here, the 2nd term of R.H.S. represents a damping-like torque that acts along the center of the circular precessional motion and reorients the magnetization along the field direction. Further, Gilbert has introduced a dimensionless damping parameter ($\alpha$) and the modified equation can be written as,

$$\frac{d\boldsymbol{M}}{dt} = -\gamma\left(\boldsymbol{M} \times \boldsymbol{H}_{eff}\right) + \frac{\alpha}{M_s}\left(\boldsymbol{M} \times \frac{d\boldsymbol{M}}{dt}\right) \tag{1.20}$$

where, $\alpha = \frac{\lambda}{\gamma M_s}$, is the Gilbert damping constant. This modified equation is well-known as the Landau-Lifshitz-Gilbert equation. A schematic of the magnetization precession in the presence of both applied field and damping torque is shown in Fig. 1.9.
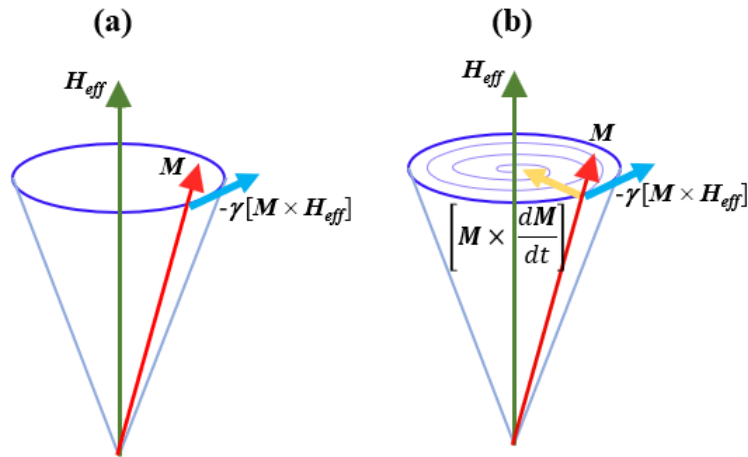


Figure 1.9. Schematic representation of magnetization ($\boldsymbol{M}$) precession around an effective field ($\boldsymbol{H}_{eff}$) in (a) absence and (b) presence of damping parameter.

**1.6 Magnetic field-induced domain wall dynamics:** Domain walls of any ferromagnetic [62–64] or ferroelectric [65] thin film can be considered as a 1D elastic interface that moves through a 2D disorder media. Similar behaviour also can be observed during fluid propagation in a porous medium or through a disordered substrate [66]. Similarly for biological

systems, inhomogeneities can impede the growth of bacterial colonies or plant species [67].

For such 1D interfaces, moving through a 2D disordered media, the total energy of the system

contains both the elastic energy and the energy associated with the interaction between the

interface and the disorder. Thus, the interface can be represented as a line propagating along

the *x*-axis having a varying height *u(x)* due to the presence of disorder, as shown in Fig. 1.10.

A height correlation function is generally used to measure the correlation between the wall

height values that are separated by a distance *L*,

$$C^2(L) = \langle[u(x) - u(x + L)]^2\rangle \qquad (1.21)$$

In 1985 Huse, Henley, and Fisher investigated the nature of this correlation function for the

case of a 1D interface moving through a 2D medium having random-bond disorder [68]. In the

absence of any driving force, and at $T = 0$K, the correlation function was found to follow a

scaling law as written below,

$$C^2(L) \propto \left(\frac{L}{L_C}\right)^{2\zeta} \qquad (1.22)$$

where, $\zeta$ is the wandering exponent and $L_C$ is the Larkin length. $\zeta$ can take different values

depending on the dimensionality of the system and the nature of random force disorder [69,70].

On the other hand, Larkin length ($L_C$) represents the length below which the elastic interface is

considered flat, because, below this length scale the elastic energy required for deformation is

higher than the energy gained from the deformed interface [71]. The presence of a rough

interface and disorder strongly affect the dynamics of the elastic interface.

Although the magnetization inside the DW rotates continuously, the dynamics of DW can be

explained by using simple models. There are several external forces, by which a DW can be

moved, e.g., application of magnetic field [72,73], electric field [74], spin-transfer-torque

(STT) [75], spin current [76], etc. In the presence of a magnetic field, the magnetic moments
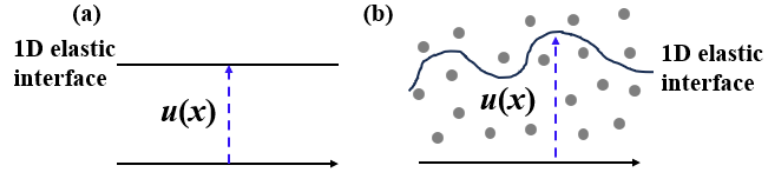
Figure 1.10. (a) A flat 1D interface moving in the absence of any impurities and disorder, (b) a rough 1D interface moving in the presence of several pinning sites and disorder.

inside the wall rotate and finally align to the applied field direction giving rise to a displacement of the wall. Walker first gave a model to describe the motion of a DW in the presence of a magnetic field [77]. This model divides the overall DW motion into two regions, namely, (i) steady region (at the lower applied field) and (ii) oscillatory region (at the higher applied field), as shown in Fig. 1.11 (a). In the steady state, the DW velocity increases linearly with the applied magnetic field, and at a particular value of the field (called as Walker field), the velocity drops suddenly. This phenomenon is known as Walker breakdown, where a sudden drop occurs due to an oscillatory motion of the magnetization inside the wall. Further, the DW enters the oscillatory region where with an increasing field amplitude the DW motion again starts increasing linearly. Such linear motion happens via a back-and-forth motion of the DW where it changes from a Bloch wall to a Néel wall and again to a Bloch wall [78].

However, the above-explained behaviour of DW is only valid for ideal systems. A real magnetic thin film usually consists of several defects, impurities, and inhomogeneities that act as pinning sites and affect the overall motion of the DW. At $T = 0$K, the DW moves only after a critical force ($F > F_{dep}$) is applied. This occurs because, at the lower force regime, the interplay between pinning potential and thermal energy mainly decides the wall motion [79]. Thus, at 0K, due to the absence of thermal energy, the DW remains strongly pinned until a critical depinning force ($F_{dep}$) is applied. When $F > F_{dep}$, the DW starts moving even at 0K, as shown in Fig. 1.11 (b).

However, when $T \neq 0\text{K}$, thermal energy could depin the DW even at $F < F_{dep}$, and hence, the DW motion is observed at a force lower than $F_{dep}$ [79]. Therefore, depending upon the strength of the driving force the DW motion is further divided into three regimes, namely, (i) creep ($F < F_{dep}$), (ii) depinning ($F > F_{dep}$), and (iii) flow, as shown in Fig. 1.11 (b).

**(i) Creep region:** Creep usually represents a very slow motion at a driving force $F$ lower than $F_{dep}$. In this region, the DW behaves as an elastic 1D interface driven by a force through a 2D disordered media. Thus, instead of a linear velocity ($v$) - force ($F$) relation, here, the DW velocity obeys an Arrhenius law written as [79,80],

$$v \sim \exp\left(-\frac{E}{k_B T}\right) \qquad (1.23)$$

where, $E$ and $k_B T$ represents the effective pinning barrier and the thermal activation energy,
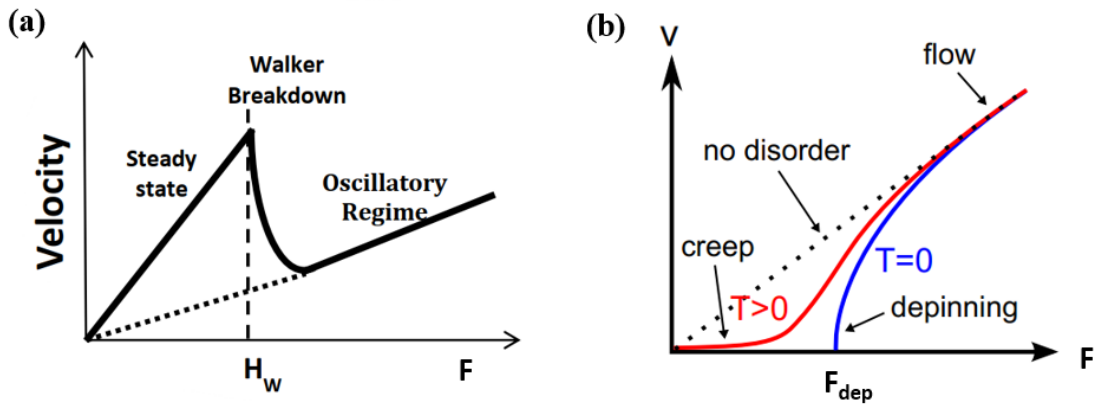


Figure 1.11. (a) Schematic of a velocity versus force curve for an elastic interface moving through an ideal medium. The linear steady and oscillatory regions are separated by the Walker field ($H_W$). (b) A theoretical velocity versus force curve for an elastic interface moving through a disordered media at, $T=0\text{K}$ (blue line) and T>0K (red line). The black dotted line represents the linear steady state in the absence of any disorder. The creep, depinning, and flow regions are also labelled. The images are taken from ref. [81,82].

respectively. For a 1D elastic interface moving through a random pinning disorder, the phenomenological scaling theory [83,84] and functional renormalization group [79] calculations show that when $F \to 0$, the pinning energy ($E$) can be presented as a universal power law variation as, $E \sim F^{-\mu}$, where $\mu$ is a critical exponent. Thus, the velocity vs. force curve in the thermally activated creep region can be rewritten as [79],

$$v = v_0 \, exp\left[-\frac{U_c}{k_B T}\left(\frac{F_{dep}}{F}\right)^{\mu}\right] \tag{1.24}$$

where, $v_0$ is a scaling parameter of velocity, $U_c = k_B T_{dep}$ is the height of pinning potential, $k_B T$ is the thermal activation energy, $F_{dep}$ is the depinning force and $\mu$ is a universal dynamic exponent, which not only depends on the dimensionality of the system but also on the wandering exponent, $\zeta$, and can be expressed as [79],

$$\mu = \frac{d-2+2\zeta}{2-\zeta} \tag{1.25}$$

where, $d$ is the dimension of the elastic interface. In general, any elastic interface can be described by its dimension $d$ (where $d$ can be 1 or 2 depending on whether the interface is a line or a surface) which can move in $n$ number of transverse directions [85]. For a magnetic DW, $d = n = 1$, as the 1D elastic DW moves along a specific direction. For $n = 1$, the wandering exponent, $\zeta = \frac{2}{3}$ [68,86]. By putting these values in equation 1.25, the exponent $\mu$ takes the value $\frac{1}{4}$. Thus, in the case of a magnetic thin film, the magnetic field ($H$) driven DW velocity can be written as,

$$v_{DW} = v_0 \, exp\left[-\frac{U_c}{k_B T}\left(\frac{H}{H_{dep}}\right)^{-\frac{1}{4}}\right] \tag{1.26}$$

where, $H$ and $H_{dep}$ are the applied and depinning threshold fields, respectively. In the year 1998, Lemerle *et al.* first showed experimentally the validity of the creep model for the

magnetic DW motion in a high-quality Pt/Co/Pt thin film and derived all the corresponding exponents [85]. This was the first concrete evidence that the creep theory could be applied to a real ferromagnetic system where the magnetic field (*H*) replaced the force term in the *v-F* curve. Since then, significant attention has been given to studying the creep region of different ferroelectric, ferromagnetic, and superconducting systems [62–65,87]. The creep region can be observed for both the magnetic field and electric current-driven DW motion.

**(ii) Depinning region:** In the presence of thermal energy, the depinning of the DW from the defects is achieved when $H > H_{dep}$. This second region of DW motion is called the depinning region where the DW velocity increases suddenly, as shown in Fig. 1.11 (b). Near the depinning region, the scaling function for the driving field and temperature is predicted by a few statistical physics approaches [79,88]. At $H = H_{dep}$, the variation of velocity with the temperature can be written using the asymptotic power law as [89],

$$v(H_{dep}, T) = v_T \left(\frac{T}{T_{dep}}\right)^{\psi} \tag{1.27}$$

whereas, at $T << T_{dep}$, the variation of velocity with a magnetic field can be written as [89],

$$v\left(H, T \ll T_{dep}\right) = v_H \left(\frac{H - H_{dep}}{H_{dep}}\right)^{\beta} \tag{1.28}$$

where, $\beta$ and $\psi$ are the depinning and thermal rounding exponents, respectively. $v_T$ and $v_H$ are the depinning velocities. Thus, the two velocity equations (1.27 and 1.28) can be combined into a generalized homogeneous function which takes a scaling form as [88],

$$y = g\left(\frac{x}{x_0}\right) \tag{1.29}$$

where, the scaled dimensionless variables are, $x = \left(\frac{H - H_{dep}}{H_{dep}}\right)^{\beta} \left(\frac{T}{T_{dep}}\right)^{-\psi}$, $y = \frac{v}{v_T} \left(\frac{T}{T_{dep}}\right)^{-\psi}$ and $x_0 = \left(\frac{v_T}{v_H}\right)$. Here, the function $g$ is predicted to be universal within a given class of universality.

Thus, the function should represent both the asymptotic velocity behaviour as mentioned in equations 1.27 and 1.28. When, $x \ll x_0$, if the function $g\left(\frac{x}{x_0}\right) \to 1$, it will represent equation 1.27, whereas for $x \gg x_0$, the function $g\left(\frac{x}{x_0}\right) \to \frac{x}{x_0}$, will represent equation 1.28. Notably, the parameters $v_T$, $v_H$, $H_{dep}$, $T_{dep}$ are all material and temperature-dependent non-universal parameters.

**(iii) Flow region:** When the magnetic field increases further to very high values, the DW velocity is found to be independent of the pinning potentials and follows a linear relation with the applied field as predicted theoretically. This region is called as flow region. The DW velocity in this region can be described well with the following equation,

$$v = mH \tag{1.30}$$

where, $m$ is the mobility of the wall. In this region instead of disorder, dissipation limits the velocity of the moving wall. Such dissipation can be characterized by a magnetic damping parameter, $\alpha$, which is also related to the mobility $(m)$ of the wall. In the case of magnetic systems, two separate flow regimes can be observed having different mobilities. This occurs due to a modification in the internal dynamics of the wall above the Walker field $(H_W)$ [77,90], as explained earlier. Below the Walker field, a steady motion of the DW is observed having mobility, $m = \frac{\gamma\delta}{\alpha}$, where $\gamma$ is the gyromagnetic ratio and $\delta$ is the DW width. However, when $H$ is sufficiently above $H_W$, a second linear region is observed where the magnetization precesses inside the wall. Due to the precessional motion, the mobility in this second region is lower than the steady one and can be represented as, $m = \frac{\gamma\delta}{\alpha+\alpha^{-1}}$. The complete flow region is thus composed of two linear flow regions separated by a non-linear intermediate region (Walker breakdown region). The Walker field corresponding to the Walker breakdown can be evaluated

from the equation, $H_W = N_y 2\pi\alpha M_S$, where $N_y$ is the demagnetizing factor along the DW and $M_S$ is the saturation magnetization of the magnetic film [64].

**1.7 Domain wall motion in the presence of both IP and OP magnetic field:** In addition to the OP pulsed field, the application of the IP magnetic field helps to probe the effective DMI field of a magnetic sample. Dzyaloshinskii first suggested a phenomenological hypothesis to explain the mild ferromagnetic effect seen in antiferromagnetic crystals, such as $\alpha$-$Fe_2O_3$ [48]. Later in 1960, Moriya used SOC to theoretically describe the antisymmetric exchange interaction [49]. In 1980, A. Fert also found a high DMI between the Mn spins in the presence of HM impurities like Pt or Au [50]. According to the Fert and Levy model, the broken inversion symmetry and high SOC of HM lead to the emergence of DM interaction from the FM/HM interface. A schematic of the interaction is shown in Fig. 1.12 (a), where at the interface of the FM and HM, two neighbouring spins $S_1$ and $S_2$ of the FM interact via a third site present in the HM having high SOC. The resultant antisymmetric exchange interaction can be written as,

$$H_{DMI} = D_{12}.(S_1 \times S_2) \tag{1.31}$$

where, the DMI vector $D_{12}$ acts along the interface of the FM/HM system. The minimization of direct exchange interaction prefers parallel alignment between neighbouring spins. Whereas minimization of DMI prefers a perpendicular alignment between the spins. A balance between these two energies gives rise to a canted spin state, and hence, a chirality to the DWs. In a magnetic thin film, two adjacent DWs may have either the same or different chirality of their magnetization vector, as depicted in Fig. 1.12 (b). If the chirality of two adjacent DWs is the same (either clock or anti-clockwise) then the DWs are called homochiral DWs. In the case of a chiral Néel wall, the core magnetization of two adjacent DWs acts opposite to each other. Thus, a system with finite DM interaction is associated with a DM field that acts in the plane
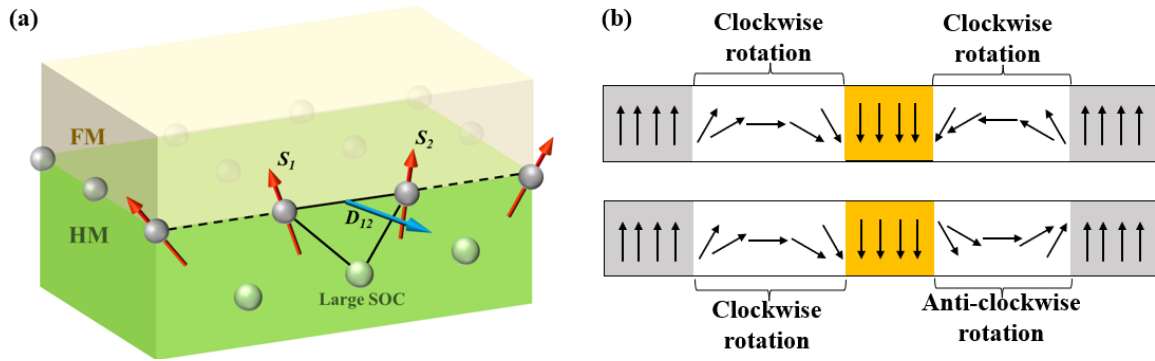
Figure 1.12. (a) Schematic representation of the DM interaction at HM/FM interface, (b) chirality of DWs due to DMI.

of the sample in the radially opposite direction of a domain. Application of an IP magnetic field probe such DM field and helps to evaluate the DMI strength. In the case of a magnetic bubble domain, application of the IP field generates an asymmetric domain expansion, due to either cancellation or enhancement of the DMI field. This gives faster DW motion along one side of the wall (say, $v_L$ or ↑↓), whereas slower motion for the other side (say, $v_R$ or ↓↑). In the creep region, the effect of applying both IP and OP fields on the DW velocity is studied by Je *et al.* [91]. In this context, the creep law for DW motion is modified by incorporating the IP field dependency into the energy barrier scaling parameter. Thus, the modified creep law is written as,

$$v_{DW}(H_{IP}) = v_0 \, exp\left[-\xi(H_{OP})^{-1/4}\right] \tag{1.32}$$

Where $\xi$ is the modified energy barrier scaling parameter written as [91];

$$\xi = \xi_0 \left(\frac{\sigma(H_{IP})}{\sigma(0)}\right)^{-1/4} = \frac{T_{dep}}{T}\left(\mu_0 H_{dep}\right)^{\frac{1}{4}}\left(\frac{\sigma(H_{IP})}{\sigma(0)}\right)^{-1/4} \tag{1.33}$$

where, $\xi_0$ depends on the pinning energy in the absence of an IP bias field. The IP field dependent DW energy $\sigma(H_{IP})$ can be expressed as [91],

$$\sigma(H_{IP})_{B-N} = \sigma(0) - \frac{\delta(\pi\mu_0 M_S)^2}{8K_D}(H_{IP} + H_{DMI})^2 \quad \text{for, } |H_{IP} + H_{DMI}| < \frac{4K_d}{\pi\mu_0 M_S}$$

$$\sigma(H_{IP})_N = \sigma(0) + 2K_D\delta - \pi\delta\mu_0 M_S|H_{IP} + H_{DMI}| , \quad \text{otherwise} \tag{1.34}$$

where, $\sigma(0) = 2\pi\sqrt{AK_{eff}}$ is the pure Bloch wall energy, $\delta = \sqrt{A/K_{eff}}$ is the DW width and $K_D = t\ln(2)\mu_0 M_s^2/2\pi\delta$ is the DW anisotropy energy density.

**1.8 Proximity-induced hybridization at ferromagnet/non-magnet interface:** When a ferromagnetic material comes in close contact with a non-magnetic material (e.g., HM or organic molecules), hybridization takes place at the interface. Such interfacial hybridization is fascinating from both fundamental physics and application viewpoints. In the case of a FM/HM system, having unfilled $d$ orbitals, the electron wavefunctions of these materials overlap at the interface. This proximity allows for a strong exchange of information between the spin and orbital degrees of freedom, leading to novel electronic and magnetic properties [92]. The strong SOC of HM atoms alters the electronic properties of both the FM as well as HM layers. This in turn modifies the exchange interaction and induces orbital moment anisotropy at the interface [93]. Such hybridization-induced anisotropy is also known as interfacial magnetic anisotropy, which plays a crucial role in spintronic device applications based on PMA. In addition, the strong SOC of the HM can generate finite spin-orbit torques, which can be used to manipulate the magnetization direction of the ferromagnetic layer. As the HMs are very few and introduce high damping in a system, the search for alternative materials is also fascinating. In this context, several light atoms-based systems (e.g., C, H, N based molecules) are being explored.

Organic molecules (OMs) are potential candidates in the field of organic spintronics owing to their light atomic weight, low SOC, less hyperfine interaction, mechanical flexibility, and chemical tunability [94,95]. In general, when OMs are far apart from a FM, they have discrete

energy levels with infinite lifetimes, as shown in Fig. 1.13 (a). However, when an OM comes closer to a FM metal, several interactions starting from mild physisorption to strong chemisorption may occur at their interface. Here, depending upon the density of states (DOS) of the FM and the adsorption geometry of the OM, the molecular levels get either broadened ($\Gamma$) or shifted ($\Delta E$) in the energy level as shown in Fig. 1.13 (b) [96,97]. Depending upon the electron affinity, charge transfer also may take place at the FM/OM interface. Thus, an effective hybridized interface (consisting of interfacial FM and OM layers) known as "spinterface" is formed at the FM/molecular interface. Depending upon the relative magnitude of the broadening ($\Gamma$) and shifting ($\Delta E$) of the molecular DOS, the spinterface spin-polarization can be inverted (when $\Gamma \gg \Delta E$) or enhanced (when $\Gamma \ll \Delta E$) [98,99]. Therefore, the formation of a spinterface can modify the electronic and magnetic properties of both the FM as well as the OM layer [100]. The impact of such FM/OM interface is well-studied in the field of organic spintronics. A few potential OMs explored in the field of organic spintronics are, metal–
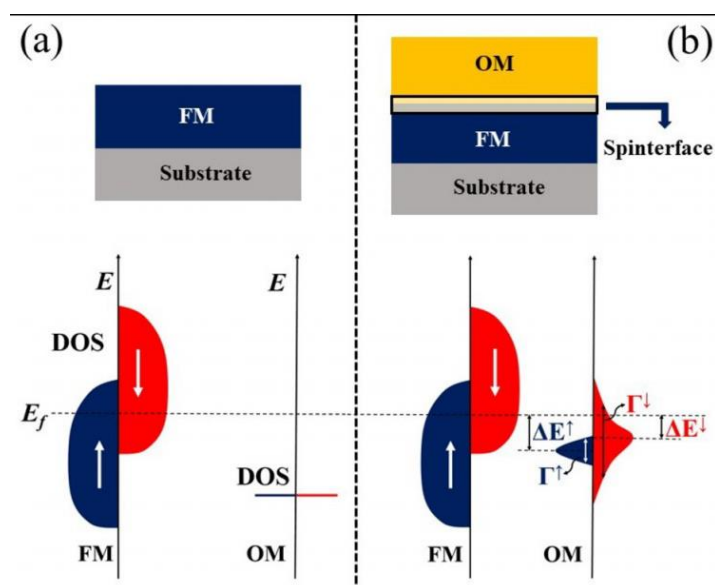


Figure 1.13. A schematic representation of the FM and OM's DOS when they are, (a) far apart, and (b) in close contact. Due to proximity-induced hybridization at the FM/OM interface, the molecular DOS is broadened ($\Gamma$) and shifted ($\Delta E$). The image is taken from ref. [97].

phthalocyanines (CuPc, ZnPc, etc.), oligothiophenes (4T, 6T, etc.), metal chelates (Alq$_3$, Coq$_3$, etc.), acenes (tetracene, pentacene, and others), fullerene (C$_{60}$), rubrene, etc. However, the impact of such OM on the HM/FM system is not known well. In addition, the potential of OMs to replace the HM layer is yet to be explored. Thus, in our thesis work, we have studied both the HM/FM/HM and HM/FM/OM systems. In this context, we have prepared both symmetric HM/FM/HM (e.g., Pt/Co/Pt, Pd/Co/Pd) and asymmetric HM/FM/OM (Pd/Co/C$_{60}$) structures. Fullerene (C$_{60}$) is used to break the symmetry of the Pd/Co/Pd structure and to study the impact of Co/C$_{60}$ spinterface formation on the magnetic properties of Pd/Co/C$_{60}$ samples. Further, the impact of external strain application on the structural and magnetic properties of these thin films is also studied in detail.

**Chapter 2: Experimental Techniques**

This chapter provides a comprehensive overview of all the experimental methods that are used in this thesis work. All the metallic layers (Ta, Pt, Co, Pd) of the samples are deposited by the DC magnetron sputtering technique, whereas the organic $C_{60}$ layer is deposited by the thermal evaporation technique. The samples are prepared upon both rigid Si and flexible polyimide substrates. The structural characterization is carried out using an X-ray diffractometer (XRD), and scanning electron microscope (SEM). For the magnetic characterization, we have used magneto-optic Kerr effect (MOKE) based microscope and superconducting quantum interference device (SQUID) magnetometer. Further, the DW velocity and the DMI strength are measured using an in-house developed symmetric and asymmetric DW velocity measurement setup integrated with the MOKE microscope. To calculate the element-specific orbital and spin magnetic moments, synchrotron-based X-ray magnetic circular dichroism (XMCD) measurements are performed at the Elettra synchrotron facility, in Italy. Further, the room temperature (RT) resistivity measurements are performed using an in-house developed four-probe setup. To comprehend the experimental results well we further performed micromagnetic simulations using MuMax3 software.

**2.1 Thin film deposition techniques:**

One can prepare thin films (ranging from a few nm to a few μm in thickness) of various materials (e.g., metal, insulator, oxides, compounds, etc.) on top of different substrates via several thin film deposition techniques. A variety of thin film deposition techniques are invented, as no unique technique meets all the requirements related to different applications. Therefore, the choice of deposition technique relies largely on the desired sample properties and its application. The development of various deposition techniques is proven to be highly beneficial for the modern semiconductor, electronics, optoelectronics, and solid-state-based device industries [101,102].
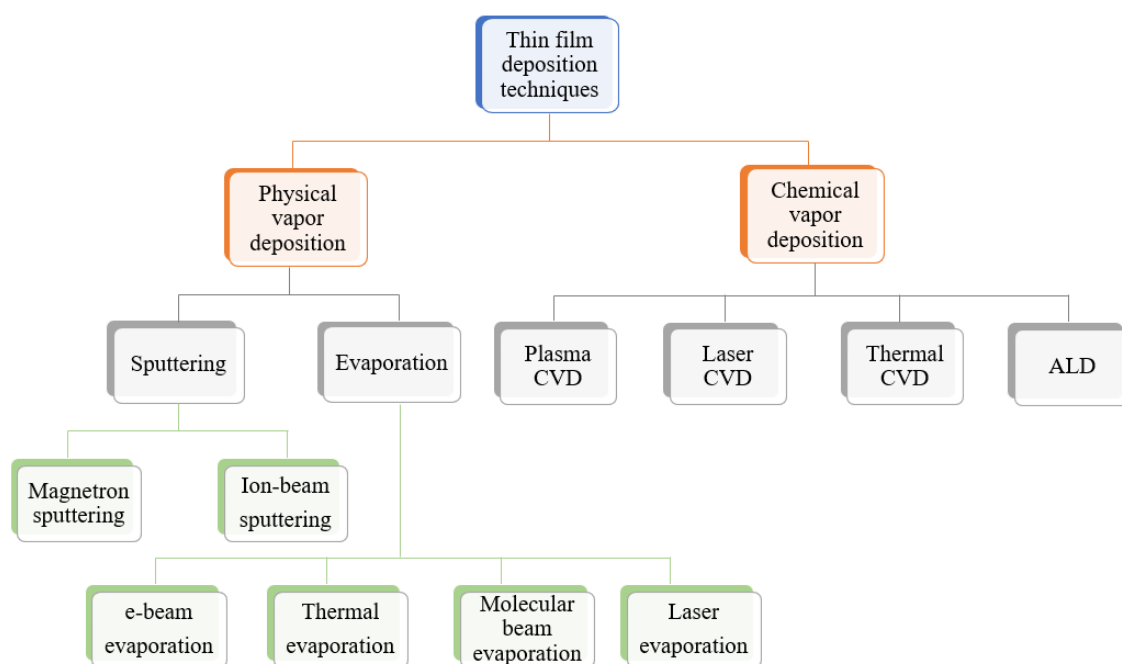
Figure 2.1 A pictorial layout of various thin film deposition techniques that are divided into mainly two categories, physical vapor deposition and chemical vapor deposition.

There are mainly two categories in which the various thin film deposition techniques can be divided, (i) physical vapor deposition (PVD) and (ii) chemical vapor deposition (CVD), as shown in the layout of Fig. 2.1. In the case of PVD, first a vapor of a solid material is formed and then it condensed on a substrate [103]. However, in the case of CVD, the vapor of a solid material goes under a chemical reaction near a heated substrate and then gets deposited on it [104]. The major advantage of PVD over CVD is here the thin film is deposited at a low working temperature. In our work, we have used two PVD-based techniques, sputtering and thermal evaporation to deposit the samples. The techniques are described below in detail.

**2.1.1 Sputtering:**   Sputtering is the most popular and versatile thin film deposition technique owing to its several advantages, e.g., uniformity, high purity, good adhesion, compatibility for depositing a variety of materials, low waste production, and ease of large-scale fabrication which is highly desired for industrial applications. In this process, a target of a certain material

to be deposited as a thin film is mounted inside the vacuum chamber. Prior to sputter deposition the desired substrate is also mounted inside the vacuum chamber. First, an inert gas (mainly Ar) is introduced inside the deposition chamber, as it does not react chemically with the target. The target is kept at some negative bias voltage and the substrate is grounded. Due to the potential difference, the neutral Ar gas forms $Ar^+$ ions. These ions further accelerate towards the target material and transfer their momentum upon collision with the target atoms. Thus, the neutral atoms, molecules, or ions of the target material get ejected and form a vapor in the vacuum chamber. Depending upon the mean free path of the ejected particles, a fraction of them finally reaches the substrate mounted on the line of sight of the target and condensed to form a thin film. In order to achieve a high deposition rate while keeping the Ar flow low, magnetron sputtering is usually used [105,106]. Here below the target a permanent magnet or an electromagnet is placed, which generates a magnetic field and traps the electrons close to the target. The localization of electrons helps to enhance the $Ar^+$ ion generation close to the target which in turn increases the deposition rate. High quality of both metallic and non-metallic films can be deposited via the magnetron sputtering technique. A schematic of the sputter deposition process is shown in Fig. 2.2.

To deposit a variety of materials having different electrical conductivities two types of sputtering techniques are available, (i) DC sputtering and (ii) RF sputtering.

(i)      **DC sputtering:** In this process a potential difference is created between the target and substrate with the help of a DC power supply. The Ar+ ions are generated and they collide with the target material. The target atoms get ejected due to the momentum transfer from the Ar ions. The sputtered target atoms then travel to the substrate and get deposited in the form of a thin film. DC sputtering is suitable for depositing conductive materials, e.g., pure metals, metallic alloys, conductive oxides, nitrides, etc. In this technique, the continuous sputtering of the target material may cause overheating issues if decent cooling facilities are not available.
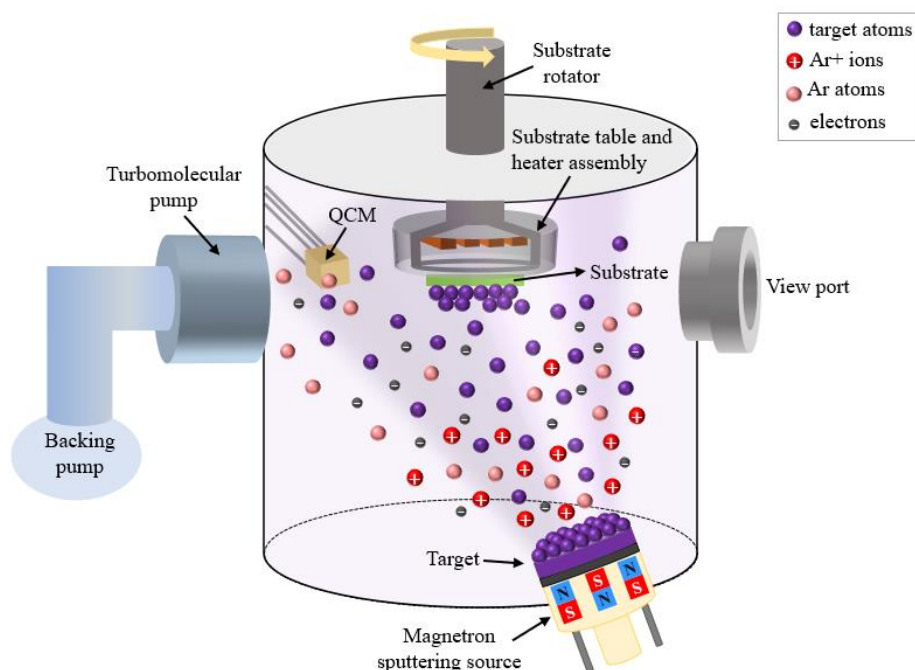
Figure 2.2 A schematic illustration of the sputter deposition technique. The backing and turbomolecular pumps help to attain a high vacuum inside the deposition chamber. The violet colour plasma is formed by the charged particles of Ar gas. The neutral target atoms, charged Ar ions, and electrons are also represented by solid circles of different colours. The quartz crystal microbalance (QCM) is located close to the substrate holder.

(ii)    **RF sputtering:** RF sputtering is suitable for depositing insulating materials owing to their low conductivities. As the negative voltage applied to an insulating target does not distribute evenly to its surface, Ar+ ions accumulate in a few places on the target surface. These piled-up positive charges hinder any further Ar+ ion bombardment on the target and stop the sputtering process. In contrast, a radio-frequency (13.56 MHz) power supply is employed in the case of RF sputtering, where the target bias is modulated in radio frequency [107]. At the negative cycle of voltage, the Ar+ ions bombard the target resulting in the deposition of target materials. In the positive cycle, electrons get attracted towards the target which eventually neutralizes Ar+ ions and clears the build-up charge in the vicinity of the target. As the

deposition happens only in the half cycle of the voltage, the deposition rate is usually low in the case of RF sputtering. However, this technique provides better control over the deposition process making it possible to deposit thin films with high uniformity.

**2.1.2 Thermal Evaporation:** Thermal evaporation is another widely used PVD technique owing to its simplicity, cost-effectiveness, and potential to deposit a wide variety of materials (including metals, semiconductors, insulators, and organics) [108,109]. Here the material to be evaporated is first kept in either a crucible or a thermal boat which is usually made up of tungsten, molybdenum, or other refractory materials. Using a resistive heating method (or Joule heating), the material kept inside the boat is heated until it melts and forms a vapor that travels inside a high vacuum chamber and reaches the substrate. A high vacuum is necessary to reduce
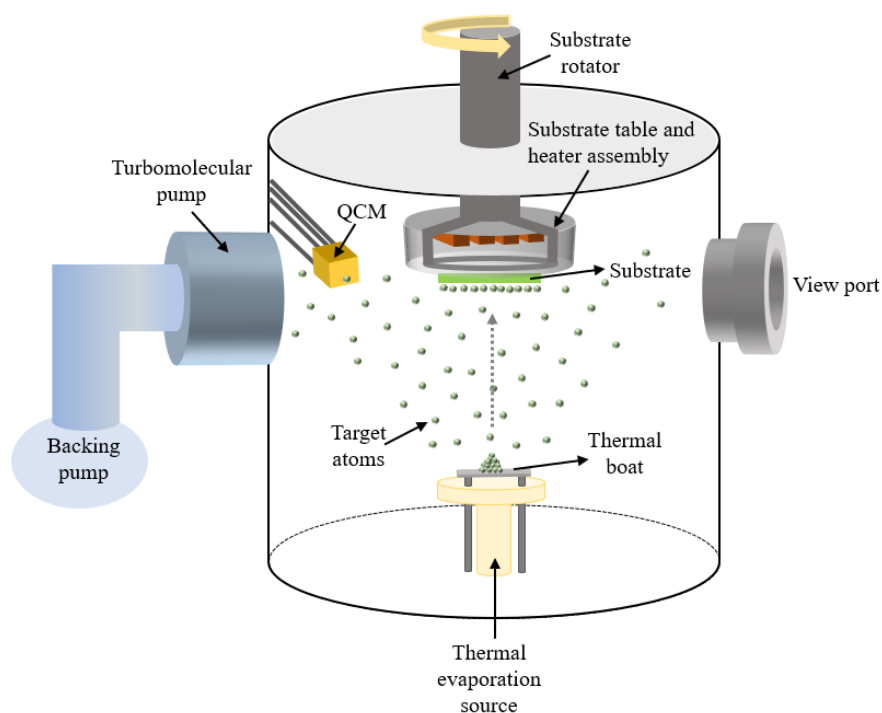
Figure 2.3 A schematic representation of the thermal evaporation technique. The evaporation source is kept at the center of the deposition system facing the substrate surface. Here target material is kept on a thermal boat and heated by a resistive heating method for the deposition.

the collision between the atoms inside the deposition chamber. In addition, the distance between the substrate and the target should be less than the mean free path of the traversing atoms. Depending on the bond strength and crystallinity of the evaporation material, melting may happen either uniformly or non-uniformly. Due to this, the thermally evaporated thin film sometimes compromises in controlling the thickness and maintaining uniformity, in comparison to a few other PVD techniques e.g., sputtering, molecular beam epitaxy. A schematic of the thermal evaporation technique is shown in Fig. 2.3.

All the samples shown in this thesis work are prepared using a multi-deposition unit of the QPrep series manufactured by Mantis Deposition Ltd. UK. The system is ultra-high vacuum (UHV) compatible, where the lowest achievable pressure is ~ $5 \times 10^{-10}$ mbar. To achieve such UHV condition three turbo pumps run in combination with two backing pumps. As the dimension of the deposition chamber is quite big, two turbo pumps are dedicatedly connected to this chamber whereas the other turbo pump is connected to the load-lock. The pressure at the main chamber is measured by a combined full-range gauge (Pirani+cold cathode gauge). A gate valve separates the load-lock from the main chamber. Thus, the load-lock provides the facility to mount or unmount substrates/samples without breaking the vacuum of the main deposition chamber. The multi-deposition unit has a total of 9 sources where 8 sources are equally spaced and located at the lower circular base of the cylindrical chamber, whereas the other source (thermal evaporator) is located at the center of the circular base. Each of these 8 equally spaced sources makes an angle of 45° with each other in the circular base. A list of all the sources is given below:

(a) 5 unbalanced magnetron sputtering sources (DC and RF)

(b) 2 thermal evaporation sources

(c) 1 electron-beam evaporator with 4 pockets

(d) A Mat60 unit to prepare oxide-based materials by producing atomic oxygen from the molecular oxygen gas.

(e) A nano-particle generator known as 'NanoGen' to deposit nanoparticles.

A colling facility is provided with each of the sources to prevent the overheating issue of the target material during deposition. The substrate table is located at the center of the upper circular base of the cylinder. All 8 sources lying in the lower base make an angle of 30° w.r.t.
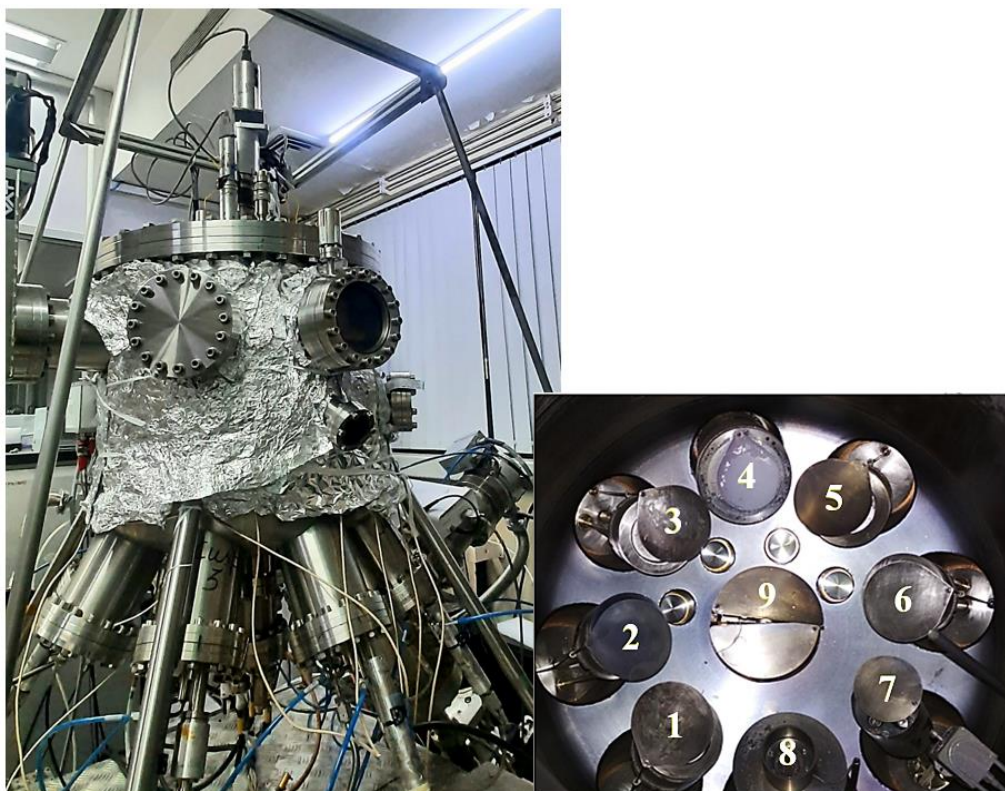


Figure 2.4 A picture of the multi-deposition unit present in our laboratory for nanomagnetism and magnetic materials (LNMM) at school of physical sciences (SPS), NISER-Bhubaneswar. The deposition chamber has a cylindrical geometry. The nine sources located inside the chamber are shown in the right-side inset image. Here, 1-3 are the DC sputtering sources, 4 is the MAT60 source, 5-6 are RF sputtering sources, 7 is the e-beam evaporator, 8 is the NanoGen source and 9 is the thermal evaporator which is located at the center of the chamber. All the sources are located at the lower circular base of the deposition chamber.

the substrate normal. To get uniformity in the deposited film the substrate table can be rotated from 0 to 20 rpm. Further, the halogen lamps positioned inside the substrate table allow to heat the table up to 800°C. A QCM is mounted near the substrate holder to accurately measure the deposition rate and thickness of the thin film. Figure 2.4 illustrates various components of the multi-deposition unit present in our lab.

## 2.2 Structural Characterization Techniques

### 2.2.1 X-ray diffraction and reflectivity:

**2.2.1.1 X-ray diffraction (XRD):** XRD is undoubtedly the most useful and non-destructive technique to characterize the structural properties of various matter starting from fluids, and powders to thin films. As the wavelength of X-ray (~ 0.15nm) is of the same order of magnitude as the atomic spacing in crystals, it can provide much valuable information, e.g., crystallinity, lattice parameters, grain size, film thickness, roughness, the density of dislocation, residual stress/strain, etc. [110,111]. Diffraction of X-rays from crystalline solids may be understood from two fundamental processes. First, the specular reflection of the X-ray helps to consider the atomic planes as a mirror. Second, as the wavelength of the X-ray and atomic spacing in the crystal is of the same order, it gives rise to both constructive and destructive interference phenomena. A schematic of the diffraction phenomena is shown in Fig. 2.5, where X-rays fall at an angle $\theta$ on the crystallographic planes having interplanar spacing $d_{hkl}$ (where *hkl* are the Miller indices), and after diffraction the beam scattered at the same angle $\theta$. The relative path difference between two consecutive X-rays scattered from the 1st and 2nd crystal planes is $2d_{hkl}\sin\theta$ as highlighted in yellow in Fig. 2.5. For constructive interference, the path difference between two consecutive X-rays should be an integral multiple of the wavelength ($\lambda$) of the X-ray [112], i.e.,

$$2d_{hkl}\sin\theta = n\lambda \tag{2.1}$$
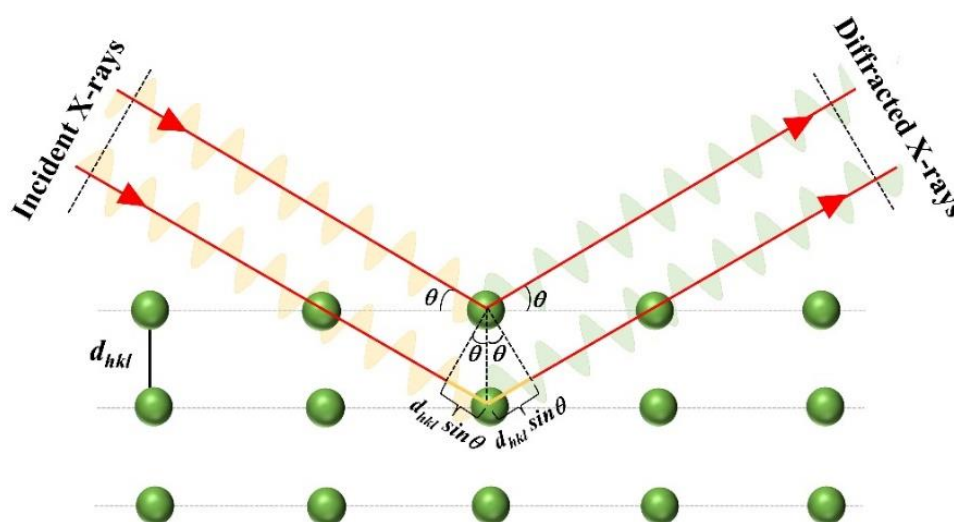
Fig. 2.5 A schematic illustration of the X-ray diffraction phenomena from crystallographic planes having interplanar spacing $d_{hkl}$, where the subscript *hkl* represents the Miller indices of the plane. The incident and scattered angle of the X-ray are the same and denoted by $\theta$. The path difference between two consecutive X-rays is $2d_{hkl} \sin \theta$, as shown in the image.

where, $n = 1, 2, 3\ldots$ is the order of diffraction maxima. Equation 2.1 is the well-known Bragg's law, where only for a few specific values of $d_{hkl}$ and $\theta$ the constructive interference appears. Thus, using the values of $\theta$ and $\lambda$, the interplanar spacing ($d_{hkl}$) can be calculated. Using the value of $d_{hkl}$, the lattice parameter also can be calculated. In the case of an orthorhombic crystal system, $d_{hkl} = \dfrac{1}{\sqrt{\left(\frac{h}{a}\right)^2 + \left(\frac{k}{b}\right)^2 + \left(\frac{l}{c}\right)^2}}$, where *a, b,* and *c* are the lattice parameters. In this thesis work, an automated multipurpose X-ray diffractometer SmartLab, manufactured by Rigaku Corporation, Japan has been used [113]. Five main components of the X-ray diffractometer are listed below [113]:

(a) X-ray source: Here in a vacuum tube X-rays are generated by bombarding high energetic electrons on the Cu anode. Here, the characteristic wavelength of the Cu $K_\alpha$ radiation is, $(\lambda)_{K\alpha}$ = 1.54 Å.

(b) Incident (or primary beam) optics: A series of optics (e.g., cross beam optics, Soller slit, incident slit, etc.) helps in making the X-ray beam collimated over a long distance and properly focus on the sample surface.

(c) Goniometer: The goniometer has a sample mounting table that can adjust the height ($z$) of the sample table as required. The stage can rotate the table in its plane (say, $\Phi$) and w.r.t. the stage normal (say, $\chi$).

(d) Receiving (or diffracted beam) optics: After reflection from the sample surface a series of optics (e.g., parallel slit analyzer, Soller slit, receiving slits, etc.) helps in directing the X-rays to the detector.

(e) The detector: A detector is used at the end to collect all reflected X-rays and convert them to electrical signals. We have mainly used scintillation counters for our measurement purposes. A general layout of the diffractometer is shown in Fig. 2.6 (a). As exposure to X-rays can cause serious health hazards the diffractometer is always kept inside a radiation enclosure, as shown in Fig. 2.6 (b).
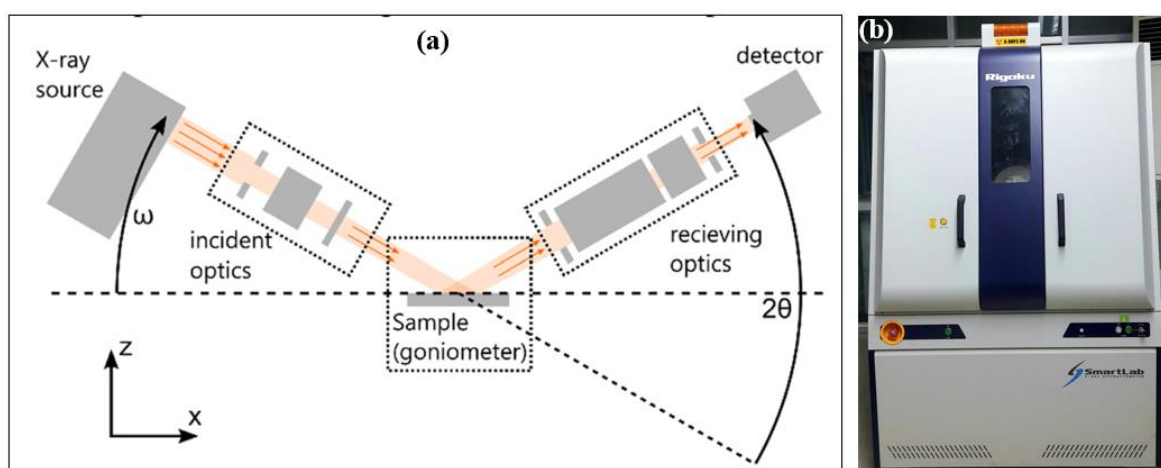


Figure 2.6 (a) A general layout of the X-ray diffractometer. The image is taken from ref. [111], (b) a photo of the automated multipurpose X-ray diffractometer, SmartLab available at the SPS, NISER-Bhubaneswar.

**2.2.1.2. X-ray reflectivity:** X-ray reflectivity (XRR) measurement helps to probe the thickness, roughness, and density of each layer in a multilayered thin film [110,114]. This technique is versatile since it is independent of the degree of crystallinity of the film. Using sophisticated optics, it can measure film thickness starting from 1 Å to a few hundred nm (~ 400 nm). When an X-ray falls at the interface of two media having different refractive indices, part of the X-ray is transmitted into the 2nd media whereas part of it is reflected back to the 1st media, as per Fresnel's reflection [115]. As shown in Fig. 2.7 (a), when the X-ray beam falls from the air to the sample surface the refractive index of the sample can be considered as [115–117],

$$\tilde{n} = 1 - \delta + i\beta \tag{2.2}$$

where, $\delta = \frac{\lambda^2}{2\pi} r_e \rho_e$ and $\beta = \frac{\lambda}{4\pi}\mu$. Here, $\lambda$ is the wavelength of the incident X-ray, $r_e, \rho_e$ and $\mu$ are the radius, density, and absorption length of the electron, respectively. $\delta$ and $\beta$ are related to the scattering mechanism and absorption of X-rays. As $\rho_e$ depends on the density of the material, $\delta$ gives information about thin film density. A typical X-ray reflectivity curve is shown in Fig 2.7 (b). To understand how the graph gives information about the thickness, density, and roughness of multilayered films, we will start with the Snell-Descartes law, $n \cos \theta_{incident} = \tilde{n} \cos \theta_{transmission}$ (for a specular reflection, $\theta_{incident} = \theta_{reflection}$). As hard X-rays are generally used for measurements, only very little of them get absorbed. Thus, $\beta$ is usually very small and can be neglected. Therefore, the modified equation 2.2 will be, $\tilde{n} = 1 - \delta$. Using this modified index the Snell-Descartes law can be written as,

$$\cos \theta_{incident} = (1 - \delta) \cos \theta_{transmission} \tag{2.3}$$

When X-rays falls at very small angles on the sample surface, all the X-rays get reflected making $\theta_{transmission} = 0$. Thus, for total external reflection, $\theta_{incident}$ becomes equal to the critical angle $\theta_C$. Hence, equation 2.3 modifies to, $\cos \theta_C = (1 - \delta)$. As $\theta_C$ is very small the

Taylor series expansion of $cos\theta_C$ will give a condition, $\theta_C^2 = 2\delta$. As discussed already that $\delta$ depends on the density of each layer, thus, $\theta_C$ gives information about the thin film density. Due to total external reflection, the detector receives a maximum number of X-rays reflected from the surface. However, when $\theta_{incident} > \theta_C$, part of the X-rays transmitted inside the sample and it reduces the intensity of the X-rays reaching the detector, as shown in Fig 2.7. For $\theta_{incident} > \theta_C$, the Fresnel's reflection coefficient ($r$) can be written as [115],

$$r = \frac{n_{air} \sin \theta_{incident} - \tilde{n} \sin \theta_{transmission}}{n_{air} \sin \theta_{incident} + \tilde{n} \sin \theta_{transmission}} \qquad (2.4)$$

For small values of $\theta_{incident}$, using Snell-Descartes law in $r$, the final reflection coefficient for an ideal flat surface can be written as [115],

$$r = \frac{\theta_{incident} - \sqrt{\theta_{incident}^2 - \theta_C^2}}{\theta_{incident} + \sqrt{\theta_{incident}^2 - \theta_C^2}} \qquad (2.5)$$

Thus, the intensity ($I$) of the X-ray reflectivity curve can be expressed by the equation [115],

$$I = R(\theta) = r\,r^* = \left| \frac{\theta - \sqrt{\theta^2 - \theta_C^2}}{\theta + \sqrt{\theta^2 - \theta_C^2}} \right|^2 \qquad (2.6)$$

From equation 2.6 we find out the following three conditions [114],

i.      When $\theta < \theta_c$, $I = R(\theta) = 1$; i.e., maximum intensity to detector

ii.     When $\theta = \theta_c$, $I$ and $R(\theta)$ start reducing significantly, as shown in Fig. 2.7 (b)

iii.    When $\theta \gg \theta_c$, $R(\theta)$ and hence, $I$ reduce as $\frac{1}{\theta^4}$ as indicated in Fig. 2.7 (b)

When $\theta > \theta_c$, X-rays penetrate inside the sample surface and the reflection occurs from both the lower and upper surfaces of the thin film. Thus, both constructive and destructive interference appear which gives rise to periodic interference patterns known as Kiessig fringes in the reflectivity curve, as shown in Fig. 2.7 (b). For a single-layer thin film, the thickness
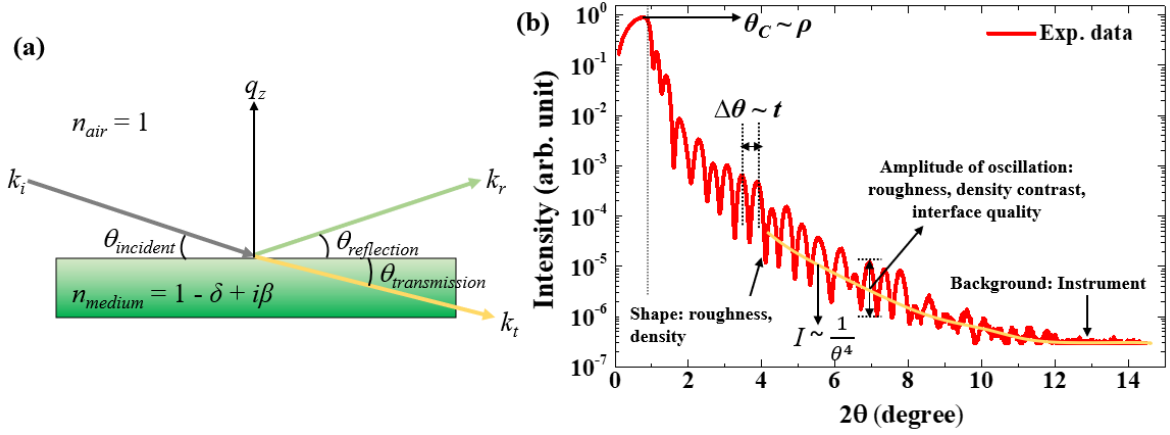
Figure 2.7 (a) Schematic of X-ray reflection and transmission in specular reflection geometry, where $k_i$, $k_r$, and $k_t$ are the incident, reflected, and transmitted wave vectors, respectively. $\theta_{incident}$, $\theta_{reflected}$, and $\theta_{transmitted}$ are the angles of incidence, reflection, and transmission of X-ray, respectively. (b) Typical XRR spectra where intensity (in log scale) is plotted w.r.t. $2\theta$. The concept of the image is adapted from ref. [114].

can be determined using Bragg's law, $t = \frac{\lambda}{2\Delta\theta}$ , where $t$ is the film thickness and $\Delta\theta$ is the difference between two consecutive maxima or minima in the periodic XRR pattern, as indicated in Fig. 2.7 (b). In the real case, the surface of a thin film is not entirely smooth. Due to the roughness of layers, the off-specular reflection takes place which reduces the amplitude of the oscillation and the intensity of the XRR curve (see Fig. 2.7 (b)). Thus, to add roughness to the reflection coefficient a new term is added to Fresnel's reflection coefficient, as written below [116];

$$r_{rough} = r_{flat}e^{-\frac{q^2\sigma^2}{2}}$$ (2.7)

where, $q = \frac{4\pi}{\lambda}\sin\theta$ and $\sigma$ is the surface roughness.

Now, for a multilayer thin film, the reflection and transmission occurring from each interface require to be calculated separately. To solve this a recursive formalism is given by Parratt which

49

is used in most commercially available X-ray reflectivity simulation software [118,119]. To fit the XRR data by this formalism a model layer structure is usually provided beforehand. The fitting provides the thickness, roughness, and density of each layer of the multilayered thin film. In the thesis work, to fit the XRR data of the multilayered thin films, we have used GenX software which is formulated using Python script and based on Parratt formalism [118].

**2.2.2 Scanning Electron Microscopy (SEM):** SEM is a very powerful and widely used imaging technique that uses electron beams to study the surface topography and composition of a sample with very high resolution [120,121]. As optical microscopes use visible light for imaging purposes, the maximum achievable resolution is ~200 nm (due to the wavelength limitation). However, in the case of an electron microscope, a very high resolution can be achieved (~ 1-5 nm) owing to the shorter wavelength of electrons ($\lambda \sim 0.1\ nm$) [122]. A beam of $e^-$ can be generated in three ways by using, (a) a tungsten filament, (b) a solid-state crystal (cerium hexaboride or lanthanum hexaboride), and (c) a field emission gun. The field emission guns have a very small tip size (~ 100 nm) which makes the $e^-$ beam more coherent and optically bright. It also provides better spatial resolution and better emitter lifetime than the other two methods. A schematic of the typical working principle of SEM is shown in Fig. 2.8. First, a highly energetic $e^-$ beam is created from the cathode of an electron gun. They are then accelerated towards the anode due to the applied bias. Further, the diverged $e^-$ beam is converged and focused at a point with the help of two condenser lenses (electromagnetic lenses). It also sets the $e^-$ beam diameter and the probe current. The objective lens consists of electrostatic and electromagnetic lenses. It focuses electrons on the sample surface and reduces the spherical and chromatic aberration. The defection system is comprised of a set of scan coils that move the $e^-$ beam in the $x$ and $y$ directions. Due to electron-matter interaction secondary electrons (SEs), back-scattered electrons (BSEs), Auger electrons, X-rays, etc. are produced. SEs are produced by inelastic collision from the place where the primary beam falls on the
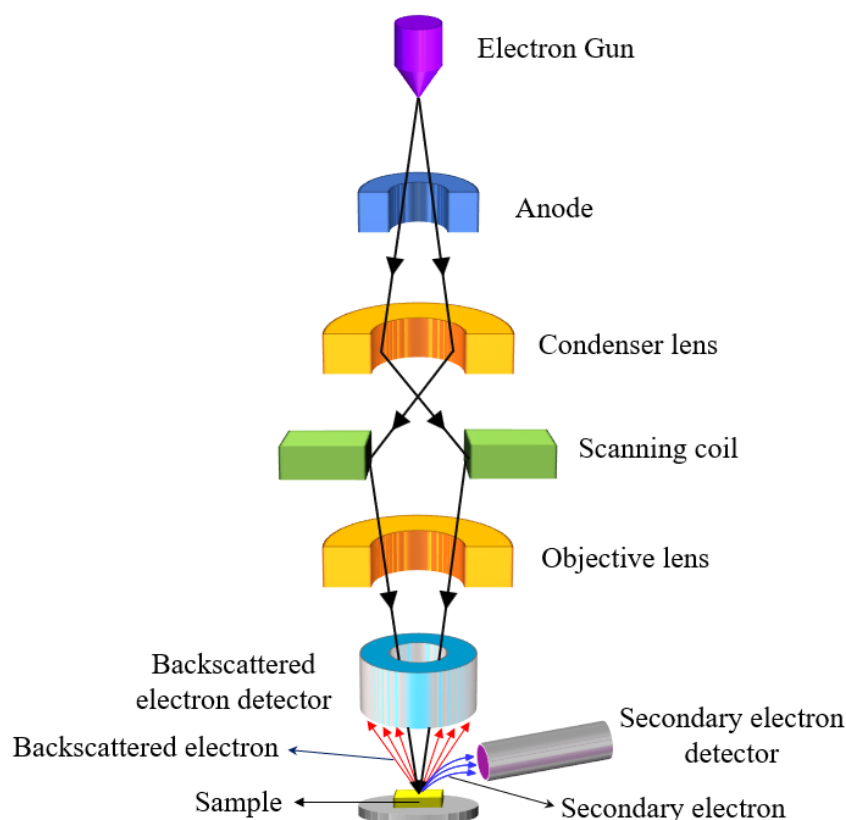
Figure 2.8. Schematic illustration of the working principle of scanning electron microscope.

sample surface. Thus, they mainly give information about the surface structure and topography of a sample. A few parts of the $e^-$ beam go inside the sample surface and experience several elastic interactions. Depending on the atomic no. of the elements, the no. of collision and their scattering direction can be different. These BSEs give information about the crystal orientation and composition of the material inside the sample surface. To collect the SEs and BSEs different types of detectors are mounted. The incoming $e^-$ signal is converted by the detector to give an idea about surface topography. The resolution of an SEM image depends on several factors, e.g., spot size and energy of the incident $e^-$ beam, $e^-$ - matter interaction volume, etc. In this thesis work to study the impact of strain application, we have scanned the sample surface at both the flat and bent states, using a field emission scanning electron microscope (FESEM) manufactured by ZEISS (Model-Sigma). For imaging, the electron energy is kept within 5 keV

and the SEs are collected using an in-lens detector. During measurements the column chamber pressure was $\sim 2 \times 10^{-5}$ mbar, whereas the gun pressure was $\sim 3 \times 10^{-9}$ mbar.

## 2.3 Magnetic Characterization:

**2.3.1 Magneto-optic Kerr effect (MOKE) microscopy:** MOKE microscopy (or sometime called as Kerr microscopy) is a widely used technique to study various magnetic properties such as magnetic anisotropy, magnetization, and domain dynamics of multilayers, thin films, and nano-particle ensembles [123–125]. It is based on the magneto-optic Kerr effect, where the plane of incident polarized light gets rotated upon reflection from a magnetic sample [126,127]. A linearly polarized light can be considered as a superposition of left circularly polarized (LCP) and right circularly polarized (RCP) light, with amplitudes, $E_L = E_R = \frac{E}{2}$. When such a linearly polarized light falls on a sample containing free electrons, the electric field of LCP light sets the electrons into a left circular motion, whereas the RCP light drives them into a right circular motion. Thus, the rotation of an electron around a positive charge center can be considered as a rotating electric dipole, where the electron feels an attractive force ($F \propto -r$, where $r$ is the radius of electron motion) towards the positive center to create charge neutrality. The radius ($r_{L,R}$) of the rotating electron can be calculated using the equilibrium of all forces acting on the electron. Thus, $r_{L,R}$ (where $L$, and $R$ in the subscript represent the left and right circular motion) can be written as [123–125,128],

$$r_{L,R} = \frac{\frac{eE}{2m}}{\omega^2 - \omega_0^2} \tag{2.8}$$

where, $e$, $m$ is the charge and mass of the electron, $E$ is the electric field of the incident polarized light, $\omega$ is the angular frequency of the light, and $\omega_0 = \sqrt{\frac{k}{m}}$ is a constant of the material. Thus, for the rotating dipole moments ($P_i \propto r_{L,R}$), the electric displacement vector ($\boldsymbol{D}$) can be written as, $\boldsymbol{D} = \epsilon \boldsymbol{E} = (\epsilon_0 \boldsymbol{E} + \boldsymbol{P})$, where $\boldsymbol{P}$ is the polarization density (depends on the no. of dipole

moments $N$ per unit volume), $\epsilon, \epsilon_0$ are the permittivity of the medium and free space, respectively. Thus, the dielectric constant, $\epsilon_r (= \frac{\epsilon}{\epsilon_0})$ can be expressed as [128],

$$\epsilon_r = \left( 1 + \frac{\frac{Ne^2}{2m\epsilon_0}}{\omega^2 - \omega_0^2} \right) \tag{2.9}$$

Hence, the refractive index $n_{L,R}$ for the left and right circular polarized light will be the same, owing to their same dielectric constant. However, if a magnetic field is applied to the material, then the Lorentz force will come into the picture. It will push the electron motion either towards or away from the circle's center, depending on whether it is a left or right circular motion. Hence, the radius of the left circular motion will squeeze whereas the right circular motion will expand, as written below [128];

$$r_{L,R} = \frac{\frac{eE}{2m}}{\omega^2 - \omega_0^2 \mp \frac{\omega Be}{m}} \tag{2.10}$$

Here, the difference in radii for the left and right circular motion will give different dipole moments, which indeed will give different dielectric constants. Thus, the refractive index $n_{L,R}$ for the left and right circularly polarized light will be different, leading to different velocities of propagation. This phenomenon is similar to the birefringence of circularly polarized light. It will further induce a phase difference ($\Delta\theta$) between the LCP and RCP waves, where, $\Delta\theta \propto (n_L - n_R)$. Thus, the reflected light upon emergence shows a rotation of its plane of polarization, known as Kerr rotation ($\theta_K$). As the Kerr rotation mainly originates from the Lorentz force induced by an applied magnetic field ($B$), it has been found that $\theta_K \propto B$. In the case of a ferromagnetic material, $\theta_K$ is dependent on total $\boldsymbol{B} (= \boldsymbol{B_0}(1 + \chi))$. As $\chi \gg 1$ for FMs, $\boldsymbol{B} = \boldsymbol{B_0}\chi$, which implies $\boldsymbol{B} = \mu_0 \boldsymbol{M}$. Thus, in FMs, the Kerr rotation $\theta_K$ represents the magnetization $\boldsymbol{M}$ of the sample. Microscopically, the spin-orbit interaction couples the spin-magnetic moment of an electron with its motion, which then reacts to the incident electric field of light. Thus,

establishing the connection between the magnetic and optical characteristics of ferromagnetic materials. Apart from rotation, the light reflected from a magnetic medium may also have some ellipticity ($\epsilon_K$), if the amplitude of the reflected LCP and RCP wave differs from each other. This makes the dielectric constant and hence, the refractive index of the magnetic medium a complex parameter. Thus, the general macroscopic explanation of magneto-optic effects is based on the dielectric tensor theory, $\boldsymbol{D} = \epsilon\boldsymbol{E}$ (where $\epsilon$ is an antisymmetric tensor) which is derived from Maxwell's equation of EM wave propagating in a magnetic media. The dielectric law also can be expressed as [123–125],

$$\boldsymbol{D} = \epsilon(\boldsymbol{E} + iQ\boldsymbol{m} \times\boldsymbol{E}) \qquad (2.11)$$

where, $Q$ is a material-dependent parameter, proportional to the saturation magnetization $M$ of the magnetic sample and hence, represents the strength of the Kerr effect. The dielectric tensor representing the magnetic media can be written as [123–125]:

$$\epsilon' = \epsilon\begin{pmatrix} 1 & iQ_v m_z & -iQ_v m_y \\ -iQ_v m_z & 1 & iQ_v m_x \\ iQ_v m_y & -iQ_v m_x & 1 \end{pmatrix}$$

where, $Q_v$ is the Voigt constant and $(m_x, m_y, m_z) = \boldsymbol{m}$ is the normalized magnetization vector. MOKE arises mainly due to the off-diagonal terms of the dielectric tensor that are dependent on the magnetization of the sample. The Kerr rotation ($\theta_K$) can be expressed in terms of the Kerr amplitude ($\boldsymbol{K}$) and normal amplitude ($\boldsymbol{N}$) of the reflected and incident polarized light. The 2nd term of equation 2.11 closely resembles the Lorentz force. Thus, by taking the projection of Lorentz movement ($\boldsymbol{v_{LOR}}$) in a plane that is perpendicular to the propagation direction of the reflected light, we can get the Kerr amplitude ($\boldsymbol{K}$) as shown in Fig. 2.9 (a). Using small angle approximation one can express the Kerr rotation $\theta_K$ as, $\theta_K = \frac{K}{N}$ [123,124]. As $\boldsymbol{K}$ is opposite for the domains with opposite spontaneous magnetization, the Kerr rotation also will be opposite. If the reflected light from one domain is completely blocked by the analyzer, then the contrast
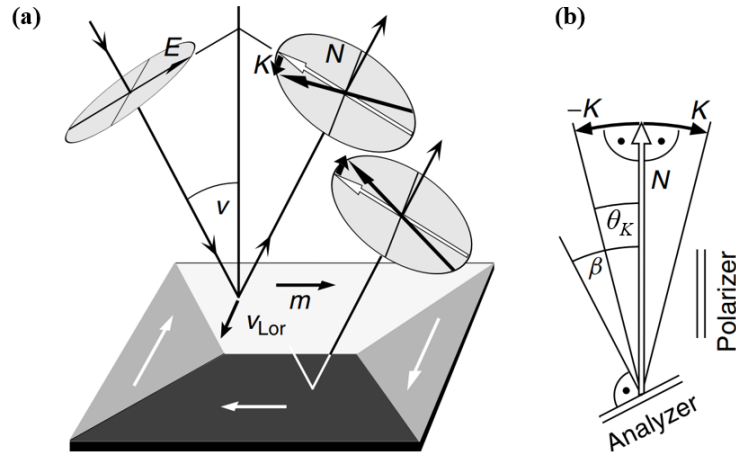
Figure 2.9. (a) Schematic illustration of MOKE interaction in the longitudinal geometry. Here, the incident light is polarized parallel to the plane of incidence and the sample has an in-plane (IP) magnetization $m$. The electric field ($E$) of incident light and the magnetization $m$ of the sample together give rise to a Lorentz motion ($v_{LOR}$) to the electrons. The Kerr amplitude ($K$) is obtained by taking a projection of $v_{LOR}$ in the plane perpendicular to the propagation direction of reflected light. (b) The relative orientation of the analyzer and polarizer are shown w.r.t the normally reflected amplitude ($N$) and Kerr amplitude ($K$). The image is taken from ref. [123].

will be black for that domain, whereas white contrast will appear for the oppositely magnetized domain. In this way, domain contrast can be obtained in the image plane. The Kerr signal $S$ is the difference between the intensities originating from the dark and bright domains and can be expressed as, $S = 4\beta KN$, where $\beta$ is the angle formed by the analyzer and $N$, as shown in Fig. 2.9 (b) [123]. Depending on the magnetization orientation of a sample and the plane of incidence of the light, three kinds of MOKE geometries are possible [124], as shown in Fig. 2.10.

(a) Longitudinal MOKE (L-MOKE): In this geometry, the magnetization of the sample is parallel to both the plane of incidence of incoming light and the sample surface.

(b) Transverse MOKE (T-MOKE): Here, the magnetization of the sample is parallel to the sample surface and perpendicular to the plane of incidence.

(c) Polar MOKE (P-MOKE): In this geometry, the magnetization of the sample is parallel to the plane of incidence and perpendicular to the sample surface.
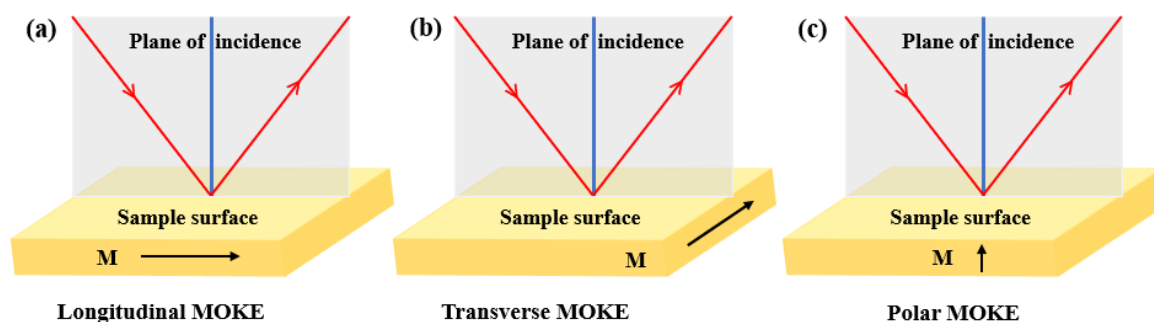


2.10. Three different kinds of MOKE geometries, (a) L-MOKE, (b) T-MOKE, and (c) P-MOKE depending upon the magnetization orientation of the sample and the plane of incidence of the polarized light.

A schematic of the Kerr microscopy set-up is shown in Fig. 2.11 (a). First, an unpolarized light passes through a polarizer and becomes linearly polarized. Let us assume that the sample has two domains having opposite spontaneous magnetization. After reflection from the sample, beam 1 and beam 2 will be rotated in equal and opposite directions. The ellipticity of the reflected light can be compensated using a quarter wave plate before the analyzer. To get contrast in the image plane the analyzer is rotated in such a way that blocks one of the reflected beams completely. This will create a dark contrast in the image plane. However, for the other beam, the contrast will be bright in the image plane. Hence, the domain states of the magnetic sample can be visualized using Kerr microscopy. A charge-coupled device (CCD) is used to convert the reflected photons to electrons and form a digital image of the domains.
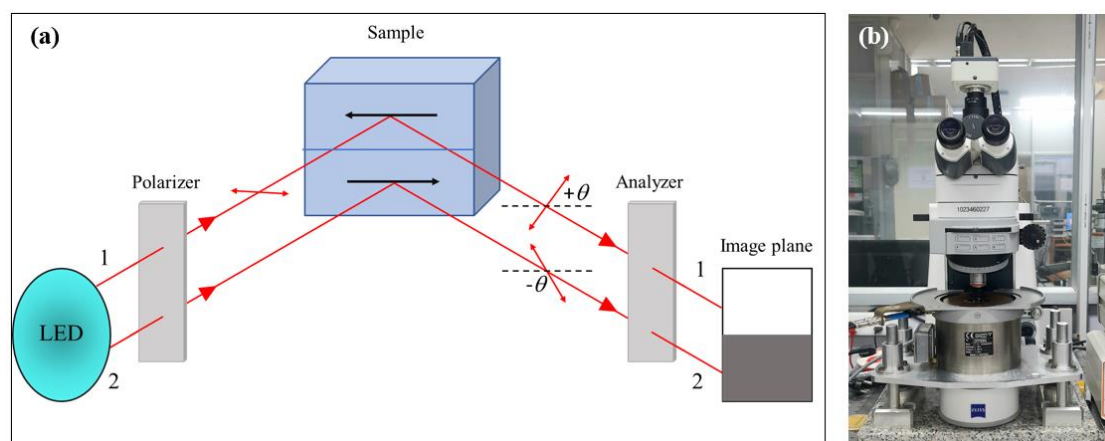
2.11 (a) Schematic illustration of the domain image formation process using MOKE-based microscopy setup, (b) MOKE microscopy facility available in our laboratory (LNMM) at NISER. The concept of the schematic shown in (a) is taken from ref. [129].

The magnetization and domain dynamics of our samples are studied using Kerr microscopy manufactured by Evico Magnetics Ltd., Germany, as shown in Fig. 2.11 (b). The microscope has eight LED sources, and it allows to change the sensitivity of the measurement by selecting the right combination of LEDs [130]. The maximum resolution possible to achieve using an oil immersion objective is ~ 300 nm. To apply magnetic field in the sample plane it has a single-axis electromagnet (maximum field ~ 1.3 T) and a biaxial quadrupole magnet (maximum field ~ 0.2 T). To apply a magnetic field perpendicular to the sample plane it also has a polar electromagnet (maximum field ~ 0.9 T). All the electromagnets have a colling facility to avoid the heating issue of the coils. Magnetic hysteresis loops and simultaneous domain images can be recorded using the KerrLab software. Magnetization relaxation measurement also can be performed using the MOKE microscope. It also enables the pulsed magnetic field-induced DW velocity measurement using small home-made coils. Further, by using both the small coil and an electromagnet, it also enables measuring the DMI strength of the magnetic samples as explained below in detail.

**2.3.2 Field-induced domain wall velocity measurement:** Domain wall (DW) dynamics have been immensely studied for the last few decades due to their rich fundamental physics and spintronics applications. Controlled DW motion has been proposed to be used in DW-based race track memories, spintronic memristors, logic units, etc. [131–133]. For such applications, ferromagnetic thin films with perpendicular magnetic anisotropy (PMA) are even more attractive (than IMA systems) due to their higher thermal stability and the requirement for lower threshold excitation current. As the DW velocity obeys an exponential relationship with the applied field ($v \propto \exp[-\left(\frac{H}{H_{dep}}\right)^{-\frac{1}{4}}]$) in the creep region, a small and steady pulses can be applied for a moderate duration [64,79]. However, in the flow region as $v \propto H$, a high pulse field can be applied for a very small duration (few μs to hundreds of ns) [64,79]. Thus, the main requirement for performing such measurements is to design a coil that meets the purpose. The magnetic field generated at the center of a coil of inner radius $r$ can be written as, $H = \frac{\mu_0 N I}{2r}$, where $\mu_0$ is the permeability of vacuum, $N$ is the total number of turns of the coil, and $I$ is the applied current. Thus, the inductance ($L$) corresponding to the coil can be written as, $L = \frac{\mu_0 \pi N^2 r}{2}$. As, $H \propto N$ and $L \propto N^2$, both $H$ and $L$ increase with increasing $N$. From a simple LR circuit analysis, we may write the rise time ($\tau$) of the coil as, $\tau = \frac{L}{R_{total}}$, where $L$ is the inductance and $R_{total}$ is the total resistance of the circuit ($R_{coil} + R_{circuit}$). To obtain a high magnetic field, one may either increase $I$, $N$, or reduce the radius ($r$) of the coil. However, an increase in $I$ will increase the Joule heating effect in the coil and may damage it if proper cooling is not provided. Further, an increase in $N$ will increases the inductance $L$, which in turn will increases the rise time ($\tau$) of the coil, and restrict to apply pulses of smaller duration. Thus, to maintain a proper balance of these two, $N$ should be chosen carefully. Hence, the enhancement in field value while keeping $\tau$ low, is only possible by reducing the value of $r$.

Thus, to apply very high field pulses one must prepare coils of few μm radius. In our case, to apply small fields we have prepared a coil of 3.25 mm inner radius having 100 number of turns. The coil can generate a maximum field of ~24 mT, where the Cu wire can sustain ~ 6A current. As the rising time for magnetic field is ~ 1 ms, the minimum pulse width used during our measurements is 5 ms. A sourcemeter unit (SMU 2461- Keithley) is used to apply pulsed currents to the coil. A gauss meter is used to calibrate the magnetic field generated by the coil. The field is uniform along the centre axis of the coil and the measurement is always taken at this place to avoid any inhomogeneity from the applied field. The sample is placed on a specially designed holder and the coil is placed below the sample holder as shown in Fig. 2.12.
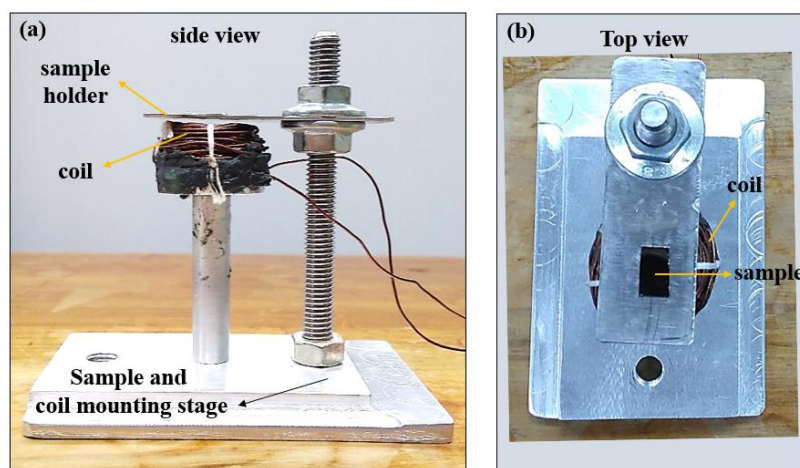


Figure 2.12. (a) Side and (b) top view of the sample and coil mounting geometry for pulsed magnetic field-induced DW velocity measurement using a MOKE microscope.

The DW velocity measurement protocol is illustrated in Fig. 2.13 and described below [82]:

(i)   First, the magnetic thin film is saturated by applying a high pulse field along the out-of-plane (OP) direction of the sample.

(ii)  Then a reverse domain is nucleated by applying a short-pulsed field in the opposite direction and the nucleated domain image is recorded.

(iii) For propagation, another pulsed field is applied and the corresponding domain image is recorded. The amplitude of the propagation pulse is varied to obtain a $v$ - $H$ curve.

To measure the velocity, the image of the nucleated domain is subtracted from the image of the propagated domain, using ImageJ software. The subtracted bright annular region is the displacement of the wall for a given pulse duration, as shown in Fig. 2.13. To avoid the impact of rough edges of the DW in the velocity calculation, we measure the DW displacement at several places of the bright annual region. Finally, the average displacement ($l$) of the DW is divided by the pulse width ($t$) to determine the domain wall velocity ($v$) as, $v = \frac{l}{t}$. To obtain a $v$ - $H$ plot, the velocity measurement is done for varied propagation field $H$. In our case, we have limited our measurement to the creep region, and the measured data plot is fitted with the creep law.
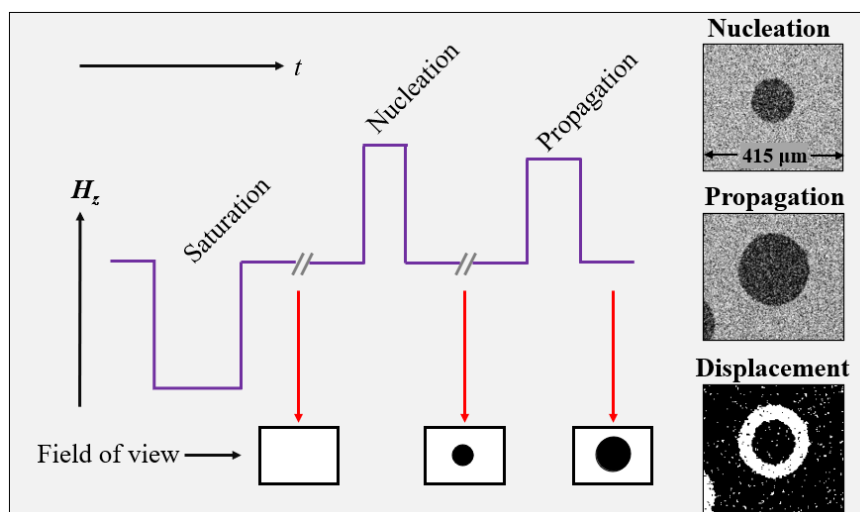


Figure 2.13. Schematic illustration of the DW velocity measurement protocol. The nucleated, propagated, and subtracted domain images are shown in the right-side column. The area of each domain image is 415 μm × 375 μm. The concept of the figure is taken from ref. [82].

**2.3.3 Evaluation of interfacial Dzyaloshinskii-Moriya interaction (iDMI) via asymmetric DW motion:** The interfacial Dzyaloshinskii-Moriya interaction (iDMI) originating from a heavy-metal (HM)/ferromagnet (FM) interface plays a crucial role in stabilizing chiral spin textures in magnetic multilayers [134,135]. In the case of a magnetic thin film consisting of

bubble domains, the presence of iDMI leads to asymmetric domain propagation when both IP and OP magnetic fields are applied. Je *et al.*, first showed that the asymmetric bubble domain expansion can be used as a method to quantify iDMI in thin films [91]. A system with a sizeable DMI generates a DM field ($H_{DMI}$) that acts in a radially opposite direction of the DW and maintains a rotational symmetry w.r.t the perpendicular $\hat{z}$-axis. The rotational symmetry is broken with the application of an IP field ($H_x$) and the asymmetric domain expansion happens. Thus, the DM field either gets cancelled or enhanced under an IP bias field, resulting in faster motion for one DW (say, $v_L$ or ↑↓) and slower motion for the other (say, $v_R$ or ↓↑) along the radial direction. If we plot the DW velocity (i.e., $v_L$ and $v_R$) w.r.t the applied IP magnetic field (at a constant OP field), then the minima of the velocity curve gives the value of $H_{DMI}$. By extracting $H_{DMI}$ one can deduce the strength of effective iDMI using the equation [91,136];

$$D_{eff} = \mu_0 H_{DMI} M_s \delta \qquad (2.12)$$

where, $\delta = \sqrt{\dfrac{A}{K_{eff}}}$ is the DW width (with $A$ = exchange constant, $K_{eff}$ = effective anisotropy constant) and $M_s$ is the saturation magnetization of the sample.

We have assembled a setup to quantify iDMI strength via the asymmetric DW expansion method using MOKE microscopy. The details of the setup and measurement protocol are described in the following. An electromagnet is used to apply a DC magnetic field in the sample plane and a coil is used to apply a pulsed magnetic field along the OP direction. Similar to the DW velocity measurement here first we saturate the sample by applying a high OP pulsed field and then nucleated a reverse domain. Further during propagation of the domain both IP and OP fields are applied simultaneously and the image is recorded. The propagation images are recorded for both the positive and negative IP applied fields. The propagated domain images are then compared to check if the $v_L$ and $v_R$ are the same for both the positive and negative IP fields. In case the propagation is higher for one field and lower for the other, there must be a

tilt in the applied IP field, as shown in Fig. 2.14. A tilt in the opposite IP field ($\pm H_x$) will generate an opposite OP field ($\pm H_z$), which will modify the DW propagation under the applied OP pulsed field. Thus, to get the correct DMI field value the tilt in the IP field should be corrected so that no component of the IP field exists in the OP direction. As the electromagnet is placed on a stage that has a rotating screw, it helps to correct the tilt by rotating the screws at a certain angle and again recording the domain images for both positive and negative IP fields (in the presence of a constant OP pulsed field). The process is continued until the domain propagation is found to be the same for both the opposite applied IP fields. As the range of the IP field used during iDMI measurement is large (~300 mT) a small tilt in the IP field may result in a finite OP field which in turn modifies the strength of the small OP pulsed field (~10-20 mT), as shown in Fig. 2.14. The tilt angle is usually found to be less than 1 degree in our case. Once the tilt is corrected then for a fixed OP pulsed field the domain propagation is recorded for varied strength of the IP bias field. To obtain DW velocity, the nucleation image is then subtracted from the propagation image, and the asymmetric domain propagation is obtained. The velocity of the left and right DW is calculated and plotted w.r.t the IP field. The minima in the velocity curve represent the value of $H_{DMI}$. In the absence of DMI, the velocity vs. IP field plot should be symmetric w.r.t the zero IP field (for zero DMI field). However, the presence of
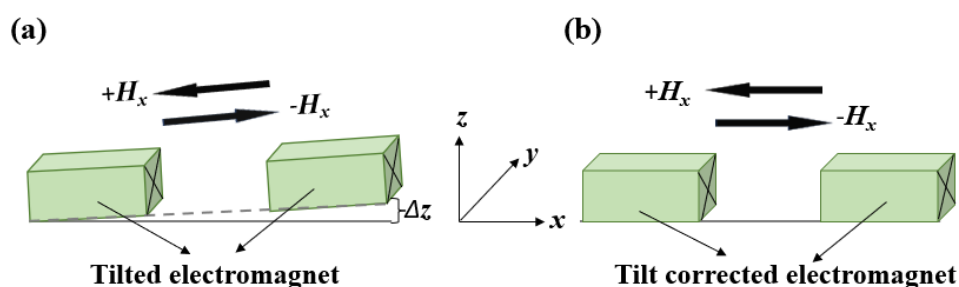


Figure 2.14. (a) The tilted *x-y* plane of the electromagnet originates a tilted IP magnetic field ($\pm H_x$) which in turn gives rise to an OP magnetic field, and (b) Tilt corrected properly aligned electromagnet. The concept of the image is taken from ref. [81].

finite DMI will shift the minima from zero to a finite IP field value i.e., comparable to the DMI

field of the sample, as shown in Fig. 2.15. The chirality (left or right-handed) and type (either

Bloch or Néel) of the DW also can be identified by measuring the displacement of the wall

along $\pm x$ and $y$ directions of the domain [137]. The ratio, $\varepsilon_1 = \frac{S_x^+}{S_x^-}$ determines the chirality

whereas, $\varepsilon_2 = \frac{S_y}{S_x^{max}}$ , determines the type of wall. Here, $\pm S_x$ and $S_y$ represent the displacement

of the DW along $\pm x$ and $y$ directions, respectively (Fig. 2.15). For, $\varepsilon_1 > 1$, right-handed chiral

DW will be formed, whereas for, $\varepsilon_1 < 1$, left-handed chiral DW will be formed. Further, $\varepsilon_2 >$

1 , represents a Bloch wall, whereas $\varepsilon_2 < 1$ indicates the formation of Néel wall. Thus, the
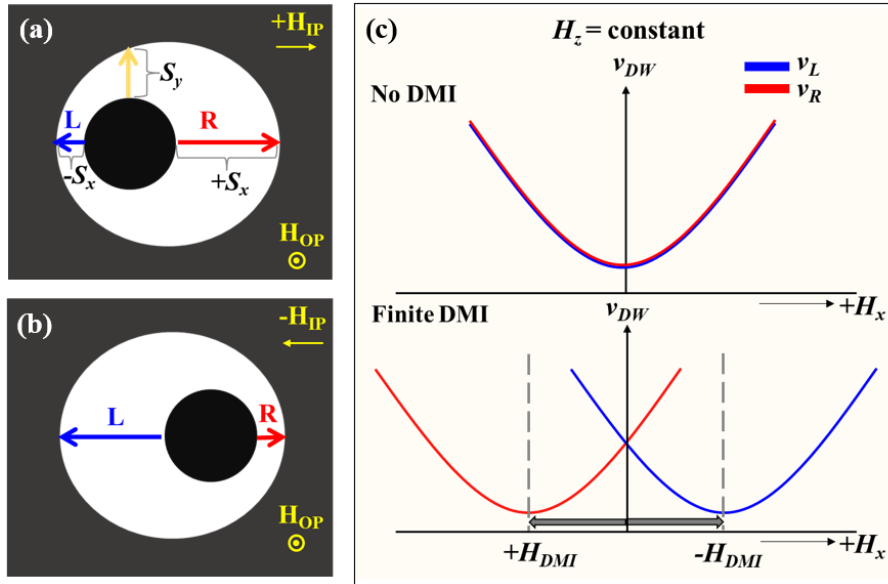


Figure 2.15. Schematic diagram of asymmetric domain propagation in the presence of both

OP pulsed field and (a) positive IP bias field, (b) negative IP bias field. R and L represent the

right, and left sides of the DW respectively. Here, $\pm S_x$ and $S_y$ represent the DW displacement

along $\pm x$ and $y$ directions, respectively. (c) A schematic of the DW velocity ($v_{DW}$) vs. IP field

($\pm H_x$) plot (at a constant $H_z$), in the presence and absence of DMI. The minima in the velocity

curve give a measurement of the DMI field ($H_{DMI}$) present in the sample. The concept of the

image is taken from ref. [81].

asymmetric DW motion measurement is a very efficient and non-destructive way to quantify the iDMI strength and identify the nature of the DW present in a sample.

**2.3.4 Superconducting quantum interference device (SQUID) magnetometry:**

Superconducting quantum interference device (SQUID) magnetometry is a very sensitive method for measuring extremely weak magnetic moments ($\sim 10^{-8}$ emu). To obtain such high sensitivity, a SQUID is used in the magnetometer which enables very precise measurement of magnetic flux [138,139]. Here, the SQUID is made up of two parallel Josephson junctions, where two superconductors are separated by a thin insulator. Tunneling of cooper pairs from one superconductor to another through the insulating layer gives rise to the generation of supercurrents ($I_s$). Each superconductor can be expressed in terms of a single wave function, due to the phase coherence of all cooper pairs present in a superconductor. Thus, the two superconductors may be represented by two separate wave functions owing to their difference in phases. By solving the Schrödinger equation for these two superconductors one can obtain the supercurrent flowing through the junction as, $I_s = I_0 \sin(\varphi_2 - \varphi_1)$, where $I_0$ is the critical current and $(\varphi_2 - \varphi_1)$ is the phase difference. This also helps to quantify the phase difference between two superconductors. In addition, the phase of a quantum state also can be altered in the presence of a magnetic field, and hence, the total quantized phase shift can be written as [140],

$$\Delta\varphi(B) + 2\Delta\varphi(I) = 2\pi n \qquad (2.13)$$

As a result, the high sensitivity of SQUID originated mainly from a change in the magnetic field that is directly connected to the flux quantization. The basic operational principle of SQUID magnetometer is as follows; the sample is first placed inside a detection coil made of superconducting wires, known as second-order gradiometer coils. Both upper and lower coils are single turn and wound in a clockwise manner. Whereas the middle coil has two turns and

is wound in an anti-clockwise manner. These coils are surrounded by two superconducting

magnets to generate a uniform magnetic field in the sample space, as shown in Fig. 2.16 (a).

The detection coils are also coupled to a SQUID which is kept well below $T_c$ (using liquid

helium) and is isolated from the external magnetic fields. To measure magnetic properties, the

sample is moved up and down vertically, which generates a flux to the detection coil. The

opposite four turns of the pick-up coil cancel out the effect of the applied magnetic field and

isolate the magnetic flux that originated only from the sample movement. As a result, a

persistent current is also generated in the coils owing to the induced flux. Further, the induced

flux is transferred to the RF SQUID which can convert the magnetic flux to a voltage signal.

The voltage versus sample position curve is then fitted with a model by using a complex

algorithm to obtain the magnetic moment of the sample. The output signal versus sample

position graph is shown in Fig. 2.16 (a). In this thesis work, we have used a MPMS3-SQUID

magnetometer manufactured by Quantum Design, USA (see Fig. 2.16 (b)), which can produce
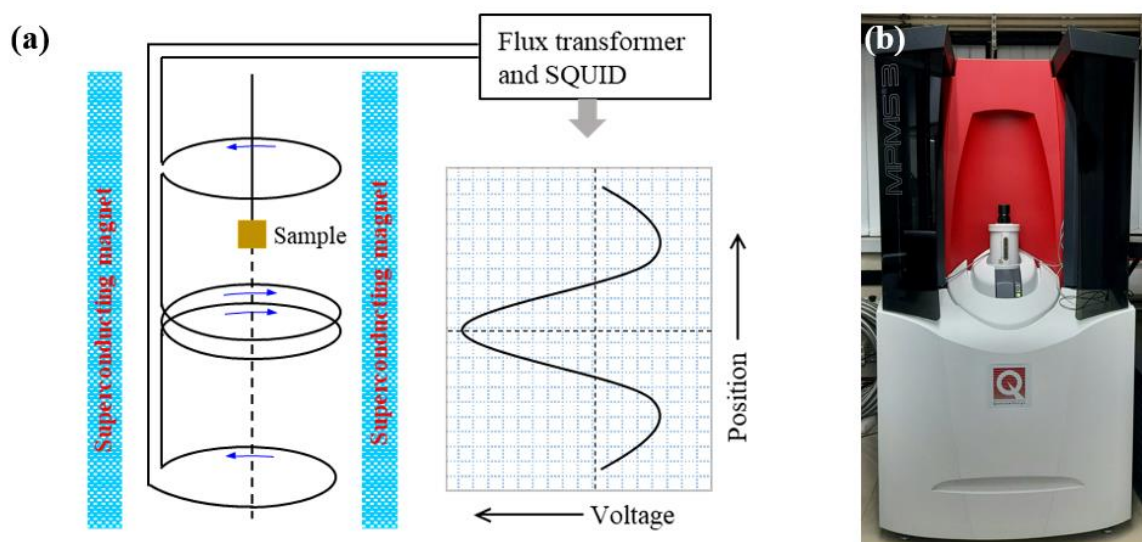


Figure 2.16 (a) A schematic of the detection coil geometry and voltage vs. sample position

plot while centering a sample in the SQUID magnetometer. (b) The MPMS3 SQUID

magnetometer facility is available in laboratory LNMM at SPS, NISER.

±7 T magnetic field and vary the temperature over a wide range from 1.8 K to 400 K. Using the SQUID-vibrating sample magnetometer we have measured the magnetic moment, saturation field, and magnetic anisotropy of our samples at RT.

**2.3.5 X-ray magnetic circular dichroism (XMCD):** XMCD is a very powerful technique to probe electron spin polarization and provide element-specific magnetic information [141,142]. In optics, dichroism means the polarization-dependent absorption of light by a material. If the symmetry of a material is broken (either inversion or time-reversal symmetry), it may give rise to circular dichroism. Thus, the difference in absorption of the left ($\mu^-$) and right ($\mu^+$) circularly polarized X-rays by a magnetic material is called X-ray magnetic circular dichroism (XMCD) [143]. From the difference between the X-ray absorption spectra (XAS) obtained for the left and right circularly polarized X-rays, the XMCD signal can be measured. The impact is generally very strong due to the significant spin-orbit coupling of the core levels (except the *K*-edge). XMCD technique can be explained in terms of a two-step process, as schematically
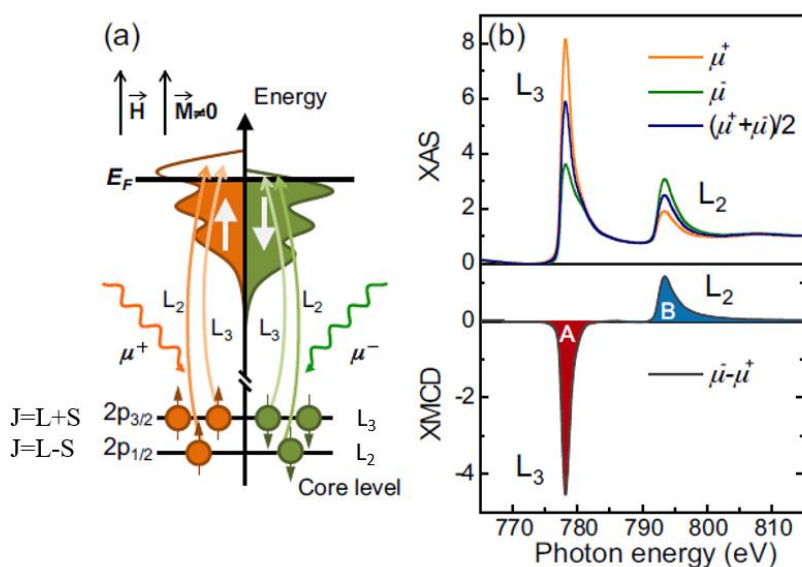


Figure 2.17 Schematic representation of (a) two-step model describing XMCD technique, (b) XAS and XMCD spectra obtained for right and left circularly polarized X-rays. The image is taken from ref. [143].

presented in Fig. 2.17 (a) [142–144]. Due to the spin-orbit coupling, the *2p* states of *3d*-transition metal are split into *j*=3/2 (*j* = *l*+*s*), and *j*=1/2 (*j* = *l*-*s*) levels. Here, the $2p_{\frac{3}{2}}$ and $2p_{\frac{1}{2}}$ states are known as $L_3$ and $L_2$ edge, respectively. In the first step, the right ($\mu^+$) and left ($\mu^-$) circularly polarized X-rays excite the spin-up and spin-down electrons from the spin-orbit split $2p_{\frac{3}{2}}$ and $2p_{\frac{1}{2}}$ states, respectively. In the second step, excited spin-polarized photoelectrons go to the unfilled *3d* bands depending upon the availability of states for the majority and minority spins. In this way, the spin-polarization of the *3d* states can be probed. If the *3d* states have a net spin-polarization, then the intensity of the XAS spectra for the left and right circularly polarized X-rays will be different for the $L_3$ and $L_2$ edges. If the spin-up electrons are less in numbers than spin-down holes in the *3d* states, then the XMCD spectra at the $L_3$ edge will be negative, and at the $L_2$ edge will be positive, as shown in Fig 2.17 (b) [143]. This technique is element-specific because by tuning the incident X-ray energy a particular edge of a specific element can be probed. Further, by using circular polarization the element-specific magnetic properties also can be studied. Element-specific hysteresis loops, orbital, spin magnetic moment and magnetic anisotropy can be determined from XMCD measurements [142,145]. The discovery of the sum rule made it possible to find out the element-specific orbital and spin moment by using integrated XMCD spectra. The orbital and spin magnetic moment can be deduced by using the following equations [146,147];

$$m_{orb} = -\frac{4 \int_{L_3+L_2} (\mu_- - \mu_+) \, dE}{3 \int_{L_3+L_2} (\mu_- + \mu_+) \, dE} (10 - n_{3d}) \tag{2.14}$$

$$m_{spin} = -\frac{6 \int_{L_3} (\mu_- - \mu_+) \, dE - 4 \int_{L_3+L_2} (\mu_- - \mu_+) \, dE}{\int_{L_3+L_2} (\mu_- + \mu_+) \, dE} (10 - n_{3d}) \tag{2.15}$$

where, $m_{orb}$ and $m_{spin}$ are the orbital and spin magnetic moments (in the unit of $\mu_B$/atom), $n_{3d}$ is the $3d$ electron occupation number. Further, the ratio of orbital and spin magnetic moments can be calculated using the following equation [146,147],

$$\frac{m_{orb}}{m_{spin}} = \frac{2 \int_{L_3+L_2} (\mu_- - \mu_+) \, dE}{9 \int_{L_3} (\mu_- - \mu_+) \, dE - 6 \int_{L_3+L_2} (\mu_- - \mu_+) \, dE} \tag{2.16}$$

For our thesis work, we measured the strain-dependent orbital and spin magnetic moment at the BACH beamline of the Elettra synchrotron facility, in Italy [148]. The synchrotron radiation source consists of the following parts, (i) an electron gun and linear accelerator (LINAC), (ii) a booster ring, (iii) a storage ring, and (iv) beamlines. Electrons are generated from an electron gun and get accelerated by the LINAC. These electrons then enter into a booster ring where they travel in a high vacuum tube under an intense electromagnetic field to attain an acceleration ~ 2.5 GeV. Then, they are transferred to a storage ring, where they travel at the speed of light for ~ 24 hours. The storage ring is made up of straight and curved sections, where at each curved section a powerful magnet forces the e-beam to deviate from its path. When such high-energy e-beams deviate, they lose some energy in the form of an extremely bright light, known as synchrotron radiation (which covers from IR to X-ray). At each curved section, the emitted beam of the light tangent to the storage ring is called a beamline. Elettra synchrotron facility has 23 beamlines where each beamline uses a specific wavelength of light depending on their requirement. In our case, for the XMCD measurement we have used the BACH (**b**eamline for **a**dvanced di**ch**roism) beamline, as it works in the soft X-ray photon energy range (35-1650 eV) with different light polarization e.g., linear horizontal and vertical, circular, and elliptical (by using two APPLE-II undulators). It also has a very high energy resolution (resolving power > 10000), high intensity, brilliance, and time resolution. The XMCD measurement takes place in UHV condition. The spot size of light on the sample was $250 \times 20$ $\mu m^2$. A layout of the BACH beamline is presented schematically in Fig. 2.18 (a) [149]. It can
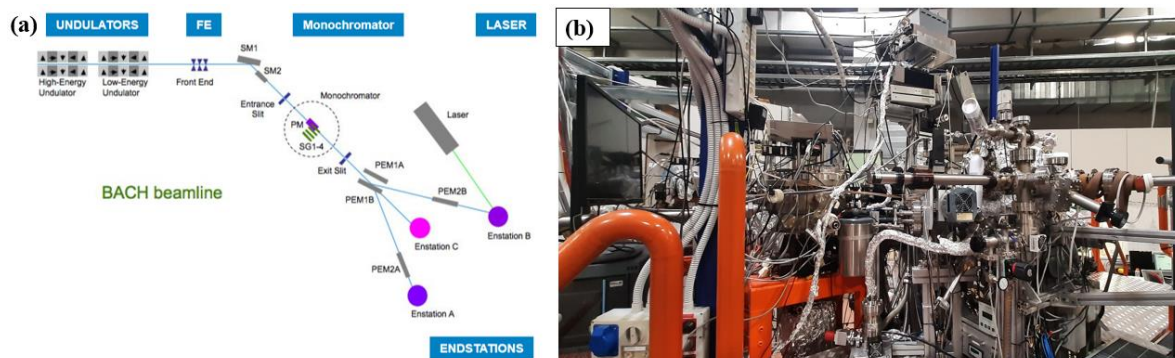
Figure. 2.18 (a) A general layout of the BACH beamline is presented where the image is taken from ref. [150], (b) XAS and XMCD measurements performed at the end station of BACH beamline, Elettra synchrotron facility, in Italy.

be divided into four sections: (i) prefocusing section, (ii) monochromator, (iii) refocusing section, and (iv) experimental chambers. For the thesis work, we have performed XMCD experiments at room temperature.

**2.4 Four-point-probe measurement:** Four-point-probe (4pp) measurement is the widely used, simplest, and non-destructive technique to find out the sheet resistance ($R_S$) of a thin film [151]. In our case, a home-made four-probe setup is used for measuring the room temperature resistance. On a wooden base, four gold-coated pins are fixed together with copper wires to measure the resistance. All four pins are equally spaced and arranged linearly. The sample is placed underneath the four probes by adjusting their height. Current is applied to the two outer probes whereas the voltage is measured via the two inner probes, as shown in the schematic of Fig. 2.19 (a). Here, to apply the current and measure the output voltage, a source meter, and a nanovoltmeter are used, respectively. The use of a nanovoltmeter helps to measure even a very small output voltage with better accuracy. The sheet resistance is calculated using the equation written below [152],

$$R_S = \frac{\pi}{\ln 2} \frac{\Delta V}{\Delta I} = 4.53 \frac{\Delta V}{\Delta I} \tag{2.17}$$
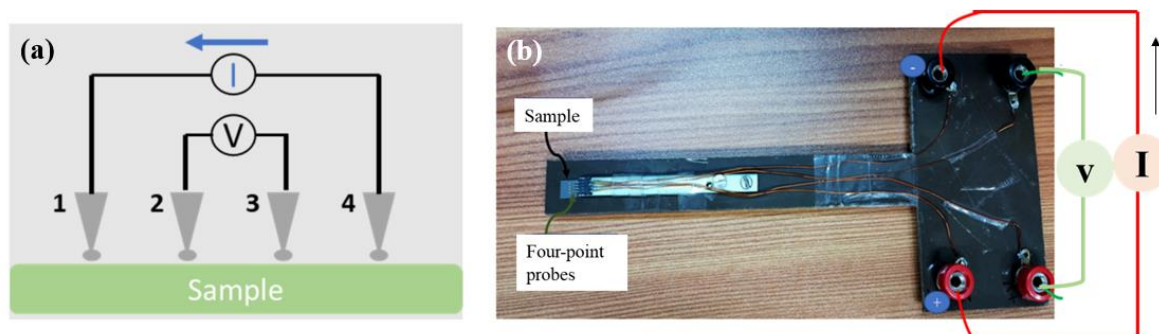
Figure 2.19. Schematic of four-probe measurement geometry, the image is taken from ref. [152], (b) a home-made four-point-probe set-up used for measuring the sheet resistance of thin films.

where, $\Delta V$ and $\Delta I$ are the output voltage and the applied current to the sample, respectively. By knowing the sheet resistance, the resistivity of the sample also can be calculated. In our thesis work, we have measured the sheet resistance for the samples at the unstrained and strained states. As the resistance of a material also depends on its dimension, the impact of a large strain should be reflected in the measured resistance. A strain-gauge also works on this principle.

## Chapter 3: Strain-engineered magnetic properties of Pt/Co/Pt thin film

The research on magnetic thin films having perpendicular magnetic anisotropy (PMA) attracts significant attention due to their superior application in various fields. They are essential in the field of magnetic data storage technology, such as hard disk drives (HDDs) and magnetic random-access memory (MRAM) [18,19]. Their high PMA enables improved areal density, and better thermal stability compared to the in-plane magnetic anisotropic (IMA) thin films. Thus, they are also suitable for various industrial, automotive, and sensor applications (e.g., magnetoresistive sensors, magnetic field sensors, biosensors, etc.) [20,21]. Notably, the PMA thin films comprised of heavy metal (HM)/ferromagnet (FM) systems have the potential to originate chiral domain walls and skyrmions, due to the presence of significant Dzyaloshinskii-Moriya interaction (DMI) at the HM/FM interface. Therefore, it is essential to fabricate a flexible counterpart of such PMA-based thin films, for flexible spintronic device applications. However, the research on flexible PMA thin films is still in its infancy. A few reports only exist on flexible Co/Pt and Co/Pd thin films [10,30,32–34]. In the case of Co/Pt flexible films, modulation of magnetic anisotropy and DMI strength is reported in the strained state [10,30,32]. Nevertheless, the impact of various modes of flexibility (e.g., bending, stretching, peeling, etc.) on the structural and magnetic properties of flexible PMA film is still lacking. In this context, we have prepared a Pt/Co/Pt thin film upon a flexible PI substrate (~25 μm thick) and studied the impact of bending-induced strain in detail.

**3.1 Method of strain generation:** In the realm of flexible spintronics, the most prevalent strain-tailored pattern is uniaxial stress ($\sigma$), which can be generated by bending and stretching mode. In this thesis work, we have studied the impact of bending-induced strain on the flexible thin film. The samples are bent using both convex and concave-shaped aluminium molds, which in turn generate a tensile and compressive strain in the sample plane, respectively, as shown in Fig. 3.1 (a-b). Flexible samples are fixed on the molds using adhesive Kapton tapes

at both ends. When a sample is bent to a convex shape tensile strain gets generated on the deposited film, as shown schematically in Fig. 3.1 (c). Similarly, when the film is mounted on a concave mold, it experiences a compressive strain, as shown schematically in Fig. 3.1 (d). From a simple deformation geometrical model, the bending-induced strain ($\varepsilon$) can be written as [153,154],

$$\varepsilon = \frac{t_{sub} + t_{film}}{2r} \tag{3.1}$$

Where, $t_{sub}$ and $t_{film}$ are the thicknesses of the flexible substrate and the deposited film, respectively. Here, $r$ is the radius of the mold used to generate the stress on the sample. The magnitude of applied strain can be varied by varying the radius of the mold. By taking into account the elastic moduli and thickness of both the substrate and the film, the corrected strain equation can be written as [155],

$$\varepsilon = \left(\frac{t}{2r}\right)\left(1 + \frac{(1-\chi)\eta}{(1+\eta)(1+\chi\eta)}\right) \tag{3.2}$$

where, $t$ is the total thickness of the film and substrate, $\eta$ ($= \frac{t_{film}}{t_{sub}}$), and $\chi$ ($= \frac{E_{film}}{E_{sub}}$) represent the thickness ratio and the elastic moduli ratio of the film and the substrate, respectively. In the limit of $\eta \rightarrow 0$, equation 3.2 takes the form of equation 3.1. As the flexible substrate has a thickness in the μm range, whereas the film has a thickness in the nm range, equation 3.1 represents the most general and suitable strain formula. When a tensile strain is applied along a longitudinal direction, it in turn induces a compressive strain in the transverse directions and vice versa, owing to the Poisson effect. The Poisson ratio is defined by the formula, $\nu = \frac{\text{transverse strain}}{\text{longitudinal strain}} = -\frac{\varepsilon_{trans}}{\varepsilon_{long}}$. Thus, the stress ($\sigma$) corresponds to applied strain ($\varepsilon$) can be evaluated using the following equation,

$$\sigma = \frac{\varepsilon E}{(1-\nu^2)} \tag{3.3}$$
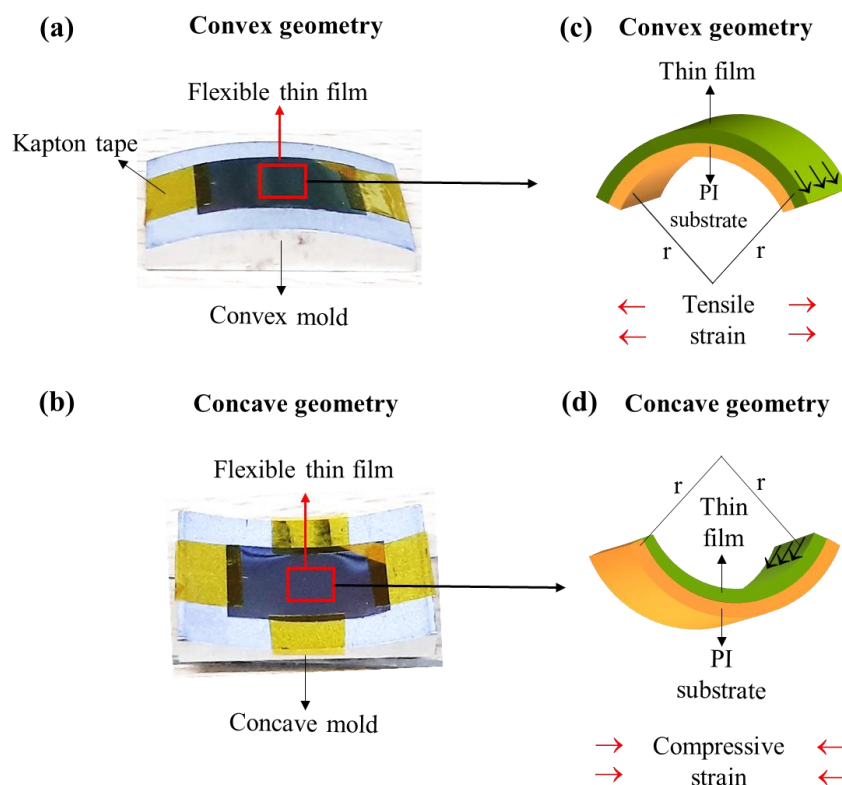
Figure 3.1 Experimental strain generation method using (a) convex and (b) concave molds. The sample is fixed on the mold using Kapton tapes. (c-d) Schematic of the tensile and compressive strain generation in the sample at convex and concave geometries, respectively.

where, $E$ is the elastic modulus and $v$ is the Poisson ratio. In our work, we have used molds of various radii starting from 40 mm to 2 mm. Depending upon the substrate thickness it can generate a strain ranging from $\sim$ 0.05% to $\sim$ 1.00%, in the plane of the sample.

**3.2 Sample details:** Prior to sample preparation, the PI substrate is cleaned ultrasonically. The sample structure is, PI/Ta(7.0nm)/Pt(10.0nm)/Co(0.70 nm)/Pt(3.0 nm), as shown schematically in Fig. 3.2 (a). All the layers are deposited using the DC magnetron sputtering technique at a base pressure lower than $1 \times 10^{-7}$ mbar. A 7 nm thick Ta layer is deposited to reduce the roughness of the PI film, improve the adhesion, and promote a (111) orientation growth of the layers. Further, a 10 nm Pt layer is deposited to enhance the strength of PMA in the sample.

The Co thickness is kept very thin (~ 0.70 nm) to obtain strong PMA in the sample, as here the interface anisotropy is expected to dominate over the volume anisotropy. Further, a 3 nm thick Pt layer is deposited as a capping layer to prevent the sample from oxidation. The rates of deposition for the Co, Pt, and Ta layers are kept at ~ 0.10, 0.15, and 0.13 Å/s, respectively. During deposition, the thickness of each layer is monitored by a quartz crystal microbalance (QCM) mounted close to the substrate holder. To achieve homogeneity in the layers, the substrate is rotated at a speed of 10 rotations per minute (rpm) during sample fabrication. A picture of the experimental flexible sample in the bent state is shown in Fig. 3.2 (b).
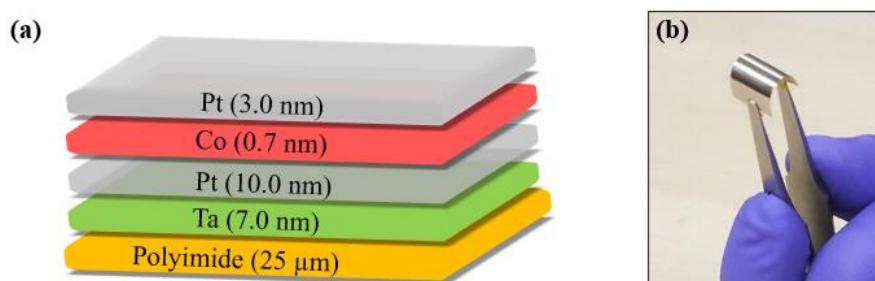


Figure 3.2 Schematic of (a) the Pt/Co/Pt sample deposited on the PI substrate [31], (b) a picture of the flexible Co/Pt film at the bent state.

**3.3 Structural Characterization:** A flexible magnetic film subjected to a large tensile and/or compressive strain may undergo two common failure modes, (i) cracking and (ii) buckling. Such failure mechanisms are shown schematically in Fig. 3.3. Crack formation occurs when a thin film undergoes a large tensile strain. The large elastic mismatch between the deposited inorganic film and the organic (polymer) substrate plays a crucial role here. Here, the Dundurs parameter ($\alpha_D$) defines the contrast between the elastic moduli of the film and substrate. Thus,

$\alpha_D = \frac{\bar{E}_f - \bar{E}_s}{\bar{E}_f + \bar{E}_s}$, where, $\bar{E}_f$ and $\bar{E}_s$ are the plane strain modulus (PSM) of the film and the substrate respectively [156]. The PSM can be calculated using the formula, $E_{PSM} = \frac{E}{1-\gamma^2}$, where $E$ is

the elastic modulus and $\gamma$ is the Poisson ratio. For a stiff substrate, $\alpha_D$ takes the value $\sim$ -1, whereas for a compliant substrate, $\alpha_D$ takes the value $\sim$ +1. In the case of a stiff substrate, the process of channel cracking releases a lower stress energy, whereas for the compliant substrate it releases a higher stress energy. At lower applied strains, the magnetoelastic effects are usually reversible in nature, however, beyond the elastic strain limit cracking and buckling of a film also may occur. Thin film buckles under compressive strain in two different modes; (i) wrinkling, and (ii) buckling. If an elastic film is bonded to an elastic substrate ($\alpha_D \sim 0$), then under compressive strain both the film and substrate deform together, known as wrinkling, as shown in Fig. 3.3 (b). The critical stress required for such wrinkle formation is [157,158]:

$$\sigma_W = \frac{\bar{E}_f}{4}\left(\frac{3\bar{E}_s}{\bar{E}_f}\right)^{\frac{2}{3}}. \tag{3.4}$$

If the applied stress ($\sigma$) is higher than $\sigma_w$, then the wrinkle pattern of specific wavelength and amplitude will occur to minimize the stress energy. However, for a stiff substrate, wrinkle formation is not preferred, and thus, under large compressive strain, the attached film gets delaminated from the substrate to release the stress energy. Buckle delamination of a deposited film depends on the adhesion between the film and the substrate and the presence of defects.



|  Cracking  |  Wrinkling  |  Buckling  |
|:----------:|:-----------:|:----------:|
|   **(a)**  |   **(b)**   |   **(c)**  |
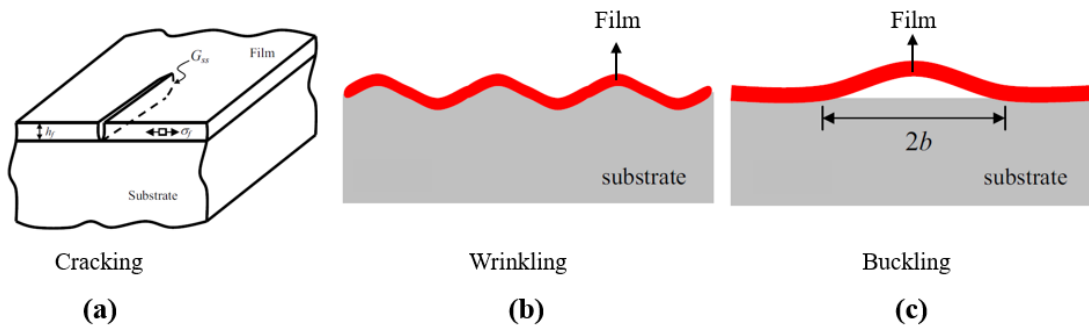
Figure 3.3 Schematic demonstration of common failure modes that occur in thin film, (a) channel cracking (under tensile strain), (b) wrinkling, and (c) buckling (under compressive strain). The image is taken from ref. [159].

The interfacial defects act as a source to originate such delamination of film as the adhesion is low there. Buckling and delamination together give rise to different blister patterns, e.g., telephone cord blister. Such blister patterns are quite localized in nature as they are sensitive to localized defects. The critical stress required for buckle formation can be calculated using the following equation [157–159],

$$\sigma_b = \frac{\pi^2}{12} \left(\frac{h}{b}\right)^2 \bar{E}_f \tag{3.5}$$

where, $h$ is the film thickness, and $b$ is the half-width of buckling, as shown in Fig. 3.3 (c). Thus, the value of $\sigma_b$ for a buckled film can be calculated using the experimentally obtained value of $b$. In our case, the inorganic thin films (Co/Pt) are deposited on the organic polymer substrates (PI), and hence, structural damage may occur at larger values of applied strains. In this context, the PSM for the film and the substrate is calculated as, $\bar{E}_s = 4.5$ GPa and $\bar{E}_f = 205$ GPa (considering Ta/Pt/Co layer). This gives the value of Dundurs parameter $(\alpha_D) \sim 0.95$. As per a few previous reports, for a flexible thin film, the crack formation initiates when the applied strain becomes higher than 1.5% [160,156]. As the applied tensile strain is below 0.50% in our case, it should not initiate any crack formation in the sample. Further, we also calculate the critical stress required for wrinkle formation using the values of $\bar{E}_f$ and $\bar{E}_s$, and it yields, $\sigma_w \approx 8$ GPa. However, in our case, the maximum applied compressive strain is, $\varepsilon_{max} = 0.42\%$, and the corresponding applied stress is, $\sigma \approx 0.8$ GPa, which is far away from the critical stress needed for wrinkle formation. Thus, within the limit of applied strain, the classical magnetoelastic effects should be observed. To confirm that no structural damage occurs upon application of strain, the sample surface is scanned at both the unstrained and strained states of the sample using a scanning electron microscope (SEM). Three pieces of the same flexible sample are used for imaging purpose, where one piece is mounted on the flat state and the other two is mounted on convex and concave-shaped molds of 3 mm radius. Fig. 3.4 shows the

surface of the sample at both unstrained and strained states. Here, no sign of damage is observed at ~ 0.42% strain applied in the sample plane, as also expected earlier. As per a previous report, Ta exhibits a stronger peel adhesion with PI substrate, and hence, in our case, the Ta seed layer may help to lower the possibility of thin film damage [161]. However, if the applied strain reaches ~ 1.0%, a pronounced structural deformation is quite probable. Few earlier report shows that damage to thin film induces an irreversible modulation in the electronic and magnetic properties of a sample [156,160]. However, in our case within the limit of applied strain, all the properties were reversible in nature which also supports no damage to the sample. However, in Chapter 5 we will discuss the structural damage formation observed due to a high peeling strain applied in the Co/Pt thin film.
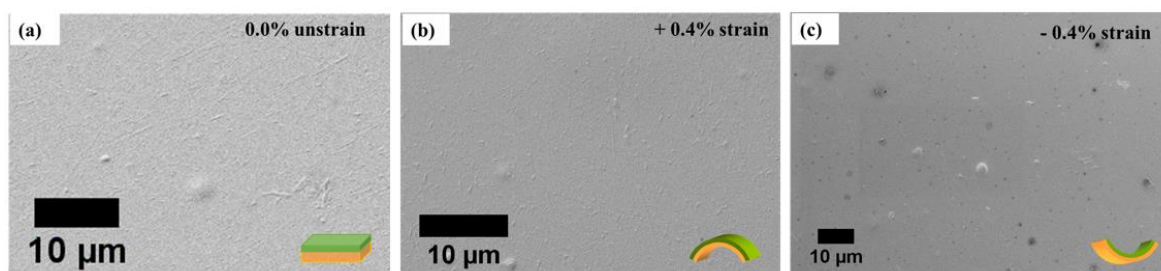


Figure 3.4 Scanning electron microscope images of the Co/Pt sample surface at (a) unstrained, (b) tensile, and (c) compressive strained states. No structural damage is found within the range of applied strain.

## 3.4 Magnetic Characterization:

**3.4.1 Magnetization reversal phenomena:** Further, to understand the impact of strain generation on the magnetic properties of the sample, we have measured the magnetization reversal and magnetic relaxation phenomena using magneto-optic Kerr effect (MOKE) based microscopy in the polar mode. Magnetic hysteresis loops and simultaneous domain images are recorded for varied strength of applied strain. The coercivity ($H_C$) of the sample increases from

27 (unstrained) to 36 mT (strained) under the application of ~ 0.4% tensile strain in the plane

of the sample. Whereas, under compressive strain (~ 0.4%) coercivity reduces to ~ 25 mT.

Thus, the impact of tensile and compressive strain is found to be opposite and asymmetric on

the coercivity, as also depicted in Fig. 3.5 (a). The opposite behaviour is due to the opposite

sign of the tensile and compressive strain, which oppositely modulates the magnetic anisotropy.

The magnetoelastic anisotropy of a thin film can be written as, $K_{MEA} = \frac{3}{2}\lambda\sigma$, where, $\lambda$ is the

magnetostriction coefficient of the Co/Pt system and $\sigma$ is the applied stress. As per a few earlier

reports, for a Co/Pt system $\lambda$ is usually negative ($\lambda \sim - 3.5\times10^{-5}$) along (111) direction [162],

whereas the sign of $\sigma$ (related to applied strain) can be either positive (for tensile strain) or

negative (for compressive strain). Thus, the product of $\lambda\sigma$ also can be positive or negative.

Here, the application of tensile strain (in the sample plane) helps to enhance the effective

magnetic anisotropy, which in turn enhances the magnetic field required for magnetization

reversal and hence, the coercivity of the sample. In contrast to this, compressive strain reduces

the total anisotropy and hence, the coercivity of the sample. Such opposite impact of tensile

and compressive strains is also reported earlier for flexible thin films [10,16,162]. In our case,

the modifications under tensile strain are higher than the compressive strain, possibly due to

the strong intrinsic PMA of the Co/Pt sample. As the thickness of Co ($t_{Co}$) is ~ 0.70 nm, it is

far away from the thickness ($t_{Co} \sim 1.60$ nm) that induces a SRT (i.e., it changes magnetic easy

axis from OP to IP) in our Co/Pt system. At SRT anisotropy goes to zero, whereas far from SRT

the strength of anisotropy increases. Thus, it could be challenging for a compressive strain to

weaken the anisotropy strength since the sample has a strong PMA. In an earlier report by

Shepley et al., authors prepared Co/Pt samples upon a glass substrate and generated strain by

using a piezoelectric transducer (where the application of voltage generates strain in the

sample). Here, the variation in magnetic anisotropy is found to be quite symmetric under both

types of strain, as the sample thickness is taken closer to the SRT region [162]. Fig. 3.5 (a)

shows the modification in coercivity under varied strengths of tensile and compressive strains. In the 1st cycle, the sample is bent for the first time at different radii and the values of coercivity are plotted. Further, the sample is kept under 0.42% tensile strain for 15 days and re-measured the coercivity values again at different strained state. This is plotted as 2nd cycle in Fig. 3.5 (a). The nature of the two graph indicates that the film has good durability even when subjected to a prolonged stress state, which is very promising for flexible spintronic device application. Moreover, it also shows that the changes under such elastic strain are reversible in nature. Bubble domains are observed at the initial flat state of the sample, as the anisotropy ratio $Q = \frac{K_u}{K_d} \gg 1$, where $K_u$ is the uniaxial anisotropy constant and $K_d$ is the stray field energy constant [163]. The domain images are recorded at saturation, near nucleation, and sub-coercive field values of each hysteresis loop as shown in Fig. 3.5 (b). All the domain images
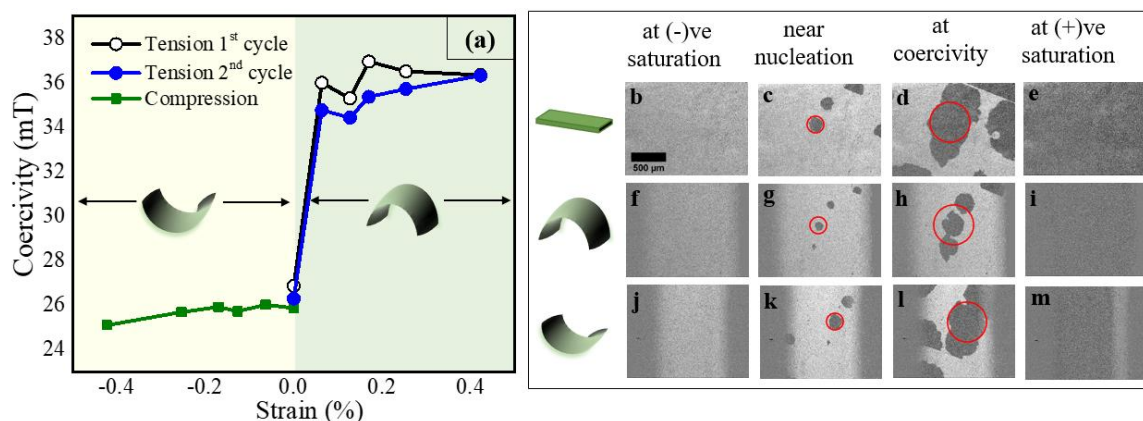


Figure 3.5 (a) Strain vs. coercivity plot for Co/Pt sample (obtained from hysteresis loops), where black open and blue filled circles represent the 1st and 2nd bending cycles under tensile strain, respectively. The square symbols represent the change in coercivity under compressive strain. Domain images recorded at saturation, nucleation, and coercive field points of the hysteresis loops measured in the unstrained (b-e), +0.13% tensile strained (f-i), and -0.13% compressive strained (j-m) states of the sample. The scale bar shown in image b is 500 µm in length and is valid for all the other domain images [31].

are captured at the same place of the sample to compare the effect of strained conditions on the domain state. A red-marked circle is used to compare the propagation of a specific domain in the strained and unstrained state. Images shown in Fig. 3.5 (d) and (h) indicate that the bubble domain moves slowly under tensile strain in comparison to the unstrained state of the sample. Whereas under the compressive strain, the domain expansion looks quite similar to the flat state. Such modification in domain propagation may be related to the induced magnetoelastic anisotropy in the sample. As the application of tensile strain helps in strengthening the PMA, it might enhance the domain wall (DW) formation energy ($\sigma_{DW} = 2\pi\sqrt{AK}$, where $A$ is the exchange stiffness constant and $K$ is the effective anisotropy) in comparison to the flat state. Whereas application of compressive strain may reduce the DW formation energy, and modify the domain propagation under strain. Similarly, strain-induced domain nucleation and DW motion is observed experimentally for PMA Co/Pt and Co/Ni systems, deposited on piezoelectric substrates [162,164]. In addition, strain-assisted domain rotation and DW motion are also observed for IMA FeGa films [165]. Theoretically, a high DW velocity is also predicted for systems at specific curved states [166]. Thus, strain engineering seems to be a promising tool to control both the static and dynamics of DW motion.

**3.4.2 Magnetic relaxation phenomena:** To better understand the reversal phenomena, we have further studied the magnetization relaxation mechanism of the Co/Pt sample under strain. The measurement reveals the efficiency of thermal activation energy to complete the magnetization reversal process. In addition, it gives more insight into whether the reversal process is dominated by domain nucleation or DW motion. Previously such magnetization relaxation has been studied for nanoparticles, magnetic antidots, and continuous thin films [167–169]. Among several models developed to explain magnetization relaxation phenomena, the Fatuzzo-Labrune model is extensively used for FM thin films [170,171]. However, the approximation of a single energy barrier considered in this model does not hold

for real thin films. An experimental sample consists of a distribution of energy barriers with defects and inhomogeneities throughout the sample surface. In this context, the Kolmogorov-Avrami model takes care of such inhomogeneities, where the relaxation is explained by a compressed or stretched exponential function [172]. Thus, the relaxation process of flexible Co/Pt thin film is also explained using the compressed exponential function. The relaxation measurement is performed using MOKE-based microscopy in the polar mode. The measurement protocol is as follows, first, the sample is saturated by applying a sufficient negative magnetic field and then the field is increased manually to a positive sub-coercive field value (say $0.95H_C$). At that constant applied field (Zeeman energy), the magnetization reversal takes place with the help of the thermal energy. All the domain images are captured during the whole thermal relaxation process, where the amount of dark grey contrast represents a measure of the magnetization in the sample. The intensity of each image is extracted by using ImageJ software and the average intensity for the domain images captured within one second is calculated. The normalized intensity is then plotted with the time taken to complete the reversal, as shown in Fig. 3.6 (a). The domain images captured during the thermal relaxation process (at $0.95H_C$ field) is shown in Fig. 3.6 (b) for all the states of the sample. The experimental data of Fig. 3.6 (a) is fitted using the compressed exponential function written as [172]:

$$I(t) = I_1 + I_2 \left( 1 - \exp\left( -\left(\frac{t}{\tau}\right)^{\beta} \right) \right) \tag{3.6}$$

where, $I(t)$ is the Kerr intensity measured at time $t$, $(I_1 + I_2)$ is the normalized Kerr intensity, $\beta$ is an exponent that may obtain values between 1 (nucleation-dominated relaxation) to 3 (DW motion-dominated relaxation), and $\tau$ is the relaxation time constant. We have extracted the values of $\tau$ and $\beta$ for the three different states of the sample. The $\beta$ value lies within 1 to 3 for
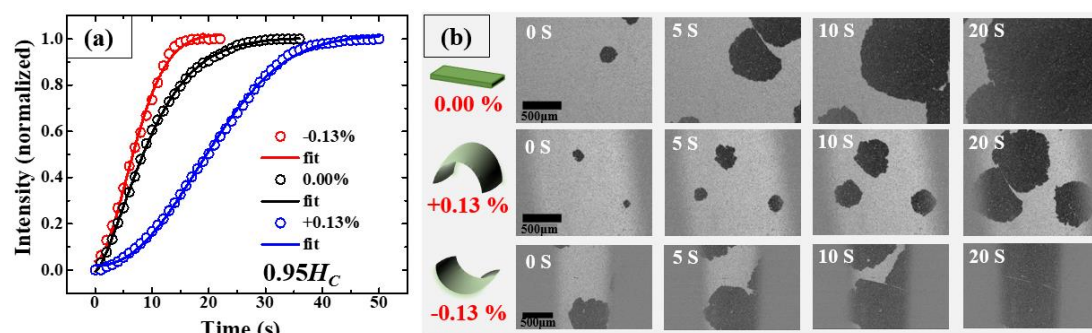
Figure 3.6 Results of the relaxation measurement performed at $0.95H_C$ field value, (a) the normalized intensity vs. time plot for the unstrained and $\pm0.13\%$ strained state of the sample. Open circles are the experimental data and the solid lines represent the fitting of the data by a compressed exponential function, and (b) domain expansion during the relaxation process at the unstrained (top panel), tensile strained (middle panel), and compressive strained (lower panel) state of the sample. Here, 0 s represents the time when the first domain image is captured after fixing the Zeeman energy. The domain images captured at different time intervals (0s, 5s, 10s, and 20s) are shown for all the states of the sample. The scale bar is 500 µm in length and valid for all the domain images [31].

all the states of the sample, which indicates that the magnetization reversal is governed by both the domain nucleation and the DW motion events. Notably, the value of $\tau$ increases ($\tau = 23.63 \pm 0.14$ s) under tensile strain and decreases ($\tau = 8.52 \pm 0.16$ s) under compressive strain in comparison to the unstrained state ($\tau = 11.00 \pm 0.04$) of the sample. It indicates that the reversal process became slower under tensile strain and faster under compressive strain, in comparison to the unstrained state. This also can be interpreted as the domain propagation becoming slower under tensile strain and faster under compressive strain, owing to the induction of magnetoelastic anisotropy in the sample. Fig. 3.6 (b) shows that in about 20 s of the relaxation process, the flat sample reaches closer to the saturation, whereas the tensile strained sample is still far away from reaching the saturation. In contrast, the compressive strained sample has
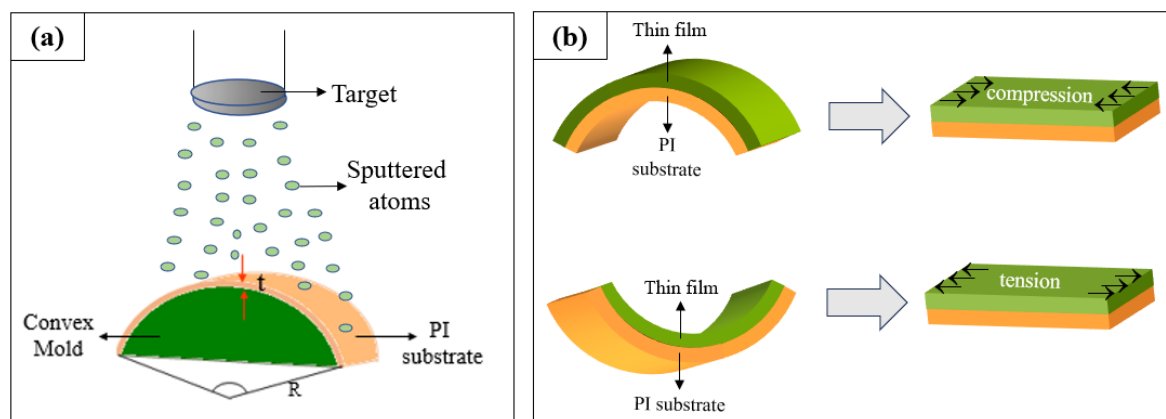
Figure 3.7 Schematic of (a) the sample deposition geometry when a PI substrate is mounted on a convex mold, (b) compressive and tensile strain generation by making the as-deposited bent sample flat.

completed the reversal process within 20 s time. Thus, the domain images also reflect a slower relaxation process under tensile strain whereas a faster one under compressive strain, as observed earlier in the magnetization reversal process [31]. Thus, the induced ME anisotropy is found to have a strong impact on both the magnetization reversal and relaxation process of the flexible Co/Pt film.

**3.5 Co/Pt sample prepared on bent PI substrates:** In order to confirm that the impact of tensile and compressive strain is opposite on the magnetic properties, we have used another method to generate strain on the sample. Here, we have prepared the same Co/Pt sample (as mentioned earlier) on the bend PI substrates. Before sample fabrication two PI substrates are fixed on convex and concave shape molds, as shown schematically in Fig. 3.7 (a). The radii of the two molds were different because of the substrate holder geometry. Here, two Co/Pt samples are deposited at the same time, where one is on convex and another is on concave-shaped bent PI substrates. Here, the as-deposited state of the Co/Pt film is considered as unstrained state. When the samples were taken out from the mold and flattened, it introduced
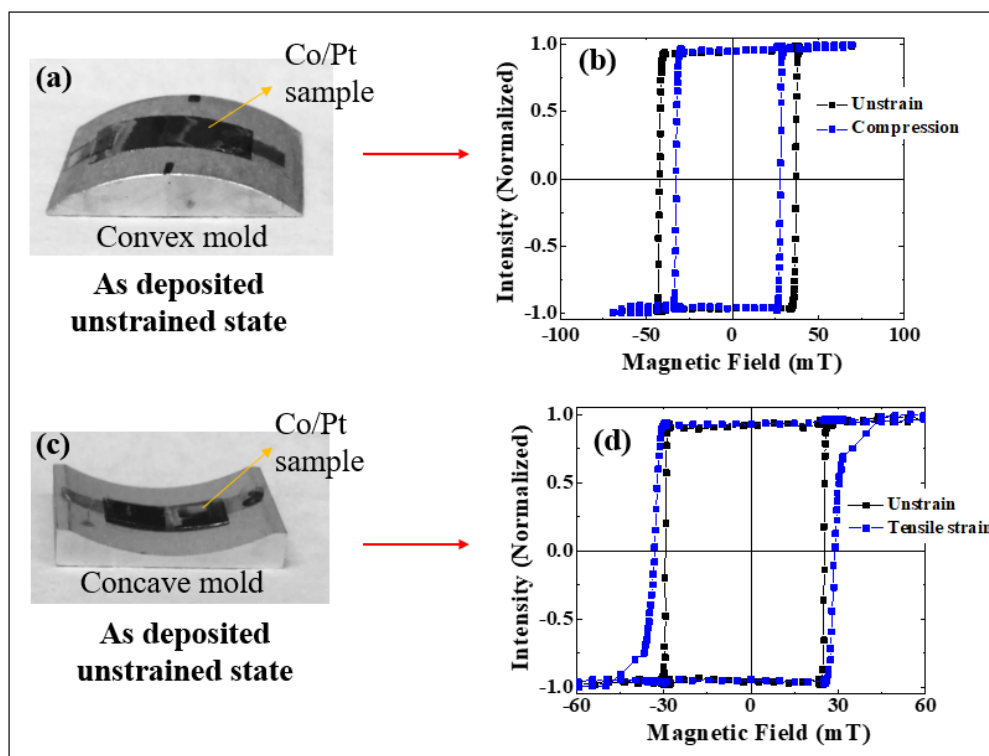
Figure. 3.8 Sample deposited on bent PI substrates, using (a) convex and (c) concave molds, (b) and (d) hysteresis loops measured in the as-deposited unstrained and strained states of the sample.

a strain on the sample. In this way, tensile and compressive strains are generated on the samples that are deposited on the concave and convex-shaped molds, respectively. A schematic of the sample deposition geometry and the method of strain generation is shown in Fig. 3.7. Hysteresis loops are measured in the polar MOKE geometry for both the as-deposited and flat state of the samples, as shown in Fig. 3.8. Here, the unstrained state loops for both the samples have different coercivity due to the different mounting geometries and heights of the molds used (see Fig. 3.8). When both the samples are made flat, the impacts of tensile and compressive strains are found to be opposite in nature, which is similar to our previous observation. This further confirms the opposite impact of tensile and compressive strains on the magnetic properties of the sample.

In summary, it can be concluded that the application of tensile and compressive strain helps to tune magnetic properties in an opposite manner which is indeed reversible within the elastic limit of applied strain. A detailed insight into the magnetization reversal and relaxation dynamics of flexible Co/Pt thin film is also provided. As the film has a non-zero magnetostriction co-efficient, the applied strain modifies the magnetic properties in the bend states of the sample. Thus, the desirable magnetic properties are possible to be achieved by proper tuning of applied strain. Further, density functional theory calculations may shed light on the exact impact of applied strain on the DOS of the samples. The observed endurance of the magnetic film against long-term strain application could be promising for spintronic device applications. In addition, such a system also has the potential for flexible strain sensors and healthcare monitoring applications.

**Chapter 4: Strain-driven magnetic properties of Pd/Co/Pd thin film**

Strain engineering seems to be a promising way to fabricate smaller, faster, and power-efficient future spintronic devices. The application of external strain is capable of tuning the structural, electronic, and magnetic properties of various magnetic systems [7,173,174]. In this context, piezoelectric and ferroelectric substrates have widely been used in the past to generate strain by applying a high voltage to the substrate [162,175,176]. In contrast to this, the flexible substrate provides the opportunity to generate multi-dimensional strain (via bending, stretching, wrinkling, and twisting methods) without the application of any voltage. The impact of such strain on the magnetic properties depends on the magnetostrictive coefficient ($\lambda$) of a material. As the magnetostrictive coefficient of Co/Pd is higher ($\lambda \sim 10^{-4}$) than the Co/Pt system ($\lambda \sim 10^{-5}$), it allows a better tuning of magnetic properties via strain [177,178]. Thus, a recent study on the flexible Co/Pd system shows a better response to applied strain [179]. In addition, flexible spin valves are also fabricated using perpendicular anisotropic Co/Pd film [33,34]. However, for device applications, it is crucial to comprehend the response of fundamental magnetic properties (such as magnetization reversal phenomena, DW dynamics, magnetic anisotropy, etc.) subjected to external strain. As the field is young, a thorough investigation of the effect of external strain on the flexible Co/Pd film is scarce. In this context, a series of flexible Co/Pd thin films are prepared upon both rigid Si and flexible PI substrate ($\sim 38\ \mu m$ thick) by varying the thickness of the Co ($t_{Co}$) layer from 0.50 to 1.10 nm. Structural and magnetic properties are studied under bending-induced uniaxial strain, as explained earlier in Chapter 3. Using molds of different radii (40 mm to 2 mm), the magnitude of uniaxial strain is varied within 0.05% to $\sim 1.00\%$, in the plane of the sample. Here, the magnitude of applied strain is different than Chapter 3, due to a different thickness of the PI substrate used.

**4.1 Sample details:** A series of flexible Pd/Co($t_{Co}$)/Pd samples are prepared with the structure, PI/Ta(20)/Pd(4)/Co($t_{Co}$)/Pd(2)/Ta(5), where the numbers in parentheses are the thicknesses in

nm and $t_{Co}$ = 0.50, 0.65, 0.80 (S1), 0.96, 1.10 (S2) nm. Here, the Co thickness is varied to tune the anisotropy strength of the samples and reach the SRT. For the Co/Pd series, the SRT is obtained when $t_{Co}$ ~ 1.30 nm. Thus, the sample with $t_{Co}$ = 1.10 nm is quite close to the SRT region of the Pd/Co film. Both Si and PI substrates are cleaned ultrasonically before film deposition. Samples are prepared via the DC magnetron sputtering technique in a high vacuum multi-deposition unit manufactured by Mantis Deposition Ltd. UK. Before deposition the base pressure of the chamber was ~ $5 \times 10^{-8}$ mbar. Deposition rates for Ta, Pd, and Co layers are maintained at 0.18 Å/s, 0.20 Å/s, and 0.16 Å/s, respectively. A QCM monitored the thickness of each layer during sample preparation. To achieve uniformity in the deposited layers the substrate is rotated at 10 rpm during sample fabrication.

**4.2 Structural Characterization:** The sample surface morphology is imaged using SEM at both the unstrained and strained states of the sample, to ensure no structural damage results from the applied strain. In this context, three pieces of the same flexible Co/Pd sample are used, where one is mounted in the flat state and the other two are mounted in the bend states using convex and concave-shaped molds. Application of ~ 0.40% strain (in the sample plane) does not initiate any damage to the film. However, under ~1.0% compressive strain few lines appeared on the sample surface, as shown in Fig. 4.1 (c). As the elastic mismatch between the organic substrate and the inorganic film is quite high, the application of high compressive strain may initiate buckling of the deposited film to release stress energy. Such buckled areas of the film may look like lines in the SEM images. However, the patterns are quite localized and are affected by the presence of defects in the sample. Notably, under ~1.0% tensile strain no sign of crack formation is observed. A few earlier report shows that fracture development starts when applied strain rises to more than 1.5% film [160,156]. Significant damage formation may induce irreversible changes in the electrical and magnetic characteristics of a sample. However,
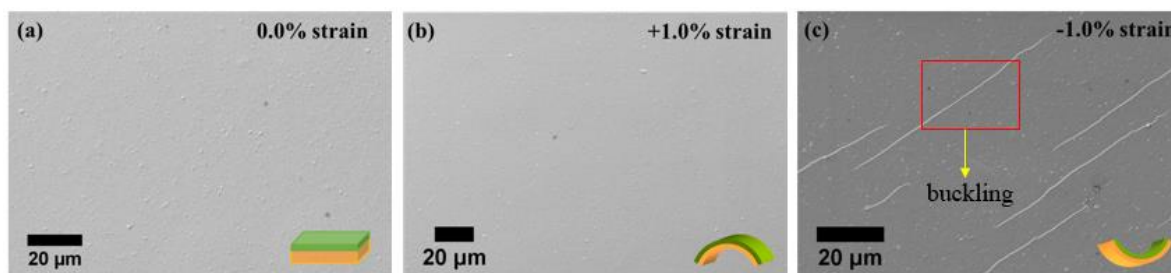
Figure 4.1 Scanning electron microscope images of the surface of Co/Pd sample (S1) at, (a) unstrained, (b) ~ 1.0% tensile, and (c) ~ 1.0% compressive strained state.

in our case, all the characteristics measured within 1.0% applied strain were reversible in nature. Thus, to observe only classical magnetoelastic effects the bending-induced strain is not exceeded more than 1.0% strain in our case.

## 4.3 Magnetic Characterization:

**4.3.1 Magnetization reversal phenomena:** Magnetization reversal is studied using magneto-optic Kerr effect (MOKE) based microscopy in the polar mode. Hysteresis loops are measured for all the samples prepared upon rigid Si and flexible PI substrates. A square-shaped hysteresis loop is found for all the samples having $t_{Co}$ between 0.50 - 0.96 nm, in their unstrained states. However, the sample with a 1.10 nm thick Co layer has a small coercivity and a tail-like feature in the loop, indicating the sample reaches closer to the SRT region of the Pd/Co system. Fig. 4.2 (a) shows the hysteresis loops measured for the Si-based samples. Here, a systematic decrease in coercivity with increasing $t_{Co}$ indicates a systematic decrease in PMA strength in the samples. Similarly, the effective magnetic anisotropy ($K_{eff}$) of the Si-based samples is measured by SQUID magnetometry, which also shows a decrement in the PMA of the samples with increasing $t_{Co}$. A more detailed discussion on the magnetic anisotropy can be found in section 4.3.4. Further, the coercivity for both the Si and PI-based samples are plotted in Fig. 4.2 (b). The coercivity of the PI-based samples is higher than the Si one possibly due to the higher roughness of PI in comparison to Si. The surface roughness of the Ta (20nm) seed layer

on both Si and PI substrate are measured using atomic force microscopy. The RMS roughness

was ~0.7 nm and 3nm on the Si and PI substrate, respectively. Therefore, the higher roughness

of the PI substrate may give rise to a higher coercivity in the flexible samples. As the Co/Pd

system has a high $\lambda$, a better strain sensitivity is expected for these flexible samples. In this

context, to study the effect of external strain on the basic magnetic properties, we have

considered two PI-based samples, one from a moderate PMA region (with $t_{Co} = 0.80$ nm), and

the other one from a lower PMA region (with $t_{Co} = 1.10$ nm) i.e., closer to SRT. For simplicity,

these two PI-based samples are called as S1 ($t_{Co} = 0.80$ nm) and S2 ($t_{Co} = 1.10$ nm) in the

further discussion of
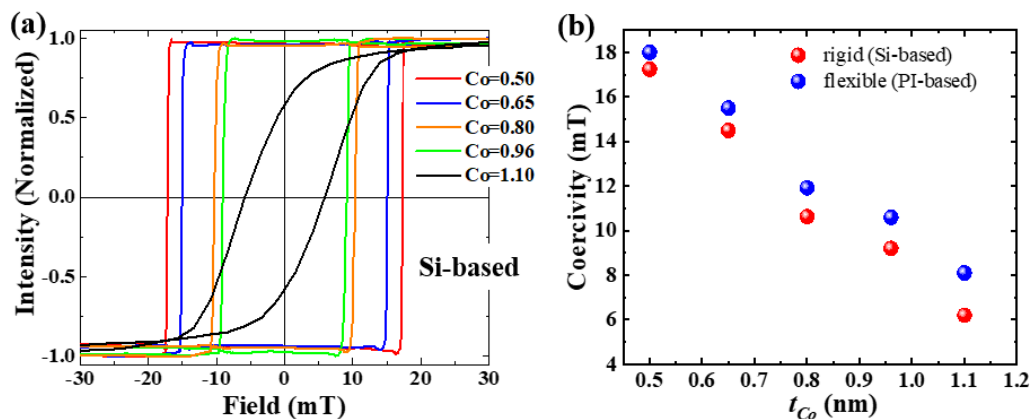


Figure 4.2 (a) Hysteresis loops of Si-based Pd/Co($t_{Co}$)/Pd samples measured by polar-MOKE microscopy, (b) coercivity vs. $t_{Co}$ plot for both rigid Si and flexible PI-based samples.

this chapter. The magnetization reversal phenomena are studied at both the flat (unstrain) and

bend (strain) states of the samples using MOKE microscopy. Figure 4.3 (a) shows the variation

of coercivity with strain for sample S1. The sample in its flat state has ~12 mT coercive field.

The impact of ~ ±0.05% strain is found to be negligible in modulating the coercivity, which

led to the plateau region of the graph. However, from ~ 0.10% strain, a finite change in the

coercivity is observed. The application of tensile (or compressive) strain in the plane of the

sample increases (or decreases) the coercivity of the film. The changes are found to be quite linear with increasing the magnitude of strain, as depicted in Fig. 4.3 (a). This can be explained in terms of the induced MEA in the system, owing to the applied strain. The MEA coefficient can be written as, $K_{MEA} = \frac{3}{2}\lambda\sigma$, where $\lambda$ is the magnetostrictive co-efficient, and $\sigma$ is the applied stress. Here, an interplay between the MEA and PMA strength decides the overall anisotropy direction. Due to the negative magnetostriction coefficient ($\lambda$) of Co/Pd, the application of tensile strain (in the sample plane) enhances the strength of effective PMA, whereas compressive strain reduces it [177,178]. Similar phenomena were also observed for Co/Pt film under strained states [10,30,162]. It is important to note that the application of a high strain (~ 1.0%) modifies the coercivity of the film by ~ 45% of its unstrained value, owing to the expected higher $\lambda$ of the Co/Pd system. Under ~ 1.0% compressive strain, the loop shape also became quite slanted indicating a significant reduction in PMA strength. Further, the domain images captured at saturation, nucleation, and sub-coercive field values of hysteresis loops are shown in Fig. 4.3 (b). Bubble domains are found in the initial flat condition of sample S1. To investigate the influence of stressed conditions, domain images are acquired at the same location of the sample. A red-marked circle highlights the changes due to applied strain. Compressive strain changes the domain shape from circular to prolate, whereas tensile strain changes it to an oblate shape, as shown in Fig. 4.3 (b). The applied strain ($\varepsilon$) acts along the *x*-axis as shown in the domain images. However, in the transverse axis (*y*) an additional strain gets generated due to the Poisson effect. It is important to note that the domain shape gets elongated along the direction of the elongation due to applied strain. For the compressive strain applied along the *x*-axis, an elongation occurs along the *y*-axis. Whereas for the tensile strain applied along the *x*-axis, an elongation occurs along the same axis. As the external strain may affect the grains of a sample, it in turn may change the shape of domains. In order to understand the magnetization reversal phenomena with more clarity, we further performed magnetic

relaxation measurements in the flattened (unstrained) and bent (strained) states of sample S1, as discussed in the following.
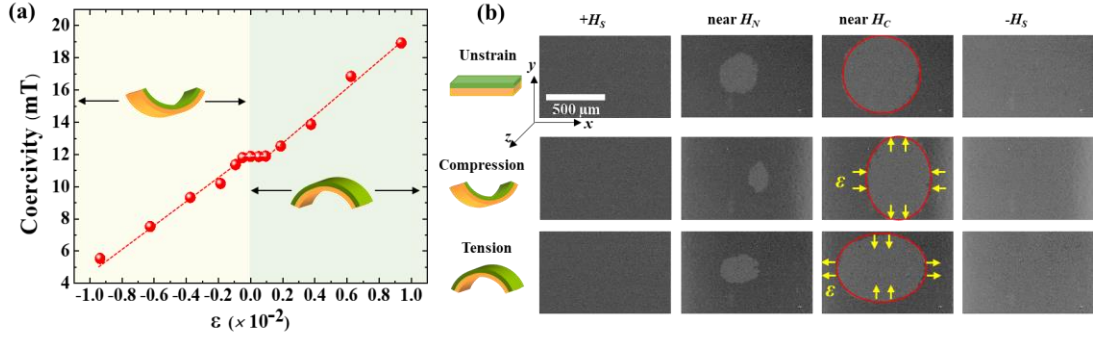


Figure 4.3 (a) Strain-driven modifications in coercivity, and (b) domain images captured at the unstrained and the strained (±0.13%) states of sample S1. The scale bar shown in the saturation image is 500 μm in length and is valid for all the other images.

**4.3.2 Relaxation dynamics:** Magnetic relaxation phenomena reveal the ability of thermal energy to complete a reversal process at a constant Zeeman energy [169,172,180]. In addition, it gives more insight into whether the reversal process is dominated by domain nucleation, DW motion events, or both. In the presence of a constant sub-coercive field value (say, $0.97H_C$), the magnetization reversal phenomena get completed with the help of thermal energy at RT. For sample S1, at $0.97H_C$ field value, the domain images are captured until the reversal process is completed. The average intensity of the domains is then plotted w.r.t the time taken to complete the reversal. Fig. 4.4 (a) represents the plot for normalized Kerr intensity vs. time, where 0s corresponds to the time when the first domain image is captured after fixing the magnetic field to $0.97H_C$. The intensity vs. time plot is then fitted by the compressed exponential function as written below [172],

$$I(t) = I_1 + I_2 \left( 1 - \exp\left( -\left(\frac{t}{\tau}\right)^{\beta} \right) \right) \qquad (4.1)$$

where, $I(t)$ is the measured Kerr intensity at time $t$, $I_1 + I_2$ is the normalized Kerr intensity, $\tau$ is the relaxation time constant, and $\beta$ is an exponent that can obtain any value between 1 to 3. We extracted the value of $\tau$ by fitting the experimental data with equation 4.1, which indeed represents the time taken to complete the reversal process. Here, the magnitude of applied strain is ~0.40% for both the strained states. For the unstrained state, $\tau \sim 7s$, which reduces ($\tau=5.6s$) under compressive strain and increases ($\tau=9.2s$) under the tensile strain. The reduction in $\tau$ indicates a faster reversal process, whereas an enhancement in $\tau$ indicates a slower reversal process under oppositely signed strain. Figure 4.4 (b) shows the domain images captured during the reversal at different intervals of time. At 5s the reversed magnetized area is larger under compressive strain in comparison to the flat and tensile strained states. At around 10 s duration,
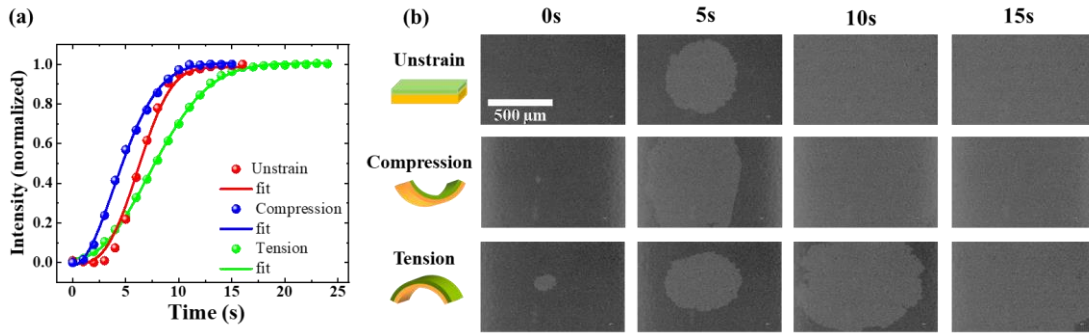


Figure 4.4 Relaxation measurement performed at $0.97H_C$ field value on sample S1, (a) intensity vs. time plot at strained (~ ±0.40%) and unstrained states, and (b) domain images captured during the reversal process at different time intervals. The scale bar shown in the domain image captured at 0s is 500 µm in length and is valid for all the other images.

the reversal is completed for the sample under both the unstrained and the compressive strained states. However, the tensile strained sample takes a longer time to complete the reversal process. As the application of strain modifies the overall anisotropy strength of the system it might change the DW dynamics w.r.t the unstrained state [181,182]. An enhanced PMA

increases the DW formation energy ($\sigma_{DW} = 2\pi\sqrt{AK}$, where $A$ is the exchange stiffness constant and $K$ is the effective anisotropy) which may reduce the DW velocity at the tensile strained state of the sample. Similarly, under compressive strain, the DW velocity might be increased, helping in accelerating the reversal process. In order to confirm the opposite impact of tensile and compressive strain on the DW dynamics of the sample, we further measured the DW velocity in the creep region under strain.

**4.3.3 Domain wall dynamics:** DW velocity is measured by the symmetric domain expansion method under OP pulsed field, using MOKE microscopy in polar mode. DW in magnetic thin film behaves as an elastic interface, moving through a 2D disordered media. The presence of impurities and disorder in real samples act as pinning sites, which hinders the smooth motion of DW. In the creep region, DW motion is mainly governed by the pinning potential and thermal energy present in the system. When $T \neq 0$, the DW follows an exponential relationship with the applied field in the creep region. In our work, we have measured pulsed magnetic field-induced DW velocity at both the unstrained and $\sim \pm 0.13\%$ strained states of sample S1. The DW velocity ($v_{DW}$) vs. field ($H_{OP}$) plot is shown in Fig. 4.5 (a), whereas the logarithm of velocity ($ln\,v_{DW}$) vs. field ($H_{OP}$) plot in Fig. 4.5 (b). The experimental data shown in Fig. 4.5 is fitted by the creep law, as written below [79,82],

$$v_{DW} = v_0\,exp\left[-\frac{U_c}{k_B T}\left(\frac{H_{OP}}{H_{dep}}\right)^{-\frac{1}{4}}\right] \qquad (4.2)$$

where, $v_0$ is the scaling parameter of velocity, $U_c = k_B T_{dep}$ is the height of pinning potential, $k_B T$ is thermal activation energy and $H_{dep}$ is the depinning threshold field. The logarithm of the above equation can be expressed as,

$$ln(v_{DW}) = ln(v_0) - \frac{T_{dep}}{T}\left(\frac{H_{OP}}{H_{dep}}\right)^{-\frac{1}{4}} \qquad (4.3)$$

The fitting of the experimental data confirms that the DW motion lies in the creep region within the range of field applied during our measurement. As depicted in Fig. 4.5 (a) at a constant applied field (~ 20 mT), the DW velocity under compressive strain is ~ 3 times higher than its unstrained state. However, under tensile strain, the velocity is reduced to a value half of its unstrained state. To well understand the origin of such behaviour, we have further extracted the values of $\frac{T_{dep}}{T}\left(H_{dep}\right)^{\frac{1}{4}}$ from the fitting of the experimental data using equations 4.2 and 4.3.

At the unstrained state, the ratio of $\frac{T_{dep}}{T}\left(H_{dep}\right)^{\frac{1}{4}}$ obtains a value of 9.51 ± 0.07, which reduces to 9.25 ± 0.06 under compressive strain and increases to 10.00 ± 0.06 under tensile strain. At a constant temperature $T$, the product of $T_{dep}$ and $H_{dep}$ gives insight into the pinning energy distribution of a sample. Pinning sites introduced a local variation in the anisotropy landscape of a sample. If the pinning potential increases it in turn will increase the factor $\frac{T_{dep}}{T}\left(H_{dep}\right)^{\frac{1}{4}}$.

Thus, the extracted parameters indicate a reduced pinning potential under compressive strain, whereas an enhanced pinning barrier under tensile strain. The modification in the pinning energy barrier under strain could be related to a local anisotropy modification due to the induction of MEA. In addition, the external strain might help in the relaxation of some strained pinning sites, modifying the effective pinning barrier. A reduced pinning barrier thus helps to move the DW faster under compressive strain. In addition, as the compressive strain reduces the effective magnetic anisotropy of the system, it in turn reduces the DW energy ($\sigma_{DW}$), leading to a faster DW motion. However, under tensile strain, the enhancement in both PMA and pinning potential might lead to a slower motion of the DW. With increasing strain further, a better tunability of the DW velocity might be possible. Such enhanced velocity could be helpful in future DW-based device applications. Strain-induced domain nucleation and DW motion were reported earlier for HM/FM (e.g., Co/Pt, Co/Ni) systems, deposited upon rigid

piezoelectric substrates [164,183]. However, in the case of a flexible HM/FM system, no such report exists to the best of our knowledge. In our case, all the changes in magnetic properties
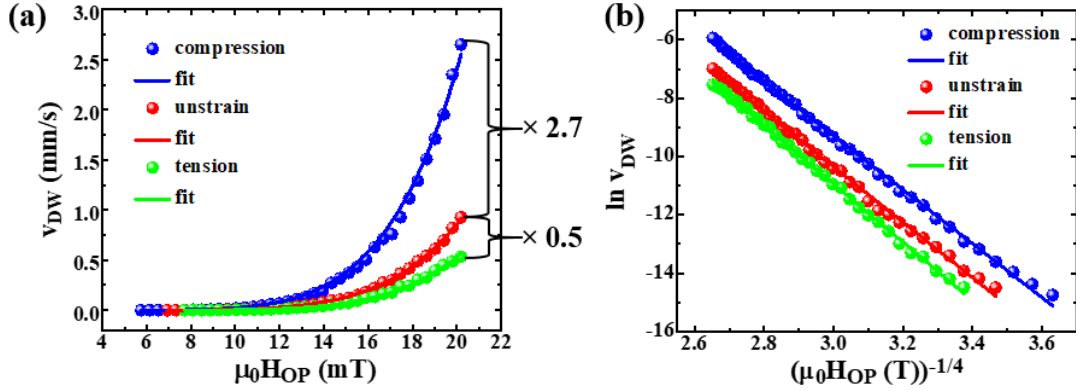


Figure 4.5 Pulsed magnetic field induced DW velocity measured using MOKE microscopy for sample S1, (a) $v_{DW}$ vs. field ($H_{OP}$) plot and (b) $ln\ v_{DW}$ vs. field ($H_{OP}$) plot at unstrained and strained states of the sample.

observed under the elastic strain are reversible in nature. Thus, strain engineering seems to be a promising tool to control both the static and dynamics of DW in flexible PMA thin films.

**4.3.4 Magnetic anisotropy:** The effective magnetic anisotropy ($K_{eff}$) is measured by SQUID magnetometry. In this context, *M-H* loops are measured along both the IP and OP directions of the samples at RT. The effective anisotropy is calculated using the following equation,

$$K_{eff} = \frac{1}{2}\mu_0 H_S M_S \qquad (4.4)$$

where, $\mu_0 H_S$ is the IP saturation field and $M_s$ is the saturation magnetization. Here, the effective anisotropy decreased from 0.80 MJ/m³ to 0.12 MJ/m³ by increasing $t_{Co}$ from 0.50 to 1.10nm. The origin of PMA in the Co/Pd system depends on several factors, viz. interfacial effects, magneto-elastic contribution, hybridization, modified orbital moment, etc. [184,185]. The strength of $K_{eff}$ decreases with increasing $t_{Co}$ as the volume anisotropy starts dominating over

the interfacial one. Application of external strain induces MEA ($K_{MEA} = \frac{3}{2}\lambda\sigma$) which modifies

the effective anisotropy of the sample further. Using the known values of applied strain ($\varepsilon$), the

value of $K_{MEA}$ can be calculated. As the tensile and compressive strains have opposite signs,

they modify $K_{eff}$ in an opposite manner. This gives rise to the opposite modulation in the

magnetic properties (e.g., magnetization reversal, relaxation, and DW dynamics) as well. Apart

from MEA, external strain also may modify the interfacial hybridization of a system. A recent

study on $Fe_2CoSi/Pt$ shows that a strained interface could change the strength of interfacial

orbital spin-polarization and hence, the interfacial hybridization of a sample [186]. Thus, to

understand the impact of applied strain on the orbital and spin magnetic moment, element-

specific XMCD measurements are performed on sample S1.

**4.3.5 X-ray magnetic circular dichroism (XMCD) measurements:** The difference in the

absorption of the left ($\mu^-$) and right ($\mu^+$) circularly polarized X-rays by a magnetic material

gives rise to a dichroic signal, known as XMCD [142,143]. The XMCD measurements are

performed at the Co $L_{2,3}$ edges of sample S1 at the BACH beamline of the Elettra synchrotron

facility, in Italy. The measurements are performed in the total-electron-yield (TEY) mode, at

the normal incidence geometry of X-rays at RT. The sample is magnetized using a permanent

magnet (~ 0.5T field strength), before loading inside the measurement chamber. Typical XAS

and XMCD ($\mu^-$- $\mu^+$) spectra are measured at both the flat and bend states of the sample, as

shown in Fig. 4.6. The integration of the XMCD spectra is also shown in each figure. From the

integration of XMCD, the ratio of the orbital to spin magnetic moment can be deduced using

the sum rule analysis as written below [147],

$$\frac{m_{orb}}{m_{spin}} = \frac{2q}{9p-6q} \tag{4.5}$$

where, $p = \int_{L_3} (\mu_- - \mu_+)\, dE$ and $q = \int_{L_3+L_2} (\mu_- - \mu_+)\, dE$, represents the integration of XMCD signal along $L_3$ and $L_3 + L_2$ edges, respectively. The strength of the XMCD signal ($\mu^-$-$\mu^+$) found to be modified at the strained state in comparison to the flat state of the sample. As the circular dichroism appears as a result of broken symmetry (either inversion or time-reversal symmetry) in a system, the application of strain could modify the broken inversion symmetry leading to a modified XMCD signal. By putting the values of $p$ and $q$ we calculated the ratio of $\frac{m_{orb}}{m_{spin}}$ for all the states of sample S1. In the flat state, the ratio of $\frac{m_{orb}}{m_{spin}}$ is found to be 0.086, which increased for both the compressive ($\frac{m_{orb}}{m_{spin}} = 0.097$) and tensile ($\frac{m_{orb}}{m_{spin}} = 0.10$) strained state of the sample. Thus, the impact of both tensile and compressive strain seems to be quite similar in modulating the orbital magnetic moment of Co. Such modification could arise due to a reduced orbital momentum quenching upon application of strain. This in turn indicates that the SOC strength of the material also enhanced via strain. A similar impact of strain on Co has previously been observed for a Heusler compound $Co_2FeSi$ deposited on a flexible PI substrate [187]. Thus, in our case, the observed opposite modulation of magnetic properties in flexible Co/Pd samples does not associate with the modification in orbital moments. As per a few theoretical reports, the application of strain changes the density of states (DOS) near the fermi level in the FM/HM systems [188]. There, the changes in DOS under tensile and compressive strain are found to be opposite in nature, which plays a crucial role in deciding the magnetic properties. Therefore, in our case, an opposite modification in DOS might originate the observed changes in the magnetic properties under strain. Theoretical analysis may help in understanding this aspect more clearly.
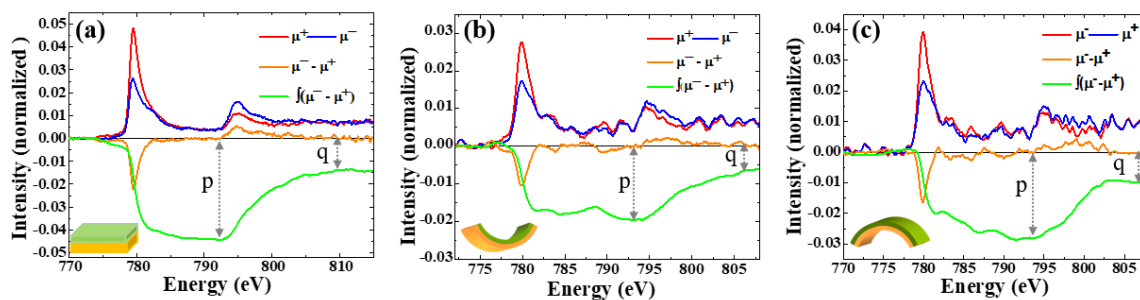
Figure 4.6 XMCD measurements performed in the NI geometry at Co $L_{2,3}$ edges of sample S1, at (a) unstrained, (b) compressive, and (c) tensile strained states. The measurements are performed at the BACH beamline of the Elettra synchrotron facility, in Italy.

| Table 4.1 Parameters at the unstrained and strained states of sample S1 ($t_{Co}$ = 0.80 nm) | | | | |
|---|---|---|---|---|
| Sample State | Coercivity ($\mu_0 H_C$) (mT) | Relaxation time constant ($\tau$) (s) | Maximum measured DW velocity ($v_{DW}$) (mm/s) | The ratio of orbital and spin magnetic moment ($\frac{m_{orb}}{m_{spin}}$) |
| Unstrained | 11.9 | 7.0 | 1.0 | 0.086 |
| Compressive strain | 10.2 | 5.6 | 2.73 | 0.097 |
| Tensile strain | 12.5 | 9.2 | 0.52 | 0.10 |

**4.3.6 Strain-driven SRT in sample S2:** Application of ~ 1.0% compressive strain does not change the square loop shape of the Co/Pd sample having 0.50 nm thick Co layer (Fig. 4.7). Here, as the Co thickness is far from the SRT region, compressive strain alone cannot modify the EA of the sample. A similar effect is also observed for the flexible Co/Pt system discussed in Chapter 3. However, for sample S1 (0.80 nm), a square to s-shape transition of the hysteresis loop is obtained by applying ~ 1.0% compressive strain (Fig. 4.7). This indicates a significant reduction in PMA strength due to the induced MEA. As localized structural damage appears at

such a high strain value, it may degrade the film quality. In an earlier work, magnetization switching from IP to OP direction is achieved by applying ~ 2.00% biaxial strain in a flexible
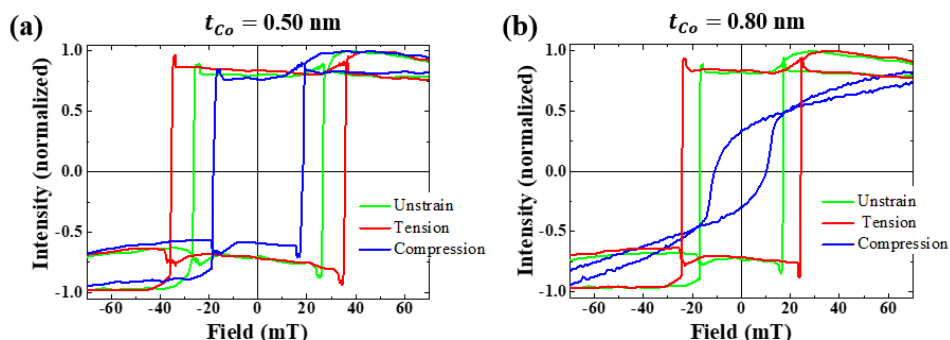


Figure 4.7 Hysteresis loops measured at the unstrained and ~ ±1.0% strained state of Co/Pd samples with (a) 0.50 nm and (b) 0.80 nm (sample S1) thick Co layers.

Co/Pd film [179], which is also not desirable from an application viewpoint. Thus, to obtain magnetization switching at lower strain values we have considered the sample S2 having Co thickness ~ 1.10 nm. Magnetization reversal study at varied strain values shows a systematic increase in coercivity under tensile strain, whereas a sudden decrease under compressive strain, as shown in Fig. 4.8 (a). As the sample thickness is closer to the SRT region, the impact of compressive strain is found to be stronger than the tensile one. Notably, under a minimal compressive strain of ~ 0.13%, the square loop shape became a slanted (s-shape) one and at ~ 0.25% strain the loop shape changed to a straight line in the polar MOKE measurement (see Fig. 4.8 (b)). This confirms a switching of magnetic anisotropy from OP to IP direction. Such changes are found to be reversible and the hysteresis loop comes back to its initial shape upon removal of the strain. Notably, the coercivity values shown in Fig. 4.8 (a) are lower than the values depicted in Fig. 4.8 (b). As the molds used during strain-dependent measurements have ~4mm height, it requires a slightly higher magnetic field to attain the coercivity. Thus, by subtracting the extra field value (~ 5mT), the actual coercivity values are plotted w.r.t strain in Fig. 4.8 (a). Further, to study the impact of such strain on the domain dynamics, we have compared the domain images captured at the coercivity of the corresponding hysteresis loops.

Bubble domains are observed at the initial flat state of the sample, which remains similar up to -0.06% strain (see Fig. 4.8 (c)). Increasing the applied strain further to -0.13% changes the loop from a square to s-shape, and hence, the reversal also happens via coherent rotation instead of DW motion. Thus, no domain formation and wall motion are observed for all the loops with an applied strain higher than -0.13%. This supports the basic magnetization reversal phenomena where the reversal happens via DW motion along EA, whereas via coherent rotation along HA. Thus, the application of compressive strain possibly changes the EA from OP to IP direction, which modulates the reversal process from DW motion to coherent rotation. Therefore, switching the magnetic anisotropy via a minimal applied strain (0.25%) in a non-volatile way
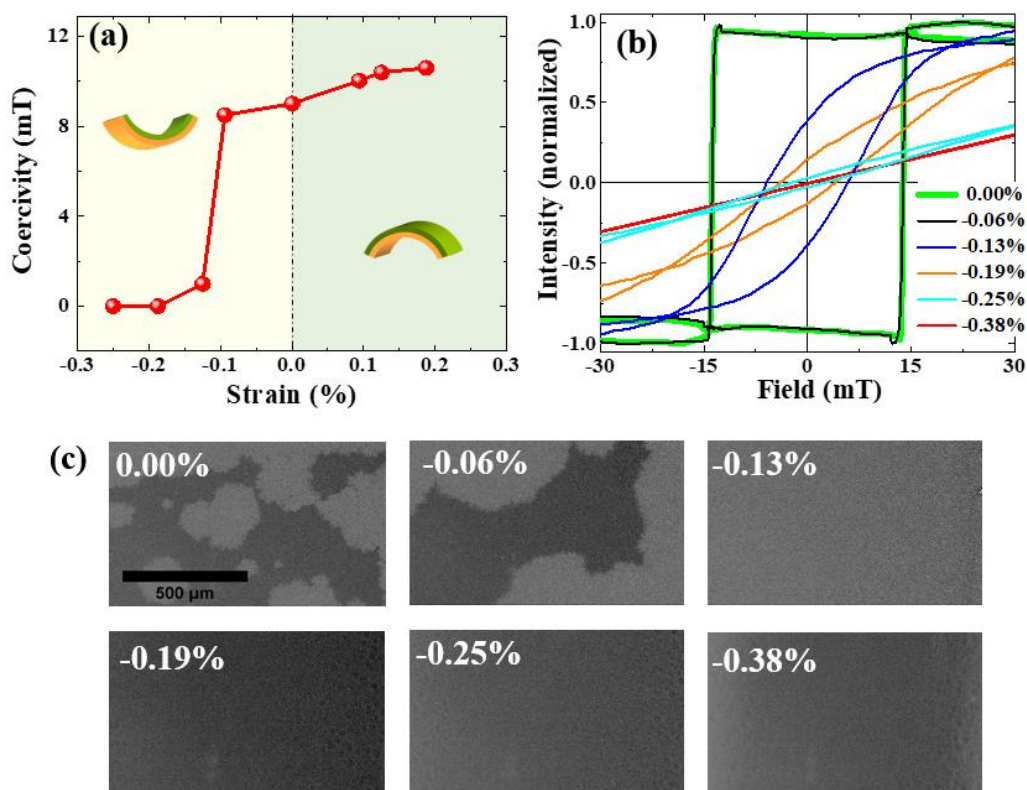


Figure 4.8 (a) Strain vs. coercivity plot for sample S2, (b) square to slanted loop shape change under compressive strain, (c) domain images captured at coercivity of hysteresis loops with varied compressive strain. The scale bar shown in the 0.0% image is 500 μm in length and is valid for all the other images.

seems to be very promising for flexible spintronic device applications. Till now magnetization switching is achieved mainly by applying high electric fields or voltages, which suffers from several issues e.g., leakage current, filament formation, sophisticated device fabrication, etc. Flexible magnetic films overcome all these issues which is indeed promising for fabricating energy-efficient flexible spintronic devices.

In summary, we have investigated the structural and magnetic properties of flexible Co/Pd thin film in a strained environment. MOKE microscopy measurements revealed an enhancement (decrement) in magnetic coercivity and relaxation time under tensile (compressive) strain. Such changes are ascribed mainly to the stress-induced anisotropy in the system. Further, the DW velocity measurements reveal ~ 3 times enhanced velocity under compressive strain owing to the reduced anisotropy and pinning potential of the sample. To understand well the origin of such strain-induced changes, synchrotron-based XMCD measurements are performed. The analysis reveals that the ratio of orbital and spin magnetic moment is independent of the sign of applied strain. Thus, there could be an opposite modification in the DOS near the Fermi level which results in such opposite modulation in the magnetic properties under tensile and compressive strain. Further, at ~0.25% compressive strain the EA of the Co/Pd sample (having 1.10 nm thick Co layer) switches from OP to IP. Such strain-assisted SRT is very promising for energy-efficient switching applications. In contrast to the flexible Co/Pt film, here the Co/Pd system shows a higher strain sensitivity owing to its high value of $\lambda$. Thus, strain engineering appears to be a promising tool for tailoring PMA, boosting DW velocity, and switching magnetization orientation, essential for faster, smaller, and power-efficient spintronic devices.

## Chapter 5: Structural deformation and irreversible magnetic properties in strained Pt/Co/Pt and Pd/Co/Pd thin film

In the last two chapters, we have studied the effect of bending-induced tensile and compressive strains on the structural and magnetic properties of flexible Pt/Co and Pd/Co samples. In those systems, a few localized damages are found when the applied strain is ~1.0%. As the sample showed classical magnetoelastic effects, the impact of strain on the magnetic properties was reversible in nature. However, apart from bending, the flexible samples are also expected to withstand the stretching, twisting, peeling, and wrinkling modes of flexibility [7,189–192]. These modes may generate biaxial or multiaxial strain on the system [192,193]. Thus, it is important to know the critical strain beyond which severe deformation may take place. The occurrence of crack formation and buckle delamination may strongly affect the functional properties of the film. This may restrict the industrialization of flexible devices and thus, necessitates a thorough understanding. However, these topics are rarely studied and discussed in detail. Faurie et al. studied the effect of applying large tensile strain on the $Co_{40}Fe_{40}B_{20}$ ($\lambda \neq 0$) film deposited on the Kapton substrate [160]. It was found that the crack initiation occurs at ~1.6% strain. Cracking and subsequent buckling increased the electrical resistance by several orders of magnitude. Further, Merabtine et al. studied the effect of large stretching strain on the magnetic properties of $Co_{40}Fe_{40}B_{20}$ ($\lambda \neq 0$) and $Ni_{80}Fe_{20}$ ($\lambda \approx 0$) thin films [156]. Here, crack formation started from ~2% strain, whereas blister kind pattern appears from ~6% strain. It is important to highlight that in their study the authors found that the structural discontinuities (due to cracks and buckles) have no impact on the magnetic properties. Only the residual stress generated during the damage of the film affects the magnetic properties. As per our earlier studies on the bending-induced strain, it is quite expected that the damages should act as pinning sites for the domain nucleation and propagation. Thus, the overall magnetization reversal mechanism should be strongly affected by such high strain. As very little is known

about the impact of damages on the magnetic properties, we tried to investigate this aspect for both the flexible Co/Pt and Co/Pd films.

**5.1 Sample details:** Pt/Co/Pt and Pd/Co/Pd thin films are prepared upon Kapton (~50μm thick) having an adhesive back. This adhesion helps to generate a strain as explained in section 5.2. The Kapton is stuck on a Si substrate and loaded inside the deposition chamber for sample fabrication. Here Si substrate is used as a flat base for mounting the flexible Kapton. The sample structure is shown schematically in Fig. 5.1. Base pressure of the deposition chamber was ~ $6\times10^{-8}$ mbar. Samples are prepared via the DC magnetron sputtering technique in a high vacuum multi-deposition chamber manufactured by Mantis Deposition Ltd. UK. The deposition rates for Ta, Pt, Pd, and Co layers are maintained at 0.18 Å/s, 0.15 Å/s, 0.20 Å/s, and 0.16 Å/s, respectively. The substrate is rotated at 10 rpm during the sample fabrication.

**Pt/Co/Pt**

| Pt (5 nm) |
| Co (0.9 nm) |
| Pt (4 nm) |
| Ta (20 nm) |
| Kapton (50μm) |
| Si |

(a)

**Pd/Co/Pd**

| Ta (5 nm) |
| Pd (2 nm) |
| Co (0.8 nm) |
| Pd (4 nm) |
| Ta (20 nm) |
| Kapton (50μm) |
| Si |

(b)
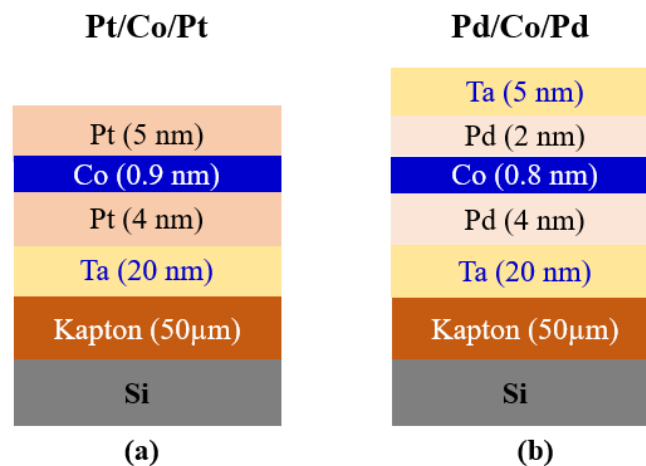
Figure 5.1 Schematic of the deposited sample structure, (a) Pt/Co/Pt and (b) Pd/Co/Pd.

**5.2 Strain generation method:** We have used a peel-off method to generate peeling strain on the deposited flexible film. In this method, the Kapton film (with the sample deposited on top) is peeled off from the Si substrate. Due to the adhesive back of the Kapton, it experiences a large force while detaching from the Si substrate. Along the applied force axis, it experiences a tensile stress whereas in the transverse axis, it will experience a compressive stress. The
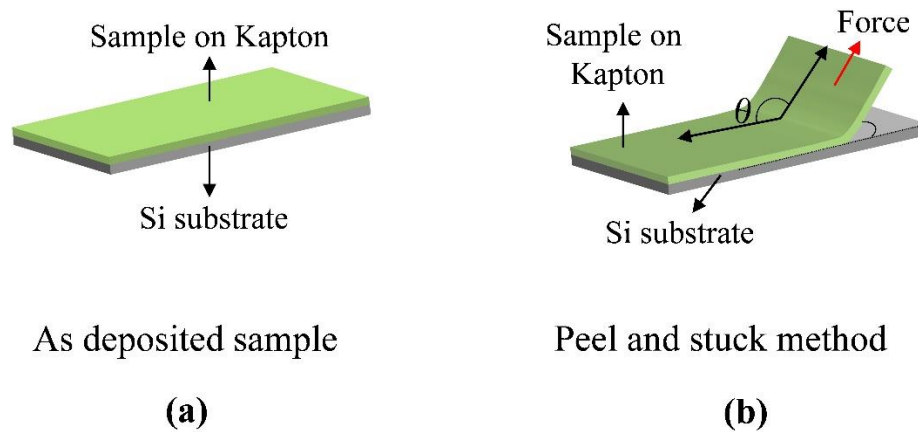
Figure 5.2 Schematic of strain generation method, (a) as-deposited sample, (b) peeling off the sample with Kapton from the Si base.

physics of such peeling-induced force was studied earlier by Lendley and Kendall in 1971 [194,195]. By varying the strength of the applied force, the strain can also be tuned. The peel-and-stuck method is used for fabricating flexible devices, as it is compatible with the roll-to-roll process technique [191,196]. A schematic of the strain generation method used in our work is shown in Fig. 5.2. The structural and magnetic properties of the samples are measured in the unstrained (as-deposited) and strained (after peeling) states. For the measurements in the strained state, the samples are first peeled off from the Si substrate and then made flat to measure the properties being subjected to a high strain.

**5.3 Structural characterization:** As discussed in Chapter 3, cracking and buckling of the thin film occur under tensile and compressive strains, respectively. However, to understand the impact of applied peeling strain, SEM imaging is performed for both the Pt/Co and Pd/Co flexible samples. Fig. 5.3 shows the SEM images captured for the Pt/Co sample deposited on Kapton. In the unstrained state, no sign of damage is found by scanning the sample surface. However, after peeling off several features appear on the sample surface, as visible in Fig. 5.3 (b-c). Here, the black dotted arrows represent the direction of applied force. Several straight
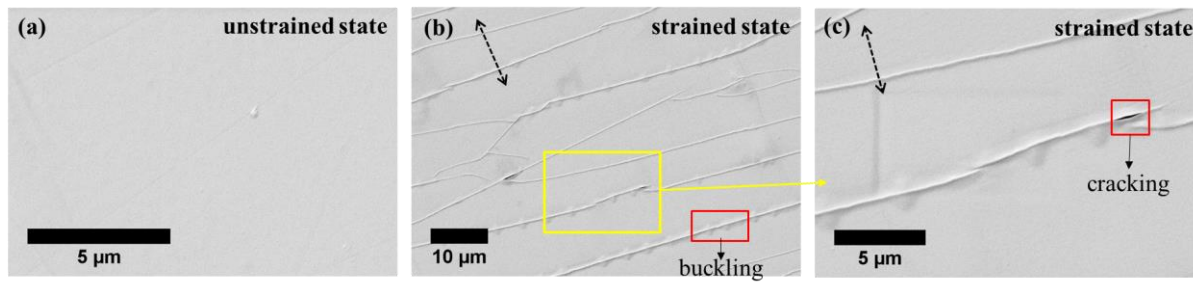
Figure 5.3 SEM images of the surface of flexible Pt/Co sample in the (a) unstrained, and (b-c) strained states. The red marks show the buckling and cracking of the film at several places owing to high strain. The zoom-in view of the yellow-marked region is shown in (c).

lines having small heights are observed on the film surface. This looks quite similar to the buckling of a thin film. As explained in Chapter 3, buckle delamination is the process where a small part of the film detaches from the substrate to release the stress energy. Here due to the applied strain, buckling of the film is observed to minimize the elastic energy. The occurrence of buckling and wrinkling modes depends on the elastic mismatch and interfacial defects present in a system [159]. In our case, the large mismatch between the elastic moduli of the inorganic films (~200 GPa) and organic Kapton substrate (~5GPa) generates strong stress gradients at the interface of the deposited film and Kapton, resulting in the buckling of the film.
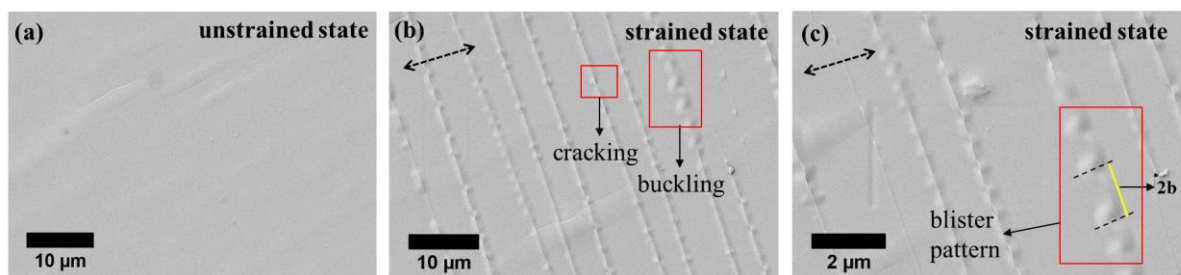


Figure 5.4 SEM images of the surface of flexible Pd/Co sample in the (a) unstrained, and (b-c) strained states. The red marks show the buckling and cracking of the film at several places owing to high strain. The zoom-in view of the blister pattern and its wavelength 2*b* is shown in (c).

In a few places, the top of the buckled film gets cracked as it experiences a high tensile strain. The red squares in Fig. 5.3 (b and c) represent the buckle delamination and crack formation in thin film. Fig. 5.3 (c) is the zoom-in view of the yellow-marked region of Fig. 5.3 (b). Similar to Pt/Co film, the flexible Pd/Co sample also shows no indication of damage in the unstrained state (Fig. 5.4 (a)). After applying strain, the Pd/Co sample also exhibits distinct features on the sample surface, as shown in Fig. 5.4 (b) and (c). Periodic lines associated with small wavy features are found on the sample surface. These buckled portions of the film have a small height, similar to our previous case. Crack formation started from the crest of such features to release the stress energy. The red-marked region in Fig. 5.4 (b) shows the buckled and cracked surface of the film. A zoom-in view of such a wavy pattern is shown in Fig. 5.4 (c). A closer look at the red-marked region confirms the formation of blister patterns. This pattern looks quite similar to a telephone cord blister which occurs when a film-substrate system undergoes a high compressive stress [197]. The critical stress required for such buckle formation can be calculated using equation 3.5 of chapter 3, as written below,

$$\sigma_b = \frac{\pi^2}{12} \left(\frac{h}{b}\right)^2 \bar{E}_f \tag{5.1}$$

where, $h$ is the film thickness, $b$ is the half-width of buckling, and $\bar{E}_f$ is the plane strain modulus (PSM) of the film. Using the value of $b$ as shown in Fig. 5.4 (c), the critical stress generated in our case is found to be ~5.0 GPa, which corresponds to ~3.0% strain. The physics of such pattern formation is quite complicated and often considered to originate from the secondary buckling of a straight-sided blister. In our case, the localized blister patterns may be associated with localized defects present at the film-substrate interface [158,197]. Thus, the crack formation, buckle delamination, and blister formation indicate a complex high-strain generation via the peeling of the flexible film. As the observed damage features appear at high strain values, a resistivity measurement is further performed to confirm the same.

**5.4 Resistivity measurement:** A homemade four-probe setup is used for measuring sample resistance at RT, as mentioned in the sub-section 2.4 of Chapter 2. Current is applied to the two outer probes whereas the voltage is measured via the two inner probes. The sheet resistance is calculated using the equation written below [152],

$$R_S = \frac{\pi}{\ln 2} \frac{\Delta V}{\Delta I} = 4.53 \frac{\Delta V}{\Delta I} \tag{5.2}$$

where, $\Delta V$ and $\Delta I$ are the output voltage and applied current to the sample, respectively. From the slope of the *V-I* curve, the sheet resistance is calculated using equation 5.2. An increasing slope of the graph in fig. 5.5 indicates an increase in sample resistance due to the numerous cracks and buckles formed after the peel test. For the Pt/Co film, the sheet resistance $R_S$ changed from $\sim 80\Omega$ to $\sim 830\Omega$. Similarly, for the Pd/Co film, $R_S$ changed from $\sim 82$ to $630\Omega$ after the peeling process. Before, the peel test both the samples had quite comparable resistance. However, after the peel test, the Pt/Co film shows a bit higher resistance than Pd/Co, possibly due to a higher number of cracks density in the film. As resistance is related to the dimension of a film, the modification in resistance confirms a significant strain generation on the samples [160].
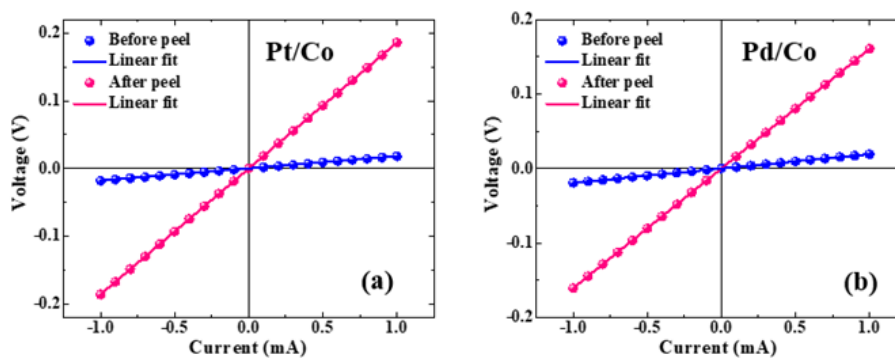


Figure 5.5 *V-I* curve measured via four probe technique is shown for (a) Pt/Co and (b) Pd/Co samples, before and after the peeling process. The solid lines are linear fits to the experimental data.

## 5.5 Magnetic characterization:

**5.5.1 Magnetization reversal phenomena:** Hysteresis loops and corresponding domain images are recorded using MOKE microscopy in the polar mode. For both the Pt/Co and Pd/Co samples, a square-shaped loop is observed in the unstrained state of the samples (see Fig. 5.6 (a, c)), owing to their moderate PMA strength. The reversal was found to be associated with bubble domain nucleation and subsequent propagation, as depicted in Fig. 5.6 (b, d). Application of strain increases the coercivity and hence, the switching field of the samples, as shown in Fig. 5.6 (a, c). This is related to an increased pinning potential due to the damage to the samples. The cracked and buckled features act as additional pinning sites and thus, a high field is required to overcome these pinning barriers. The domain nucleation and propagation
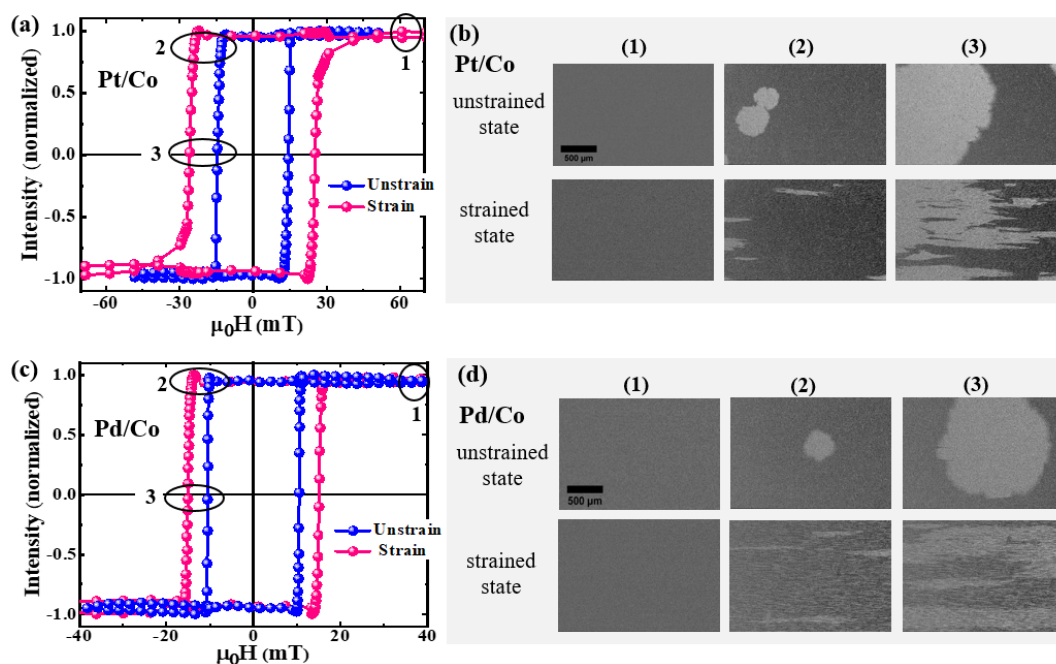


Figure 5.6 Magnetization reversal was studied in the unstrained and strained states of both the Pt/Co and Pd/Co films via polar MOKE microscopy, where (a, c) hysteresis loops, and (b, d) domain images of both the samples. The images are associated with the points (1, 2, 3) marked in the corresponding hysteresis loops. The scale bar shown in the saturation images (1) is 500 μm in length and is valid for all the other images.

events are also strongly affected by the damage of the film. Due to the periodic buckled features, the bubble domain formation is not observed in the strained sample. Instead, the domains get elongated and propagate in the transverse direction of the applied stress. Due to the numerous pinning barriers along the stress axis, the domains mainly propagate along the other transverse axis and get elongated. The observed magnetic properties are also found to be irreversible in nature. In an earlier study by Merabtine et al., the authors predicted that the structural discontinuity due to the cracks and buckles should not affect the magnetic properties of a sample [156]. However, our study contradicts this statement and shows that the magnetization reversal phenomena get strongly modified by the appearance of such structural discontinuity in the film.

**5.5.2 Relaxation dynamics:** We also performed relaxation measurements to investigate whether thermal energy (in addition to a fixed Zeeman energy) could saturate the samples in such a highly strained state or not. Relaxation measurements are performed at both the strained
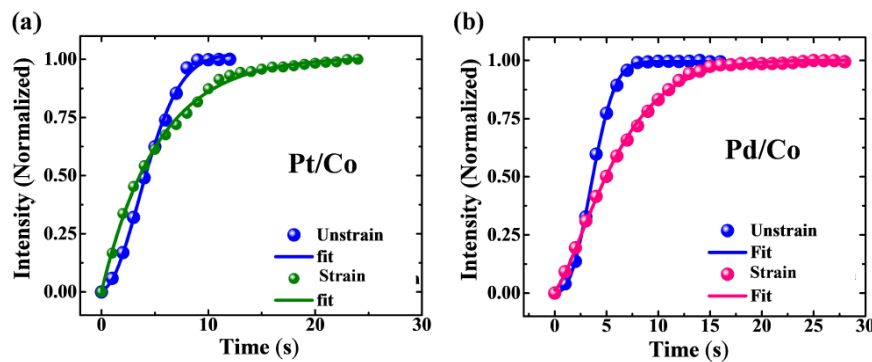


Figure 5.7 Magnetization relaxation measurement performed at $0.99H_c$ field value, using the MOKE microscopy in the polar mode. The intensity vs. time plot is shown at the unstrained and strained states of (a) Pt/Co and (b) Pd/Co samples.

and unstrained states of Pt/Co and Pd/Co samples. At a fixed applied field value all the domain images are captured during the whole thermal relaxation process. The normalized intensity is

then plotted with the time taken to complete the reversal. The experimental data is usually fitted

by a compressed exponential function as mentioned earlier. Fig. 5.7 shows the intensity vs.

time plot and Fig. 5.8 shows the domain images captured at different time intervals during the

relaxation measurement. By fitting the experimental data, the values of $\beta$ and $\tau$ are extracted at

the unstrained states of the samples. The value of $\tau$ is $\sim$ 5s for both the samples in their

unstrained states. However, for the strained condition, the saturated state is not reached even

after $\sim$ 30 seconds of reversal as shown in Fig. 5.8. A few unreversed areas were still present

due to the structural discontinuities formed in the strained state of the samples. Such unreversed

areas are marked with red colour in Fig. 5.8 (f and k). Such high-pinning areas seem tough to
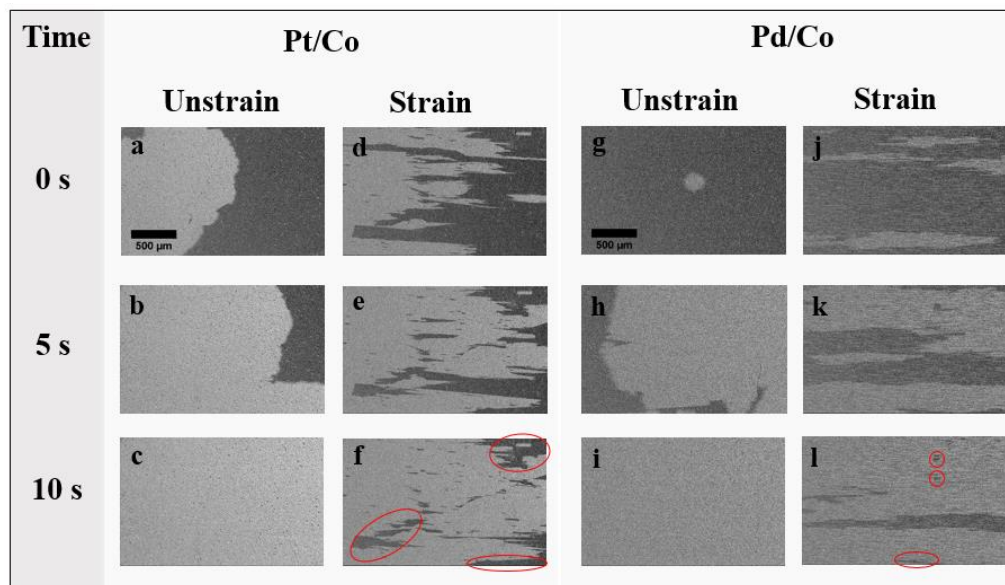


Figure 5.8 Domain images captured during the relaxation measurement of both Pt/Co and

Pd/Co samples. Here, (a-c) unstrained and (d-f) strained states domain images for the Pt/Co

film, whereas (g-i) unstrained and (j-l) strained states domain images for the Pd/Co film. The

red-marked areas highlight the unreversed regions of the samples. The scale bar shown in

the domain image captured at 0s is 500μm in length and is valid for all the other images.

overcome via the thermal energy and require the application of an additional Zeeman energy in the system. Thus, in the strained state, the relaxation time constant ($\tau$) extracted from an intensity ($I(t)$) vs. time ($t$) plot will accompany a finite error, which is not desirable. Thus, the fitted values of $\beta$ and $\tau$ in the strained state should not be compared with the unstrained state. However, the domain images and relaxation curves clearly show that the relaxation mechanism is slower for the samples under strained state. Notably, when the sample was in the unstrained state, the reversal was found to be dominated via both domain nucleation and propagation (as $\beta$ obtains a value within 2-2.5). However, after the application of strain, the reversal was mainly dominated by domain nucleation, owing to the several hindrances for DW propagation. Thus, the relaxation measurement was found to be strongly affected by the damage of the film and the thermal energy is unable to complete the reversal even in the presence of a constant Zeeman energy. Thus, the structural discontinuities largely impact the local magnetization reversal, domain, and relaxation dynamics of the flexible film.

In summary, the impact of thin-film damage on the magnetic properties of flexible Co/Pt and Co/Pd film is investigated. SEM imaging shows that peeling-induced strain generates significant damage (cracking, buckling, etc.) to both films owing to the high elastic mismatch and interfacial defects between the film and substrate. Further, the resistivity measurement also shows a significant increment of sample resistance in the strained environment. Magnetization reversal and domain dynamics are found to be strongly affected by the structural discontinuities present in the strained state of the samples. Few pinning barriers are even tough to saturate during the relaxation measurement. Such modifications in magnetic properties are also irreversible in nature. Thus, the presence of structural discontinuities strongly affects the local magnetic properties (e.g., magnetization reversal, DW dynamics, etc.) whereas the global properties are mainly affected by the residual stress generated during the damage of the film.

## Chapter 6: Effect of strain on the magnetic properties of asymmetric Pd/Co/C$_{60}$/Pd system

The formation of chiral domain walls and skyrmions in HM/FM-based thin films depends strongly on the strength of the interfacial DMI. However, symmetric magnetic stacks (say, HM1/FM/HM1) do not originate a significant effective DMI, owing to the cancellation of DMI from the top and bottom HM/FM interfaces. In contrast to this, asymmetric structures (say, HM1/FM/HM2, HM1/FM/Oxide) were found to generate a strong DMI, making them promising candidates in the field of spintronics and spin orbitronics. They can host chiral DWs, skyrmions and move them efficiently by applying fields or current pulses. These chiral textures are intended to be binary information carriers in logic devices and racetrack memories. For a long period, the search for high DMI was limited to only HMs and oxide-based asymmetric magnetic stacks. In this context, significant attention is given to the Pt/Co/Ir system, as the opposite sign of DMI is theoretically predicted from the Pt/Co and the Co/Ir interfaces [198]. In addition, a few other systems such as Pt/Co/Al, Pt/Co/Cu, Ta/CoFeB/MgO, Pd/Co/Cu, etc. are also studied [24,25,199]. Here, the DW velocity is found to be strongly dependent on the choice of the top layer, and it increases while changing a HM with a light metallic layer [25]. An increase in DMI strength helps to increase the DW velocity. As a HM layer also enhances the damping of a system, the search for alternative DMI host material composed of light atoms has drawn enough research attention. In this context, a few recent studies revealed that the light atom carbon (C) based graphene can originate a significant Rashba-DMI from the graphene/Co interface, due to a Rashba interaction mediated high SOC of graphene [26]. This DMI also transforms a Bloch wall into a chiral Néel wall structure. Similar to graphene, a few other allotropes of C, e.g., fullerene (C$_{60}$), carbon nanotubes (CNTs) also exhibit a high SOC strength [28,29]. Even though they are made up of light element C, the enhancement in SOC is related to their curved structure and Rashba-type interactions. Fullerene molecule is

composed of exactly 12 pentagons and 20 hexagons which help to form a closed cage-like structure with proper curvature. This buckyball structure helps in electron hopping between the adjacent π and σ bonds of C atoms, which generates an additional SOC along with the weak intrinsic SOC [29,200,201]. Thus, fullerene also may generate a strong DMI and host chiral textures when deposited on top of a FM layer.

Further, the C-based materials, e.g., C$_{60}$, graphene, and CNTs, are important in spintronic applications as they provide a long spin diffusion length, a large spin relaxation time, and less hyperfine interaction than in other materials [202,203]. All of these carbon allotropes (e.g., C$_{60}$, graphite, and CNTs) can be formed from a single structural unit known as graphene. The low atomic number of C and the absence of hydrogen (H) atoms in these allotropes helps to transport spin information over a long distance without scattering [204]. In addition, a fullerene molecular layer also may reduce the impedance-mismatch issue by forming a hybridized interface when placed next to a FM. At the interface of a FM/C$_{60}$ heterostructure, broadening ($\Gamma$) and shifting ($\Delta E$) of the molecular density of states occur due to the spin-dependent orbital hybridization [100]. This results in an effective hybridized interface known as a "spinterface." Such a spinterface acquires a net spin polarization and modulates the magnetic properties (e.g., magnetic anisotropy, magnetoresistance, saturation magnetization, and domain structure) of the FM/organic molecular heterostructure [205,206].

In this context, we have prepared an asymmetric magnetic stack of Pd/Co/C$_{60}$ upon the rigid Si substrate and studied the effect of spinterface formation (at the Co/C$_{60}$ interface) on the magnetization reversal, magnetic anisotropy, relaxation, and DW dynamics. Further, we also quantified the strength of interfacial DMI originating from the Co/C$_{60}$ interface. A few recent theoretical and experimental work also shows the possibility of tuning the DMI strength by applying external strain [32,207]. Thus, to tune the DW velocity and DMI strength further we

have prepared the asymmetric Pd/Co/C$_{60}$ stack upon the flexible PI substrate. Here, the effect of bending-induced strain on the magnetic properties of the samples is studied in detail.

**Magnetic properties of Pd/Co/C$_{60}$/Pd samples prepared upon rigid Si substrate:**

**6.1 Sample details:** A series of samples are prepared by varying the thickness of the C$_{60}$ ($t_{C_{60}}$) layer, where the structure is as follows, Si(100)/Ta(10 nm)/Pd(4 nm)/Co(0.5 nm)/C$_{60}$($t_{C_{60}}$) nm)/Pd(2 nm)/Ta(3 nm). For simplicity, the samples are named S1 ($t_{C_{60}}$= 0nm), S2 ($t_{C_{60}}$= 0.8nm), and S3 ($t_{C_{60}}$=1.6nm). All the metallic layers are deposited by DC magnetron sputtering whereas the C$_{60}$ layer is deposited by thermal evaporation technique at a base pressure of ∼ 6× 10$^{-8}$ mbar in the high vacuum multi-deposition chamber manufactured by Mantis Deposition Ltd., UK. The growth rates of Ta, Pd, and Co layers were 0.18 Å/s, 0.20 Å/s, and 0.16 Å/s, respectively. The rate for the C$_{60}$ layer was varied between 0.10 – 0.16 Å/s during deposition. Deposition rates and thicknesses were monitored by a QCM, while the substrate was rotated at 10 rpm during deposition.

**6.2 Structural characterization:** X-ray reflectivity (XRR) measurement is performed to quantify the structural parameters (e.g., thickness, roughness, and density) of the multilayered samples using an X-ray-diffractometer (XRD) manufactured by Rigaku Corp., Japan. For sample S2 the fullerene layer is very thin (∼ 0.80nm) and comparable to its roughness, hence, a continuous layer is quite unlikely to form. Here, C$_{60}$ acts as a dusting layer and at some places top Pd layer might have been in direct contact with the Co layer leading to the formation of an intermixed layer of Co-C$_{60}$-Pd. However, for sample S3, fullerene forms a continuous layer as the thickness of the layer (∼ 1.60nm) is higher than the roughness (∼ 0.70nm). Thus, the XRR data for samples S2 and S3 are fitted by considering an interdiffusion layer of Co-C$_{60}$-Pd and Co-C$_{60}$, respectively. XRR fits for all the samples are shown in Fig. 6.1 and corresponding fitting parameters are listed in Table 6.1.
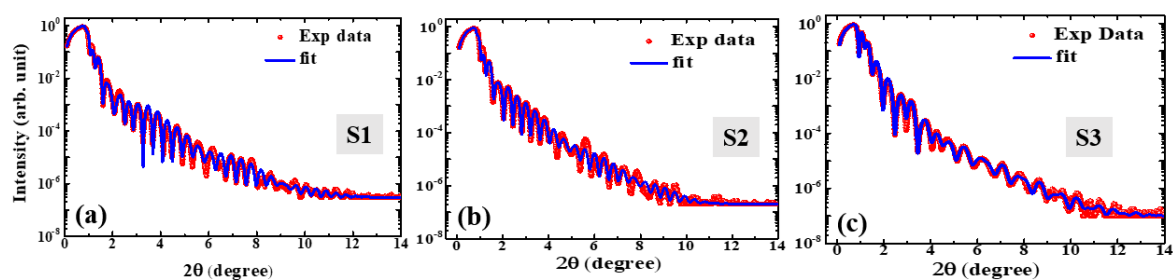
Figure 6.1 XRR fits for samples S1, S2, and S3 are shown in (a), (b), and (c), respectively.

| Table 6.1 Thickness and roughness of Pd/Co/C$_{60}$/Pd samples obtained from XRR fits considering interdiffusion layers | | | |
|---|---|---|---|
| Parameters | C$_{60}$-0nm (S1) | C$_{60}$-0.8nm (S2) | C$_{60}$-1.6nm (S3) |
| Pd thickness | 4.50 | 3.80 | 3.90 |
| Pd roughness | 1.10 | 0.90 | 1.00 |
| Co thickness | 0.51 | 0.40 | 0.35 |
| Co roughness | 0.27 | 0.29 | 0.28 |
| Co-C$_{60}$ thickness | ---- | ---- | 0.40 |
| Co-C$_{60}$ roughness | ---- | ---- | 0.24 |
| Co-C$_{60}$-Pd thickness | ---- | 0.80 | ---- |
| Co-C$_{60}$-Pd roughness | ---- | 0.40 | ---- |
| C$_{60}$ thickness | ---- | ---- | 1.46 |
| C$_{60}$ roughness | ---- | ---- | 0.72 |
| Pd thickness | 2.14 | 1.20 | 2.00 |
| Pd roughness | 0.53 | 0.52 | 0.80 |

## 6.3 Magnetic Characterization:

### 6.3.1 Magnetization reversal phenomena:

Polar MOKE (P-MOKE) hysteresis loops for samples S1-S3 are shown in Fig. 6.2 (a), where the coercivity ($H_C$) decreases systematically with increasing C$_{60}$ coverage. Such a decrease in $H_C$ reflects a decrease in effective PMA in the samples by substituting the top Pd layer with a C$_{60}$ layer. Here, $H_C$ decreases systematically from 15.98 (in S1) to 3.12 mT (in S3), indicating
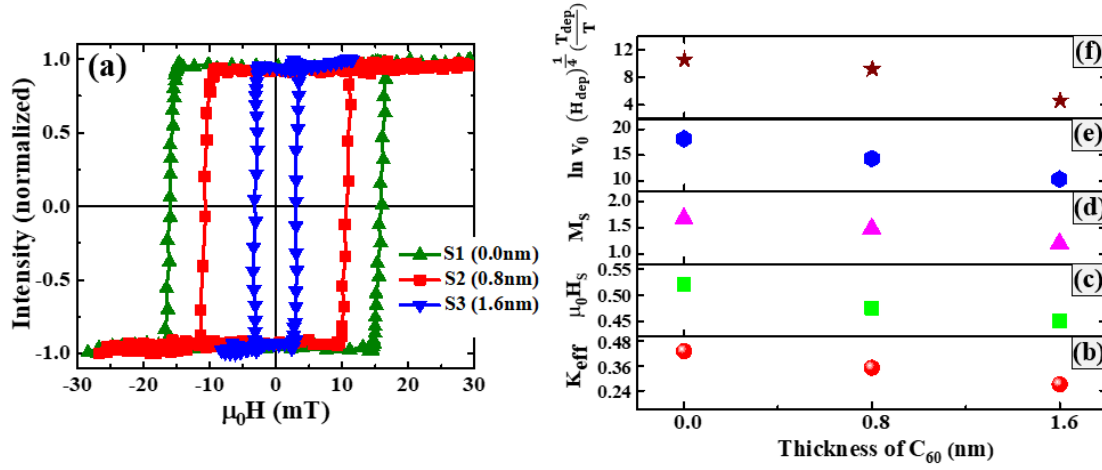
Figure 6.2 Magnetic properties of Pd(4)/Co(0.5)/C$_{60}$($t_{C_{60}}$)/Pd(2) samples, (a) hysteresis loops measured by polar MOKE microscopy, (b) $K_{eff}$ (in MJ/m$^3$), (c) $\mu_0 H_S$ (in T), and (d) $M_S$ (in MA/m) were extracted from hysteresis loops measured by SQUID magnetometer. (e-f) $ln\ v_0$ and $\frac{H_{dep}^{\frac{1}{4}} T_{dep}}{T}$ (in T$^{0.25}$) extracted from the DW velocity measurements using MOKE microscopy [208].

a magnetic softening along with sharp magnetization reversal upon C$_{60}$ insertion. In contrast to the 3*d*-4*d* hybridization that should arise at the top Co/Pd interface [209], the deposition of an organic layer (C$_{60}$) on top of Co results in an interfacial hybridization between C-*p* and Co-3*d* orbitals [210]. Such hybridization leads to the formation of a spinterface at the Co/C$_{60}$ interface and modifies the magnetic anisotropy, as well as the coercive field of the samples. Due to the interfacial nature of the hybridization, a reduction in coercivity is observed until the formation of a 1.6 nm thick C$_{60}$ in S3. A minor change in magnetic characteristics might be anticipated upon the formation of 2 ML fullerene, followed by no discernible changes with further increase in $t_{C_{60}}$.

**6.3.2 Magnetic anisotropy:**

To calculate the magnetic anisotropy ($K_{eff}$) we have measured *M-H* loops by SQUID magnetometry along both the IP and OP directions of the samples. The effective anisotropy has been calculated using the formula,

$$K_{eff} = \frac{1}{2}\mu_0 H_S M_S \qquad (6.1)$$

where $\mu_0 H_S$ is the IP saturation field and $M_s$ is the saturation magnetization [211]. The values of $\mu_0 H_S$, $M_s$, and $K_{eff}$ for all the samples are listed in Table 6.2 and shown in Figure 6.2 (b-d). Due to the high electron affinity of carbon (2.6 eV), spin-polarized charge transfer may occur from Co to C$_{60}$ giving rise to the observed reduction in saturation magnetization in the Pd/Co/C$_{60}$ samples. The role of the Co/C$_{60}$ interface on magnetic softening can be well understood by analyzing the nature of orbital hybridization that occurs at the Co/C$_{60}$ interface. In a fullerene molecule, each C atom forms three $\sigma$ bonds (between $sp^2$ orbitals) and one $\pi$ bond (between $p_z$ orbitals) with the neighboring C atoms [212]. As the $p_z$ orbital of fullerene spreads extra along the exterior of the molecule rather than into the interior of the sphere, they make a strong bond with the 3$d$ orbitals of a FM metal when placed next to it. Hybridization between $p_z$ -$d_{xy,x^2-y^2}$ or $p_z$ -$d_{yz,zx}$ orbital leads to a reduction in PMA at the interface of the Co/C$_{60}$ system [210]. Notably for a Pd/Co/Pd system, DFT calculation indicates that both the 3$d_{xy,x^2-y^2}$ and 3$d_{yz,zx}$ orbitals of Co give rise to PMA at the interface [209]. In our case, we expect that a similar hybridization occurs between $p_z$ -$d_{xy,x^2-y^2}$ and $p_z$ -$d_{yz,zx}$ orbitals leading to a decrease in the effective PMA of the system. Future DFT calculations may shed light on the exact nature of hybridization for the occurrence of magnetic softening in such systems. The strength of magnetic anisotropy for a Co/C$_{60}$ system also depends on the choice of the buffer layer (e.g. Pd, Pt, or Au) and adsorption geometry (either hexagonal or pentagonal rings of C) of the C$_{60}$ molecule upon a FM layer [213]. The decrease in the MA landscape is consistent with the

decrement in coercivity as observed from the hysteresis loops. It has been reported earlier that the spinterface thickness in FM/organic molecular system can extend up to 2-3 nm and hence, for higher thicknesses of C$_{60}$ a minor change in anisotropy is possible [206]. In order to further understand the effect of spinterface formation on the magnetization reversal phenomena, we have performed magnetization relaxation measurements for all the samples.

### 6.3.3 Magnetization relaxation measurements:

Magnetization relaxation measurement demonstrates the potential of thermal energy to complete a reversal process via domain nucleation and DW motion events. Here, first, the sample is saturated by applying a high magnetic field (-$H_S$) and then the field is reduced to a positive sub-coercive field value (+0.99$H_c$). At this constant field, we have captured all the domain images until the completion of the reversal process. Further, the intensity of the domain images is plotted w.r.t. the time taken to complete the reversal. Fig. 6.3 shows the relaxation data measured at 0.99$H_c$ for all the samples and fitted by the compressed exponential function written as [172],

$$I(t) = I_1 + I_2 \left( 1 - \exp\left( -\left(\frac{t}{\tau}\right)^{\beta} \right) \right) \tag{6.2}$$

where, $I(t)$ is the measured Kerr intensity at time $t$, $I_1 + I_2$ is the normalized Kerr intensity, $\tau$ is the relaxation time constant, and $\beta$ is an exponent that can obtain any value between 1 to 3. Values of $\tau$ and $\beta$ are extracted by fitting the relaxation data with equation 6.2. A faster relaxation process is observed for sample S2 ($\tau = 12.70 \pm 0.13$ s) and S3 ($\tau = 10.50 \pm 0.20$ s) in comparison to sample S1 ($\tau = 19.70 \pm 0.21$ s). For sample S2 as the fullerene layer is very thin, it forms an intermixed layer of Co-C$_{60}$-Pd rather than a continuous layer of C$_{60}$, leading to a decrease in domain size and increase in domain nucleation density. This increased domain nucleation density helps to achieve a faster relaxation in sample S2 in comparison to sample
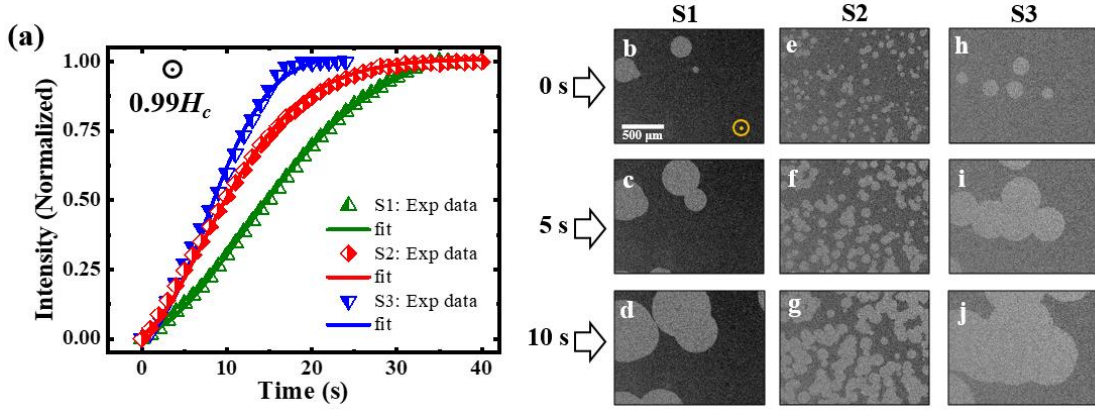
Figure 6.3 (a) Relaxation measurements performed at $0.99H_c$ field value for samples S1, S2, and S3. The solid lines represent the best fit by the compressed exponential function. The domain images captured during the thermal relaxation process at different time intervals (0, 5, and 10 seconds) is shown for sample S1 (b-d), S2 (e-g), and S3 (h-j). The scale bar shown in image b is 500 µm in length and applies to all the other domain images [208].

S1, as shown in Fig. 6.3. However, for sample S3, as the thickness of the fullerene layer is quite higher than the roughness, hence, it forms a continuous layer. The formation of a continuous fullerene layer and the spinterface at the Co/C$_{60}$ interface leads to a significant reduction in PMA which reduces the DW formation energy ($\sigma_{DW} = 2\pi\sqrt{AK}$) of the sample. This reduction in DW energy may induce a higher DW velocity and thus, initiates a faster relaxation mechanism for sample S3 in comparison to S1.

**6.3.4 Domain wall dynamics:** To unravel the impact of asymmetric Pd/Co/C$_{60}$ stack on the DW velocity of the samples, we have measured the pulsed field-induced DW velocity for all the samples in the creep region. Fig. 6.4 shows the DW velocity ($v_{DW}$) vs. field ($H_{OP}$) and $ln\,v_{DW}$ vs. $(H_{OP})^{-\frac{1}{4}}$ plot for all the samples. The experimental data is fitted by the creep law, as written below [79],

$$v_{DW} = v_0 \, exp\left[-\frac{U_c}{k_B T}\left(\frac{H_{OP}}{H_{dep}}\right)^{-\frac{1}{4}}\right] \tag{6.3}$$

and, the logarithm of the above equation can be expressed as:

$$ln(v_{DW}) = ln(v_0) - \frac{T_{dep}}{T}\left(\frac{H_{OP}}{H_{dep}}\right)^{-\frac{1}{4}} \tag{6.4}$$

The experimental data are fitted well with equations 6.3 and 6.4 which confirms that the DW lies in the creep region for all the samples. It is evident from Fig. 6.4 that at a constant magnetic field (say, $\sim$ 10mT) the DW velocity for sample S3 is considerably higher than the reference sample S1. A few possible explanations for this velocity increment could be as follows, lowering in depinning field ($H_{dep}$), reduction in effective PMA ($K_{eff}$), modified DW structure (from Bloch to Néel), and an enhanced DM interaction in Pd/Co/C$_{60}$ samples. The values of *ln* ($v_0$) and $\frac{T_{dep}}{T}\left(H_{dep}\right)^{\frac{1}{4}}$ are extracted by fitting the experimental data of Fig. 6.4 with equations 6.3 and 6.4. The extracted data are plotted in Fig. 6.2 (e-f). It is well known that the depinning field ($H_{dep}$) is strongly related to the defects present in a system and represents a local variation in an anisotropy landscape. Modification in local anisotropy is viable for systems with a hybridized interface (e.g., Co/C$_{60}$). For sample S2 formation of an intermixed Co-C$_{60}$-Pd layer affects the growth quality of the film, increases interfacial roughness, and modifies the anisotropy landscape locally. Therefore, when compared to sample S1, a higher domain nucleation density, smaller domain size, and comparable DW velocity were found for sample S2. However, for sample S3, the ratio of $\frac{T_{dep}}{T}\left(H_{dep}\right)^{\frac{1}{4}}$ is reduced from 10.56 (for sample S1) to 4.65 (for sample S3) which supports the observed two-order enhancement in DW velocity. Sample S3 does not form small-size bubble domains with high domain nucleation density, like sample S2. Further, for sample S3, a considerable decrease in PMA ($\sim$ 37%), aids in lowering the DW formation energy ($\sigma_{DW}$), which in turn helps to achieve a higher DW velocity. In
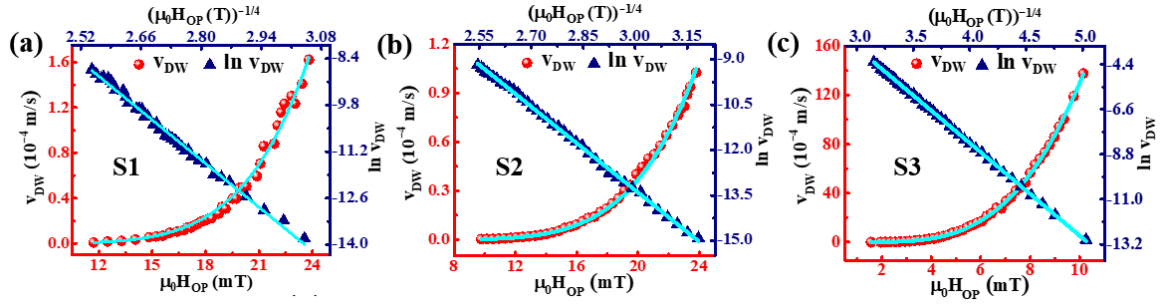
Figure 6.4 DW velocity ($v_{DW}$) vs. field ($\mu_0 H_{OP}$) and $\ln v_{DW}$ vs. $(\mu_0 H_{OP})^{-\frac{1}{4}}$ plots for samples (a) S1 (b) S2, and (c) S3. Here, $\mu_0 H_{OP}$ represents the pulsed magnetic field applied along the OP direction. The solid lines represent the best fits using equation 6.3 and 6.4 [208].

addition, the DMI strength is also found to increase from -0.077 (sample S1) to -0.46 mJ/m$^2$ (sample S3), which turns the Bloch wall into a Néel wall and supports the observed increase in DW velocity in sample S3. A detailed discussion of the DMI is given in the next section. Thus, the insertion of a continuous fullerene layer is found to play an important role in tailoring the DW velocity via tuning both PMA and DMI energy.

**6.3.5 Dzyaloshinskii-Moriya Interaction:** According to the Fert and Levy model, DM interaction originates at the interface of an HM/FM system as a consequence of broken inversion symmetry and the high SOC of HM. SOC in C-based materials is considered to be weak due to the low atomic number of C (*Z*=6). However, the SOC of fullerene is composed of two parts, (i) intrinsic SOC ($\Delta_{int}$), whose strength is small due to weak intra-atomic SOC of C, and (ii) curvature-driven SOC ($\Delta_{curv}$), whose strength can be large due to the hybridization between the adjacent $\pi$ and $\sigma$ bonds of C atoms in the buckyball structure. The $\pi$ electrons of C atoms do not contribute to SOC due to their quenched angular momentum whereas $\sigma$ electrons do contribute to SOC due to the overlapping of $\pi$ and $\sigma$ bonds by the curvature. Such curvature-enhanced SOC also could be a source to generate a finite DMI from the FM/C$_{60}$ interface. We have quantified the interfacial DMI strength emanating from the Co/C$_{60}$ interface

via the asymmetric domain expansion method (discussed earlier in Chapter 2) as proposed by Je *et al*. [91]. The DMI field ($H_{DMI}$) can be deduced from the $v_{DW}$ ($H_{IP}$) vs. $H_{IP}$ plot, where at a certain value of IP field the DW velocity become minimum. That particular IP field is a measure of the DMI field of a sample. As $H_{DMI}$ acts in the radially opposite direction of a DW surrounding a bubble, it either gets cancelled or enhanced under an IP bias field. A complete cancellation of the DMI field minimizes the DW velocity for one side of the wall (say, left DW) whereas enhances the velocity for the other side (say, right DW). In this work, we have measured $v_{DW}$ ($H_{IP}$) vs. $H_{IP}$ for all three samples at a constant applied OP field ($H_{OP}$) field as shown in Fig. 6.5. In this context, the earlier creep law is modified by incorporating the IP field dependency into the energy barrier scaling parameter. The modified creep law can be written as [91],

$$v_{DW}\ (H_{IP}) = v_0\ exp\ [-\xi(H_{OP})^{-1/4}] \tag{6.5}$$

where, $\xi$ is the modified energy barrier scaling parameter written as [91];

$$\xi = \xi_0 \left(\frac{\sigma(H_{IP})}{\sigma(0)}\right)^{-1/4} = \frac{T_{dep}}{T}\left(\mu_0 H_{dep}\right)^{\frac{1}{4}} \left(\frac{\sigma(H_{IP})}{\sigma(0)}\right)^{-1/4} \tag{6.6}$$

Where, $\xi_0$ depends on the pinning energy in the absence of an IP bias field. Thus, the IP field-dependent DW energy $\sigma(H_{IP})$ can be expressed as [91],

$$\sigma(H_{IP})_{\boldsymbol{B-N}} = \sigma(0) - \frac{\delta(\pi\mu_0 M_S)^2}{8K_D}(H_{IP} + H_{DMI})^2 \quad \text{for,} |H_{IP} + H_{DMI}| < \frac{4K_d}{\pi\mu_0 M_S}$$

$$\sigma(H_{IP})_{\boldsymbol{N}} = \sigma(0) + 2K_D\delta - \pi\delta\mu_0 M_S|H_{IP} + H_{DMI}|\ , \quad \text{otherwise} \tag{6.7}$$

where, $\sigma(0) = 2\pi\sqrt{AK_{eff}}$ is the pure Bloch wall energy, $\delta = \sqrt{A/K_{eff}}$ is the DW width and $K_D = t\ln(2)\mu_0 M_S^2/2\pi\delta$ is the DW anisotropy energy density. The velocity curve for sample S1 is very symmetric in nature (Fig. 6.5) owing to its low DMI strength. The DMI field ($H_{DMI}$) is extracted by fitting both the left and right velocity curves with equation 6.7 and the average
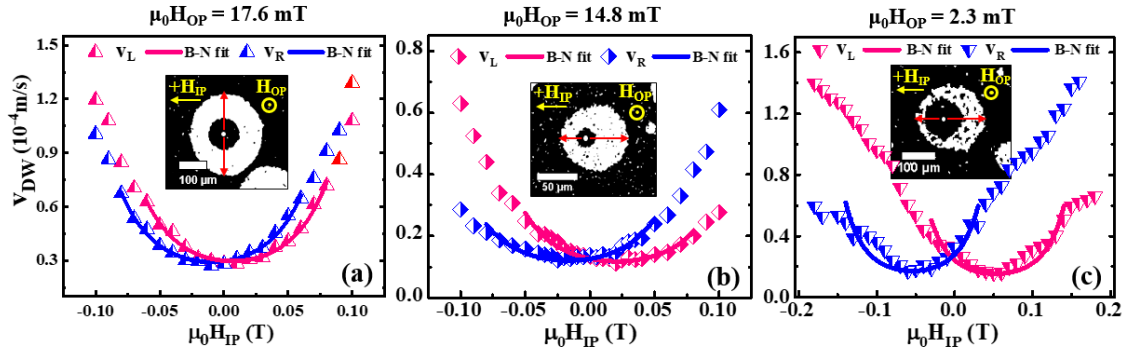
Figure 6.5 $v_L$ (pink) and $v_R$ (blue) represent the DW velocities along the left and right sides of the domains, plotted against the IP bias field ($\mu_0 H_{IP}$) at a constant OP field ($\mu_0 H_{OP}$) for samples (a) S1, (b) S2 and (c) S3. The solid lines represent the Bloch- Néel (B-N) fit of the curves by the modified creep law. The inset in each figure shows the direction of domain elongation w.r.t. $\mu_0 H_{IP}$. The scale bar for domains is shown in each figure separately [208].

$H_{DMI}$ value is used to measure the effective DMI strength using the following equation,

$$D_{eff} = \mu_0 H_{DMI} M_S \delta \tag{6.8}$$

where, $M_S$ is the saturation magnetization and $\delta = \sqrt{\frac{A}{K_{eff}}}$ is the DW width. A non-zero DMI field as found for sample S1 ($\mu_0 H_{DMI} \sim 8$mT), is due to the different interfacial roughness, strain, and growth conditions of the top and bottom Pd layers w.r.t. the Co layer. This generates a small DMI, ($D_{eff} = -0.077 \pm 0.015$ mJ/m$^2$) in the symmetric sample S1. Conversion of a Bloch wall into a Néel wall requires the presence of a critical DMI field ($H_{DMI}$) greater than the DW anisotropy field ($\frac{4K_d}{\pi M_S}$) of a sample. Here, as the DMI field ($\sim 8$mT) is lower than the critical DW anisotropy field ($\frac{4K_d}{\pi M_S} \sim 25$mT) for sample S1, it should form a Bloch wall structure.

For sample S2, the insertion of a C$_{60}$ layer shifted the velocity minimum and the average $\mu_0 H_{DMI}$ to ~19 mT (Fig. 6.5). This gives rise to an enhanced DMI strength (-0.174 $\pm$ 0.018 mJ/m$^2$) in sample S2. Here, the critical DW anisotropy field is quite comparable to the DMI

field of the sample which may support the formation of an intermediate Bloch- Néel wall. Further, for sample S3, the minima of the velocity curve shifted to ∼ 53 mT which further increased the DMI strength to -0.462 ± 0.013 mJ/m$^2$. Here, the critical DW anisotropy field (∼ 14mT) is found to be very small compared to the DMI field (∼ 53mT) of the sample, which favours the formation of a Néel wall in sample S3. The values of $\mu_0 H_{DMI}$, $D_{eff}$, and $\delta$ for all the samples are listed in Table 6.2. The negative sign of DMI found for the Pd/Co interface is consistent with the earlier reports for [Co/Pd]$_N$ stacks [214]. The chirality and type of DW for all the samples are further confirmed by measuring the displacement (*S*) of the DW along both the parallel (*x*) and transverse (*y*) directions of the applied IP field, as proposed by Kim et al. [137]. In this context, we evaluated two parameters $\varepsilon_1$ and $\varepsilon_2$ by measuring the DW displacement, as indicated in the inset of Fig. 6.5. The parameter $\varepsilon_1 (= \frac{S_x^+}{S_x^-})$ determines the chirality of DW, where $S_x^+$ and $S_x^-$ denote the displacement of the wall along $+H_x$ and $-H_x$ directions (parallel to IP field axis), respectively [215]. Here, $\varepsilon_1 < 1$ denotes the formation of a left-handed chiral wall, whereas, for $\varepsilon_1 > 1$, a right-handed DW is formed. The other parameter $\varepsilon_2 (= \frac{S_y}{S_x^M})$ determines the type of the wall (either Bloch or Néel), where $S_y$ denotes the elongation along the transverse *y*-axis and $S_x^M$ denotes the maximum elongation observed along the IP magnetic field axis (i.e. *x*-axis) [215]. For sample S1, we found $\varepsilon_2 > 1$, which confirms the formation of an achiral Bloch wall, whereas for samples S2 and S3, $\varepsilon_2 < 1$ confirms the formation of Néel wall. Conversion of a Bloch wall into a Néel wall requires the presence of a critical DMI field ($H_{DMI}$) greater than the DW anisotropy field ($\frac{4K_d}{\pi M_S}$) of the sample. As the DMI field of samples S2 and S3 are higher than their DW anisotropy field (discussed earlier), it helps to form a Néel wall. Thus, it gets reflected in the domain expansion and the value of $\varepsilon_2$ found to be < 1 for samples S2 and S3. To further investigate the chirality of samples S2 and S3 we have evaluated the parameter $\varepsilon_1$. As $\varepsilon_1$ is found to be < 1 for both

the samples, this signifies the formation of a left-handed chiral DW where $H_{DMI}$ acts in radially inward direction. The chirality of the walls is also shown in Fig. 6.7 (b-c).

Now, to quantify whether the Co/C$_{60}$ interface gives a non-zero DMI or not, we disentangle the DMI contribution originating from the bottom Pd/Co and top Co/C$_{60}$ interface (if any) in sample S3. In this context, we have prepared two control samples with structure, Si/Ta(10.0 nm)/ Pd(4.0 nm)/Co(0.5 nm)/Cu($t_{Cu}$ nm)/Pd(2.0 nm)/Ta(3.0 nm), where $t_{Cu}$ is taken as 2 and 5 nm. Here Cu is taken as a spacer layer due to its immiscibility with Co and low SOC which gives rise to a negligible or no DMI from the Co/Cu interface. In the work by F. Ajejas et al., the authors have shown experimentally that the Co/Cu interface originates no DMI owing to a negligible work function ($\Delta\phi \sim 6$ meV) assigned to this interface [216]. Hence, the effective DMI of a control sample can be assigned to the bottom Pd/Co interface considering no additive or subtractive DMI from the top Co/Cu interface. Then by comparing the DMI of Pd/Co/Cu with sample S3 (Pd/Co/C$_{60}$), one can find the DMI originating from the top Co/C$_{60}$ interface. IP field-dependent DW velocity measurements shown in Fig. 6.6 indicate a minimum of the velocity curve at 46 and 43 mT, for samples with 2 and 5 nm Cu spacer layers, respectively.
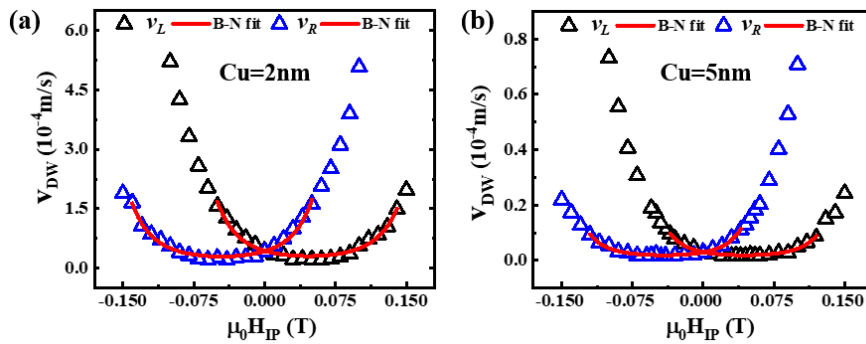


Figure 6.6 $v_L$ (black) and $v_R$ (blue) are plotted against $\mu_0 H_{IP}$, at a constant OP field ($\mu_0 H_{OP}$) for the control samples with (a) $t_{Cu}$ = 2.0 and (b) $t_{Cu}$ = 5.0nm. The red solid lines represent the B-N fit of the curves by the modified creep law [208].

Using these values we have calculated the effective DMI using equation 6.8. The effective DMI for the sample with 2nm of Cu spacer layer is found to be, $D_{eff} \sim$ -0.36 ± 0.01 mJ/m$^2$, where $\mu_0 H_{DMI}$ = 46 mT, $M_S$ = 1.30 MA/m, $\delta$ = 6.11 nm. Notably, a similar effective DMI ($D_{eff} \sim$ -0.35 ± 0.01 mJ/m$^2$) is found to be originating from the other control sample with 5nm of Cu spacer layer, where $\mu_0 H_{DMI}$ = 43 mT, $M_S$ = 1.36 MA/m, $\delta$ = 6.17 nm. Hence, the maximum iDMI originating from a Pd/Co/Cu sample will be within -0.35 ± 0.01 mJ/m$^2$. Thus comparing the DMI with sample S3, one can conclude that a non-zero DMI ($D_{Co/C_{60}} \sim$ -0.11 mJ/m$^2$) originates from the top Co/C$_{60}$ interface, due to the curvature-induced high SOC of fullerene [208]. In another work by Dong Li et al., the authors explored the Co/carbon interface and found no DMI associated with that interface [217]. In contrast, we have extracted a finite DMI from the Co/C$_{60}$ interface due to the enhanced SOC induced by the curved structure of the fullerene. A schematic illustration of DMI originating from sample S3 and the chirality of the DWs for both samples S1 and S3 is shown in Fig. 6.7. For the bottom Pd/Co interface, DMI ($D_{12}$) originated due to the interactions of the canted spins $S_1$ and $S_2$ of the Co layer with the Pd
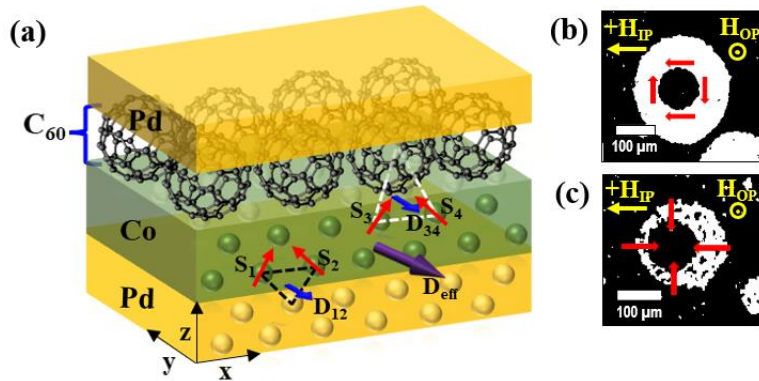


Figure 6.7 (a) Schematic demonstration of the effective DMI in Pd/Co/C$_{60}$ sample (S3), and the chirality of the domain walls for sample, (b) S1 (achiral Bloch) and (c) S3 (chiral Néel). Here the yellow and red arrows represent the directions of the applied IP field and the spins in DW, respectively [208].

atoms. Hence, the DMI vector $D_{12}$ acts along the -$y$ direction. Similarly, for the Co/C$_{60}$ interface, $D_{34}$ also acts along the same direction, giving rise to an additive effective DMI ($D_{eff}$) along the –$y$ axis. The sign of DMI for the Co/C$_{60}$ interface is found to be analogous to that of the Co/Graphene interface as reported earlier [26]. Thus, the enhanced DW velocity, increased DMI strength, and formation of chiral wall structure in the Pd/Co/C$_{60}$ samples prepared upon rigid Si substrate seems to have the potential for future spintronic device application. If the DW velocity and iDMI of such Pd/Co/C$_{60}$ samples are further enhanced, then C$_{60}$ may become a viable option for hosting chiral spin textures along with their long spin transport channels. Thus, we aim to tune the above-mentioned properties via strain engineering by depositing the Pd/Co/C$_{60}$ samples upon the flexible substrate, as discussed in the next section.

| Table 6.2 Parameters of the Pd/Co/C$_{60}$/Pd multi-layered samples (S1-S3) | | | | | | | | |
|---|---|---|---|---|---|---|---|---|
| Sample name | $\mu_0 H_C$ (mT) | $\tau$ (s) | $\mu_0 H_S$ (mT) | $M_s$ (MA/m) | $K_{eff}$ (MJ/m³) | $\delta = \sqrt{\dfrac{A}{K_{eff}}}$ (nm), $A$= 14 pJ/m | $\mu_0 H_{DMI}$ (mT) | $D_{eff} = \mu_0 H_{DMI} M_S \delta$ (mJ/m²) |
| S1 ($t_{C_{60}}$=0.0) | 15.98 | 19.70 ± 0.21 | 520 | 1.66 | 0.43 ± 0.010 | 5.69 ± 0.06 | 8.09 | -0.077±0.015 |
| S2 ($t_{C_{60}}$=0.8) | 10.70 | 12.70 ± 0.13 | 475 | 1.45 | 0.34 ± 0.007 | 6.42 ± 0.07 | 18.70 | -0.174±0.018 |
| S3 ($t_{C_{60}}$=1.6) | 3.12 | 10.50 ± 0.20 | 450 | 1.20 | 0.27 ± 0.006 | 7.21 ± 0.08 | 53.40 | -0.462±0.013 |

## 6.4 Strain-engineered magnetic properties of Pd/Co/C$_{60}$/Pd samples prepared upon flexible PI substrate:

A series of samples are prepared upon a flexible PI substrate by varying the thickness of the C$_{60}$ ($t_{C_{60}}$) layer. The sample structure is as follows, PI/Ta(20nm)/Pd(4nm)/Co(0.5nm)/C$_{60}$($t_{C_{60}}$ nm)/Pd(2nm)/Ta(3nm), where $t_{C_{60}}$= 0, 0.8 and 1.6nm. The deposition condition is kept the same as for the rigid Si-based samples mentioned in section 6.1. The magnetization reversal
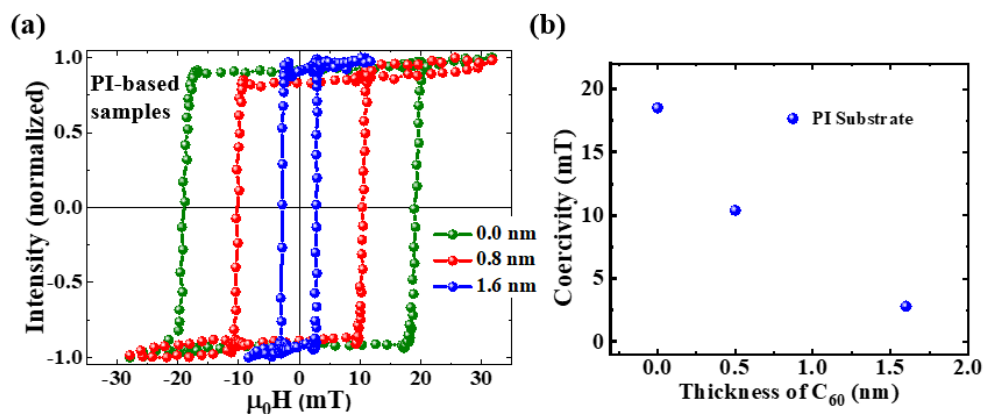
Figure 6.8 (a) Hysteresis loops of PI-based Pd/Co/C$_{60}$ samples for different thicknesses of C$_{60}$ layer measured using MOKE microscopy, (b) coercivity vs. thickness of C$_{60}$, for PI-based samples.

measurement is performed using MOKE microscopy in polar mode for all the samples. At the unstrained state of the samples, the hysteresis loops show a similar decrease in coercivity with increasing $t_{C_{60}}$(Fig. 6.8), as also observed earlier for the Si-based Pd/Co/C$_{60}$ samples. The strain-driven magnetization reversal for the reference PI-based Pd/Co(0.5nm)/Pd sample is discussed earlier in Chapter 4. There, the application of ~1.0% strain changes the coercivity of the sample by ~50%. Thus, here we will mainly discuss the impact of strain application on the magnetic properties of the PI-based Pd/Co/C$_{60}$ sample with a 1.60 nm thick C$_{60}$ layer. Magnetization reversal is measured by varying the strain within ~ ±1.0% strain. To generate strain sample is mounted on molds having ~4 mm height. As the hysteresis was measured when the sample was on a mold, the values of coercivity shown in Fig. 6.9 (a) and (b) are different. Fig. 6.9 (b) represents the actual values of coercivity by subtracting the extra field added due to the height of the mold. The coercivity of the sample in the unstrained state was ~ 2.8mT, which increases (decreases) systematically with increasing tensile (compressive) strain, as shown in Fig. 6.9. The maximum modification in coercivity under ~1.0% strain was ~40%. Thus, in comparison to the reference sample Pd/Co(0.5nm)/Pd sample ($t_{C_{60}}$= 0nm), the

asymmetric Pd/Co(0.5nm)/C$_{60}$(1.6nm) sample shows a lower strain-sensitivity. As the bottom Pd/Co interface remains the same for both the samples and only the top Co/non-magnet interface gets modified, the formation of the Co/C$_{60}$ hybridized interface might play a crucial role here. Till now it is well understood that the application of strain introduces a magnetoelastic anisotropy in the system, which depends on the magnetostrictive coefficient ($\lambda$) of a sample. A few earlier reports show that interfacial hybridization plays a crucial role in determining $\lambda$ for a multilayered thin film [177]. Thus, in the case of a Pd/Co/C$_{60}$ system, the formation of spinterface via *p-d* hybridization at the Co/C$_{60}$ interface might modify the strength of $\lambda$. This, in turn, may modify the impact of strain application in the asymmetric magnetic stacks. A detailed theoretical investigation may shed more light on this aspect. Further, we have measured the field-induced DW velocity at both the unstrained and ~ 0.13% compressive strained state of the flexible Pd/Co/C$_{60}$ sample via MOKE microscopy, as shown in Fig. 6.10. The experimental data are fitted by the creep law as written in equations 6.3 and 6.4. The fitting of the experimental data confirms that the DW lies in the creep region within the range of the applied field. As depicted in Fig. 6.10 (a) at a constant applied field (~ 14 mT), the DW velocity under compressive strain is ~ 2 times higher than its unstrained state. To understand the origin of such behaviour, we have further extracted the values of $\frac{T_{dep}}{T}\left(H_{dep}\right)^{\frac{1}{4}}$ from the fitting of the experimental data using equations 6.3 and 6.4. At the unstrained state, the ratio of $\frac{T_{dep}}{T}\left(H_{dep}\right)^{\frac{1}{4}}$ is found to be 6.73 for the flexible sample. The value of $\frac{T_{dep}}{T}\left(H_{dep}\right)^{\frac{1}{4}}$ for its Si-based counterpart was ~4.7. As the product of the depinning field and depinning temperature for the flexible sample is higher than the Si counterpart, the DW velocity in the flexible sample is lower than the Si counterpart. As PI substrate has a higher roughness than Si, it affects the growth quality of the flexible magnetic film and increases the depinning field and depinning temperature. The application of compressive strain slightly reduced the ratio of $\frac{T_{dep}}{T}\left(H_{dep}\right)^{\frac{1}{4}}$ to
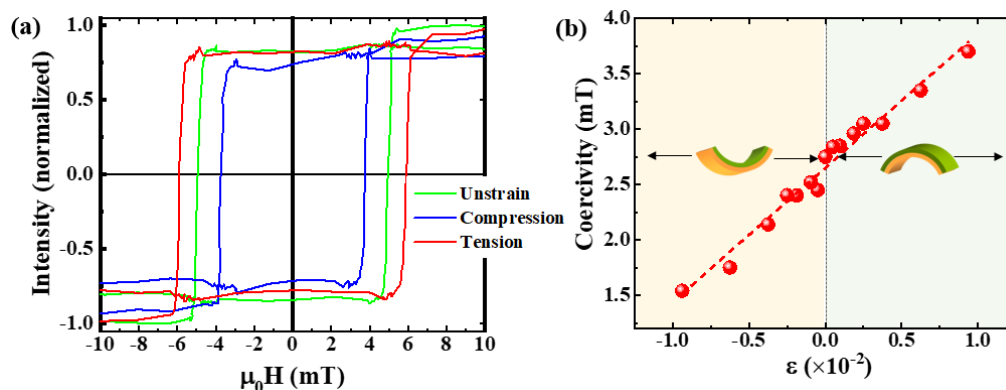
Figure 6.9 (a) Hysteresis loops measured at unstrained and $\sim \pm 1.0\%$ strained state of flexible Pd/Co/C$_{60}$ (1.6nm) sample using polar-MOKE microscopy, (b) coercivity vs. strain plot for the Pd/Co/C$_{60}$ (1.6nm) sample.

6.68. This reduced depinning parameters and reduced PMA help to double the DW velocity under compressive strain. Similar to the magnetization reversal measurement, here a smaller impact of applied strain is also evident on the DW velocity. Further, we performed DMI measurement in order to investigate if any enhancement of DMI is also responsible for the observed increment in DW velocity under compressive strain. In this context, we have tried to measure the asymmetric domain expansion in the presence of both IP and OP fields. However, the asymmetric expansion could not be measured for the higher values of the applied IP field. The domains merged with each other in the presence of a high IP field which limits us to measure the minima of the velocity curve and hence, the DMI of our sample. Thus, we further aim to perform Brillouin light scattering (BLS) spectroscopy measurements to directly quantify the DMI strength of the Pd/Co/C$_{60}$ sample in the presence and absence of strain. The BLS measurements are performed at CNR-IOM Perugia, Italy. BLS experiments generally require $\sim 200$mW of monochromatic laser light to be focused on the sample. Thus, to avoid sample damage usually a substrate (semiconductor or metallic) with high thermal conductivity is necessary. As the flexible substrate was coated by ~30 nm metallic layer we tried to perform
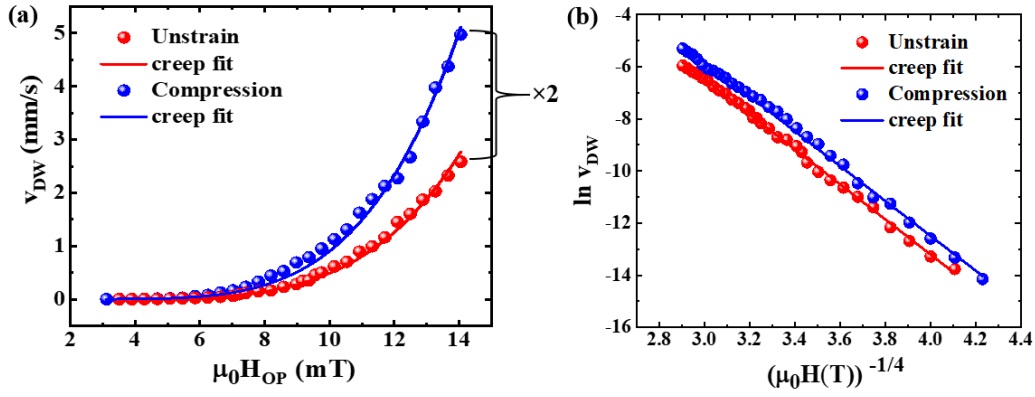
Figure 6.10 Pulsed magnetic field induced DW velocity measured for flexible Pd/Co/C$_{60}$ sample using MOKE microscopy, (a) $v_{DW}$ vs. $\mu_0 H_{OP}$, and (b) $ln\, v_{DW}$ vs. $(\mu_0 H_{OP})^{-1/4}$ at unstrained and compressive strained states of the sample.

the BLS experiments on this sample. However, the PI substrate could not withstand such high laser power owing to its very low thermal conductivity. Further, performing BLS measurements at a very low laser power increases the data acquisition time significantly, and thus, we could not measure the DMI strength under strain also via this method. Thus, for flexible PI-based samples, the DMI measurements were quite difficult, and hence, in the next chapter, we tried to qualitatively determine the impact of applied strain on the DMI strength using micromagnetic simulations.

In summary, a systematic investigation is conducted in Chapter 6 to comprehend the impact of the Co/fullerene interface on the magnetization reversal, DW dynamics, and DMI of a Pd/Co/C$_{60}$ system. A continuous decrease in coercivity with increasing C$_{60}$ thickness is corroborated by a reduction in the effective PMA of the samples. Further, the significant enhancement in the magnetization relaxation mechanism is attributed to a decrease in the depinning field and an increase in DW velocity upon C$_{60}$ insertion. Notably, DW structure also changes from achiral Bloch ($t_{C_{60}} = 0$ nm) to left-handed chiral NW ($t_{C_{60}} = 1.6$ nm) owing to an enhancement in iDMI from -0.07 mJ/m$^2$ ($t_{C_{60}} = 0$nm) to -0.46 mJ/m$^2$ ($t_{C_{60}} = 1.6$ nm) in the Si-

based asymmetric Pd/Co/C$_{60}$ samples. The signature of a non-zero DMI ($D_{Co/C_{60}} \sim$ -110 µJ/m$^2$) emanating from the Co/C$_{60}$ interface is the result of a curvature-driven SOC of fullerene molecule. Thus, the emergence of DM interaction from the Co/fullerene interface is quite appealing for both the fundamental study as well as the chiral structure-based application viewpoint. Further, we aim to study the magnetic properties of asymmetric Pd/Co/C$_{60}$ sample at strained conditions. Notably, the impact of applied strain was found to be lower on the asymmetric stack in comparison to its symmetric counterpart. This could be due to a modified magnetostrictive co-efficient in the asymmetric sample owing to the interfacial hybridization at the Co/C$_{60}$ interface. We anticipate that our findings will spur the development of theoretical modelling to clarify the exact role of fullerene molecules in originating DM interaction and modifying the magnetostrictive coefficient in the Pd/Co/C$_{60}$ samples.

## Chapter 7: Strain-driven magnetic properties of symmetric [Co/Pd]$_N$ multilayer stack

The effect of external strain on the iDMI could not be measured experimentally in Chapter 6 due to many limitations. Apart from experiments, the DMI strength of a sample is also possible to extract qualitatively via simulation, as reported in a few earlier works [214,218,219]. The experimentally obtained domains and hysteresis loops can be simulated to qualitatively measure the DMI strength of a sample. In this context, the superlattice stacks, e.g., [Co/Pt]$_N$, [Co/Pd]$_N$, etc. show a major variation in the loop shape with increasing N [214,220–223]. As the no. of bilayer increases it introduces a high magnetostatic energy in the system. In addition, for [Co/Pd]$_N$ stacks, a systematic increase in DMI strength is also reported by increasing N [214,223]. Thus, a competition between PMA, DMI, and magnetostatic energies changes the hysteresis loop shape from a square to a slanted one. In addition, the bubble domains also get modified to stripe domains. Moreover, the enhanced dipolar energy may demagnetize the superlattice stack and stabilize skyrmions even if the strength of DMI is low. Thus, such multilayered stacks are promising candidates for chiral DW-based device applications. To enhance the efficiency of spintronic devices it is important to have control over the PMA, DMI, and exchange energy. Among them controlling DMI is challenging as it is of interfacial nature. There are several approaches by which the DMI strength can be tailored, e.g., by changing the HM and FM layers [135,224], introducing a sub-monolayer capping of different materials at the FM/HM interface [208,218,225], by strain engineering [32,207], tuning the interface properties (say, roughness, sharpness) [226], etc. A few recent reports show that the application of strain can tune the DMI strength significantly and may generate chiral textures, which is very promising from application viewpoint [32,207,227–229]. Therefore, in this context, we have also prepared the multilayer stack of [Co/Pd]$_N$ upon both rigid Si and flexible PI substrate and studied their magnetic properties in detail. Further, the hysteresis loops are simulated using

MuMaX3 software to investigate the effect of strain on both the PMA and DMI strength of the samples.

**7.1 Sample details:** A series of [Co/Pd]$_N$ samples are prepared upon both rigid Si and flexible PI substrate by varying N. The sample structure is as follows, Substrate/Ta(20)/Pd(4)/ [Co(0.8)/Pd(1.8)]$_N$/Ta(5), where the numbers mentioned in parentheses are the thicknesses in nm and N = 1, 3, 5, 10. A schematic of the deposited sample structure is shown in Fig. 7.1. The samples are prepared via the DC magnetron sputtering technique in a high vacuum multi-deposition unit manufactured by Mantis Deposition Ltd. UK. Before deposition the base pressure of the chamber was ~ $5 \times 10^{-8}$ mbar. Deposition rates for Ta, Pd, and Co layers are maintained at 0.18 Å/s, 0.20 Å/s, and 0.16 Å/s, respectively. A QCM monitored the thickness of each layer during sample preparation. To achieve uniformity in the deposited layers the substrate is rotated at 10 rpm during sample fabrication.
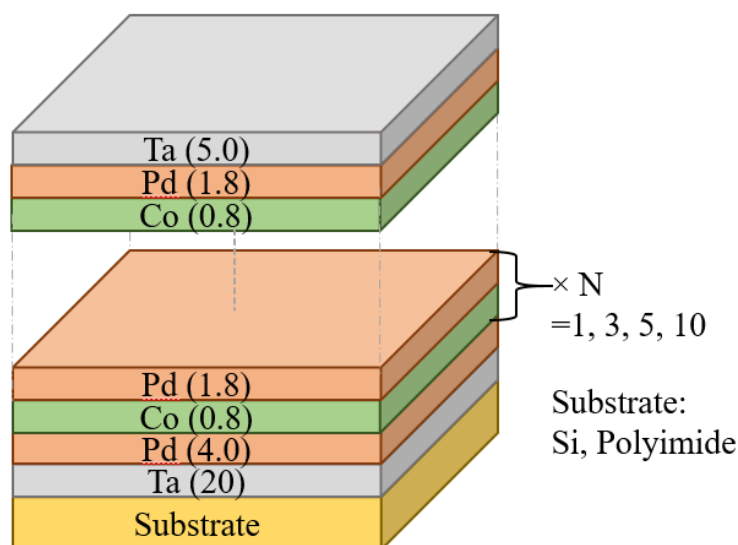


Figure 7.1 A schematic of the [Co/Pd]$_N$ multilayer structure deposited by the DC magnetron sputtering technique upon both the rigid Si and flexible PI substrates.

**7.2 Magnetic Characterization:**

**7.2.1 Magnetization reversal phenomena:** Magnetization reversal phenomena are first studied for the rigid Si-based samples using magneto-optic Kerr effect (MOKE) based microscopy in the polar mode. Figure 7.2 (a) shows the hysteresis loops and simultaneous domain images with increasing N. The coercivity of the samples increases systematically with increasing the bilayer repetition up to 5. However, no significant changes in coercivity is observed for the N=10 repetition sample. Such enhancement in coercivity is possibly related to an increase in magnetic anisotropy strength while increasing N. Further, a more detailed investigation reveals that with increasing N the tail-like feature becomes more pronounced. Such a tail-like feature arises probably due to an enhanced inter-layer magneto-static interaction in the stacks, as reported earlier [214,219,220,222]. Such long tails also indicate the formation of highly stable domain states which require a higher field to change their spin configuration from one saturation state to the other. Such highly stable domains could be associated with a higher DMI strength due to increasing N. To understand the impact of N on the domain shape and size, Fig. 7.2 (b) shows the domain images that are captured near the co-
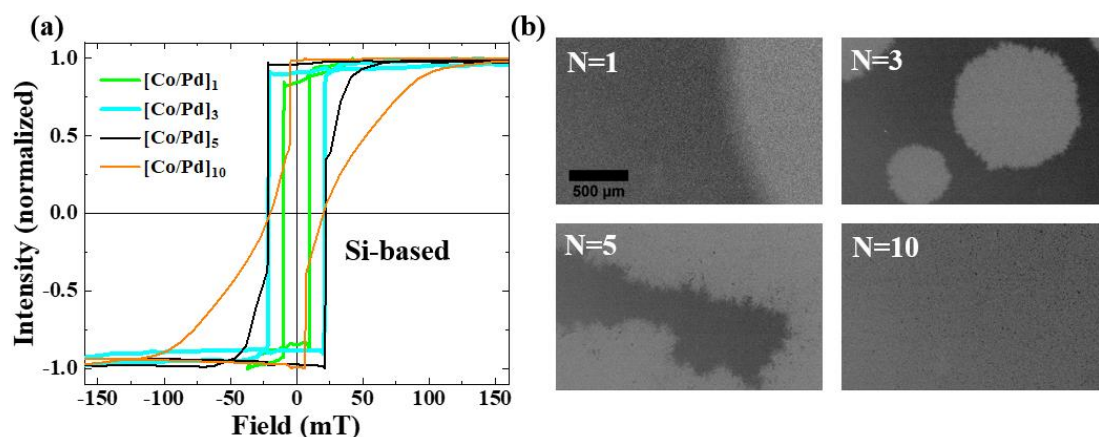


Figure 7.2 (a) Hysteresis loops of Si-based [Co/Pd]$_N$ stack measured by polar MOKE microscopy, (b) domain images captured near coercivity of each hysteresis loops where the scale bar shown in N=1 image is 500 μm in length and is valid for all the other images.

ercivity of each hysteresis loop. Bubble domains are observed for both the 1 and 3-repetition

samples as the anisotropy ratio $Q = \frac{K_u}{K_d} \gg 1$, where $K_u$ is the uniaxial anisotropy constant and

$K_d$ is the stray field energy constant [163]. For the N=10 repetition sample, magnetization

reversal is found to be governed by one sharp and another tail-like transition state, as shown in

Fig. 7.3 (a). The domain nucleation and propagation events are mainly observed along the sharp

transition region, whereas domain rotation events are quite dominating along the tail of the

hysteresis loop. Such lengthy tails could be related to the creation of very stable domain states

that require a stronger field to alter their spin configuration from one saturation state to another.

The domain images correspond to the points that are marked in the hysteresis loop of Fig. 7.3

(a). Here, the domains look quite similar to the dendritic-type domains, with a significant

reduction in size, as shown in Fig. 7.3 (b). To understand the relation between increasing N

and the domain size, Sbiaa *et al.* considered the impact of both inter and intra-layer

magnetostatic interaction on the DW width and found that the DW width decreases

exponentially with increasing no. of repetition [222]. An increased magnetostatic interaction

will modify the anisotropy ratio $\left( = \frac{K_U}{K_d} \right)$, which in turn may change the domain shape. Thus, in
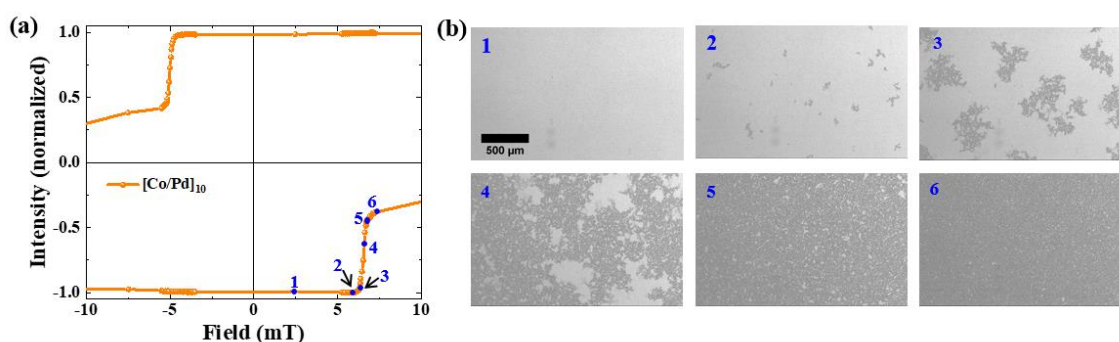


Figure 7.3 (a) Zoom-in view of the hysteresis loop of Si-based [Co/Pd]$_{10}$ sample, (b) domain

images correspond to the points marked in the hysteresis loop. The scale bar is 500 μm in

length and is valid for all the other images.

our case we also observed a significant modification in domain shape and size with increasing the repetition of the bilayers.

**7.2.2 Magnetic anisotropy:** To explore the origin behind the systematic enhancement of coercivity with increasing N, we have measured the magnetic anisotropy of Si-based samples using SQUID magnetometry. *M-H* loops are measured along both the IP and OP directions of the sample. The effective anisotropy is calculated using the following equation,

$$K_{eff} = \frac{1}{2}\mu_0 H_S M_S \qquad (7.1)$$

where, *μ₀H$_S$* is the IP saturation field and *M$_s$* is the saturation magnetization. With increasing N, the anisotropy field increases which in turn enhances the PMA strength. However, the *M$_s$* is found to have no systematic variation with N. Fig. 7.4 shows the variation in $K_{eff}$, $\mu_0 H_S$ and *M$_s$* with increasing N. A modification in PMA strength by varying N was also reported earlier due to an increase in magnetic volume in the samples. In our case, the enhanced PMA possibly increases the coercivity in the samples. In addition, an increase in bilayer repetition may increase the interface roughness which also may participate in modulating the coercivity of the samples.
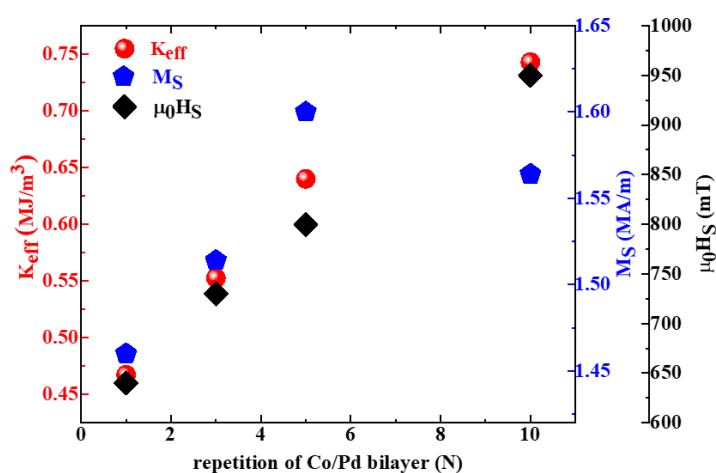


Figure 7.4 Variation of magnetic anisotropy (*K$_{eff}$*), saturation magnetization (*M$_s$*) and saturation field (*H$_S$*) with increasing the repetition (N) of [Co/Pd] bilayer.

**7.2.3 Strain-assisted magnetization reversal:** To understand the impact of bending-induced strain on the magnetization reversal phenomena of flexible [Co/Pd]$_N$ stacks, we have first measured the hysteresis loops and simultaneous domain images at the unstrained states of all the samples, as shown in Fig. 7.5. Similar to the Si counterparts, here also a systematic increase in coercivity, decrease in domain size, and modification in domain shape is observed with increasing N. Further, to understand the strain-sensitivity of the samples by varying N, we studied the magnetization reversal phenomena of the flexible samples at varied strained states. The coercivity vs. strain plot is shown in Fig. 7.6 for all the flexible samples. Similar to our previous observations, the tensile strain increases the coercivity whereas compressive strain decreases it for all the multilayer stacks. This can be explained by the magnetoelastic anisotropy induced by the applied strain in the system. Notably, a small plateau region was observed for the N=1 repetition (Fig. 7.6), owing to the smaller strength of the MEA. For N=1 repetition sample, a strain-sensitivity is observed only when the applied strain reaches ~0.10%.
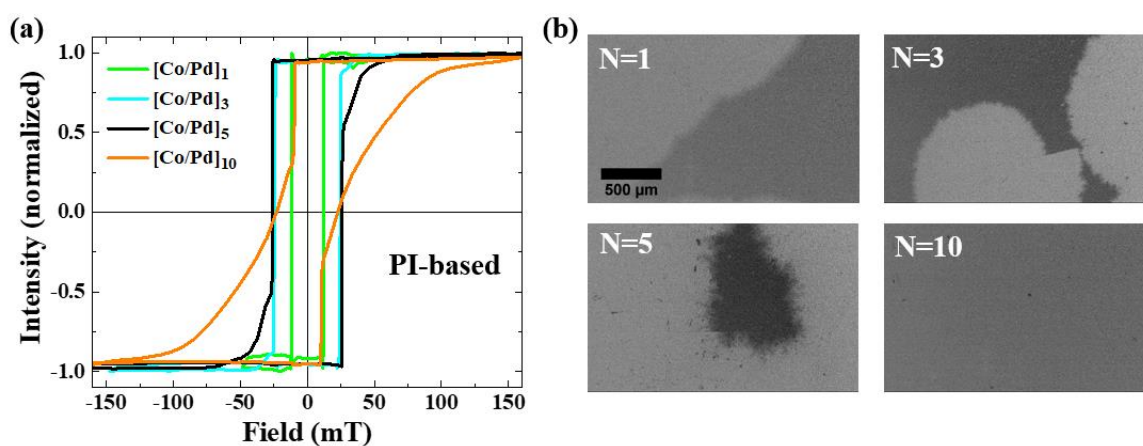


Figure 7.5 (a) Hysteresis loops of PI-based [Co/Pd]$_N$ multilayered stack measured by polar MOKE microscopy, (b) domain images captured near coercivity of each hysteresis loop, where the scale bar shown in N=1 image is 500 μm in length and is valid for all the other images.
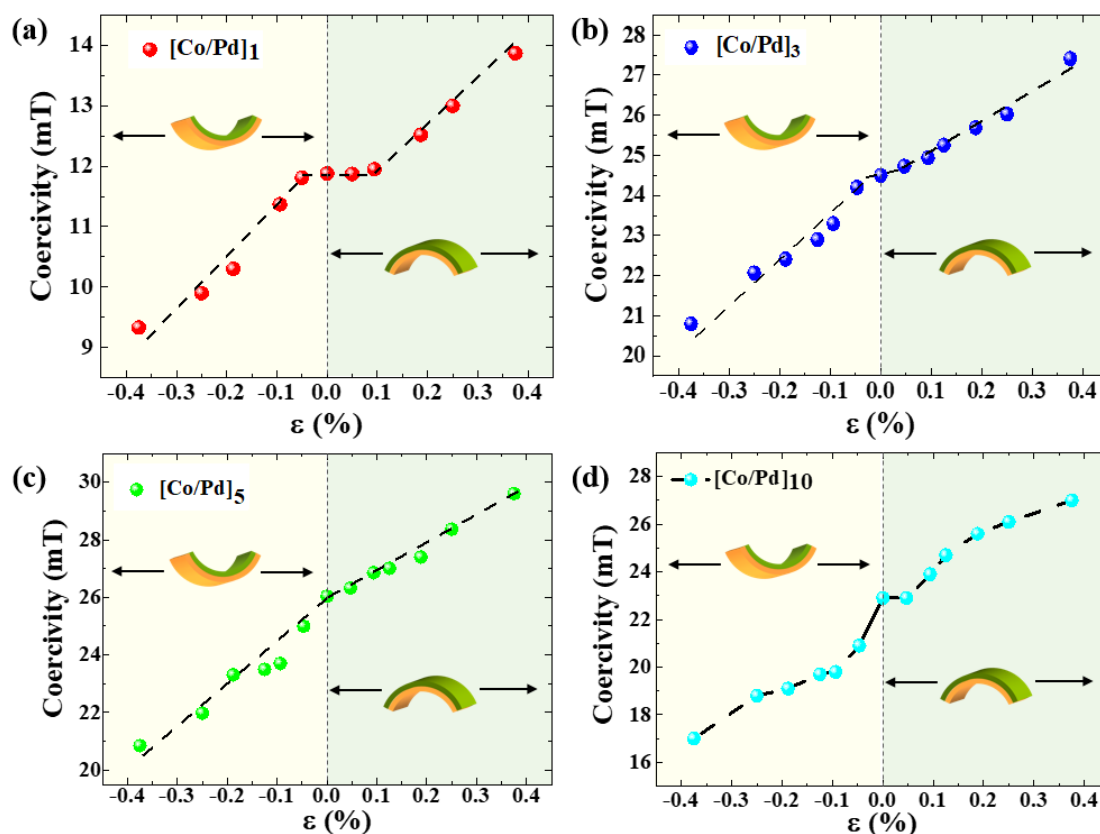
Figure 7.6 Coercivity vs. strain plot for the multilayer samples having Co/Pd bilayer repetition (a) N=1, (b) N=3, (c) N=5, and (d) N=10.

However, for N ≥ 3, all the samples show strain- sensitivity even at ~0.05% strain (Fig. 7.6). This indicates a better strain sensitivity by using the multilayer stacks and could be promising for sensor applications. The enhanced strain sensitivity is possibly due to the interplay between several energy terms in the multilayer stacks, e.g., PMA, MEA, magnetostatic, and DMI energy. Here, the variation in coercivity is found to be quite linear with increasing strain for all the flexible samples. Further, a closer look at the hysteresis loops measured under tensile and compressive strain shows a few interesting features that are highlighted in Fig. 7.7. The magnetization reversal measured at the strained and unstrained states consists of mainly two parts, (i) a sharp reversal, and (ii) a long tail which saturates at higher fields. In the compressive (tensile) strained state, the length of the sharp switching line decreases (increases) in comparison to the unstrained state. Further, the length of the tail also increases under external
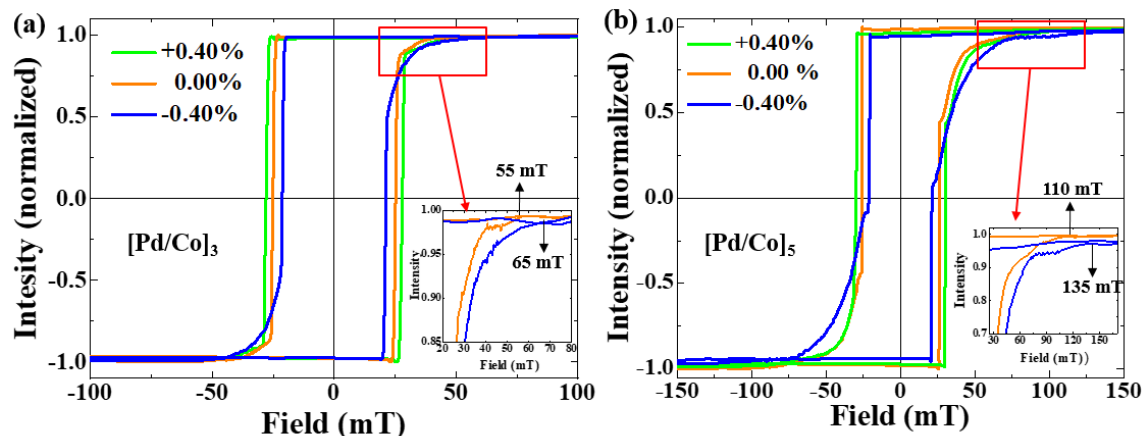
Figure 7.7 Hysteresis loops measured using the polar MOKE microscopy, at unstrained and strained states of Co/Pd samples with (a) N=3 and (b) N=5 repetition.

strain, as shown in the insets of figure 7.7. This indicates that apart from the coercivity, the overall magnetization reversal phenomena get significantly modified via strain. Here, the length of the tail of hysteresis loops depends on the contribution of both magnetostatic and DMI energies. Thus, apart from magnetic anisotropy, the applied strain seems to modify these energy values as well. Strain-dependent tuning of DMI has already been reported in a few experimental and theoretical works. However, the impact of applied strain on the interlayer magnetostatic interaction is not known yet. As the application of strain modifies the distance between the neighbouring atoms (Co-Co or Co-Pd), it, in turn, may modify the strength of DMI and magnetostatic interaction. In order to well understand the effect of PMA, magnetostatic energy, and DM interaction on the magnetization reversal process of the magnetic stacks in the absence and presence of external strain, we have performed micromagnetic simulations using MuMax3 software.

**7.3 Micromagnetic simulation using MuMax:**

MuMax is a micromagnetic simulation application developed and maintained at the DyNaMat group at Ghent University that runs on a GPU [230,231]. It employs a finite-difference discretization method to compute the space and time-dependent magnetization dynamics of nm to μm sized FMs. MuMax3 is a free and open-source software written in Go [232] and CUDA [233], that is distributed under the GPLv3 license. To write an input script, MuMax3 has a scripting language that is similar to a subset of the Go programming language. The software makes it easier to create quite sophisticated simulations. For the input and output of all space-dependent values, MuMax3 employs OOMMF's "OVF" data format. MuMax3 uses 2D or 3D grids of orthorhombic cells to discretize space using the finite difference (FD) approach. MuMax3 calculates the time-dependent change in reduced magnetization $\overrightarrow{m}$ $(\vec{r}, t)$, by solving the LLG equation as discussed earlier. It uses a few explicit Runge-Kutta (RK) techniques for solving the Landau Lifshitz equation, e.g., RK45, RK32, RK23 etc. To start a simulation a script is provided where all the necessary information is mentioned, e.g., grid size, cell size, boundary conditions, saturation magnetization, magnetic anisotropy, exchange interaction, applied field range, stopping criterion, etc. By using a relax () function MuMax3 tries to determine the minimum energy state of a system at each step of the simulation. Here, simulations can be performed at any temperature. In this chapter, MuMax3 is used to reproduce the experimentally obtained hysteresis loops. It further helps to understand the impact of external strain on different magnetic parameters. In addition, it also gives a qualitative idea about the strength of different interactions present in our systems.

**7.3.1 Micromagnetic simulations and the effective medium model:** Micromagnetic simulations are performed to mimic the experimentally obtained hysteresis loops using MuMax3 software [230,231]. As the magnetostatic energy increases with increasing the no. of Co/Pd bilayer, here we have used the effective medium model to simulate the experimentally

obtained hysteresis loops and domains, as described in ref. [224]. In this model, the multilayer stacks with $N$ repetition can be considered as a single layer having an effective thickness, $t_{eff} = (t_{Co} + t_{Pd})N$, where $t_{Co} = 0.8\ nm$, $t_{Pd} = 1.8\ nm$, and $N$ is no. of Co/Pd bilayers in the stack. To simulate the loops each input parameter is scaled by a factor $f$ which can be expressed as,

$$f = \frac{t_{Co}}{t_{Co} + t_{Pd}} = 0.307$$

where, $t_{Co}$ and $t_{Pd}$ are the thicknesses of the Co and Pd layers, respectively. The simulation area was 1.0μm × 1.0μm × ($N$2.6) nm. The cell size was 2.0nm × 2.0nm × ($N$2.6) nm. To exclude the finite size effects periodic boundary condition is considered in the *x-y* plane of the simulation area. To minimize the total energy of the system, a built-in function minimize () is used. The initial magnetization is considered along the out-of-plane direction and a relax () function is used to obtain the initial relaxed state. The exchange constant ($A_{ex}$) is considered as 20 pJ/m for all the samples. The saturation magnetization ($M_S$) and magnetic anisotropy ($K_U$) values used in the simulation are taken from the *M-H* loops measured via SQUID-VSM magnetometry. However, as the simulation area is far from the case of a real thin film, the experimentally obtained values of $K_U$ and $M_s$ are tuned a bit to match the loop shape. Further, the interfacial DMI value is also tuned to mimic the loop shape, as shown in Table 7.1[214,219]. In the experimental sample structure, the FM layer has a thickness $t_m$ (=0.8 nm), and the repetitive layer, [Pd (0.9nm)/Co (0.8nm)/Pd (0.9nm)] has a thickness $t_r$ (=2.6nm). Here, the thickness of the effective FM layer ($t_{m'}$) is considered to be the same as $t_r$, to obtain a homogeneously magnetic medium for the simulation. Thus, the saturation magnetization ($M_S$), effective magnetic anisotropy ($K_{eff}$), exchange constant ($A_{ex}$), and DMI strength ($D_{eff}$) related to the experimental film also should be the same in the effective medium. Woo et al. have concluded that the effective medium will follow the same magnetization dynamics as the
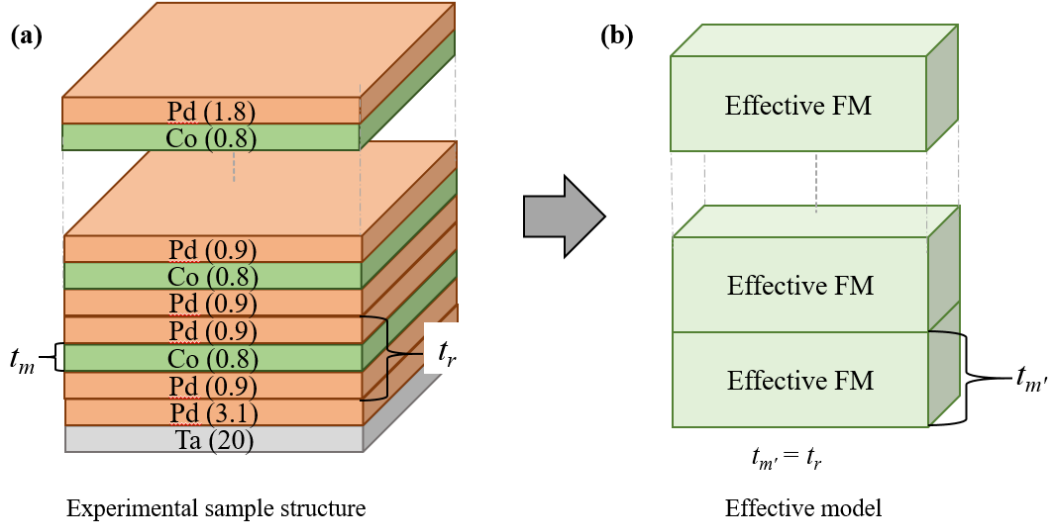
Figure 7.8 A schematic of the [Co/Pd]$_N$ multilayer structure, (a) experimentally prepared, and (b) considered in the simulation. Here, $t_m$ is the thickness (0.8nm) of the single FM layer, whereas $t_r$ is the thickness of one repetition of the Pd (0.9nm)/Co (0.8nm)/Pd (0.9nm) layer. This $t_r$ is considered as the thickness of the effective FM layer ($t_{m'}$) in the simulation.

experimental sample if the relevant parameters follow a scaling as mentioned below [224],

$$\frac{M_S'}{M_S} = \frac{A'}{A} = \frac{K_{eff}'}{K_{eff}} = \frac{D'}{D} = \frac{t_m}{t_m'} = \frac{t_m}{t_r} = f \tag{7.2}$$

which further scales the uniaxial anisotropy constant ($K_U$) as,

$$K_U' = K_U f - \frac{\mu_0 M_S^2}{2}(f - f^2) \tag{7.3}$$

The parameters with a prime as introduced in equations 7.2 and 7.3 are related to the effective medium. We have used a scaled value of the input parameters for simulating the experimentally obtained hysteresis loops. A uniform magnetization with one bubble domain is considered as the initial state for the simulations. The simulations revealed that the tail of the hysteresis loops is strongly dependent on the DMI strength of a sample. Thus, it helps to get a qualitative idea about the DMI values of our samples with increasing N. The best-fitted curves for all the samples are shown in Fig. 7.9. Corresponding DMI strength is also mentioned in each plot

separately. For [Co/Pd]$_1$ stack the best-fitted curve is obtained when the DMI is ~ 0.30 mJ/m$^2$. Although a symmetric Pd/Co/Pd sample is expected to show a zero DMI, the presence of interfacial strain and different growth conditions for the bottom and top Pd/Co interfaces may give rise to a non-zero DMI. From the simulation, it is found that with increasing $N$, the DMI also increases from 0.30 to ~1.15 mJ/m$^2$, to mimic the experimental loops well. A similar
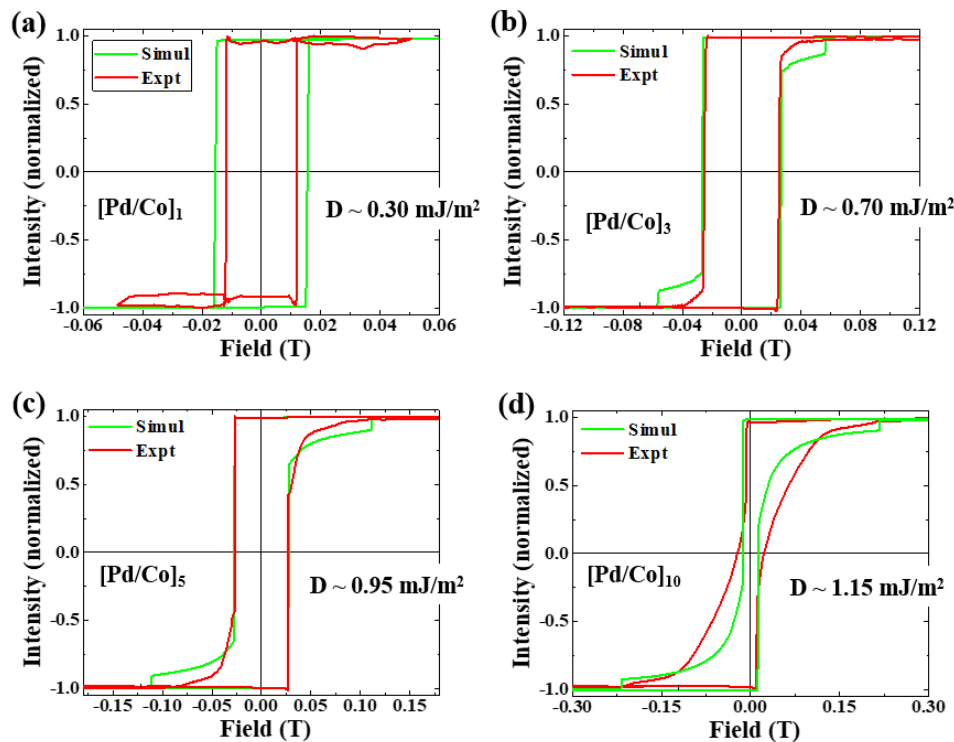


Figure 7.9 Simulated hysteresis loops using MuMax3 software for (a) [Co/Pd]$_1$, (b) [Co/Pd]$_3$, (c) [Co/Pd]$_5$, and (d) [Co/Pd]$_{10}$ samples. Here, the red curves are experimentally measured whereas the green curves are the simulated ones.

enhancement in DMI with N was also reported earlier by Pollard et al. and Davydenko et al. for [Co/Pd]$_N$ stacks [214,223]. The authors indicated that it could be related to an increase in the interfacial roughness of the samples with increasing N. It should be noted that the DMI values extracted from the simulations give only a qualitative measure of the parameter and will vary if measured experimentally. Further to understand the impact of external strain on the

| Table 7.1 Best fitted parameters for simulating hysteresis loops of [Co/Pd]$_N$ stacks | | | | |
|---|---|---|---|---|
| Sample | $A$ (pJ/m) | $M_s$ (MA/m) | $K_U$ (MJ/m$^3$) | $D_{eff}$ (varied) (mJ/m$^2$) |
| [Co/Pd]$_1$ | 20 | 1.59 | 1.84 | 0.30 |
| [Co/Pd]$_3$ | 20 | 1.50 | 1.89 | 0.70 |
| [Co/Pd]$_5$ | 20 | 1.47 | 2.17 | 0.95 |
| [Co/Pd]$_{10}$ | 20 | 1.35 | 2.42 | 1.15 |

magnetization reversal phenomena, we have simulated the hysteresis loops taken under ~0.40% compressive strain for the [Co/Pd]$_3$ sample. As strain may modify both the magnetic anisotropy and the DMI of a sample, we have varied the values of both $K_{eff}$ and $D_{eff}$ to mimic the experimentally obtained loop under strain. The switching field and the tail of the simulated hysteresis loop match well with the experimental one when $K_{eff} = 0.44$ MJ/m$^3$ and $D_{eff} = 0.85$ mJ/m$^2$ at the strained state (see Fig. 7.10). Notably, the values obtained at the unstrained state are, $K_{eff} = 0.49$ MJ/m$^3$ and $D_{eff} = 0.70$ mJ/m$^2$. This indicates that under compressive strain effective anisotropy of the sample decreases whereas the DMI strength increases. The decrement in anisotropy is due to the induced MEA under strain. However, the changes in DMI
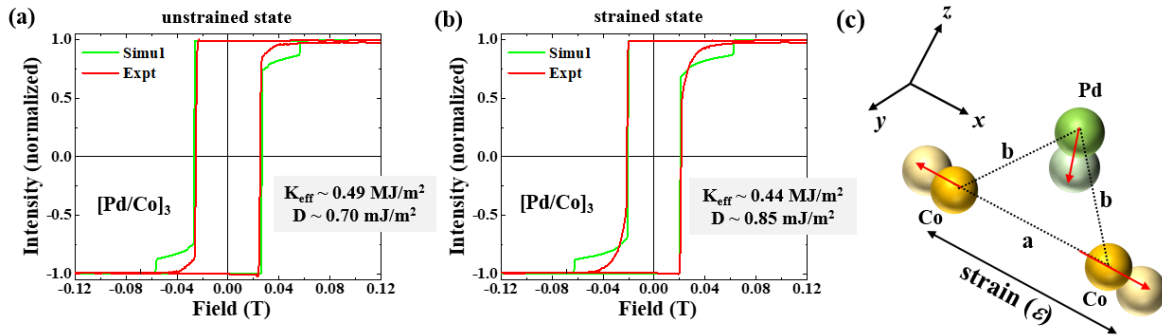


Figure 7.10 Hysteresis loops simulated for [Co/Pd]$_3$ sample at (a) unstrained and (b) strained states of the sample by varying the strength of $K_{eff}$ and $D$. The red and green curves represent the experimental and simulated hysteresis loops, respectively. (c) A schematic of the effect of external strain on the interatomic distance between HM and FM ions. The concept of the image is taken from ref. [32].

possibly due to a change in the distance between the adjacent atoms via strain. As the DM interaction is mediated via conduction electrons, it has an oscillatory nature and can be expressed as [32],

$$W_{DMI} \sim \sin[k_F\,(a + 2b) + \pi Z_d/10]\,\sin(2\theta)/(ab^2) \qquad (7.4)$$

where, $k_F$ is the Fermi momentum, $a$ is the distance between the FM (Co) ions, $b$ is the distance between the FM and HM ions (shown in Fig. 7.10 (c)), $Z_d$ is the number of $d$ electrons, and $\theta$ is the angle made by vectors connecting the HM ion and two FM ions. As shown in the schematic of Fig. 7.10 (c), the application of strain in the sample plane changes the distance $a$ between the FM (Co) ions, which in turn changes the distance $b$ between the FM and HM ions due to the Poisson effect. Such changes in $a$ and $b$ lead to a change in the DMI energy according to the Fert-Levy model. Apart from these a few other possibilities for the variation of DMI under strain could be, a variation in the effective mass of electrons and a variation in the exchange constant. However, earlier literature shows that the impact of these two mechanisms is quite small and thus the major reason behind DMI variation is related to the varying distance between the FM and HM ions.

In summary, the [Co/Pd]$_N$ stacks shows a systematic increase in coercivity, decrease in domain size, and shape with increasing N. This is corroborated to a modified PMA, magnetostatic and DMI energy in the samples. Further, the samples with N $\geq$ 3, shows a better strain sensitivity and more elongated tails in the hysteresis loops. Micromagnetic simulations are performed to reproduce the experimentally obtained hysteresis loops. By varying the strength of PMA and DMI, the hysteresis loops measured under bending-induced strains are reproduced. This indicates that the nature of loop change under strain could be associated to a modified anisotropy and DMI strength in the samples. Therefore, strain-engineering could be a promising tool to tune the anisotropy and DMI strength to optimize chiral structures for spintronic device applications.

**CHAPTER 8: Summary and Conclusion**

The rapid growth of "flexible electronics" has brought a paradigm shift in the concept of traditional rigid electronic equipment. Since spintronics will undoubtedly play a crucial role in the future of electronics, research on flexible spintronics is equally important. As spintronic devices rely largely on magnetic thin films, it is important to understand the basic properties of flexible magnetic thin films under different strained states. However, the field is in its infancy and requires a significant effort from both experimental and theoretical investigations. In this context, this thesis work has focused on preparing PMA thin films on flexible PI substrates (along with rigid substrates) and studying their structural and magnetic properties at different strained states. These PMA films have either symmetric (HM1/FM/HM1) or asymmetric (HM/FM/non-magnet) structures owing to their potential in future spintronic device applications. Here, Pt/Co/Pt and Pd/Co/Pd are considered as standard symmetric systems, whereas Pd/Co/$C_{60}$ is fabricated to study a unique asymmetric system. Here, $C_{60}$ (fullerene) is chosen due to its curvature-enhanced SOC strength and the rich physics associated with the "spinterface" formed at the FM/$C_{60}$ interface. In this thesis work, the samples are deposited by DC magnetron sputtering and thermal evaporation techniques. The structural characterizations are performed using an X-ray diffractometer and scanning electron microscopy. The magnetic characterizations are performed using magneto-optic Kerr effect (MOKE) based Kerr microscopy, and a superconducting quantum interference device (SQUID) magnetometer. Further, the DW velocity and the iDMI strength are measured using an in-house developed symmetric and asymmetric DW velocity measurement setup integrated with the Kerr microscope. To evaluate the element-specific orbital and spin magnetic moment, synchrotron-based X-ray magnetic circular dichroism (XMCD) measurements are performed at the ELETTRA synchrotron facility in Italy. The resistivity measurements are carried out using an in-house developed four-point probe setup at RT. Convex and concave-shaped molds are used

147

to study the structural and magnetic properties of the films under bending-induced strain. Additionally, micromagnetic simulations are carried out using the MuMax3 software to better understand the experimental data.

Currently, there are very few reports that concentrate on preparing flexible Pt/Co films and examining their characteristics in detail. In this context, the structural and magnetic properties of flexible Pt/Co film are studied systematically and discussed in the third chapter of the thesis. Here, Pt/Co/Pt film is deposited upon a flexible PI substrate (25 μm thick) and the impact of bending-induced tensile and compressive strains is studied thoroughly. No structural damage is observed within the applied range of bending strain. However, as the Pt/Co system has a non-zero magnetostriction coefficient ($\lambda \sim 10^{-5}$), the application of bending strain affects the magnetic properties of the sample. Due to the opposite nature of the tensile and compressive strains, an opposite tuning of magnetic characteristics is possible here. This provides the opportunity to control magnetic properties to the desired level via strain. Within the elastic limit of bending-induced strain the changes in the magnetic properties are reversible in nature. Notably, the magnetic anisotropy and DW dynamics are possible to be tuned quite well via the strain. This leads to a modified magnetization reversal and relaxation dynamics of the sample in the strained state. The observed sensitivity of magnetic properties towards external strain seems promising for various sensor-based devices applications.

Further, to improve the strain-sensitivity we have considered the Co/Pd system owing to its higher magnetostrictive coefficient ($\lambda \sim 10^{-4}$) in comparison to Co/Pt. Thus, a series of Co/Pd films are prepared upon flexible PI substrates, and their structural and magnetic properties are studied under bending-induced uniaxial strain, as discussed in the fourth chapter of the thesis. No significant deterioration of film surface quality is observed when the applied strain is below 1%. However, ~1.0% of compressive strain, few localized buckling appears owing to the large elastic mismatch between the inorganic film and the organic polymer substrate. Further, the

coercivity and relaxation time constant were enhanced (reduced) under tensile (compressive) strain, due to the stress anisotropy induced by the applied stress. This further modifies the DW dynamics and reduces (enhances) the DW velocity under tensile (compressive) strain, in comparison to the unstrained state of the sample. Such modified DW dynamics were found to be related to the modified PMA and pinning potential of the samples. Furthermore, the strain-dependent XMCD measurements revealed an enhanced orbital to spin magnetic moment ratio under both tensile and compressive strain, possibly due to a modified orbital momentum quenching via strain. As here the changes in $\frac{m_{orb}}{m_{spin}}$ is independent of the type of strain (whether tensile or compressive), it indicates the possibility of opposite modification in the DOS of the Co/Pd system, under the tensile and compressive strain. Further, the Co/Pd samples having thickness closer to the SRT region were found to have a better strain sensitivity. This allows to switch the magnetization orientation from the OP to the IP direction of the sample by applying a minimal compressive strain, which is indeed promising for energy-efficient switching applications.

Within the elastic limit of bending-induced uniaxial strain the magnetic properties are quite reversible in nature. However, the successful commercialization of flexible spintronic devices also requires to study the response of such systems under a larger complex strain. Significant multidimensional strain can be generated via wrinkling, twisting, or peeling a flexible film. Thus, in the fifth chapter of the thesis, we have presented the impact of peeling-induced strain on the structural and magnetic properties of both Co/Pt and Co/Pd films prepared on Kapton. Such peeling methods damage the thin film by forming numerous cracks, buckles, and telephone cord blisters to reduce the stress energy. This in turn enhanced the sample resistance and introduced irreversible changes in the magnetic properties. The magnetization reversal study indicates that the coercivity of the samples increases due to the structural discontinuities that appeared in the films. The bubble domains in the unstrained films even get converted to

elongated-shaped domains due to several hindrances to the DW motion after strain application. Further, relaxation measurements reveal that the thermal energy is even insufficient to switch the magnetization of a few areas due to the high pinning barriers associated with the damages. Notably, all the changes appeared due to the peeling strain are found to be irreversible in nature. This restricts one from applying a very high strain on the flexible films during their device applications.

As symmetric magnetic stacks (say, HM1/FM/HM1) lead to very low DMI, we have further prepared a unique asymmetric system comprised of Pd/Co/$C_{60}$. Here, $C_{60}$ is chosen to break the symmetry and also to explore the possibility of originating DMI from the FM/$C_{60}$ interface. In this context, Pd/Co/$C_{60}$ samples are prepared upon both rigid Si and flexible PI substrates and their structural and magnetic properties are studied in detail, as discussed in chapter 6. The DW velocity and iDMI are found to be enhanced for the Pd/Co/$C_{60}$ samples in comparison to the symmetric Pd/Co/Pd sample. Further, a non-zero iDMI originating from the Co/$C_{60}$ interface is reported for the first time due to the curvature-enhanced SOC of fullerene. This also motivates to use the C-based materials for chiral DW-based device applications. To find the strain-sensitivity of this asymmetric sample structure we have studied the impact of bending-induced strain. Here, the magnetization reversal and DW velocity are tuned via external strain, however, the impact of strain was lesser in comparison to the symmetric Pd/Co/Pd film. It may be associated with a reduced magnetostrictive coefficient due to the formation of a spinterface at the Co/$C_{60}$ interface. Future experimental and theoretical works may shed light on this aspect.

Apart from asymmetric magnetic stacks (HM/FM/non-magnet), the symmetric multilayer stacks of ([HM/FM]$_N$) also may host chiral textures via a proper balance of PMA, DMI, and dipolar energy. This is generally achieved by increasing the repetition (N) of HM/FM bilayers. However, the application of external strain also may create chiral textures in such systems by

proper tuning of the PMA, DMI, and dipolar energy. In this context, the multilayer [Co/Pd]$_N$ stack is deposited upon both rigid Si and flexible PI substrates, and their magnetic properties are studied in detail, as discussed in Chapter 7. With increasing N, the PMA and dipolar energy increased, which enhanced the coercivity and introduced a tail-like feature in the hysteresis loops. The domain size and shape are also modified with increasing N possibly due to the strong dipolar energy and enhanced iDMI strength in the samples, which in turn give a better stability of the domains. Further, the magnetization reversal phenomena are studied under strain and it indicates a better strain-sensitivity with increasing N. This indicates that other than PMA, the dipolar and DMI energy also may be tuned via strain. To understand these aspects qualitatively, micromagnetic simulations are performed using MuMax3 software. The simulation revealed that not only the strength of PMA but also the strength of iDMI increases with increasing N. Further, the application of strain may tune both the PMA and iDMI strength of the samples. The modulation of DMI via strain could be related to the modification in the distance between the neighbouring FM atoms and FM-HM atoms at the FM/HM interface, as per the Fert-Levy model. Therefore, strain engineering appears to be a promising tool to advance the field of flexible spintronics while tuning the functionalities of spintronic devices.

**Future Outlook:**

This thesis work shows the impact of bending and peeling mode-induced strain on the structural and magnetic properties of Pt/Co/Pt, Pd/Co/Pd, and Pd/Co/C$_{60}$ systems. In the due course of the study, we find a few questions that should be addressed in the future as mentioned below.

1. To validate the impact of tensile and compressive strains on the DOS of the Co/Pd and Co/Pt systems, theoretical work is needed. It may give further insight into the opposite impact of tensile and compressive strains on the magnetic properties.

2. Similar to Co/Pd system, magnetization switching via strain also should be explored for other FM/HM systems. This will be highly beneficial for low-energy spintronic device applications.

3. Apart from bending strain, the impact of wrinkling and twisting modes of flexibility also needs to be investigated in detail. It will help in understanding the limitations and suitability of a particular material system for flexible spintronic device applications.

4. Theoretical modelling is required to clarify the exact role of spherical fullerene molecules in exhibiting DM interaction from a fullerene/FM interface.

5. The impact of spinterface formation (at the $Co/C_{60}$ interface) on the magnetostrictive coefficient ($\lambda$) of Co should be studied both experimentally and theoretically. Other types of FM/organic semiconductor (OSC) systems may be studied to understand the impact of external strain on the spinterface to tune the global magnetic properties.

6. Measuring iDMI for samples prepared on polymer substrates faces several challenges. To remedy this, new flexible substrates or measurement methodologies must be considered.

7. The effect of strain on DMI should be explored more for designing chiral magnetic textures in flexible magnetic thin films/multilayers.

**References:**

[1]     R. L. Crabb and F. C. Treble, *Thin Silicon Solar Cells for Large Flexible Arrays*, Nature **213**, 5082 (1967).

[2]     D. Baran, D. Corzo, and G. Blazquez, *Flexible Electronics: Status, Challenges and Opportunities*, Frontiers in Electronics **1**, (2020).

[3]     H. Shirakawa, E. J. Louis, A. G. MacDiarmid, C. K. Chiang, and A. J. Heeger, *Synthesis of Electrically Conducting Organic Polymers: Halogen Derivatives of Polyacetylene, (CH)x*, J. Chem. Soc., Chem. Commun. 578 (1977).

[4]     H. Liu, D. Liu, J. Yang, H. Gao, and Y. Wu, *Flexible Electronics Based on Organic Semiconductors: From Patterned Assembly to Integrated Applications*, Small **19**, 2206938 (2023).

[5]     R. C. Chittick, J. H. Alexander, and H. F. Sterling, *The Preparation and Properties of Amorphous Silicon*, J. Electrochem. Soc. **116**, 77 (1969).

[6]     I.-C. Cheng and S. Wagner, *Overview of Flexible Electronics Technology*, in *Flexible Electronics: Materials and Applications*, edited by W. S. Wong and A. Salleo (Springer US, Boston, MA, 2009), pp. 1–28.

[7]     X. Chen and W. Mi, *Mechanically Tunable Magnetic and Electronic Transport Properties of Flexible Magnetic Films and Their Heterostructures for Spintronics*, J. Mater. Chem. C **9**, 9400 (2021).

[8]     X. Shi, M. Wu, Z. Lai, X. Li, P. Gao, and W. Mi, *Bending Strain-Tailored Magnetic and Electronic Transport Properties of Reactively Sputtered Γ'-Fe4N/Muscovite Epitaxial Heterostructures toward Flexible Spintronics*, ACS Appl. Mater. Interfaces **12**, 27394 (2020).

[9]     M. Guo et al., *A Flexible and High Temperature Tolerant Strain Sensor of La0.7Sr0.3MnO3/Mica*, Journal of Materials Science & Technology **44**, 42 (2020).

[10]    S. Zhao, Z. Zhou, C. Li, B. Peng, Z. Hu, and M. Liu, *Low-Voltage Control of (Co/Pt)x Perpendicular Magnetic Anisotropy Heterostructure for Flexible Spintronics*, ACS Nano **12**, 7167 (2018).

[11]    O. Lee, L. You, J. Jang, V. Subramanian, and S. Salahuddin, *Flexible Spin-Orbit Torque Devices*, Applied Physics Letters **107**, 252401 (2015).

[12]    M. Melzer, M. Kaltenbrunner, D. Makarov, D. Karnaushenko, D. Karnaushenko, T. Sekitani, T. Someya, and O. G. Schmidt, *Imperceptible Magnetoelectronics*, Nat Commun **6**, 1 (2015).

[13]    H. Matsumoto, S. Ota, A. Ando, and D. Chiba, *A Flexible Exchange-Biased Spin Valve for Sensing Strain Direction*, Applied Physics Letters **114**, 132401 (2019).

[14]    B. D. Cullity and C. D. Graham, *Magnetostriction and the Effects of Stress*, in *Introduction to Magnetic Materials* (John Wiley & Sons, Ltd, 2008), pp. 241–273.

[15]    H.-J. Kim et al., *Field-Free Switching of Magnetization by Tilting the Perpendicular Magnetic Anisotropy of Gd/Co Multilayers*, Advanced Functional Materials **32**, 2112561 (2022).

[16]    P. Sheng, B. Wang, and R. Li, *Flexible Magnetic Thin Films and Devices \**, J. Semicond. **39**, 011006 (2018).

[17]    F. Zighem and D. Faurie, *A Review on Nanostructured Thin Films on Flexible Substrates: Links between Strains and Magnetic Properties*, J. Phys.: Condens. Matter **33**, 233002 (2021).

[18]    B. Tudu and A. Tiwari, *Recent Developments in Perpendicular Magnetic Anisotropy Thin Films for Data Storage Applications*, Vacuum **146**, 329 (2017).

## References

[19]    B. Dieny and M. Chshiev, *Perpendicular Magnetic Anisotropy at Transition Metal/Oxide Interfaces and Applications*, Rev. Mod. Phys. **89**, 025008 (2017).

[20]    M. Mühlenhoff, Perpendicular Magnetic Anisotropy for Magnetoresistive Sensor Technologies, Doctoral Thesis, Augsburg University, 2021.

[21]    S. Ikeda, K. Miura, H. Yamamoto, K. Mizunuma, H. D. Gan, M. Endo, S. Kanai, J. Hayakawa, F. Matsukura, and H. Ohno, *A Perpendicular-Anisotropy CoFeB–MgO Magnetic Tunnel Junction*, Nature Mater **9**, 9 (2010).

[22]    A. Hrabec, N. A. Porter, A. Wells, M. J. Benitez, G. Burnell, S. McVitie, D. McGrouther, T. A. Moore, and C. H. Marrows, *Measuring and Tailoring the Dzyaloshinskii-Moriya Interaction in Perpendicularly Magnetized Thin Films*, Physical Review B **90**, 020402 (2014).

[23]    T. H. Pham et al., *Very Large Domain Wall Velocities in Pt/Co/GdOx and Pt/Co/Gd Trilayers with Dzyaloshinskii-Moriya Interaction*, EPL **113**, 6 (2016).

[24]    P. Agrawal, F. Büttner, I. Lemesh, S. Schlotter, and G. S. D. Beach, *Measurement of Interfacial Dzyaloshinskii-Moriya Interaction from Static Domain Imaging*, Phys. Rev. B **100**, 104430 (2019).

[25]    F. Ajejas, V. Křižáková, D. de Souza Chaves, J. Vogel, P. Perna, R. Guerrero, A. Gudin, J. Camarero, and S. Pizzini, *Tuning Domain Wall Velocity with Dzyaloshinskii-Moriya Interaction*, Applied Physics Letters **111**, 202402 (2017).

[26]    F. Ajejas et al., *Unraveling Dzyaloshinskii–Moriya Interaction and Chiral Nature of Graphene/Cobalt Interface*, Nano Lett. **18**, 5364 (2018).

[27]    H. Yang et al., *Significant Dzyaloshinskii–Moriya Interaction at Graphene–Ferromagnet Interfaces Due to the Rashba Effect*, Nature Mater **17**, 605 (2018).

[28]    D. Huertas-Hernando, F. Guinea, and A. Brataas, *Spin-Orbit Coupling in Curved Graphene, Fullerenes, Nanotubes, and Nanotube Caps*, Phys. Rev. B **74**, 155426 (2006).

[29]    S. Liang, R. Geng, B. Yang, W. Zhao, R. Chandra Subedi, X. Li, X. Han, and T. D. Nguyen, *Curvature-Enhanced Spin-Orbit Coupling and Spinterface Effect in Fullerene-Based Spin Valves*, Sci Rep **6**, 1 (2016).

[30]    S. Ota et al., *Strain-Induced Reversible Modulation of the Magnetic Anisotropy in Perpendicularly Magnetized Metals Deposited on a Flexible Substrate*, Appl. Phys. Express **9**, 043004 (2016).

[31]    E. Pandey, B. B. Singh, P. Sharangi, and S. Bedanta, *Strain Engineered Domain Structure and Their Relaxation in Perpendicularly Magnetized Co/Pt Deposited on Flexible Polyimide*, Nano Ex. **1**, 010037 (2020).

[32]    N. S. Gusev, A. V. Sadovnikov, S. A. Nikitov, M. V. Sapozhnikov, and O. G. Udalov, *Manipulation of the Dzyaloshinskii--Moriya Interaction in Co/Pt Multilayers with Strain*, Phys. Rev. Lett. **124**, 157202 (2020).

[33]    M. Hassan, S. Laureti, C. Rinaldi, F. Fagiani, S. Varotto, G. Barucca, N. Y. Schmidt, G. Varvaro, and M. Albrecht, *Perpendicularly Magnetized Co/Pd-Based Magneto-Resistive Heterostructures on Flexible Substrates*, Nanoscale Adv. **3**, 3076 (2021).

[34]    M. Hassan, S. Laureti, C. Rinaldi, F. Fagiani, G. Barucca, A. Gerardino, N. Schmidt, M. Fix, M. Albrecht, and G. Varvaro, *Co/Pd-Based Spin-Valves with Perpendicular Magnetic Anisotropy on Flexible Substrates. Direct Deposition vs Transfer-and-Bonding Approaches*, Applied Surface Science **635**, 157740 (2023).

[35]    M. Getzlaff, *Fundamentals of Magnetism* (Springer, Berlin, Heidelberg, 2006).

*References*

[36] B. D. Cullity and C. D. Graham, *Magnetic Anisotropy*, in *Introduction to Magnetic Materials* (John Wiley & Sons, Ltd, 2008), pp. 197–239.

[37] M. J. Dapino, *MAGNETOSTRICTIVE MATERIALS*, Encyclopedia of Smart Materials **2**, 600 (2002).

[38] N. B. Ekreem, A. G. Olabi, T. Prescott, A. Rafferty, and M. S. J. Hashmi, *An Overview of Magnetostriction, Its Use and Methods to Measure These Properties*, Journal of Materials Processing Technology **191**, 96 (2007).

[39] E. W. Lee, *Magnetostriction*, Science Progress (1933- ) **41**, 58 (1953).

[40] J. Luzar et al., *Zero-Magnetostriction Magnetically Soft High-Entropy Alloys in the AlCoFeNiCux (x = 0.6–3.0) System for Supersilent Applications*, Advanced Materials Interfaces **9**, 2201535 (2022).

[41] K. B. Hathaway and A. E. Clark, *Magnetostrictive Materials*, MRS Bull. **18**, 34 (1993).

[42] C. Kittel, *Physical Theory of Ferromagnetic Domains*, Rev. Mod. Phys. **21**, 541 (1949).

[43] F. J. A. den Broeder, W. Hoving, and P. J. H. Bloemen, *Magnetic Anisotropy of Multilayers*, Journal of Magnetism and Magnetic Materials **93**, 562 (1991).

[44] M. T. Johnson, P. J. H. Bloemen, F. J. A. den Broeder, and J. J. de Vries, *Magnetic Anisotropy in Metallic Multilayers*, Rep. Prog. Phys. **59**, 1409 (1996).

[45] B. D. Cullity and C. D. Graham, *Induced Magnetic Anisotropy*, in *Introduction to Magnetic Materials* (John Wiley & Sons, Ltd, 2008), pp. 335–357.

[46] S. Blundell, *Magnetism in Condensed Matter* (OUP Oxford, 2001).

[47] P. Bruno and C. Chappert, *Oscillatory Coupling between Ferromagnetic Layers Separated by a Nonmagnetic Metal Spacer*, Phys. Rev. Lett. **67**, 1602 (1991).

[48] I. Dzyaloshinsky, *A Thermodynamic Theory of "Weak" Ferromagnetism of Antiferromagnetics*, Journal of Physics and Chemistry of Solids **4**, 241 (1958).

[49] T. Moriya, *Anisotropic Superexchange Interaction and Weak Ferromagnetism*, Phys. Rev. **120**, 91 (1960).

[50] A. Fert and P. M. Levy, *Role of Anisotropic Exchange Interactions in Determining the Properties of Spin-Glasses*, Phys. Rev. Lett. **44**, 1538 (1980).

[51] P. W. Anderson, *Antiferromagnetism. Theory of Superexchange Interaction*, Phys. Rev. **79**, 350 (1950).

[52] P. Weiss, *L'hypothèse Du Champ Moléculaire et La Propriété Ferromagnétique*, J. Phys. Theor. Appl. **6**, 661 (1907).

[53] B. D. Cullity and C. D. Graham, *Domains and the Magnetization Process*, in *Introduction to Magnetic Materials* (John Wiley & Sons, Ltd, 2008), pp. 275–333.

[54] F. Bloch, *Zur Theorie des Austauschproblems und der Remanenzerscheinung der Ferromagnetika*, Z. Physik **74**, 295 (1932).

[55] L. Landau and E. Lifshits, *ON THE THEORY OF THE DISPERSION OF MAGNETIC PERMEABILITY IN FERROMAGNETIC BODIES*, Ukr. J. Phys. **53**, (2008).

[56] L. Néel, *Some Theoretical Aspects of Rock-Magnetism*, Advances in Physics **4**, 191 (1955).

*References*

[57] D. Kumar, T. Jin, R. Sbiaa, M. Kläui, S. Bedanta, S. Fukami, D. Ravelosona, S.-H. Yang, X. Liu, and S. N. Piramanayagam, *Domain Wall Memory: Physics, Materials, and Devices*, Physics Reports **958**, 1 (2022).

[58] N. Chowdhury, S. Bedanta, and G. S. Babu, *Study of Magnetization Reversal Processes in a Thin Co Film*, Journal of Magnetism and Magnetic Materials **336**, 20 (2013).

[59] C. Appino, M. Valsania, and V. Basso, *A Vector Hysteresis Model Including Domain Wall Motion and Coherent Rotation*, Physica B: Condensed Matter **275**, 103 (2000).

[60] L. D. Landau and E. Lifshitz, *On the Theory of the Dispersion of Magnetic Permeability in Ferromagnetic Bodies*, Phys. Z. Sowjet. **8**, 153 (1935).

[61] T. L. Gilbert, *Classics in Magnetics A Phenomenological Theory of Damping in Ferromagnetic Materials*, IEEE Trans. Magn. **40**, 3443 (2004).

[62] L. Krusin-Elbaum, T. Shibauchi, B. Argyle, L. Gignac, T. Zabel, and D. Weller, *Dynamics of One-Dimensional Domain Walls Interacting with Disorder Potential*, Journal of Magnetism and Magnetic Materials **226–230**, 1317 (2001).

[63] T. Shibauchi, L. Krusin-Elbaum, V. M. Vinokur, B. Argyle, D. Weller, and B. D. Terris, *Deroughening of a 1D Domain Wall in an Ultrathin Magnetic Film by a Correlated Defect*, Phys. Rev. Lett. **87**, 267201 (2001).

[64] P. J. Metaxas, J. P. Jamet, A. Mougin, M. Cormier, J. Ferré, V. Baltz, B. Rodmacq, B. Dieny, and R. L. Stamps, *Creep and Flow Regimes of Magnetic Domain-Wall Motion in Ultrathin Pt / Co / Pt Films with Perpendicular Anisotropy*, Phys. Rev. Lett. **99**, 217208 (2007).

[65] T. Tybell, P. Paruch, T. Giamarchi, and J.-M. Triscone, *Domain Wall Creep in Epitaxial Ferroelectric P b ( Z r 0.2 T i 0.8 ) O 3 Thin Films*, Phys. Rev. Lett. **89**, 097601 (2002).

[66] M. A. Rubio, C. A. Edwards, A. Dougherty, and J. P. Gollub, *Self-Affine Fractal Interfaces from Immiscible Displacement in Porous Media*, Phys. Rev. Lett. **63**, 1685 (1989).

[67] T. Vicsek, M. Cserző, and V. K. Horváth, *Self-Affine Growth of Bacterial Colonies*, Physica A: Statistical Mechanics and Its Applications **167**, 315 (1990).

[68] D. A. Huse, C. L. Henley, and D. S. Fisher, *Huse, Henley, and Fisher Respond*, Phys. Rev. Lett. **55**, 2924 (1985).

[69] D. S. Fisher, *Interface Fluctuations in Disordered Systems: 5 − ε Expansion and Failure of Dimensional Reduction*, Phys. Rev. Lett. **56**, 1964 (1986).

[70] M. Kardar, G. Parisi, and Y.-C. Zhang, *Dynamic Scaling of Growing Interfaces*, Phys. Rev. Lett. **56**, 889 (1986).

[71] G. Blatter, M. V. Feigel'man, V. B. Geshkenbein, A. I. Larkin, and V. M. Vinokur, *Vortices in High-Temperature Superconductors*, Rev. Mod. Phys. **66**, 1125 (1994).

[72] G. S. D. Beach, C. Nistor, C. Knutson, M. Tsoi, and J. L. Erskine, *Dynamics of Field-Driven Domain-Wall Propagation in Ferromagnetic Nanowires*, Nature Mater **4**, 10 (2005).

[73] J. Gorchon, S. Bustingorry, J. Ferré, V. Jeudy, A. B. Kolton, and T. Giamarchi, *Pinning-Dependent Field-Driven Domain Wall Dynamics and Thermal Scaling in an Ultrathin Pt / Co / Pt Magnetic Film*, Phys. Rev. Lett. **113**, 027205 (2014).

[74] K. J. A. Franke, B. Van De Wiele, Y. Shirahata, S. J. Hämäläinen, T. Taniyama, and S. Van Dijken, *Reversible Electric-Field-Driven Magnetic Domain-Wall Motion*, Phys. Rev. X **5**, 011010 (2015).

# References

[75]     Z. Li and S. Zhang, *Domain-Wall Dynamics Driven by Adiabatic Spin-Transfer Torques*, Phys. Rev. B **70**, 024417 (2004).

[76]     M. Kläui, P.-O. Jubert, R. Allenspach, A. Bischof, J. A. C. Bland, G. Faini, U. Rüdiger, C. A. F. Vaz, L. Vila, and C. Vouille, *Direct Observation of Domain-Wall Configurations Transformed by Spin Currents*, Phys. Rev. Lett. **95**, 026601 (2005).

[77]     N. L. Schryer and L. R. Walker, *The Motion of 180° Domain Walls in Uniform Dc Magnetic Fields*, Journal of Applied Physics **45**, 5406 (1974).

[78]     A. Mougin, M. Cormier, J. P. Adam, P. J. Metaxas, and J. Ferré, *Domain Wall Mobility, Stability and Walker Breakdown in Magnetic Nanowires*, EPL **78**, 57007 (2007).

[79]     P. Chauve, T. Giamarchi, and P. Le Doussal, *Creep and Depinning in Disordered Media*, Phys. Rev. B **62**, 6241 (2000).

[80]     M. Yamanouchi, J. Ieda, F. Matsukura, S. E. Barnes, S. Maekawa, and H. Ohno, *Universality Classes for Domain Wall Motion in the Ferromagnetic Semiconductor (Ga,Mn)As*, Science **317**, 1726 (2007).

[81]     S. CHENATTUKUZHIYIL, Study of Domain Wall Dynamics in the Presence of Large Spin Orbit Coupling: Chiral Damping and Magnetic Origami, Doctoral Thesis, Grenoble Alpes University Community, 2015.

[82]     P. Metaxas, Domain Wall Dynamics in Ultrathin Ferromagnetic Film Structures: Disorder, Coupling and Periodic Pinning, Doctoral Thesis, 2009.

[83]     M. V. Feigel'man, V. B. Geshkenbein, A. I. Larkin, and V. M. Vinokur, *Theory of Collective Flux Creep*, Phys. Rev. Lett. **63**, 2303 (1989).

[84]     T. Nattermann, *Scaling Approach to Pinning: Charge Density Waves and Giant Flux Creep in Superconductors*, Phys. Rev. Lett. **64**, 2454 (1990).

[85]     S. Lemerle, J. Ferré, C. Chappert, V. Mathet, T. Giamarchi, and P. Le Doussal, *Domain Wall Creep in an Ising Ultrathin Magnetic Film*, Phys. Rev. Lett. **80**, 849 (1998).

[86]     M. Kardar, *Replica Bethe Ansatz Studies of Two-Dimensional Interfaces with Quenched Random Impurities*, Nuclear Physics B **290**, 582 (1987).

[87]     Y. Yamaguchi, G. Rajaram, N. Shirakawa, A. Mumtaz, H. Obara, T. Nakagawa, and H. Bando, *Vortex Creep Characteristics via Magnetic Relaxation of Bi2Sr2CaCu2O8+δ Crystals*, Physica C: Superconductivity **361**, 203 (2001).

[88]     S. Bustingorry, A. B. Kolton, and T. Giamarchi, *Thermal Rounding Exponent of the Depinning Transition of an Elastic String in a Random Medium*, Phys. Rev. E **85**, 021144 (2012).

[89]     R. Diaz Pardo, W. Savero Torres, A. B. Kolton, S. Bustingorry, and V. Jeudy, *Universal Depinning Transition of Domain Walls in Ultrathin Ferromagnets*, Phys. Rev. B **95**, 184434 (2017).

[90]     J. C. Slonczewski, *Theory of Domain-wall Motion in Magnetic Films and Platelets*, Journal of Applied Physics **44**, 1759 (2003).

[91]     S.-G. Je, D.-H. Kim, S.-C. Yoo, B.-C. Min, K.-J. Lee, and S.-B. Choe, *Asymmetric Magnetic Domain-Wall Motion by the Dzyaloshinskii-Moriya Interaction*, Phys. Rev. B **88**, 21 (2013).

[92]     O.-O. INYANG, Magnetic Proximity Effect and Interfacial Spin Dependent Transport in Ferromagnet/Heavy Metal Thin Films, Doctoral Thesis, Durham University, 2018.

[93]     N. Nakajima, T. Koide, T. Shidara, H. Miyauchi, H. Fukutani, A. Fujimori, K. Iio, T. Katayama, M. Nývlt, and Y. Suzuki, *Perpendicular Magnetic Anisotropy Caused by Interfacial Hybridization via*

*Enhanced Orbital Moment in Co / Pt Multilayers: Magnetic Circular X-Ray Dichroism Study*, Phys. Rev. Lett. **81**, 5229 (1998).

[94]    L. B. Niu, L. J. Chen, P. Chen, Y. T. Cui, Y. Zhang, M. Shao, and Y. X. Guan, *Hyperfine Interaction vs. Spin–Orbit Coupling in Organic Semiconductors*, RSC Adv. **6**, 111421 (2016).

[95]    X. Sun, A. Bedoya-Pinto, R. Llopis, F. Casanova, and L. E. Hueso, *Flexible Semi-Transparent Organic Spin Valve Based on Bathocuproine*, Applied Physics Letters **105**, 083302 (2014).

[96]    S. Sanvito, *The Rise of Spinterface Science*, Nature Phys **6**, 8 (2010).

[97]    E. Pandey, P. Sharangi, A. Sahoo, S. P. Mahanta, S. Mallik, and S. Bedanta, *A Perspective on Multifunctional Ferromagnet/Organic Molecule Spinterface*, Applied Physics Letters **123**, 040501 (2023).

[98]    C. Barraud et al., *Unravelling the Role of the Interface for Spin Injection into Organic Semiconductors*, Nature Phys **6**, 8 (2010).

[99]    M. Galbiati, S. Tatay, C. Barraud, A. V. Dediu, F. Petroff, R. Mattana, and P. Seneor, *Spinterface: Crafting Spintronics at the Molecular Scale*, MRS Bulletin **39**, 602 (2014).

[100]    S. Delprat, M. Galbiati, S. Tatay, B. Quinard, C. Barraud, F. Petroff, P. Seneor, and R. Mattana, *Molecular Spintronics: The Role of Spin-Dependent Hybridization*, J. Phys. D: Appl. Phys. **51**, 473001 (2018).

[101]    K. Seshan, *Handbook of Thin Film Deposition Processes and Techniques* (William Andrew, 2001).

[102]    O. O. Abegunde, E. T. Akinlabi, O. P. Oladijo, S. Akinlabi, A. U. Ude, O. O. Abegunde, E. T. Akinlabi, O. P. Oladijo, S. Akinlabi, and A. U. Ude, *Overview of Thin Film Deposition Techniques*, AIMSMATES **6**, 174 (2019).

[103]    J. E. Mahan, *Physical Vapor Deposition of Thin Films* (Wiley-VCH, 2000).

[104]    T. M. Besmann, D. P. Stinton, and R. A. Lowden, *Chemical Vapor Deposition Techniques*, MRS Bull. **13**, 45 (1988).

[105]    G. Bräuer, B. Szyszka, M. Vergöhl, and R. Bandorf, *Magnetron Sputtering – Milestones of 30 Years*, Vacuum **84**, 1354 (2010).

[106]    J. Musil, *Recent Advances in Magnetron Sputtering Technology*, Surface and Coatings Technology **100–101**, 280 (1998).

[107]    P. D. Davidse, *Theory and Practice of RF Sputtering*, Vacuum **17**, 139 (1967).

[108]    K. S. Sree Harsha, *Chapter 2 - Evaporation*, in *Principles of Vapor Deposition of Thin Films*, edited by K. S. Sree Harsha (Elsevier, Oxford, 2006), pp. 11–143.

[109]    K. S. Sree Harsha, *Chapter 5 - Thermal Evaporation Sources*, in *Principles of Vapor Deposition of Thin Films*, edited by K. S. Sree Harsha (Elsevier, Oxford, 2006), pp. 367–452.

[110]    E. S. Ameh, *A Review of Basic Crystallography and X-Ray Diffraction Applications*, Int. J. Adv. Manuf. Technol. **105**, 3289 (2019).

[111]    G. F. Harrington and J. Santiso, *Back-to-Basics Tutorial: X-Ray Diffraction of Thin Films*, J. Electroceramics **47**, 141 (2021).

[112]    W. H. Bragg and W. L. Bragg, *The Reflection of X-Rays by Crystals*, Proc. R. Soc. Lond. A **88**, 428 (1913).

[113]    K. Inaba, *X-Ray Thin-FIlm Measurement Techniques*, The Rigaku Journal **24**, 10 (2008).

## References

[114]   M. Yasaka, *X-Ray Thin-FIlm Measurement Techniques*, The Rigaku Journal **26**, 1 (2010).

[115]   S. A. Veldhuis, P. Brinks, T. M. Stawski, O. F. Göbel, and J. E. ten Elshof, *A Facile Method for the Density Determination of Ceramic Thin Films Using X-Ray Reflectivity*, J. Sol-Gel Sci. Technol. **71**, 118 (2014).

[116]   T. P. Russell, *X-Ray and Neutron Reflectivity for the Investigation of Polymers*, Materials Science Reports **5**, 171 (1990).

[117]   Y. Fujii, *Recent Developments in the X-Ray Reflectivity Analysis for Rough Surfaces and Interfaces of Multilayered Thin Film Materials*, Journal of Materials **2013**, 1 (2013).

[118]   M. Björck and G. Andersson, *GenX: An Extensible X-Ray Reflectivity Refinement Program Utilizing Differential Evolution*, J. Appl. Cryst. **40**, 6 (2007).

[119]   L. G. Parratt, *Surface Studies of Solids by Total Reflection of X-Rays*, Phys. Rev. **95**, 359 (1954).

[120]   B. J. Inkson, *2 - Scanning Electron Microscopy (SEM) and Transmission Electron Microscopy (TEM) for Materials Characterization*, in *Materials Characterization Using Nondestructive Evaluation (NDE) Methods*, edited by G. Hübschen, I. Altpeter, R. Tschuncky, and H.-G. Herrmann (Woodhead Publishing, 2016), pp. 17–43.

[121]   A. Ul-Hamid, *A Beginners' Guide to Scanning Electron Microscopy* (Springer International Publishing, Cham, 2018).

[122]   M. M. Freundlich, *Origin of the Electron Microscope: The History of a Great Invention, and of a Misconception Concerning the Inventors, Is Reviewed.*, Science **142**, 185 (1963).

[123]   R. Schäfer, *Investigation of Domains and Dynamics of Domain Walls by the Magneto-Optical Kerr-Effect*, in *Handbook of Magnetism and Advanced Magnetic Materials*, edited by H. Kronmüller and S. Parkin, Vol. 3 (John Wiley & Sons, Ltd, Chichester, UK, 2007), pp. 1–29.

[124]   J. McCord, *Progress in Magnetic Domain Observation by Advanced Magneto-Optical Microscopy*, Journal of Physics D: Applied Physics **48**, 333001 (2015).

[125]   Z. Q. Qiu and S. D. Bader, *Surface Magneto-Optic Kerr Effect*, Review of Scientific Instruments **71**, 1243 (2000).

[126]   J. Kerr, *XLIII.* On Rotation of the Plane of Polarization by Reflection from the Pole of a Magnet, The London, Edinburgh, and Dublin Philosophical Magazine and Journal of Science **3**, 321 (1877).

[127]   J. Kerr, *XXIV.* On Reflection of Polarized Light from the Equatorial Surface of a Magnet, The London, Edinburgh, and Dublin Philosophical Magazine and Journal of Science **5**, 161 (1878).

[128]   T. Haider, *A Review of Magneto-Optic Effects and Its Application*, Int. J. Electromagn. Appl **7**, 17 (2017).

[129]   S. Bedanta, Supermagnetism in Magnetic Nanoparticle Systems, PhD Thesis, 2007.

[130]   I. V. Soldatov and R. Schäfer, *Selective Sensitivity in Kerr Microscopy*, Review of Scientific Instruments **88**, 073701 (2017).

[131]   S. S. P. Parkin, M. Hayashi, and L. Thomas, *Magnetic Domain-Wall Racetrack Memory*, Science **320**, 190 (2008).

[132]   X. Wang and Y. Chen, *Spintronic Memristor Devices and Application*, in *2010 Design, Automation & Test in Europe Conference & Exhibition (DATE 2010)* (2010), pp. 667–672.

[133]   D. A. Allwood, G. Xiong, C. C. Faulkner, D. Atkinson, D. Petit, and R. P. Cowburn, *Magnetic Domain-Wall Logic*, Science **309**, 1688 (2005).

# References

[134]  A. Hrabec, N. A. Porter, A. Wells, M. J. Benitez, G. Burnell, S. McVitie, D. McGrouther, T. A. Moore, and C. H. Marrows, *Measuring and Tailoring the Dzyaloshinskii-Moriya Interaction in Perpendicularly Magnetized Thin Films*, Phys. Rev. B **90**, 020402 (2014).

[135]  C. Moreau-Luchaire et al., *Additive Interfacial Chiral Interaction in Multilayers for Stabilization of Small Individual Skyrmions at Room Temperature*, Nature Nanotech **11**, 5 (2016).

[136]  A. Thiaville, S. Rohart, É. Jué, V. Cros, and A. Fert, *Dynamics of Dzyaloshinskii Domain Walls in Ultrathin Magnetic Films*, EPL **100**, 57002 (2012).

[137]  D.-Y. Kim, D.-H. Kim, J. Moon, and S.-B. Choe, *Determination of Magnetic Domain-Wall Types Using Dzyaloshinskii–Moriya-Interaction-Induced Domain Patterns*, Applied Physics Letters **106**, 262403 (2015).

[138]  R. L. Fagaly, *Superconducting Quantum Interference Device Instruments and Applications*, Review of Scientific Instruments **77**, 101101 (2006).

[139]  M. Schmelz and R. Stolz, *Superconducting Quantum Interference Device (SQUID) Magnetometers*, in *High Sensitivity Magnetometers*, edited by A. Grosz, M. J. Haji-Sheikh, and S. C. Mukhopadhyay (Springer International Publishing, Cham, 2017), pp. 279–311.

[140]  C. Ryu, E. C. Samson, and M. G. Boshier, *Quantum Interference of Currents in an Atomtronic SQUID*, Nat Commun **11**, 1 (2020).

[141]  T. Funk, A. Deb, S. J. George, H. Wang, and S. P. Cramer, *X-Ray Magnetic Circular Dichroism—a High Energy Probe of Magnetic Properties*, Coordination Chemistry Reviews **249**, 3 (2005).

[142]  J. Stöhr, *X-Ray Magnetic Circular Dichroism Spectroscopy of Transition Metal Thin Films*, Journal of Electron Spectroscopy and Related Phenomena **75**, 253 (1995).

[143]  G. van der Laan and A. I. Figueroa, *X-Ray Magnetic Circular Dichroism—A Versatile Tool to Study Magnetism*, Coordination Chemistry Reviews **277**, 95 (2014).

[144]  H. Wende, *Recent Advances in X-Ray Absorption Spectroscopy*, Reports on Progress in Physics **67**, 2105 (2004).

[145]  J. Stöhr, *Exploring the Microscopic Origin of Magnetic Anisotropies with X-Ray Magnetic Circular Dichroism (XMCD) Spectroscopy*, Journal of Magnetism and Magnetic Materials **200**, 470 (1999).

[146]  B. T. Thole, P. Carra, F. Sette, and G. Van Der Laan, *X-Ray Circular Dichroism as a Probe of Orbital Magnetization*, Phys. Rev. Lett. **68**, 1943 (1992).

[147]  C. T. Chen, Y. U. Idzerda, H.-J. Lin, N. V. Smith, G. Meigs, E. Chaban, G. H. Ho, E. Pellegrin, and F. Sette, *Experimental Confirmation of the X-Ray Magnetic Circular Dichroism Sum Rules for Iron and Cobalt*, Phys. Rev. Lett. **75**, 152 (1995).

[148]  M. Zangrando, M. Finazzi, G. Paolucci, G. Comelli, B. Diviacco, R. P. Walker, D. Cocco, and F. Parmigiani, *BACH, the Beamline for Advanced Dichroic and Scattering Experiments at ELETTRA*, Review of Scientific Instruments **72**, 1313 (2001).

[149]  M. Zangrando, M. Finazzi, F. Parmigiani, G. Paolucci, and D. Cocco, *Optical Layout of BACH: A Beamline for Advanced Dichroism at Elettra*, Proceedings of SPIE - The International Society for Optical Engineering **4146**, (2000).

[150]  *Elettra Sincrotrone Trieste*, https://www.elettra.eu/lightsources/elettra/elettra-beamlines/bach/bach-beamline-description.html?showall=.

## References

[151]    I. Miccoli, F. Edler, H. Pfnür, and C. Tegenkamp, *The 100th Anniversary of the Four-Point Probe Technique: The Role of Probe Geometries in Isotropic and Anisotropic Systems*, J. Phys.: Condens. Matter **27**, 223201 (2015).

[152]    M. Naftaly, S. Das, J. Gallop, K. Pan, F. Alkhalil, D. Kariyapperuma, S. Constant, C. Ramsdale, and L. Hao, *Sheet Resistance Measurements of Conductive Thin Films: A Comparison of Techniques*, Electronics **10**, 8 (2021).

[153]    J. Zhao, C. He, R. Yang, Z. Shi, M. Cheng, W. Yang, G. Xie, D. Wang, D. Shi, and G. Zhang, *Ultra-Sensitive Strain Sensors Based on Piezoresistive Nanographene Films*, Applied Physics Letters **101**, 063112 (2012).

[154]    G. Dai, Q. Zhan, Y. Liu, H. Yang, X. Zhang, B. Chen, and R.-W. Li, *Mechanically Tunable Magnetic Properties of Fe81Ga19 Films Grown on Flexible Substrates*, Applied Physics Letters **100**, 122407 (2012).

[155]    Z. Suo, E. Y. Ma, H. Gleskova, and S. Wagner, *Mechanics of Rollable and Foldable Film-on-Foil Electronics*, Applied Physics Letters **74**, 1177 (1999).

[156]    S. Merabtine, F. Zighem, A. Garcia-Sanchez, V. Gunasekaran, M. Belmeguenai, X. Zhou, P. Lupo, A. O. Adeyeye, and D. Faurie, *Origin of Relationship between Ferromagnetic Response and Damage in Stretched Systems*, Sci Rep **8**, 1 (2018).

[157]    R. Huang, *Kinetic Wrinkling of an Elastic Film on a Viscoelastic Substrate*, Journal of the Mechanics and Physics of Solids **53**, 63 (2005).

[158]    A. Panin and A. Shugurov, *Multi-Level Deformation of Thin Films Caused by Stress–Strain Distribution at the Film-Substrate Interface*, Procedia Engineering **1**, 23 (2009).

[159]    H. Mei, Y. Pang, S. H. Im, and R. Huang, *Fracture, Delamination, and Buckling of Elastic Thin Films on Compliant Substrates*, in *2008 11th Intersociety Conference on Thermal and Thermomechanical Phenomena in Electronic Systems* (2008), pp. 762–769.

[160]    D. Faurie, F. Zighem, A. Garcia-Sanchez, P. Lupo, and A. O. Adeyeye, *Fragmentation and Adhesion Properties of CoFeB Thin Films on Polyimide Substrate*, Applied Physics Letters **110**, 091904 (2017).

[161]    L. P. Buchwalter and K. Holloway, *Tantalum, Tantalum Nitride, and Chromium Adhesion to Polyimide: Effect of Annealing Ambient on Adhesion*, Journal of Adhesion Science and Technology **12**, 95 (1998).

[162]    P. M. Shepley, A. W. Rushforth, M. Wang, G. Burnell, and T. A. Moore, *Modification of Perpendicular Magnetic Anisotropy and Domain Wall Velocity in Pt/Co/Pt by Voltage-Induced Strain*, Sci Rep **5**, 1 (2015).

[163]    Alex Hubert and Rudolf Schäfer, *Magnetic Domains* (Springer, Berlin, Heidelberg, 1998).

[164]    D. B. Gopman, C. L. Dennis, P. J. Chen, Y. L. Iunin, P. Finkel, M. Staruch, and R. D. Shull, *Strain-Assisted Magnetization Reversal in Co/Ni Multilayers with Perpendicular Magnetic Anisotropy*, Sci Rep **6**, 1 (2016).

[165]    G. Dai, X. Xing, Y. Shen, and X. Deng, *Stress Tunable Magnetic Stripe Domains in Flexible Fe81Ga19 Films*, J. Phys. D: Appl. Phys. **53**, 055001 (2019).

[166]    R. Streubel, P. Fischer, F. Kronast, V. P. Kravchuk, D. D. Sheka, Y. Gaididei, O. G. Schmidt, and D. Makarov, *Magnetism in Curved Geometries*, J. Phys. D: Appl. Phys. **49**, 363001 (2016).

[167]    R. Prozorov, Y. Yeshurun, T. Prozorov, and A. Gedanken, *Magnetic Irreversibility and Relaxation in Assembly of Ferromagnetic Nanoparticles*, Phys. Rev. B **59**, 6956 (1999).

References

[168]   S. Mallick and S. Bedanta, *Size and Shape Dependence Study of Magnetization Reversal in Magnetic Antidot Lattice Arrays*, Journal of Magnetism and Magnetic Materials **382**, 158 (2015).

[169]   N. Chowdhury, S. Mallick, S. Mallik, and S. Bedanta, *Study of Magnetization Relaxation in Co Thin Films Prepared by Substrate Rotation*, Thin Solid Films **616**, 328 (2016).

[170]   E. Fatuzzo, *Theoretical Considerations on the Switching Transient in Ferroelectrics*, Phys. Rev. **127**, 1999 (1962).

[171]   M. Labrune, S. Andrieu, F. Rio, and P. Bernstein, *Time Dependence of the Magnetization Process of RE-TM Alloys*, Journal of Magnetism and Magnetic Materials **80**, 211 (1989).

[172]   H. Xi, K.-Z. Gao, J. Ouyang, Y. Shi, and Y. Yang, *Slow Magnetization Relaxation and Reversal in Magnetic Thin Films*, J. Phys.: Condens. Matter **20**, 295220 (2008).

[173]   A. A. Bukharaev, A. K. Zvezdin, A. P. Pyatakov, and Y. K. Fetisov, *Straintronics: A New Trend in Micro- and Nanoelectronics and Materials Science*, Phys.-Usp. **61**, 1175 (2018).

[174]   D. Makarov, M. Melzer, D. Karnaushenko, and O. G. Schmidt, *Shapeable Magnetoelectronics*, Applied Physics Reviews **3**, 011101 (2016).

[175]   B. Peng et al., *Deterministic Switching of Perpendicular Magnetic Anisotropy by Voltage Control of Spin Reorientation Transition in (Co/Pt)3/Pb(Mg1/3Nb2/3)O3–PbTiO3 Multiferroic Heterostructures*, ACS Nano **11**, 4 (2017).

[176]   Z. Li, Y. Zhang, Y. Huang, C. Wang, X. Zhang, Y. Liu, Y. Zhou, W. Kang, S. C. Koli, and N. Lei, *Strain-Controlled Skyrmion Creation and Propagation in Ferroelectric/Ferromagnetic Hybrid Wires*, Journal of Magnetism and Magnetic Materials **455**, 19 (2018).

[177]   S. Hashimoto, Y. Ochiai, and K. Aso, *Perpendicular Magnetic Anisotropy and Magnetostriction of Sputtered Co/Pd and Co/Pt Multilayered Films*, Journal of Applied Physics **66**, 4909 (1989).

[178]   H. Takahashi, S. Tsunashima, S. Iwata, and S. Uchiyama, *Measurement of Magnetostriction Constants in Polycrystalline Alloy and Multilayer Films of PdCo and PtCo*, Journal of Magnetism and Magnetic Materials **126**, 282 (1993).

[179]   H. Matsumoto, S. Ota, T. Koyama, and D. Chiba, *Control of Magnetic Anisotropy in a Co Thin Film on a Flexible Substrate by Applying Biaxial Tensile Strain*, Applied Physics Letters **118**, 022406 (2021).

[180]   A. Adanlété Adjanoh, R. Belhi, J. Vogel, M. Ayadi, and K. Abdelmoula, *Compressed Exponential Form for Disordered Domain Wall Motion in Ultra-Thin Au/Co/Au Ferromagnetic Films*, Journal of Magnetism and Magnetic Materials **323**, 504 (2011).

[181]   G. Catalan, J. Seidel, R. Ramesh, and J. F. Scott, *Domain Wall Nanoelectronics*, Rev. Mod. Phys. **84**, 119 (2012).

[182]   E.-J. Guo, R. Roth, A. Herklotz, D. Hesse, and K. Dörr, *Ferroelectric 180° Domain Wall Motion Controlled by Biaxial Strain*, Advanced Materials **27**, 1615 (2015).

[183]   P. M. Shepley, A. W. Rushforth, M. Wang, G. Burnell, and T. A. Moore, *Modification of Perpendicular Magnetic Anisotropy and Domain Wall Velocity in Pt/Co/Pt by Voltage-Induced Strain*, Sci Rep **5**, 7921 (2015).

[184]   D. Weller, Y. Wu, J. Stöhr, M. G. Samant, B. D. Hermsmeier, and C. Chappert, *Orbital Magnetic Moments of Co in Multilayers with Perpendicular Magnetic Anisotropy*, Phys. Rev. B **49**, 12888 (1994).

[185]   D. Wang, R. Wu, and A. J. Freeman, *Magnetocrystalline Anisotropy of Co-Pd Interfaces*, Phys. Rev. B **48**, 15886 (1993).

*References*

[186]  Y. Liu, A. P. Chen, L. Ren, Y. Liu, S. Srivastava, H. Yang, Y. P. Feng, and K. L. Teo, *Engineering Interfacial Perpendicular Magnetic Anisotropy in Fe2CoSi/Pt Multilayers with Interfacial Strain and Orbital Hybridization*, ACS Appl. Electron. Mater. **1**, 1251 (2019).

[187]  Z. Zhang et al., *Strain-Controlled Spin Wave Excitation and Gilbert Damping in Flexible Co2FeSi Films Activated by Femtosecond Laser Pulse*, Advanced Functional Materials **31**, 2007211 (2021).

[188]  K. Tao, P. Liu, Q. Guo, L. Shen, D. Xue, O. P. Polyakov, and V. S. Stepanyuk, *Engineering Magnetic Anisotropy and Magnetization Switching in Multilayers by Strain*, Phys. Chem. Chem. Phys. **19**, 4125 (2017).

[189]  Z. Bao and X. Chen, *Flexible and Stretchable Devices*, Advanced Materials **28**, 4177 (2016).

[190]  Y.-H. Duan, Y. Duan, X. Wang, D. Yang, Y.-Q. Yang, P. Chen, F.-B. Sun, K.-W. Xue, and Y. Zhao, *Highly Flexible Peeled-off Silver Nanowire Transparent Anode Using in Organic Light-Emitting Devices*, Applied Surface Science **351**, 445 (2015).

[191]  Y. Huang, H. Liu, Z. Xu, J. Chen, and Z. Yin, *Conformal Peeling of Device-on-Substrate System in Flexible Electronic Assembly*, IEEE Trans. Compon., Packag. Manufact. Technol. **8**, 1496 (2018).

[192]  J.-K. Yang, Y.-J. Lee, S.-M. Yi, B.-J. Kim, and Y.-C. Joo, *Effect of Twisting Fatigue on the Electrical Reliability of a Metal Interconnect on a Flexible Substrate*, Journal of Materials Research **33**, 138 (2018).

[193]  S. Hong, V. P. Rachim, J.-H. Baek, and S.-M. Park, *Real-Time Multiaxial Strain Mapping Using Computer Vision Integrated Optical Sensors*, Npj Flex Electron **7**, 1 (2023).

[194]  K. Kendall, *The Adhesion and Surface Energy of Elastic Solids*, J. Phys. D: Appl. Phys. **4**, 1186 (1971).

[195]  K. Kendall, *Thin-Film Peeling-the Elastic Term*, J. Phys. D: Appl. Phys. **8**, 1449 (1975).

[196]  C. H. Lee, J.-H. Kim, C. Zou, I. S. Cho, J. M. Weisse, W. Nemeth, Q. Wang, A. C. T. van Duin, T.-S. Kim, and X. Zheng, *Peel-and-Stick: Mechanism Study for Efficient Fabrication of Flexible/Transparent Thin-Film Electronics*, Sci Rep **3**, 1 (2013).

[197]  Y. Ni, S. Yu, H. Jiang, and L. He, *The Shape of Telephone Cord Blisters*, Nat Commun **8**, 1 (2017).

[198]  H. Yang, A. Thiaville, S. Rohart, A. Fert, and M. Chshiev, *Anatomy of Dzyaloshinskii-Moriya Interaction at $\mathrm{Co}/\mathrm{Pt}$ Interfaces*, Phys. Rev. Lett. **115**, 267210 (2015).

[199]  A. V. Davydenko, A. G. Kozlov, M. E. Stebliy, A. G. Kolesnikov, N. I. Sarnavskiy, I. G. Iliushin, and A. P. Golikov, *Dzyaloshinskii-Moriya Interaction and Chiral Damping Effect in Symmetric Epitaxial Pd/Co/Pd(111) Trilayers*, Phys. Rev. B **103**, 094435 (2021).

[200]  T. D. Nguyen, F. Wang, X.-G. Li, E. Ehrenfreund, and Z. V. Vardeny, *Spin Diffusion in Fullerene-Based Devices: Morphology Effect*, Phys. Rev. B **87**, 075205 (2013).

[201]  H. Liu, J. Wang, A. Chanana, and Z. V. Vardeny, *Studies of Spin Transport in Fullerene Films*, Journal of Applied Physics **125**, 142908 (2019).

[202]  W. Han, R. K. Kawakami, M. Gmitra, and J. Fabian, *Graphene Spintronics*, Nature Nanotech **9**, 794 (2014).

[203]  P. Chen and G. Zhang, *Carbon-Based Spintronics*, Sci. China Phys. Mech. Astron. **56**, 207 (2013).

[204]  L. Guo, Y. Qin, X. Gu, X. Zhu, Q. Zhou, and X. Sun, *Spin Transport in Organic Molecules*, Frontiers in Chemistry **7**, (2019).

*References*

[205]    E. Pandey, P. Sharangi, A. Sahoo, S. P. Mahanta, S. Mallik, and S. Bedanta, *A Perspective on Multifunctional Ferromagnet/Organic Molecule Spinterface*, Applied Physics Letters **123**, 040501 (2023).

[206]    S. Mallik, S. Mattauch, M. K. Dalai, T. Brückel, and S. Bedanta, *Effect of Magnetic Fullerene on Magnetization Reversal Created at the Fe/C60 Interface*, Sci Rep **8**, 1 (2018).

[207]    O. G. Udalov and I. S. Beloborodov, *Strain-Dependent Dzyaloshinskii-Moriya Interaction in a Ferromagnet/Heavy-Metal Bilayer*, Phys. Rev. B **102**, 134422 (2020).

[208]    E. Pandey, B. Ojha, and S. Bedanta, *Emergence of Sizeable Interfacial Dzyaloshinskii-Moriya Interaction at Cobalt/Fullerene Interface*, Phys. Rev. Appl. **19**, 044013 (2023).

[209]    J. Okabayashi, Y. Miura, and H. Munekata, *Anatomy of Interfacial Spin-Orbit Coupling in Co/Pd Multilayers Using X-Ray Magnetic Circular Dichroism and First-Principles Calculations*, Sci Rep **8**, 1 (2018).

[210]    K. Bairagi et al., *Tuning the Magnetic Anisotropy at a Molecule-Metal Interface*, Phys. Rev. Lett. **114**, 24 (2015).

[211]    M. T. Johnson, P. J. H. Bloemen, F. J. A. den Broeder, and J. J. de Vries, *Magnetic Anisotropy in Metallic Multilayers*, Rep. Prog. Phys. **59**, 1409 (1996).

[212]    S. K. Tiwari, V. Kumar, A. Huczko, R. Oraon, A. D. Adhikari, and G. C. Nayak, *Magical Allotropes of Carbon: Prospects and Applications*, Critical Reviews in Solid State and Materials Sciences **41**, 257 (2016).

[213]    K. Bairagi et al., *Experimental and Theoretical Investigations of Magnetic Anisotropy and Magnetic Hardening at Molecule/Ferromagnet Interfaces*, Phys. Rev. B **98**, 8 (2018).

[214]    A. V. Davydenko, A. G. Kozlov, A. G. Kolesnikov, M. E. Stebliy, G. S. Suslin, Yu. E. Vekovshinin, A. V. Sadovnikov, and S. A. Nikitov, *Dzyaloshinskii-Moriya Interaction in Symmetric Epitaxial ${[\mathrm{Co}/\mathrm{Pd}(111)]}_{N}$ Superlattices with Different Numbers of Co/Pd Bilayers*, Phys. Rev. B **99**, 014433 (2019).

[215]    D.-Y. Kim, D.-H. Kim, J. Moon, and S.-B. Choe, *Determination of Magnetic Domain-Wall Types Using Dzyaloshinskii–Moriya-Interaction-Induced Domain Patterns*, Appl. Phys. Lett. **106**, 262403 (2015).

[216]    F. Ajejas, Y. Sassi, W. Legrand, S. Collin, J. Peña Garcia, A. Thiaville, S. Pizzini, N. Reyren, V. Cros, and A. Fert, *Interfacial Potential Gradient Modulates Dzyaloshinskii-Moriya Interaction in Pt/Co/Metal Multilayers*, Phys. Rev. Mater. **6**, L071401 (2022).

[217]    D. Li et al., *Current-Induced Domain Wall Motion and Tilting in Perpendicularly Magnetized Racetracks*, Nanoscale Research Letters **13**, 1 (2018).

[218]    D. A. Dugato, J. Brandão, R. L. Seeger, F. Béron, J. C. Cezar, L. S. Dorneles, and T. J. A. Mori, *Magnetic Domain Size Tuning in Asymmetric Pd/Co/W/Pd Multilayers with Perpendicular Magnetic Anisotropy*, Applied Physics Letters **115**, 182408 (2019).

[219]    A. G. Kozlov, A. G. Kolesnikov, M. E. Stebliy, A. P. Golikov, and A. V. Davydenko, *Domain-Period Method for Determination of the Energy of the Dzyaloshinskii-Moriya Interaction in ${[\mathrm{Co}\text{/}\mathrm{Pd}(111)]}_{5}$ Superlattices*, Phys. Rev. B **102**, 144411 (2020).

[220]    A. Barman, S. Wang, O. Hellwig, A. Berger, E. E. Fullerton, and H. Schmidt, *Ultrafast Magnetization Dynamics in High Perpendicular Anisotropy [Co/Pt]n Multilayers*, Journal of Applied Physics **101**, 09D102 (2007).

[221]    N. Siadou, M. Androutsopoulos, I. Panagiotopoulos, L. Stoleriu, A. Stancu, T. Bakas, and V. Alexandrakis, *Magnetization Reversal in [Ni/Pt]6/Pt(x)/[Co/Pt]6 Multilayers*, Journal of Magnetism and Magnetic Materials **323**, 1671 (2011).

# References

[222]   R. Sbiaa, Z. Bilin, M. Ranjbar, H. K. Tan, S. J. Wong, S. N. Piramanayagam, and T. C. Chong, *Effect of Magnetostatic Energy on Domain Structure and Magnetization Reversal in (Co/Pd) Multilayers*, Journal of Applied Physics **107**, 103901 (2010).

[223]   S. D. Pollard, J. A. Garlow, J. Yu, Z. Wang, Y. Zhu, and H. Yang, *Observation of Stable Néel Skyrmions in Cobalt/Palladium Multilayers with Lorentz Transmission Electron Microscopy*, Nat Commun **8**, 14761 (2017).

[224]   S. Woo et al., *Observation of Room-Temperature Magnetic Skyrmions and Their Current-Driven Dynamics in Ultrathin Metallic Ferromagnets*, Nature Mater **15**, 5 (2016).

[225]   A. Samardak, A. Kolesnikov, M. Stebliy, L. Chebotkevich, A. Sadovnikov, S. Nikitov, A. Talapatra, J. Mohanty, and A. Ognev, *Enhanced Interfacial Dzyaloshinskii-Moriya Interaction and Isolated Skyrmions in the Inversion-Symmetry-Broken Ru/Co/W/Ru Films*, Applied Physics Letters **112**, 192406 (2018).

[226]   X. Ma, G. Yu, S. A. Razavi, L. Chang, L. Deng, Z. Chu, C. He, K. L. Wang, and X. Li, *Correlation between the Dzyaloshinskii-Moriya Interaction and Spin-Mixing Conductance at an Antiferromagnet/Ferromagnet Interface*, Phys. Rev. B **98**, 104428 (2018).

[227]   C. Deger, *Strain-Enhanced Dzyaloshinskii–Moriya Interaction at Co/Pt Interfaces*, Sci Rep **10**, 1 (2020).

[228]   Z. Xu, Q. Liu, Y. Ji, X. Li, J. Li, J. Wang, and L. Chen, *Strain-Tunable Interfacial Dzyaloshinskii–Moriya Interaction and Spin-Hall Topological Hall Effect in Pt/Tm $_3$ Fe $_5$ O $_{12}$ Heterostructures*, ACS Appl. Mater. Interfaces **14**, 16791 (2022).

[229]   Y. Zhang et al., *Strain-Driven Dzyaloshinskii-Moriya Interaction for Room-Temperature Magnetic Skyrmions*, Phys. Rev. Lett. **127**, 117204 (2021).

[230]   A. Vansteenkiste and B. Van de Wiele, *MuMax: A New High-Performance Micromagnetic Simulation Tool*, Journal of Magnetism and Magnetic Materials **323**, 2585 (2011).

[231]   A. Vansteenkiste, J. Leliaert, M. Dvornik, M. Helsen, F. Garcia-Sanchez, and B. Van Waeyenberge, *The Design and Verification of MuMax3*, AIP Advances **4**, 107133 (2014).

[232]   *The Go Programming Language*, https://go.dev/.

[233]   *CUDA Toolkit Documentation 12.2*, https://docs.nvidia.com/cuda/index.html.